Synthesis-Structure-Performance Relationships for Supported Metal Catalysts

Peter Munnik

ISBN: 978-90-393-6233-4

Synthesis-Structure-Performance Relationships for Supported Metal Catalysts

Relatie tussen Synthese, Structuur en Prestaties van Gedragen Metaalkatalysatoren

(met een samenvatting in het Nederlands)

Proefschrift

ter verkrijging van de graad van doctor aan de Universiteit Utrecht op gezag van de rector magnificus, prof.dr. G.J. van der Zwaan, ingevolge het besluit van het college voor promoties in het openbaar te verdedigen op woensdag 19 november 2014 des middags te 2.30 uur.

door

Peter Munnik

geboren op 4 oktober 1985 te De Bilt

Promotoren: Prof. dr. ir. K.P. de Jong
Prof. dr. P.E. de Jongh

Dit proefschrift werd (mede) mogelijk gemaakt met financiële steun van de Nederlandse Organisatie voor Wetenschappelijk Onderzoek (TOP/ECHO 700.57.341).

Contents

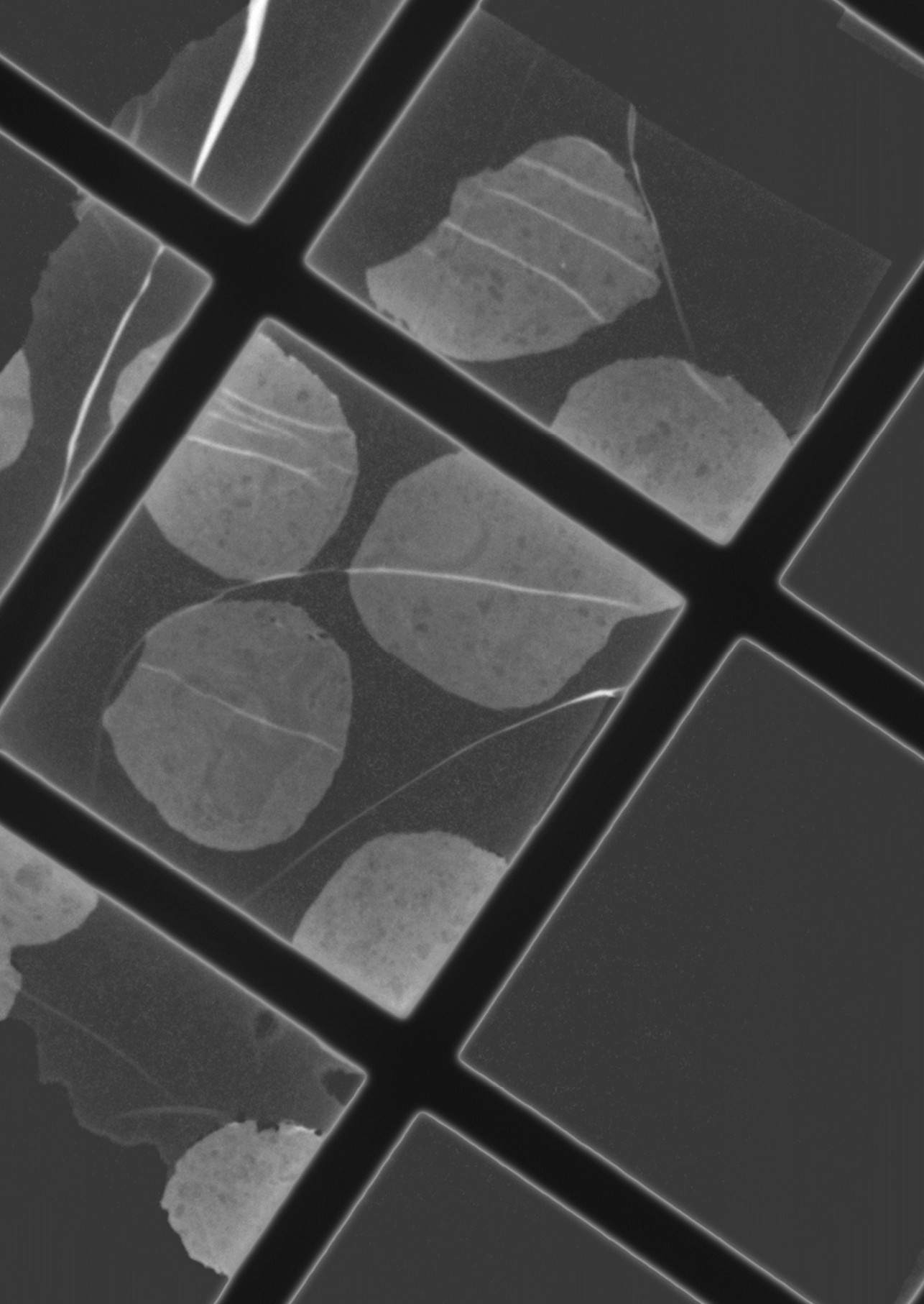

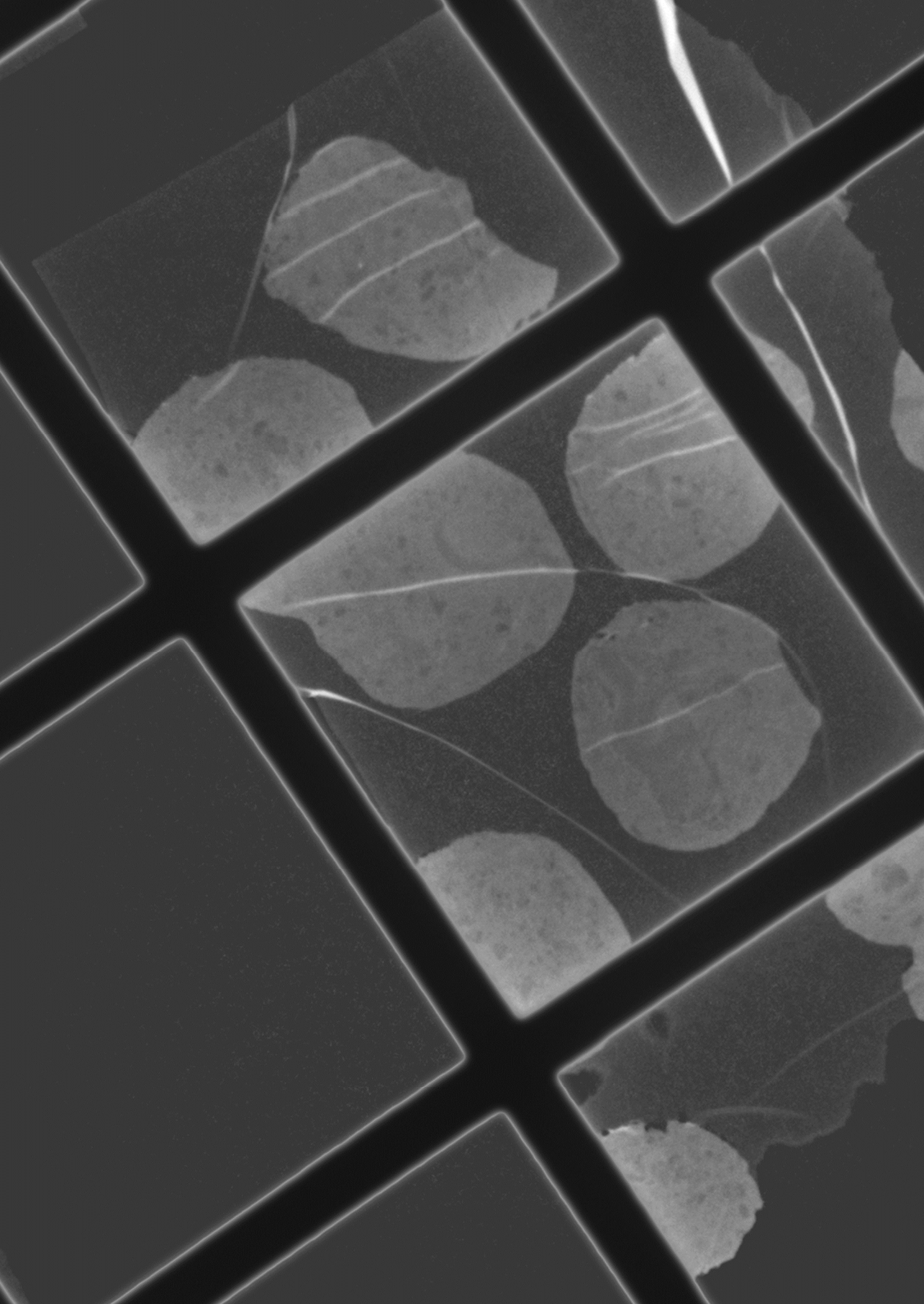

Chapter 1

General Introduction

CATALYSIS

With the growing world population there is an increasing demand for energy. As of today, the majority of this energy comes from fossil fuels: coal, natural gas and oil (Figure 1.1).[1] Moreover, the transportation sector is almost exclusively reliant on liquid transportation fuels produced from oil. However, oil is a finite resource, and at the current rate of production, the known oil reserves will be depleted in roughly 55 years.[1] This does not mean that oil will be gone in 55 years; new reserves are still being found and techniques are constantly developed to more efficiently recover oil from known fields. Combined with more fuel efficient cars, reducing fuel consumption per distance travelled, the period in which oil is readily available is likely more extensive. However, reserves will eventually deplete. Natural gas and coal are equally or even more abundant, so that using these as a feedstock for fuels could extend this period significantly. Using biomass, preferably non-competing with the world food production, could even result in a renewable cycle. However, it is not possible to simply put these alternative feedstocks directly into the process plants currently used for oil, much less in a regular engine, and conversion of these alternative feedstocks to fuels is not facile.

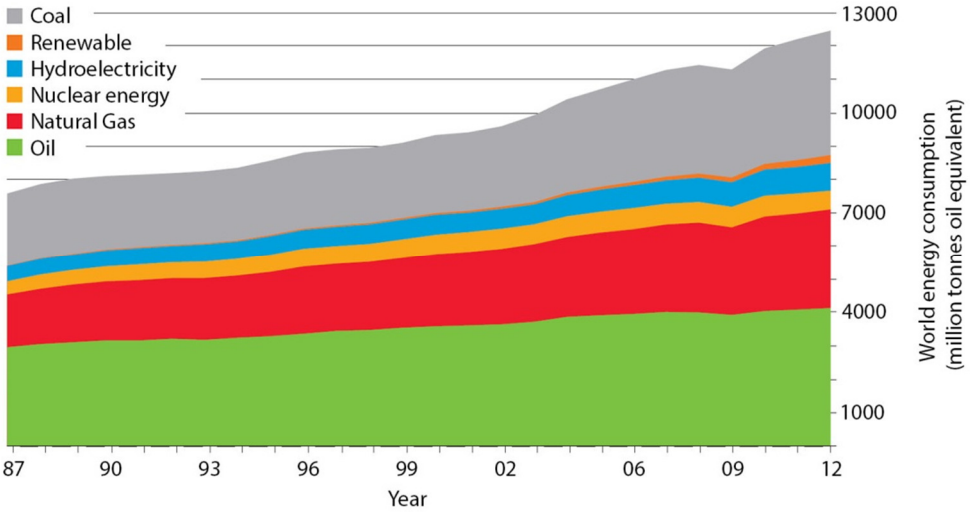

Figure 1.1. World energy consumption development over time in million tonnes of oil equivalent per annum. Currently, over 85% of the energy used comes from fossil fuels (coal, natural gas and oil), while about 7% comes from renewable energy (hydro, biomass, wind, solar, etc.).[1]

This is where catalysis comes in. A catalyst is a material that can increase the rate of a reaction without being consumed itself, so that in the ideal case a catalyst can be used indefinitely without being renewed. It often permits reactions to take place under milder conditions, and allows one to steer the reaction products by increasing the rate of the desired reaction while secondary or side reactions, that would produce undesired byproducts, are not catalyzed. The most familiar example is the catalytic converter that controls exhaust emissions

from cars, converting toxic gasses to less harmful ones. However, catalysts are used in a huge variety of processes on an industrial scale. It has been estimated that roughly 70% of all chemical processes use heterogeneous catalysts,[2] whereby a solid catalyst is used in combination with liquid or gas phase reactants and products, with applications not only in oil refining and (petro)chemical processes, but also in food, pharmaceutical, environmental, and fine chemical industries.[3]

A specific and growing application of catalysis is the conversion of alternative feedstocks into transportation fuels. First, these feedstocks need to be converted into an intermediate gas composition called synthesis gas (in short syngas), which consists of H_2 and CO. This is done at high temperatures by a process called gasification for coal and biomass[4], or by steam reforming over nickel catalysts in the case of natural gas.[5] Moreover, the H_2 to CO ratio of syngas can be tuned by use of a so-called water-gas-shift catalyst, usually based on iron oxide or copper.[6]

The resulting syngas can then be transformed into long chain alkanes via a process called the Fischer-Tropsch synthesis as by Equation 1.1. This synthesis method was already discovered in the early 1920s by Franz Fischer and Hans Tropsch to provide Germany with an alternative source of fuel, and was further developed in South Africa during the apartheid regime to meet the energy demands.[7] More recently, with rising energy consumption and concurrent oil prices, it has received increased attention both academically and industrially, and has led to commercialization of the Fischer Tropsch process for the production of fuels from natural gas, often referred to as gas to liquids technology (GTL). Several large industrial plants have been constructed by companies such as Shell, Sasol, PetroSA, Petrolium and Chevron, reaching an approximate total capacity of 400 000 barrels per day in 2014, equivalent to about 0.5% of the world daily oil consumption.[8]

$$n\,CO + (2n+1)\,H_2 \rightarrow C_nH_{2n+2} + n\,H_2O \qquad \text{(Equation 1.1)}$$

The Fischer-Tropsch process is mostly done over cobalt catalysts. Due to the polymerization nature of the reaction, the final product contains a broad range of products ranging from methane, CH_4, to hydrocarbons with 50 or more carbon atoms, mostly parrafinic and unbranched. Because the raw feedstock is often natural gas, which consists mostly out of methane, formation of methane during the Fischer-Tropsch process is highly undesirable and catalysts and reaction conditions need to be tuned to shift the selectivity towards the long alkane side of the product spectrum, often expressed as the C_{5+} selectivity.[9] The resulting long chain alkanes can be further processed (cracking, isomerization) for application as transportation fuels. The fuels thus obtained are much cleaner compared to conventional diesel fuels. They display a high cetane number, which may translate to a higher fuel efficiency, and contain virtually no sulfur, nitrogen compounds or aromatics, which is beneficial for the environment for example as lower soot emissions from diesel cars.[10] Therefore, fuels produced via the GTL procedure, or blends of GTL fuels with conventional fuels, easily meet the

increased demand for cleaner fuels due to the global urbanization and the increasing trend towards clean and sustainable technologies.

Other syngas based reactions are equally important industrially. For example, while nickel catalysts are used to form syngas from natural gas at high temperature, the reverse reaction is possible at lower temperatures, so that methane is produced from CO + H_2, known as the methanation reaction. This reaction is highly important for purification of the H_2 gas stream in ammonia plants, a huge industry for the production of fertilizer and other nitrogen containing compounds, and for which CO is detrimental for the catalyst stability. Moreover, the methanation reaction can potentially be used for the production of natural gas from other sources such as coal or biomass, to reduce the reliance of countries without natural gas on its import for domestic use.[11]

Each of the catalysts described above are used in the form of so-called supported metal catalyst. These consist of an active metal, such as nickel or cobalt, supported on a mostly inert material that provides mechanical structure to the catalysts, and generally has a high thermal stability and high porosity but is often otherwise chemically inert.[12,13] The catalytic reaction takes place at the interface between the reactants and the metal, on the surface of the metal. Because these metals are often expensive, and because reactor designs are often limited in size for practical reasons, maximal efficiency is desired to make reactions economically viable. This is done through use of very small metallic particles, of the order of a few nanometers, so that the surface area per gram of metal is maximized. Moreover, high metal loadings are often desired to increase the activity per unit of volume of catalyst, and thereby make maximum use of the available reactor space.

Even though the catalyst itself is theoretically not consumed during the reaction, in practice catalysts do exhibit a loss of activity over their lifetime.[14] This is highly undesirable, as it reduces the productivity of the catalytic process. Moreover, if the output of one chemical plant is reduced, all other processes that are reliant on it are also affected. Since industrial catalytic processes are often intensely integrated, this can have great implications for an entire chemical production site. In addition, taking down the chemical plant and replacing the catalyst is often complicated and can take weeks, an expensive endeavor. Thus, the stability of a catalyst is often just as important as its activity.

Deactivation of catalysts can go via a multitude of ways.[15] Unreactive carbon, also known as coke, can form on the support or the metal particles, blocking access to the nanoparticles. Even minute traces of certain compounds, such as sulfur, can poison many types of catalysts by adsorbing strongly on the metals, making them unavailable for the desired reactants. Attrition can take place, whereby support pellets or grains break up into smaller particles which are swept out of the reactor. Finally, an important deactivation mechanism is particle growth, whereby several small metal nanoparticles form one bigger particle (Figure 1.2), thereby reducing the metal surface area per gram of metal, resulting in a loss of activity.

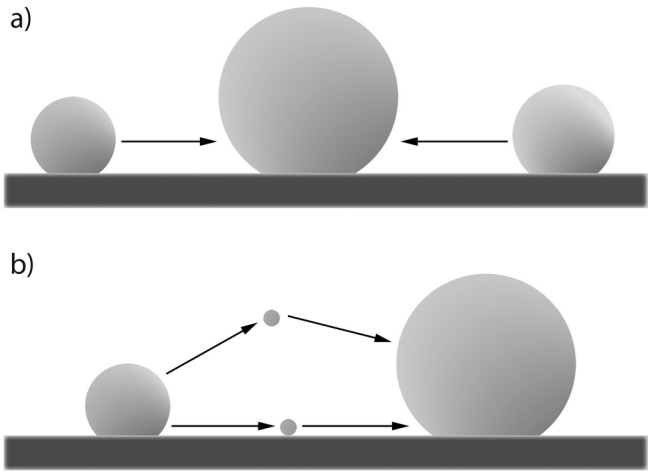

Figure 1.2. Two possible mechanisms for particle growth. (a) migration and coalescence, also known as sintering, whereby two particles migrate across the surface of the support, forming one bigger particle when they meet. (b) Ostwald ripening, whereby monomeric species or small clusters migrate from small to large particles across the surface of the support or through the vapor phase.

These deactivation pathways can often be partially mitigated by proper choice of the catalyst and reaction conditions. For example, attrition strongly depends on the choice of support and modifications made to it. Poisoning can often be reduced by purifying the reactant feed, or by synthesizing the catalyst such that active sites are deep inside the support grains or pellets, so they are difficult for the poison to reach. Particle growth was recently shown to be greatly dependent on the distance between particles for the synthesis of methanol from syngas over copper catalysts.[16] However, all of these solutions greatly depend on the specifics of the catalytic reactions and conditions involved. For example, nickel supported on alumina in a H_2 atmosphere at 700 °C exhibited a relatively slow particle growth by migration of the particles across the surface, resulting in coalescence of smaller particles into one larger particle when they met. However, at 800 °C particle growth was much more rapid, and it was observed that apart from migration and coalescence, Ostwald ripening could also take place, whereby monoatomic species or small clusters transport from small to large particles, resulting in growth of the large particles at the expensive of smaller ones.[17] Thus, the specifics of the reaction conditions determine the requirements of the catalysts.

By now, it should be evident that the performance of the catalyst, in particular its activity, selectivity and stability, is highly dependent not only on the active metal(s) and reaction conditions, but on many aspects of the catalyst, such as the support, metal particle size, and their location. Because of this, preparation of a catalyst is extremely intricate. Obtaining the desired properties has long been achieved largely by trial and error, such that the field of catalyst preparation used to be regarded as an art rather than a science, and resulting catalysts are often not ideal (Figure 1.3). However, recent years have shown an exponential increase in the number of fundamental studies on the preparation of catalysts, so that rational synthesis of catalysts is increasing.

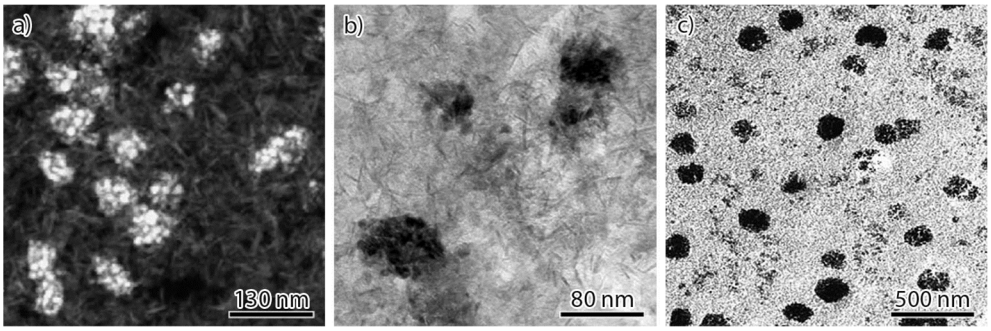

Figure 1.3. Examples of catalysts with inhomogeneous cobalt metal distributions on the support, which are often undesirable. (a) HAADF-STEM (cobalt bright) of Co/γ-Al_2O_3 (adapted from [18]), (b) TEM (cobalt dark) of Co/γ-Al_2O_3 (adapted from [19]) and (c) TEM of Co/SiO_2 (adapted from [20]). In each case, the small 5-10 nm cobalt particles are very closely together in aggregates of 50-300 nm, while large parts of the support are empty.

OUTLINE

In **chapter 2**, the important aspects and recent developments in the field of support metal catalyst synthesis were reviewed. Techniques to prepare supported catalysts include synthesizing metal particles in solution followed by deposition on the support, deposition of the metal via the vapor phase, or precipitation of (a precursor of) the active metal from a solution, either in the presence of the support material (deposition precipitation) or by precipitating the support and metal from the same solution (coprecipitation). The most applied method in academia and industry alike remains impregnation of a precursor solution into the existing support material, followed by drying and a calcination or other activation treatment. While this method is simple in its execution, optimization of the catalyst is often difficult due to the complicated physiochemical processes involved in the process.

Catalysts synthesized by impregnation and drying often result in inhomogeneous distributions of the metal particles on the nanoscale, so that the small particles are grouped together into large clusters or aggregates, while the majority of the support remains empty. This problem was investigated in **chapter 3**, where freeze-drying was utilized to demonstrate the large importance of the drying step on the nanoscale aggregation of Co/SiO_2 Fischer Tropsch catalysts made from a cobalt nitrate precursor.

In **chapter 4**, the drying step was further studied by drying impregnated silica supports in an N_2 flow in a fluidized bed mode, which allowed for the synthesis of catalysts with differently sized aggregates of similarly sized cobalt particles. These catalysts were subsequently tested under industrially relevant Fischer-Tropsch conditions to study the effect of particle aggregation. Through use of imaging techniques at different length scales a relatively unknown deactivation mechanism was revealed, whereby particles migrated tens of micrometers to the external surface of the support grain, with the extent of migration highly dependent on the initial degree of cobalt particle aggregation.

A more fundamental insight in the cause of aggregation during drying was obtained in **chapter 5** by immobilization of the precursor after drying. This allowed for the distinction of two different aggregation pathways, between which an optimum existed whereby no aggregates were formed. Moreover, while drying in stagnant air, commonly used in literature, often results in aggregation, use of an N_2 flow during drying provided a facile way to avoid aggregation for different support materials.

In **chapter 6**, the obtained knowledge on catalyst synthesis was utilized to prepare several nickel catalysts with different particle sizes and interparticle distances. These catalysts were subsequently tested in the synthesis of natural gas from syngas. During this reaction, catalysts often rapidly deactivate due to Ostwald ripening by nickel carbonyl species. We show that by controlling the initial Ni particle size, this deactivation can be greatly reduced.

Finally, a summary and outlook are provided in **chapter 7**.

REFERENCES

(1) *BP Statistical Review of World Energy*; http://www.bp.com/statisticalreview, **2013**.

(2) *Catalysis Looks to the Future*; National Academy Press: Washington D.C., **1992**.

(3) *Handbook of Heterogeneous Catalysis*; Ertl, G.; Knözinger, H.; Schuth, F.; Weltkamp, J., Eds.; WILEY-VCH Verlag GmbH& Co. KGaA: Weinheim, **2008**.

(4) Pinto, F.; André, R.; Costa, P.; Carolino, C.; Lopes, H.; Gulyurtlu, I. In *Solid Biofuels for Energy*; Grammelis, P., Ed.; Springer: London, **2011**, 151.

(5) Sehested, J. *Catal. Today* **2006**, *111*, 103.

(6) Ratnasamy, C.; Wagner, J. P. *Catal. Rev.* **2009**, *51*, 325.

(7) Casci, J. L.; Lok, C. M.; Shannon, M. D. *Catal. Today* **2009**, *145*, 38.

(8) Van de Loosdrecht, J.; Botes, F. G.; Ciobica, I. M.; Ferreira, A.; Gibson, P.; Moodley, D. J.; Saib, A. M.; Visagie, J. L.; Weststrate, C. J.; Niemantsverdriet, J. W. In *Comprehensive Inorganic Chemistry II*; Reedijk, J.; Poeppelmeier, K., Eds.; Elsevier, **2013**; Vol. 7, 525.

(9) Khodakov, A. Y.; Chu, W.; Fongarland, P. *Chem. Rev.* **2007**, *107*, 1692.

(10) Sajjad, H.; Masjuki, H. H.; Varman, M.; Kalam, M. a.; Arbab, M. I.; Imtenan, S.; Rahman, S. M. A. *Renew. Sustain. Energy Rev.* **2014**, *30*, 961.

(11) Kopyscinski, J.; Schildhauer, T. J.; Biollaz, S. M. a. *Fuel* **2010**, *89*, 1763.

(12) De Jong, K. P. *Synthesis of Solid Catalysts*; WILEY-VCH, **2009**.

(13) Regalbuto, J. R. *Catalyst Preparation*; CRC Press, **2007**.

(14) Moulijn, J. A.; Diepen, A. E. Van; Kapteijn, F. *Appl. Catal. A Gen.* **2001**, *212*, 3.

(15) Bartholomew, C. H. *Appl. Catal.* **2001**, *212*, 17.

(16) Prieto, G.; Zečević, J.; Friedrich, H.; de Jong, K. P.; de Jongh, P. E. *Nat. Mater.* **2013**, *12*, 34.

(17) Kim, K.; Ihm, S. *J. Catal.* **1985**, *22*, 12.

(18) Saib, A. M.; Moodley, D. J.; Ciobîc, I. M.; Hauman, M. M.; Sigwebela, B. H.; Weststrate, C. J.; Niemantsverdriet, J. W.; van de Loosdrecht, J. *Catal. Today* **2010**, *154*, 271.

(19) Borg, Ø.; Walmsley, J. C.; Dehghan, R.; Tanem, B. S.; Blekkan, E. A.; Eri, S.; Rytter, E.; Holmen, A. *Catal. Letters* **2008**, *126*, 224.

(20) Zhang, Y.; Liu, Y.; Yang, G.; Sun, S.; Tsubaki, N. *Appl. Catal. A Gen.* **2007**, *321*, 79.

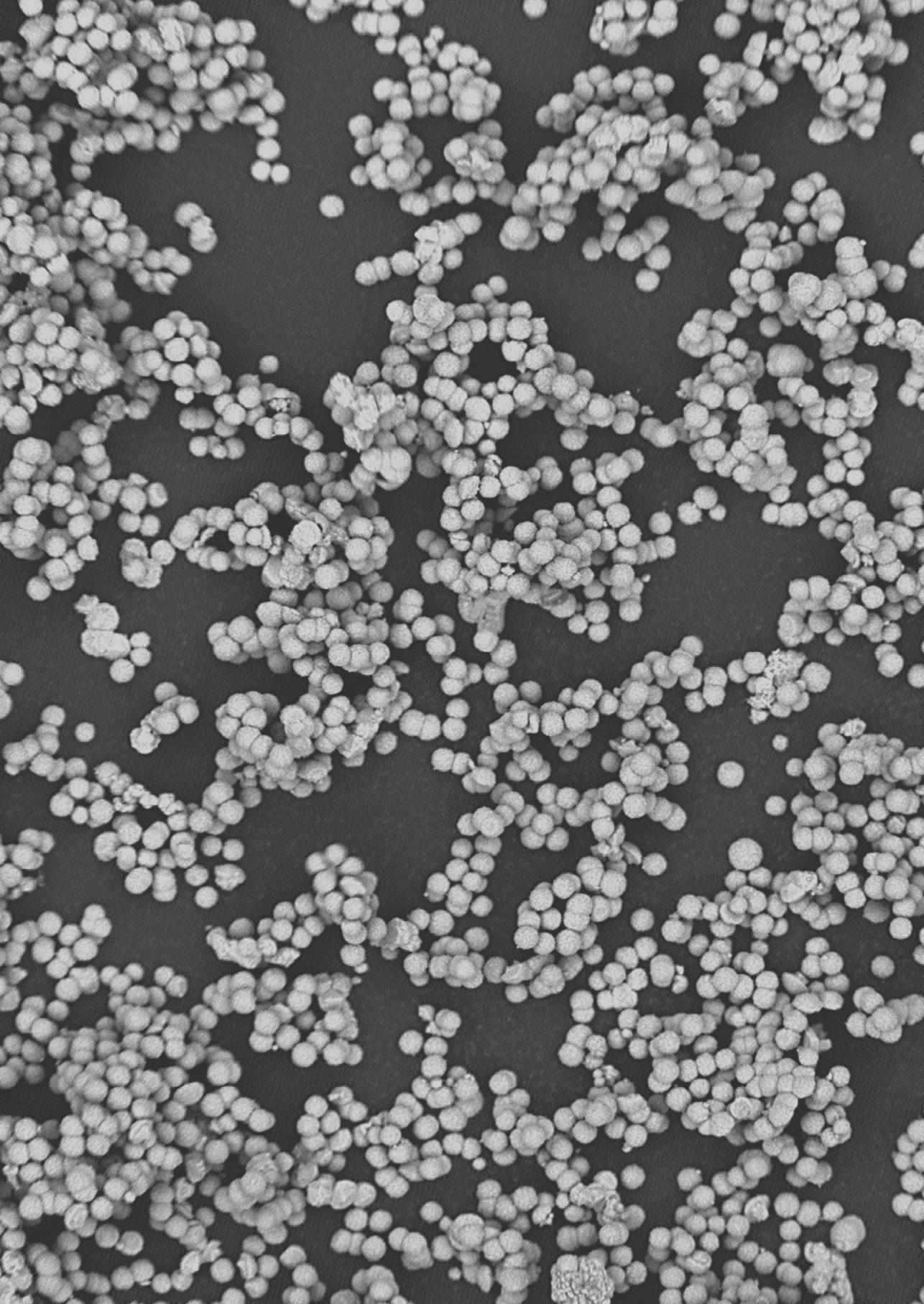

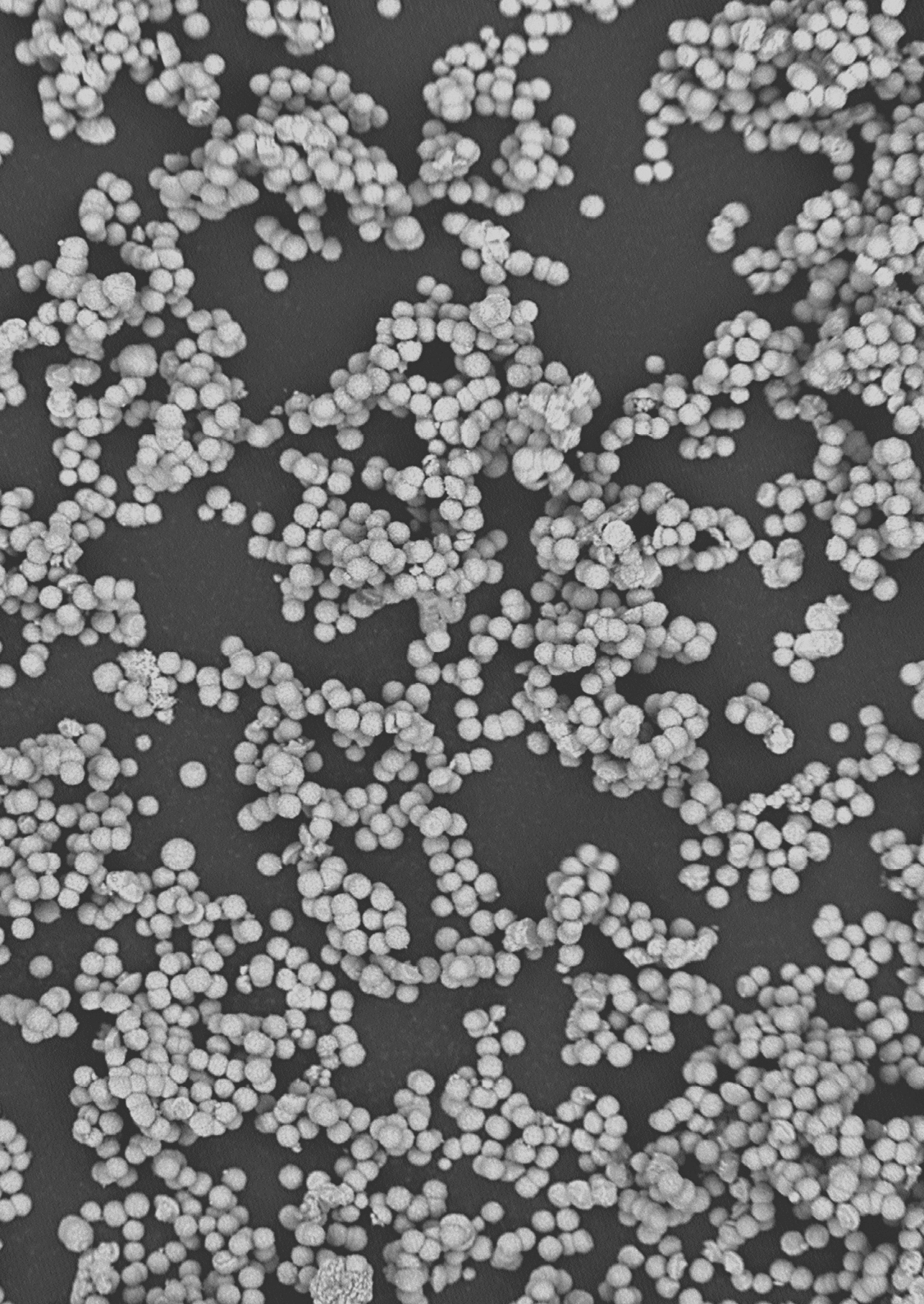

Chapter 2

Recent Developments in the Synthesis of Supported Catalysts

Adapted from: P. Munnik et al. *Chem. Rev.* submitted.

1. INTRODUCTION

Heterogeneous catalysis, whereby a gas or liquid phase reaction is performed over a solid catalyst, is at the heart of the modern energy and chemical industries. Most chemical processes, both established[1–3] and emerging[4–7], are performed using functional nanomaterials as catalysts. Moreover, upcoming fields such as nanoelectronics and energy conversion and storage are based upon the application of similar nanomaterials. The catalytic activity for these materials often resides with metal(oxide, sulfide) surface sites, and efficient use of the metals and space available demands for small particles, located on a mostly inert support to enhance the thermal stability of the catalyst. The field of catalyst synthesis, also known as catalyst preparation or catalyst manufacturing, is aimed to establish the desired composition and structure of these materials.

Catalyst synthesis has often been regarded as an art rather than a science. Recently an exponential increase of the number of scientific papers on supported catalysts greatly enhances the ability to rationally synthesize active, selective and stable catalysts.[8] However, many of the fundamental mechanisms concerning catalyst synthesis are as yet not fully understood. For example, there is almost no knowledge on the mechanisms and rates of particle formation in supported catalyst synthesis.[9]

In this chapter, we review recent developments in the synthesis of supported catalysts reported over the last 5 to 10 years. First, the main requirements of solid catalysts are discussed. Next, recent developments of two main preparation methods, precipitation and impregnation, are highlighted. In both of these methods, a metal precursor, mostly an inorganic salt, is used in some form to deposit the active metal onto the support. With precipitation techniques, metal particle growth is stimulated by the induction of supersaturation of the precursor in solution, resulting in nucleation and growth of metal particles. This can happen in conjunction with the formation of the support (coprecipitation) or onto an existing support (deposition precipitation). With impregnation techniques, the support is contacted with a precursor solution. Low loadings, often for precious metals, are achieved by adsorption of the precursor molecules onto surface groups of the support (ion adsorption) or through the exchange of ions in for example zeolites (ion exchange), after which excess precursor is removed. When higher loadings are required, the washing step is skipped and the support is directly dried, so that all precursor ends up on the support (impregnation and drying). Impregnation can be performed to incipient wetness, whereby only the pores of the support are filled with precursor solution, as to prevent deposition on the external surface of the catalyst grains and limiting waste. Besides these traditional methods, emerging preparation techniques are discussed. Precursors with low melting points can be heated and contacted directly with the support, such that capillary forces suck up the precursor upon melting (melt infiltration). Particles can also be formed in solution (colloidal route) controlled through use of stabilizing agents or ligands, after which the formed particles are deposited on a support. Vapor deposition is used whereby gaseous metal atoms, clusters or organics are selectively reacted with support surface groups.

Finally, we provide an outlook on the anticipated developments in the field of supported catalyst synthesis.

2. CATALYST REQUIREMENTS

Catalysts come in a wide variety to accommodate the large differences in operating conditions, feedstocks and products. Even so, high activities and selectivity towards the desired product are always required. Moreover, stability of the catalyst is highly important and processes such as the irreversible growth of particles or poisoning of the active sites have to be prevented.[10] The performance of the catalyst is determined by what we refer to as the **DNA** of the catalyst, that is the **D**ensity, **N**ature and **A**ccessibility of the active sites, with the accessibility largely determined by the support pore architecture.

The density of active sites is important primarily for the activity through the number of particles on the support connected to the metal loading. Since industrial reactors are generally limited in size for practical reasons, it is often desirable to use a high density of active sites (high metal loading) to maximize the activity per unit volume. The local particle density, and so the distance between particles, can also be important for the stability of the catalysts. Maximizing the spacing between Cu particles on an SBA-15 support proved greatly beneficial for the stability of methanol catalysts.[11] Similarly, reducing the size of aggregates of cobalt nanoparticles on silica gel in Fischer Tropsch catalysts has been shown to improve catalyst stability.[12]

The nature of the active sites has direct bearing on the surface-specific activity, often referred to as Turn Over Frequency (TOF) and the catalyst selectivity. This nature is determined by the composition, size, and shape (i.e. type of metal and promoters or bimetallics) of the nanoparticles. Reduction of the size of the nanoparticles increases the amount of surface sites per unit weight of metal and generally results in more active catalysts. For structure sensitive reactions that require specific surface sites, such as a low-coordination sites found on defects, corners, steps or edges, reduction of the particle size may enhance TOF.[13] However, maximum weight-based activities at a certain particle sizes have also been reported. In the dehydrocyclization of n-heptane over Pt catalysts a large increase in TOF was observed with decreasing particle size from 4 to 1.5 nm, whereas further reduction in size resulted in a large decrease.[14] Similarly, the TOF of Fischer-Tropsch cobalt catalysts were found to be constant for particles larger than 6 nm, while below 6 nm it steeply decreased.[15,16]

The catalyst stability is also greatly influenced by the nature of metal(s) and the support. For example, small Ag particles displayed a much higher adhesion energy when supported on reduced CeO_2 compared to MgO,[17] and 4 nm bimetallic PtRh particles exhibited higher thermal stability compared to individual Pt particles.[18] The initial particle size might play a role as well, since 2 nm Pt nanoparticles in polymer electrolyte membrane fuel cells were found to be very unstable, while 5 nm particles exhibited almost no deactivation.[19] Similarly, 3 - 4 nm Ni particles on silica gel used in the methanation reaction exhibited rapid particle growth

resulting in particles up to 100 nm in size, whereas 8 - 9 nm initial particles remained of a size similar to the pore diameter (10 nm) of the silica gel support.[20]

Accessibility of active sites calls upon control of the catalyst porosity. This is key for the rate of mass transfer of reactants to and products from the active sites, and affects activity by diffusion rates, selectivity by the extent of secondary reactions, and stability via processes such as coke formation and poisoning. In academia, fine powder grains are often used to ensure good accessibility of the active sites to prevent mass-transfer-limitations. However, small grains cause a large pressure drop over a catalyst bed of significant height. Therefore, catalyst support bodies or pellets of a few millimeters in size are often used in industry. For these relatively large bodies, the macroscopic distribution of the active sites becomes important, and a useful tool to estimate the degree of mass-transfer limitations in a catalytic system is the Thiele modulus ϕ:

$$\phi = \frac{V_p}{A_p} \cdot \sqrt{\frac{k_r}{D_e}} \qquad \text{(Equation 2.1)}$$

whereby V_p is the volume of the pellet, A_p is the external surface area of the pellet, k_r is the first-order rate constant, and D_e the effective diffusion coefficient. A ϕ greater than 0.3 is an indication that diffusion of the reactant through the pores is rate limiting. Thus, for large catalyst bodies a homogeneous distribution of the active phase is only preferential for relatively slow catalytic reactions, providing reactants time to diffuse to the active sites. If the reaction is fast or if secondary reactions are problematic, a different macroscopic distribution of the active phase might be preferred, such as an egg-shell distribution, or an egg-white distribution if the catalyst is prone to attrition. If the reactants contain poisons, an egg-yolk distribution may be favorable so that the poison can be captured at the edge of the catalyst body, where few active sites are present (Figure 2.1).

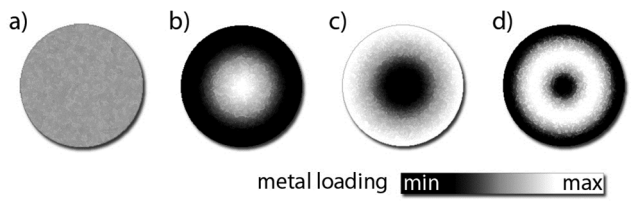

Figure 2.1. Different types of macroscopic metal distributions across a support body. (a) homogeneous distribution, (b) egg-yolk distribution, (c) egg-shell distribution, (d) egg-white distribution. (white: high concentration of metal, black: low concentration of metal)

To maintain activity as well as for practical reasons, the support requires a high mechanical strength and the macroscopic bodies should be resistant to attrition if the catalyst is vigorously agitated such as in fluid bed or slurry bed reactors. Common support materials consist of refractory oxides such as SiO_2, Al_2O_3 or TiO_2. These materials exhibit high specific surface areas, high porosities, high thermal and mechanical stability and come in a variety of pore sizes, while they are mostly chemically inert. Carbon is also widely used, while zeolites are often applied in many oil refining and petrochemical applications. Recently, an increasing variety of

ordered mesoporous materials is used as model supports.[21] Finally, metal organic frameworks are showing an increased use as catalysts or as support for metal(oxide) nanoparticles.[22]

The surface of oxidic supports generally contains a significant concentration of hydroxyl groups when contacted with an aqueous solution, which act as adsorption sites for metal complexes and are key to many interactions between the precursor and solvent with the support. Depending on the type of support and the pH of the aqueous solution, these groups can become protonated or deprotonated.[23] For each support, in water there exists a pH for which the net charge of these groups is zero, so that the net particle charge can be considered nil. Above this pH, more groups are deprotonated and the surface is negatively charged, whereas below the PZC the surface is positively charged due to protonation. Table 2.1 shows the PZC for several important supports. An extensive list can be found elsewhere.[24]

Table 2.1. Point of zero charge for several important supports in aqueous solution.[24]

Support	PZC range
SiO_2	2-4
Oxidized activated carbon	2-4
TiO_2	5-7
γ-Al_2O_3	8-9
Activated carbon	8-10

3. PRECIPITATION

Precipitation techniques have long been used to produce supported catalysts. Controlled precipitation from a precursor solution follows the principles of nucleation and growth. An initial nucleation boom of tiny crystallites followed by growth without the formation of new nuclei can result in small and quite monodisperse particles. This concept is known as “burst nucleation” and is not only important for precipitation techniques but is also key in the synthesis of colloids and plays a role in the synthesis of catalysts via impregnation.

3.1 Coprecipitation

In Coprecipitation, salts of the active metal and support are dissolved and mixed such that nucleation and growth of a combined solid precursor of the active metal and support is obtained in a single step. Very high metal loadings of 70 wt.% and higher can be achieved while maintaining small particle sizes through creating a very high degree of supersaturation, so that all components nucleate at a high rate and at the same time. This is often realized by mixing two concentrated solutions, the components of which result in an insoluble material when combined. Highly soluble metal nitrates, chlorides or sulfides can be mixed with basic reagents like alkali carbonates or hydroxides so that metal carbonates or hydroxides are formed.

The low solubility of these compounds causes most of the precursor to precipitate. During coprecipitation, great care has to be taken to prevent local fluctuations in the conditions caused by for example temperature gradients, insufficient mixing or concentration gradients, which can cause additional nucleation events, different or inhomogeneous growth patterns, or the precipitation of different phases. New techniques such as spray-drying and continuous consecutive precipitation can help overcome these practical problems during synthesis.[25,26]

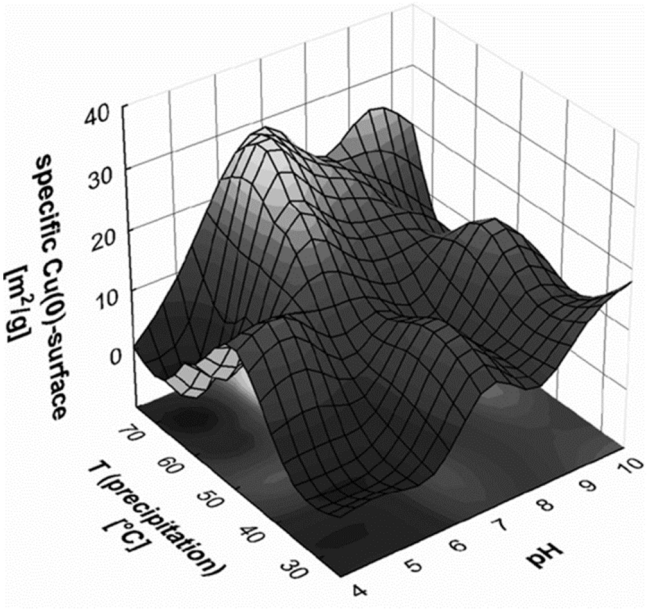

Figure 2.2. Influence of the pH and temperature during the precipitation of Cu/Zn/Al catalysts on the final specific Cu(0) surface area. After precipitation, all catalysts were aged for 1 hour, calcined at 300 °C and reduced at 300 °C. (Adapted with permission from ref 31. Copyright 2008 Elsevier)

Coprecipitation can be utilized to produce catalysts such as nickel alumina for steam reforming[27] or iron copper potassium for Fischer-Tropsch synthesis[28], while most recent studies focus on $Cu/ZnO/Al_2O_3$ catalysts for the methanol synthesis. The active sites for this catalyst are metallic copper step sites which are in close contact with Zn.[1] Molar Cu/Zn ratios of 70:30 are most common, while the molar Al_2O_3 content is generally below that of Zn, and preparation is done by combining Cu, Zn and Al nitrates and precipitated using alkali (bi)carbonates.[29] Titration experiments have shown that precipitation is preferably performed at constant pH. When the pH is slowly increased, sequential precipitation results, whereby Cu is first precipitated followed by Zn.[30] Baltes *et al.* systematically studied the precipitation at different pH (4.5 to 10) and temperature (30 to 70 °C), while keeping the subsequent treatments the same (1 hour aging, calcination at 300 °C).[31] The precipitation conditions had little effect on the Cu/Zn/Al ratio, which was similar in all precipitated samples, and close to that of the initial solution (60/30/10). However, large differences were observed in the BET and Cu(0) surface areas after reduction at 300 °C in H_2 (Figure 2.2). The lowest Cu(0) surface areas were found at a very low pH, where XRD revealed large CuO crystallites and ZnO diffraction lines after calcination. High Cu(0) surface areas were generally found at higher temperatures, with a maximum at a pH of 6-7 at a temperature of >60 °C, in agreement with

previous studies. Under these conditions, small CuO particles and some residual zincian malachite, $(Cu,Zn)_2(CO_3)(OH)_2$, was reported after calcination.[31]

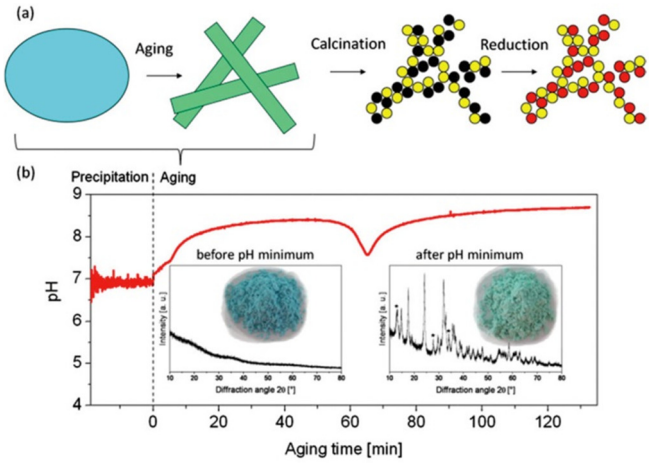

Figure 2.3. (a) Cartoon of the steps during coprecipitation of Cu/ZnO catalysts. During precipitation, an amorphous material is obtained, which is turned into a crystallite phase during aging. A subsequent calcination step forms small CuO and ZnO particles, the former of which can be reduced. (b) Evolution of the pH during precipitation and aging of a typical Cu/ZnO sample, along with the associated change in color and crystallinity during aging (inset). (Adapted with permission from ref 32. Copyright 2012 Royal Society of Chemistry)

Zincian malachite has previously been reported to be the desired precursor for the formation of active methanol catalysts. The crystalline phase is formed during the aging process after initial precipitation, which generally forms an amorphous product due to the fast kinetics of the precipitation process (Figure 2.3).[32] The resulting zincian malachite consists of thin needles 5-15 nm in width, and forms the general mesostructure of the catalyst. By incorporation of Zn, close Cu-Zn interactions enable the formation of small Cu particles during subsequent calcination and reduction.[33] Zander *et al.* analyzed the aging process of Cu/Zn (molar ratio 70:30) in detail with in-situ EDXRD and UV-Vis measurements. The precipitate was formed at pH 7 at 65 °C, close to the previously found optimum, and immediately spray-dried to allow separation of the precipitation and aging steps. Subsequently, the aging step was studied in a pH range between 5 and 8, and at temperatures between 50 and 70 °C.[32] Two mechanisms were found for the formation of high Zn incorporation into zincian malachite. At pH > 7, a sodium zinc salt precipitated along with a low Zn content zincian malachite, followed by slow dissolution of the sodium zinc salt and incorporation of the Zn into the zincian malachite during aging. At pH between 5 and 6.5, direct co-condensation of copper and zinc caused direct formation of the zincian malachite, resulting in the highest amount of Zn incorporation (29.2%), close to the theoretical maximum.[33] A study on different precipitation agents for Cu/Zn/Al precipitated at pH 6 and aged for 2 hours showed little difference in the obtained crystalline phases and final BET surface area between sodium, potassium or ammonium carbonate precipitating agents, although use of sodium hydroxide provided a notably lower surface area.[34]

After aging, the zincian malachite precursor is converted into CuO and ZnO particles by a calcination step. Stepwise calcination at 100 °C intervals from 200 to 700 °C showed the best

result was usually obtained at 300 °C. At this point, most of the copper was present in the form of small CuO particles, while some degree of zincian malachite was still present. Although decomposition of these last traces was possible at higher temperatures, this also resulted in a sharpening of the CuO XRD diffraction line, corresponding to larger CuO particles due to sintering at the increased temperature.[31] Other studies on Cu/Zn/Al coprecipitates also reported an increase in CuO particle size upon increasing the severity of the calcination procedure. Increasing the calcination time at 350 °C from 1 h to 3 h increased the CuO particle size from 3.0 nm to 3.7 nm, which increased further to 5.0 nm at 400 °C.[35] Similarly, increasing the calcination temperature from 400 to 700 °C brought about a gradual increase from 5.3 nm to 15.8 nm, highlighting the importance of a relatively mild activation treatment.[36]

Although water is normally used as solvent for precipitation techniques, high Cu surface areas have been obtained in a solvent mixture of ethylene glycol and water at a ratio of 4:1.[37] Cu/Zn/Al at a ratio of 3/3/1 was precipitated at pH 5 and 70 °C, aged for 2 hours and calcined at 350 °C. It was postulated that the ethylene glycol works as a surfactant that adsorbs on the surface of growing crystallites, thereby inhibiting further growth so that small particles and high surface areas were obtained. However, mixing other polar solvents with water, such as ethanol, tetrahydrofuran and 1,4-dioxane had a negative effect on the Cu surface area.[37]

Microwave irradiation has been investigated as an alternative heat source during the precipitation and aging process of Cu/Zn/Al at a molar ratio of 64/32/4 at pH 7.5 - 8.[38] Although microwave irradiation had little effect on the precipitation process between 60 and 80 °C, aging at 70 to 90 °C using microwave irradiation showed an increased incorporation of Zn compared to regular aging at the same temperature, eventually leading to more dispersed CuO particles after activation.[38]

'Greener' Coprecipitation Methods. Coprecipitation methods generally require numerous washing steps after precipitation, which produces large amounts of waste water contaminated with nitrates. Although this is undesired, other precursor salts based on sulfate or chloride introduce poisons for the methanol catalyst. To circumvent this, metal formates have been investigated as a precursor replacement. Titration experiments revealed that Cu and Zn formates have a higher tendency to simultaneously precipitate, increasing the homogeneity of the metal distribution in the precipitate. In the absence of nitrates, zincian malachite is not possible and instead a phase with the general formula $(Cu_{1-x}Zn_x)_2(OH)_3HCO_2$ was formed.[39] Investigation of the crystal structure revealed a maximum Zn incorporation in the precursor phase of around 20% (x = 0.2), somewhat lower compared to the 20-30% generally found in zincian malachite when using nitrate precursors. Upon coprecipiatation of Cu/Zn from formate precursors, 12 nm CuO particles were found, somewhat larger than present in conventional systems. However, this was attributed to the lack of Al_2O_3 in the sample and relatively lower amount of Zn. Even so, the catalyst showed a relatively good activity, possible due to the good interaction of the Cu and Zn phases, showing formates are promising nitrate substitutes.[39]

Alternatively, altering the calcination treatment has been shown to circumvent the need for a multitude of washing steps to remove residual nitrates altogether.[40] Cu/Zn/Al catalysts with a molar ratio of 55/30/15 were precipitated using Na_2CO_3 or $(NH_4)HCO_3$ at a pH of 7 and a temperature of 70 °C and aged for 2 hours. If no washing was performed, very low BET surface areas of 15 m^2/g were found after calcination in stagnant air for the sample precipitated with Na_2CO_3. This increased significantly with each washing step, to a maximum of 115 m^2/g after 7 steps, illustrating the importance of removing nitrates to prevent agglomeration of the resulting copper particles. When $(NH_4)HCO_3$ was used as precipitating agent, the values varied from 70 to 100 m^2/g after calcination in stagnant air depending on the number of washing steps. However, if the calcination was performed in a high flow of N_2, 120 m^2/g was obtained without performing a single washing step (Table 2.2). Moreover, although washing is normally needed to remove sodium from the sample, by using $(NH_4)HCO_3$ the need for a washing step was circumvented altogether, albeit at less than quantitative precipitation of copper.[40] Alteration of the thermal treatment step has been rarely studied for precipitated catalysts, in contrast to catalysts prepared by impregnation and drying, which is discussed in detail in section 4.4.

Table 2.2. Catalysts properties prepared using $(NH_4)HCO_3$ as precipitating agent. (Adapted with permission from ref 40. Copyright 2013 Elsevier)

Number of washing steps	Calcination gas composition	Calcination gas flow (h-1)	B.E.T. surface area (m2/g)	CuO crystallite size (nm)
0	Air	0	70	12
7	Air	0	100	9
0	Air	$1{\cdot}10^3$	105	8.8
0	N_2	$1{\cdot}10^3$	110	8
0	N_2	$12{\cdot}10^3$	120	7
0	1% NO/N_2	$1{\cdot}10^3$	115	7.6
0	1% NO/N_2	$12{\cdot}10^3$	120	7.2

3.2 Deposition Precipitation

Deposition precipitation concerns precipitation of the active metal onto an existing support material. Preferential precipitation on the support can be achieved because introduction of the support in the solution either causes a reduction of the surface free energy, or stabilization of the bulk precipitate, decreasing the energy barrier for nucleation. Because of this, conditions exist where nucleation can only occur on the support and not in the bulk solution, so that the support surface functions as a seed for nucleation.[41]

Nucleation of the metal species is generally induced by changing the pH so compounds with a low solubility are formed. When this is done by injection of the precipitant, great care

has to be taken to prevent local concentrations exceeding the critical supersaturation, which would cause bulk precipitation. Because of this, homogeneous deposition precipitation methods are often preferred, whereby precipitation is induced homogeneously throughout the reaction vessel. This can be achieved by adding urea at room temperature, which when heated to 90 °C will slowly enhance the pH upon decomposition. Other popular precipitation techniques include the direct reduction of solvated metal ions to the metal[42] or the removal of ligands such as ammonia via evaporation.[43]

Classically, deposition precipitation was developed to produce catalysts with metal loadings that greatly exceed those obtained by a more simple impregnation method,[44] however few recent studies it in this respect are noted. In one study, hexachloroplatinic acid was used as a precursor to deposit up to 60 wt.% Pt on a high surface area carbon black via deposition of $PtCl_x(OH)_y(H_2O)_z$ species formed by the decomposition of urea.[45] Increasing the urea/Pt molar ratio from 0 to 80 showed a decrease in size of the Pt particles from 5 to 2 nm (Figure 2.4) before reduction. Note that deposition was also possible without addition of urea, suggesting adsorption of Pt complexes also played a role (see section 4.2). It was postulated that the observed reduction in size was mainly due to electrostatic charge effects: at a higher pH, obtained by more urea addition, Pt complexes with larger negative charges were formed, so that their growth was limited by repulsion. The reduction step was also found to be important for the final metal particle size. When reduction was performed by addition of $NaBH_4$ at room temperature, large particles and agglomerates were found related to its high reduction potential. When ethylene glycol was added at room temperature instead, small monodispersed Pt particles were obtained by *in-situ* formation of acetaldehyde at 120 °C, which functioned as a reducing agent.[45] A separate study focused on the initial pH of the solution for the production of 40 wt.% PtRu (equal molar ratio) on carbon black. Through addition of NaOH, the initial solution was varied between pH 3 and 10 before the temperature was raised to 90 °C to start decomposition of urea (urea/PtRu molar ratio of 20). The metal particle size varied from 3.6 nm at pH 3 - 4 to 2.6 nm at pH 9 - 10 after reduction in a flow of H_2.[46]

Cobalt has been deposited on silica gel and carbon nanofiber (CNF) supports using deposition precipitation starting from cobalt nitrate and urea. At 15 wt.% loading of cobalt the resulting material consisted of mainly cobalt hydrosilicates on silica, whereas on CNF a low interaction with the precursor resulted in limited nucleation on the support, with both materials exhibiting large cobalt particles after reduction (40 and 25 nm, respectively). Uniform deposition was more successful when cobalt carbonate and a high initial pH were used instead, and precipitation was induced by evaporation of ammonia at 90 °C, slowly lowering the pH. Using this method, much smaller particles of 8 and 13 nm were obtained for CNF and silica, respectively.[47] Similar results were obtained in a separate study on Co/TiO_2 at loadings varying between 4 and 24 wt.%. Although some small 2 nm particles were found using urea and cobalt nitrate, unsupported particles were observed, resulting in an average of 20 nm particles at 4 wt.% Co and 50 nm at 24 wt.% on titania. Deposition precipitation onto titania of cobalt carbonate by evaporation of ammonia resulted in a homogeneous distribution

of 9 nm particles at 4 wt.% Co, growing only to 15 nm for the sample prepared at 24 wt.%.[48] These results show the interaction of the precursor and the support is important to the method of deposition precipitation; when the interaction is too strong, such as with cobalt nitrate and silica, mixed metal-support phases are formed, whereas a too weak interaction, such as with cobalt nitrate and CNF or TiO_2, results in large, unsupported particles. In all reported cases, deposition precipitation of cobalt carbonate by evaporation of ammonia resulted in a more optimal interaction.

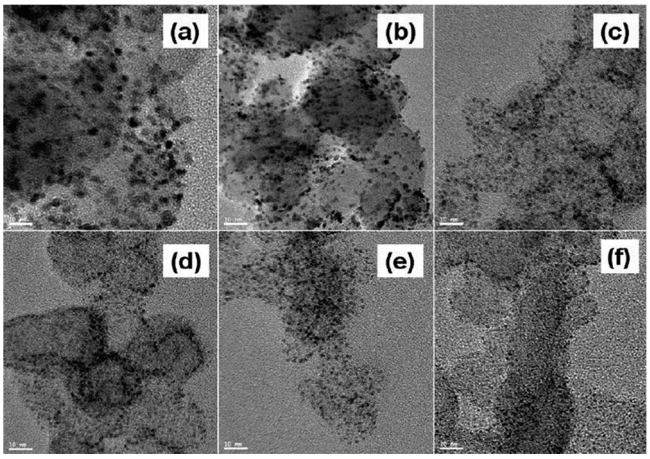

Figure 2.4. TEM of 60 wt.% Pt/C before reduction, showing the size of the Pt nanoparticle complexes dependent on the amount of urea used during deposition. (a) no urea, (b) urea/Pt molar ratio of 5, (c) 10, (d) 20, (e) 40, (f) 80. Scale bar: 10 nm. (Adapted with permission from ref 45. Copyright 2009 American Chemical Society)

Gold Catalysts. Recently, deposition precipitation has frequently been used for the preparation of finely dispersed gold particles at relatively low loadings. A facile and common proceeding starts with an aqueous solution of $HAuCl_4$ to arrive at 0.5-2 wt.% loading. The pH of the solution is raised using NaOH, followed by addition of the support under vigorous stirring, and heating to 70 °C.[49] In general, not all gold is deposited from solution, and investigation on the effects of pH during deposition for Au/TiO_2 revealed the uptake of gold was maximum at a pH around 6, close to the PZC of the TiO_2 support. However, this resulted in the formation of large Au particles, while a good compromise between particle size and uptake was obtained at pH 9.[50,51] This technique has been applied to deposit Au on a variety of supports such as a hydrotalcite,[52] diamond,[53] SiO_2/TiO_2,[54] and Al_2O_3.[55] However, several studies on the mechanism argue that it is technically not a deposition precipitation.[50,56–59] Moreau *et al.* proposed that electrostatic adsorption takes places at a pH below the PZC for gold deposited on titania, while above the PZC a neutral $Au(OH)_3 \cdot H_2O$ species adsorbs on 2 TiO^- surface sites.[59] Cellier *et al.* compared anion adsorption at pH 3 to deposition precipitation at pH 7 on two titania supports. In both cases, evidence of gold chloride complexes on the surface of the support was obtained, suggesting $AuCl_{4-x}(OH)_x^-$ complexes had reacted with surface OH groups to form surface species, rather than forming a precipitate of the type $Au(OH)_xCl_{3-x}$. Moreover, when titania with a higher surface area was used a higher Au loading was achieved, corroborating the mechanism of surface adsorption rather than

precipitation. It has been argued that an adsorption equilibrium explains why not all Au precipitates from solution, although finite solubility of a precipitate offers an alternative explanation.[58]

Zanella *et al.* already postulated a similar mechanism of gold surface complexation for the NaOH "deposition precipitation" method in 2002, and compared it with the more conventional deposition precipitation method using urea to slowly raise the pH for the preparation of Au/TiO_2 catalyst with a nominal loading of 8 wt.% Au. Complete precipitation of gold was achieved using the urea deposition precipitation method, whereas maximum Au loadings of only 3 wt.% were obtained using the NaOH method, suggesting the two concern fundamentally different deposition pathways.[57] Further study suggested $AuCl(OH)_3^-$, the dominant species at pH 8, reacts with the surface hydroxyl species in the NaOH method. For the urea deposition method, a gold-urea or urea derivative complex formed with a high N content, although the exact nature of the complex was not reported. It was postulated that initially some $AuCl_{4-x}(OH)_x^-$ anions adsorbed on the positively charged support surface hydroxyl groups at low pH, which serve as nucleation sites for the precipitation of the gold-urea complex species in the first hour. These form relatively large particles, which fragment forming smaller particles upon aging as the pH rises further (Figure 5).[60]

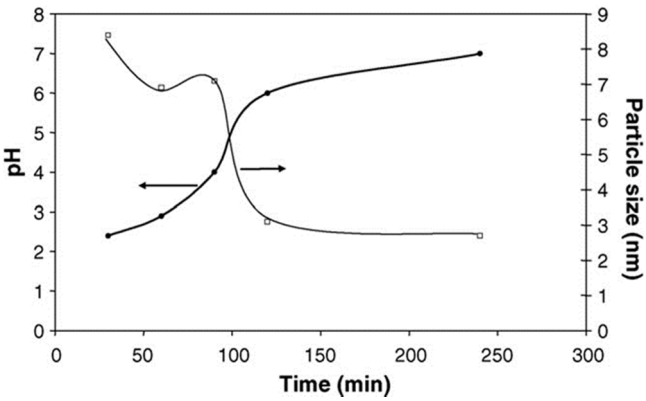

Figure 2.5. Time-evolution of the pH and the Au particle size estimated by TEM during the preparation of 8 wt.% Au/TiO_2 prepared by deposition precipitation using urea. (Adapted with permission from ref 60. Copyright 2005 Elsevier)

The urea deposition precipitation method was further used to deposit Au on Al_2O_3, TiO_2, ZrO_2 and CeO_2 at wt.% loadings between 1 and 7 wt.%. In each case, small particles of around 2 nm were found by TEM analysis, and the synthesis was readily scaled up to 50 grams without compromise. Moreover, it was concluded that at loadings of 1 wt.%, which was found to be below the absorption capacity of the supports investigated, all the gold was initially adsorbed by the support as $AuCl_{4-x}(OH)_x^-$ species. This first adsorption step was then rapidly followed by a change of speciation by adsorbed gold-urea complex formation, so that again this technically is not a deposition precipitation.[61] Using this method, 1 wt.% AuPd bimetallic particles were deposited on TiO_2 and Al_2O_3 with different Au/Pd ratios and very good incorporation of Pd into the Au particles.[62–64]

A thermodynamic model has been proposed to rationalize the cluster size of Au particles during deposition precipitation using urea. A key part of the model is the dependency of the interfacial energy on the electrostatic interaction between nanoparticles and support, which was related to the PZC of the support and the pH of the solution. Experimental data of 2 wt.% Au deposited at a pH of 8 on different supports (Al_2O_3, PZC 8; TiO_2, PZC 6; and SiO_2, PZC 4), showed a decrease in particle size going from 2.3 to 1.6 nm with decreasing support PZC. This was in fair agreement with model predictions, even though further thermal treatment such as drying and calcination was not taken into account, and the authors acknowledged that the model provides only some qualitative tendencies, while the interactions involved are likely more complicated.[65]

4. IMPREGNATION & DRYING

4.1 Impregnation

Impregnation and drying is the most frequently used preparation method amongst others due to its simple execution and low waste streams. The first step of obtaining supported metal catalysts via impregnation and drying is contacting a metal precursor solution with a porous support. Common precursors include inorganic metal salts, such as metal sulfates, carbonates, chlorides, nitrates or acetates, and organic metal complexes such as metal acetylacetonates. The most commonly used solvent for inorganic salts is water because of the high solubility of many precursors, whereas organic solvents are mainly used for organometallic precursors. To prevent premature deposition of the metal precursor in bulk solution, concentrations below (super)saturation are required.

Two main impregnation methods are distinguished, namely wet impregnation (WI), whereby an excess amount of solution is used, and pore volume impregnation (PVI), in which an amount to just fill to the pore volume of the support is used. The latter method is also known as incipient wetness impregnation (IWI) or dry impregnation (DI), because the impregnated material keeps a dry character at a macroscopic scale. Uptake of the liquid into the pores of the support occurs due to the capillary pressure difference Δp across a hemispherical meniscus in a pore with radius r_p according to the Young-Laplace equation:[66]

$$\Delta p = (2\,\gamma_{lv} / r_p) \cdot \cos\theta \qquad \text{(Equation 2.2)}$$

whereby γ_{lv} is the surface tension between the liquid and vapor interface and θ is the wetting angle between the solid and the liquid. If $\theta < 90°$, the liquid is considered as wetting and will penetrate the support spontaneously, which is the case with water in combination with most oxidic supports. If the liquid is non-wetting ($\theta > 90°$), the pressure becomes negative and an external pressure is needed to force the liquid into the pores. This can occur for hydrophobic supports such as carbon materials, for which a less polar solvent such as ethanol or isopropanol

may be more appropriate, although this usually comes at the expense of a lower precursor solubility. From Equation 2 it is clear the pressure difference depends inversely on the pore size, so that liquid is preferentially sucked up by the smallest pores. The rate at which the liquid fills the pores is generally fast and often not considered critical for catalyst synthesis. According to the Washburn equation,[67] infiltration of a wetting liquid into a porous body of a few millimeter can occur in seconds to minutes, as has been experimentally verified.[68] However, when the support is prewetted with the same solvent before loading the precursor via wet impregnation, capillary forces do not play a role and the only driving force for the precursor to enter the support is diffusion, which can take significantly longer.[69]

Pore Filling. Although pore filling occurs rapidly, whether or not all pores are filled after impregnation to incipient wetness has been questioned. Inhomogeneous MnO_2 and Fe distributions have been observed after calcination on SBA-15 and MCM-41, respectively and attributed to inhomogeneous filling during impregnation.[70,71] Direct imaging of the impregnated precursor solution is difficult, due to evaporation and decomposition induced by a high intensity beam of an electron microscope.

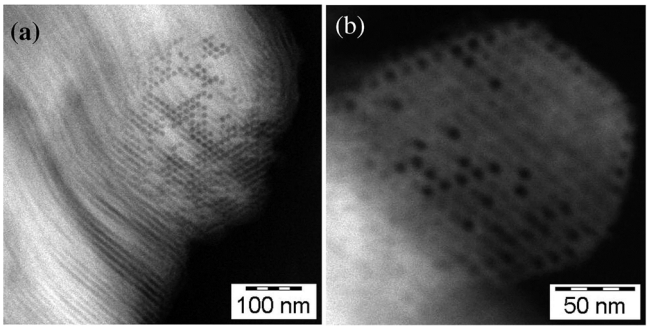

Figure 2.6. Cryo HAADF-STEM images of SBA-15 pore volume impregnated with an aqueous nickel nitrate solution and frozen to -196 °C, showing several pores remained empty after impregnation. (Adapted with permission from ref 72. Copyright 2008 American Chemical Society)

Using Cryo-TEM, SBA-15 impregnated with a nickel nitrate hexahydrate solution was frozen to -197 °C and imaged by Sietsma *et al.*.[72] Many pores were found empty after impregnation (Figure 2.6), which was performed to incipient wetness of the pore volume as determined by N_2-physisorption. This inhomogeneous filling was attributed to the relatively low hydroxyl density of SBA-15 compared to that of regular silica, resulting in incomplete wetting. It is also possible N_2-physisorption underestimated the total pore volume of the SBA-15, so that there was not enough liquid to fill all the pores. A more detailed Cryo-TEM tomography study was performed by Eggenhuisen *et al.* on SBA-15 impregnated with cobalt nitrate or nickel nitrate solutions. Although a few empty pores were found mainly on the external edge of the support particles, the majority was filled, and it was concluded that impregnation does lead to an almost homogeneous and complete pore filling.[73] Measurements on larger samples by differential scanning calorimetry (DSC) have also provided evidence on the complete filling of porous supports (Figure 2.7).[74] Due to the downward shift in the melting point of liquid confined in nanopores, a distinction was made between extra-porous and intra-porous liquid in the material. Incipient wetness impregnation of several ordered

mesoporous silicas and silica gels with a eutectic nickel nitrate solution resulted in fillings between 90-100%, while additional liquid was no longer accommodated inside the pores but present outside the pores instead.[74]

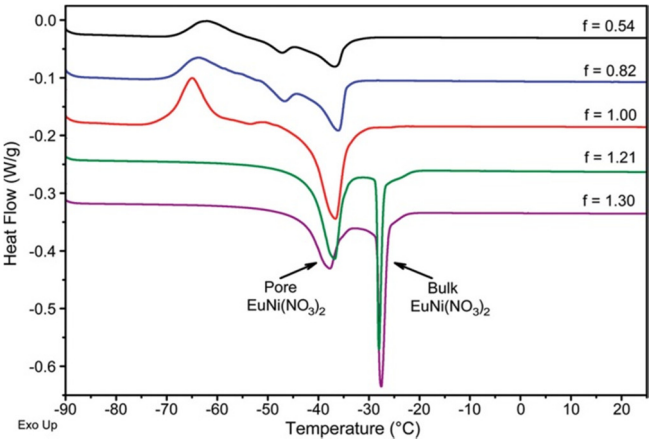

Figure 2.7. DSC measurements during the heating of a silica gel with 16 nm pores filled with a eutectic nickel nitrate solution ($EuNi(NO_3)_2$). The theoretical filled fraction f is defined by $f = V_{EuNi(NO3)2} / V_{SiO2}$. Due to confinement, the solution in the pores melts (endothermic peak) at a lower temperature compared to the extra-porous or bulk solution. Even at a theoretical filling of 1.00, no bulk melting was detected, indicating all of the impregnation solution was located inside the pores. (Adapted with permission from ref 74. Copyright 2009 American Chemical Society)

The two-solvent impregnation method, also known as the double solvent technique, offers an alternative to ensure no material ends up at the outer surface of the support particle.[70] In this method, the support is first dispersed in an apolar solvent such as pentane or cyclohexane. Subsequently, an aqueous solution containing the metal precursor is added. Due to the favorable wetting properties of the aqueous solvent, i.e. the aqueous phase has a lower contact angle θ, it replaces the apolar solvent in the mesopores of the support. However, inhomogeneous distributions inside the catalyst grains are often reported after drying and calcination when using this method,[75–78] which is at least partly influenced by the choice of the apolar solvent. Van der Meer *et al.* studied pentane, hexane, heptane, and cyclohexane as apolar solvent for the production of Co_3O_4/SBA-15 from an aqueous solution of cobalt nitrate, followed by drying and calcination. Use of cyclohexane resulted in large aggregates of cobalt particles of a few hundred nanometers, whereas pentane resulted in relatively small aggregates of several tens of nanometers.[78] It was proposed that the aggregate size is influenced by the size of the aqueous droplets that form in the alkane phase, which is influenced by the interfacial tension between the polar and apolar solvent. This was lowest for pentane, resulting in the smallest droplets and subsequent aggregates.[79] Comparison of nickel actetate and nickel nitrate on MCM-41 (Ni loading of 1 and 5 wt.%) showed more homogeneous distributions were obtained using nickel acetate, suggesting the thermal treatment after impregnation plays a significant role in the distribution of the precursor. In this case, it was postulated that nickel acetate exhibited stronger adsorption on the support surface thereby limiting redistribution, whereas nickel nitrate redistributed during further treatment due to a weak interaction with the

support, as will be discussed in the following sections.[76] Also note that organic material present during subsequent thermal treatments can greatly affect the final dispersion of the catalyst, as discussed in section 4.4.

4.2 Adsorption

In general, adsorption of metal ions from aqueous solution onto a support plays an important role when low metal loadings are applied. Electrostatic adsorption requires the pH of the solution to be different from the PZC of the support in order create adsorption sites in the form of charged surface hydroxyl groups. This ability of support surface hydroxyl groups in water to become protonated or deprotonated also allows them to function as a pH buffer. When a γ-alumina with a surface area of 200 m^2/g, pore volume of 0.5 mL/g and surface hydroxyl density of 8 groups/nm^2 is impregnated to incipient wetness with an acidic solution of pH 3, only 1/5000 surface groups become protonated so that the surface will be negligibly charged. However, the pH of the solution will rise from 3 to that close to the PZC charge of the γ-alumina, about 8 to 9.[80] Therefore, adsorption is often low upon incipient wetness impregnation, especially with high precursor concentrations, and when adsorption is desired wet impregnation is generally applied. It should be noted that the change in pH of the impregnating solution upon impregnation to incipient wetness is often not considered, even though many transition metals are hydrolyzed at high pH, which may result in premature precipitation of metal hydroxides.

Varying names are used for adsorption techniques, such as strong electrostatic adsorption (SEA), ion adsorption (IA), and equilibrium deposition filtration (EDF). All these methods are based on the same general principle. To achieve adsorption, wet impregnation is performed with a large excess of solution, low concentration of the precursor, and a predetermined pH. The modes of deposition can be globally divided into two main modes of adsorption. Outer sphere complex formation concerns non-specific, coulombic or electrostatic interactions of the precursor with the support, whereby the support surface charge is compensated by a layer of charged metal ion complexes in solution. Inner sphere complex formation occurs when support surface groups become directly involved in binding the complex, e.g. when a surface oxygen or hydroxyl group enters the first coordination sphere of the metal complex. A detailed review on the fundamentals of adsorption can be found elsewhere.[81]

Outer and Inner Sphere Complex Formation. Adsorption via outer sphere complex formation concerns mainly electrostatic interactions, and has been formulated into a relatively simple model.[82] In general, multivalent ions preferentially adsorb over monovalent ions.[83] This type of adsorption is highly pH dependent; at a pH at the PZC, the net charge of the surface is zero and very limited or no adsorption takes place. Anions are adsorbed at a pH below the PZC, while cations are adsorbed when the pH is higher. Care should be taken not to use extreme pH values, whereby high ionic strength of the solution diminishes the adsorption equilibrium constant, so that adsorption is actually reduced instead of improved.

Recently, Regalbuto *et al.* used Pd, Cu, Co, Ru and Ni ammine complexes to obtain silica supported catalysts at loadings between 1 and 3 wt.%. After deposition at a pH of 12, the catalysts were dried and directly reduced. Small particles between 1 and 3 nm were found, and calculations showed that these metal loadings were close to the maximum obtainable by electrostatic adsorption for the used silica with a surface area of 180 m^2/g and a PZC of 4.0. It was postulated that the maximum loading mainly depends on the surface area of the support.[84] A follow up study focused on SBA-15 supports with different surface areas. Ammine complexes were used to deposit Pd nanoparticles of 1.3 nm at a relatively high loading of 8.7 wt.% on a 1000 m^2/g SBA-15, and 1.9 nm Pt particles were synthesized on an SBA-15 with 600 m^2/g with a loading of 9.2 wt.%, showing high surface areas were indeed beneficial for adsorption.[85] Co particles were also synthesized using this method but larger particles of 7 nm at a loading of 5.1 wt.% resulted. This was attributed to particle growth that occurred during the high reduction temperature of 800 °C needed to reduce the strongly adsorbing cobalt complexes, whereas the Pt and Pd catalysts were reduced at 350 °C or lower.[85]

Recent studies have focused on adsorption on high surface area carbon supports to obtain high metal loadings. Hexachloroplatinate was deposited on several carbon xerogels with BET surface areas of 650 m^2/g (at pH 11, PZC 9.4), while platinum tetraamine was deposited on oxidized carbon (at pH 2.5, PZC 2.4). The maximum loading of hexachloroplatinate was found to be 9.2 wt.%, while that of platinum tetraamine was only 4 wt.%, and scaled linearly with the mesoporous surface area of the support. It was hypothesized that the Pt ammine complexes, which retain two hydration sheaths, were too large to enter the micropores of the carbon, which was not a problem for the smaller hexachloroplatinate. In each case, small Pt particles between 1.1 and 1.3 nm were obtained.[86] 2 nm Pt particles at very high loadings of 28 wt.% were obtained on a carbon black material with 1500 m^2/g using hexachloroplatinate at high pH.[87] Regalbuto *et al.* have shown for support material with a lower surface area that high loadings can be achieved by successive impregnation and reduction steps. On carbon xerogel with a surface area of about 600 m^2/g, hexachloroplatinate was deposited at loadings of 7.5, 15.0 and 22.3 wt.% for the first, second and third step, respectively. Thus, it appeared the adsorbed metal ions formed small particles during reduction, thereby fully regenerating the adsorption sites, as has also been observed during atomic layer deposition (see section 5.3). Moreover, the particle size did not increase significantly upon additional treatments, but stayed constant at 2.0 nm, resulting in an increased particle density upon multiple deposition cycles.[88]

Although short contact times (1 h) resulted in outer sphere complex formation, longer contact time between platinum tetraammine and oxidized carbon at low pH gave rise to reduction of Pt concurrent with oxidation of the carbon surface.[87] Similarly, when trying to deposit cobalt on a carbon support at high pH, it was found that the cobalt ammine complex was completely converted to Co_3O_4 after 1 h, which did not occur on silica.[89] Reductive ammination of the precursor took place, forming different precipitates depending on the pH (CoO at pH 9.2, Co_3O_4 at pH 9.8 and $Co(OH)_4^{2-}$ at pH > 11 when NH_4OH was used as a base), so that the process is better described as a deposition precipitation. Moreover, at higher

pH the cobalt ammine reacted to $[Co(NH_3)_5Cl]Cl_2$, which did not adsorb at all.[90] Nonetheless, particles of 5 nm were obtained at a Co loading of 6.7 wt.% at a pH of 10.

While in each of the previously discussed studies diluted slurries of a powdered support in a large excess of solvent were used, it was recently shown that significant adsorption is also possible during incipient wetness impregnation, in a modified method called charge enhanced dry impregnation (CEDI).[91] To overcome the buffering effect and charge the support, very high or low pH values were required (Figure 2.8). While dissolution of the support could be an issue at such extreme pH, it was reasoned that the buffering effect of the support would result in relatively fast pH equilibration, so that the pH drops to a value where the surface is charged but dissolution is less problematic. Using this method, 2 wt.% Pt was deposited on carbon (PZC 2, pH 13), silica (PZC 4, pH 13), and alumina (PZC 8, pH 1). Small particles between 1.5 and 3 nm were obtained, much smaller compared to a conventional dry impregnation whereby the pH of the impregnating solution was not optimized. Thus, CEDI provides the advantage of obtaining high dispersions without high amounts of waste water, albeit at relatively low metal loadings.

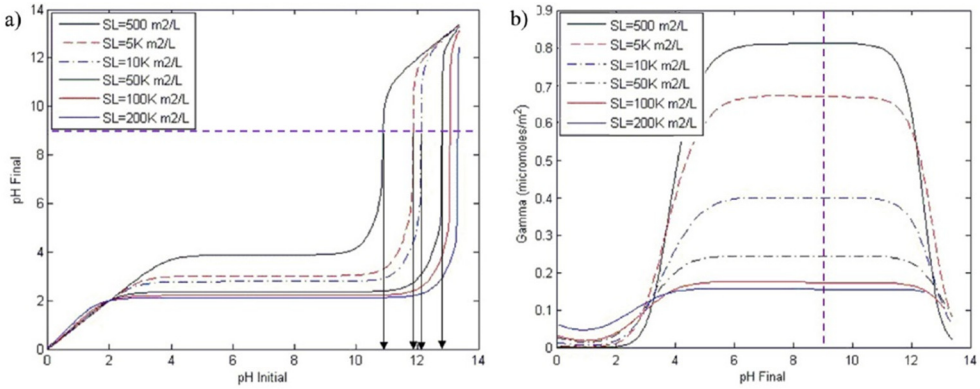

Figure 2.8. Estimation of the pH needed to obtain maximum cation adsorption for a material with PZC 2. (a) Difference in initial pH of the solution and the final pH caused by buffering of the support, dependent on the surface loading (SL, defined as the amount of support surface area present in the slurry per liter). (b) Cation uptake, dependent on the final pH and surface loading. Dashed blue line in (b) shows maximum uptake around a final pH of 9. In (a), it can be seen that to obtain this final pH, the slurry should be at an initial pH of 9 for very low SL (highly diluted slurry), whereas at high SL, such as is the case for incipient wetness impregnation, an initial pH of 13 can be required (SL at incipient wetness for a material with surface area of 200 m^2/g and pore volume of 1 mL/g is 200 K). (Adapted with permission from ref 91. Copyright 2013 American Chemical Society)

The principles of strong electrostatic adsorption have also been used to selectively deposit metals on specific surface sites. Using the difference in PZC between Co_3O_4 (PZC 8) and TiO_2 (PZC 4), manganese was selectively deposited on cobalt in a Co_3O_4/TiO_2 catalyst by using $KMnO_4$ at a pH of 1, whereby the TiO_2 was negligibly charged.[92] STEM-EELS showed MnO was located preferentially on the Co_3O_4, (Figure 2.9) while samples prepared by conventional

incipient wetness impregnation whereby the pH was not regulated resulted in MnO dispersed all over the TiO_2 support.[93] However, reduction of the catalyst resulted in migration of the MnO in both cases to the Co/TiO_2 interface, which appeared to be thermodynamically favorable. Similar results were obtained for $MnO/Co/SiO_2$ and $MnO/Rh/SiO_2$, where MnO was preferentially adsorbed on Co_3O_4 or Rh_2O_3, respectively, However no MnO migration was observed after reduction on the silica support.[94,95]

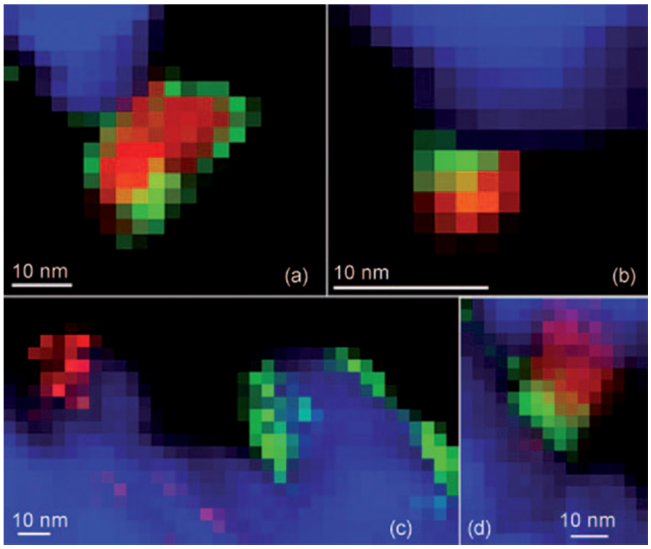

Figure 2.9. STEM-EELS map for $Mn/Co/TiO_2$. Strong electrostatic adsorption resulted in manganese (green) deposited on the cobalt (red) after calcination (a), which moved to the cobalt titania (blue) interface after reduction (b). By deposition via IWI MnO was present on the TiO_2 support after calcination (c), which after reduction also migrated to the Co/TiO_2 interface (d). (Adapted with permission from ref 93. Copyright 2010 Wiley)

Inner sphere complex formation concerns a chemical adsorption, whereby metal complexes are covalently coordinated to the hydroxyl groups (Figure 2.10). Because a charged complex is bonded to the support, this is generally compensated through the release or accumulation of protons by the support for a positive or negative metal complex, respectively, leading to a change in the pH of the impregnating solution. Therefore, to optimize procedures whereby inner sphere complex formation occurs, it is often important to actively regulate the pH during the equilibration procedure. In addition, adsorption can occur at a pH similar to the PZC, as described for Au on Al_2O_3 or TiO_2 (see section 3.2). The exact nature of adsorption depends on the support, precursor and conditions, and often both inner and outer sphere complex formation can occur simultaneously.

In a series of papers, Lycourghiotis *et al.* investigated the method of adsorption on titania (PZC 6.5, BET surface area 50 m^2/g) supported chromium, molybdenum, tungsten, cobalt and nickel at various pH ranging from below to above the PZC.[96–100] It was found that CrO_4^{2-}, $HCrO_4^-$ and CrO_7^{2-} mainly adsorb through electrostatic forces to form outer sphere complexes, at a maximum of 1 wt.% at pH 4.5.[99] However, the other metals all showed some form of covalent bonding of the metal precursor complex and the titania support. Mo and W complexes showed the highest adsorption of 3 and 10 wt.%, respectively, at pH 4. Mainly

mononuclear MoO_4^{2-} and WO_4^{2-} species were observed, whereby the complexes were formed via hydrogen bonds or substitution of one or two oxygen ligands with terminal oxygen groups of the titania. Polymeric species were also found in both cases when high initial concentrations and low pH were used, which adsorbed mainly through electrostatic forces. $Co(H_2O)_6^{2+}$ and $Ni(H_2O)_6^{2+}$ species preferentially adsorbed as mononuclear species, whereby one water ligand was replaced by a surface oxygen group, at a maximum of about 2 wt.% at pH 7.5. In addition, one or more water ligands not bonding with the support could be hydrolyzed.

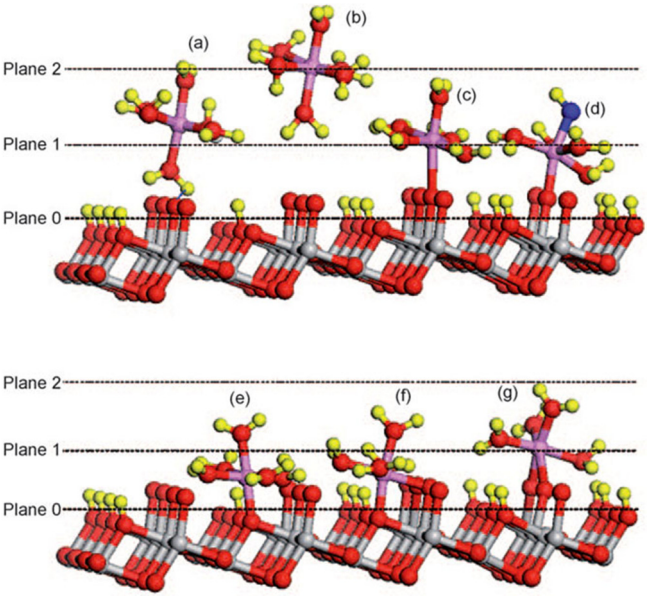

Figure 2.10. Schematic representation of various deposition possibilities of $Co(H_2O)_6^{2+}$ on (101) anatase. (a) hydrogen bonding, (b) outer sphere complex formation via electrostatic adsorption, (c) inner sphere complex formation via mono-substitution of a H_2O ligand with a terminal surface oxygen atom, (d) mono-substitution with a hydrolyzed compound, (e) mono-substituted complex with a bridging surface oxygen, (f) di-substituted complex with one briding and one terminal surface oxygen, (g) di-substituted complex with two terminal oxygen groups. Ti in gray, H in yellow, O in red, Co in pink, oxygen of hydrolyzed group in blue. (Adapted with permission from ref 96. Copyright 2009 Wiley)

The knowledge of the type of species adsorbed at different pH has allowed for the rational synthesis of supported catalysts. In the synthesis of 1.5 wt.% MoO_3/TiO_2 catalysts, it was found that deposition at a constant pH of 6 resulted in much better dispersed catalysts as determined by XPS, which showed a Mo/(Mo+Ti+O) ratio of 2.2 compared to 1.3 for the catalyst prepared at pH 9. It was postulated that the di-substituted MoO_4^{2-} that formed at pH 6, whereby two oxygen ligands of the precursor are replaced with terminal oxygen groups of the TiO_2, was more stable to sintering during subsequent calcination compared to the mono-substituted species which dominated at pH 9.[101] Studies on Co/Al_2O_3 and Mo/Al_2O_3 illustrated the technique is not always easy, as deposition of large crystals or too strongly interacting species which were difficult to reduce also occurred depending on the conditions.[102,103] Nonetheless, Kordulis *et al.* showed Co/Mo (2/17 wt.%) bimetallic catalysts can be synthesized on a Al_2O_3/SiO_2 mixed support. Co-adsorption of ammonium heptamolybdate and cobalt nitrate at pH 5 resulted in the selective deposition of MoO_4^{2-} on

the positively charged alumina while the silica was negatively charged. Alternatively, Co was preferentially deposited on the silica surface, which resulted in fewer irreducible Co/Al_2O_3 sites. The resulting catalyst was over 10% more active for the hydrodesulphurization of thiophene compared to a similar one prepared via regular impregnation.

In the synthesis of 1 wt.% Ni/SiO_2 catalysts using nickel ethylenediamene (*en*) complexes from nickel nitrate and ethylenediamene, the NiO species were controlled via different grafting of the nickel precursor complex. Both $Ni(en)(H_2O)_4$ and $Ni(en)_2(H_2O)_2$ were grafted onto the support via replacement of two H_2O ligands with surface hydroxyl groups. After calcination, grafted $Ni(en)(H_2O)_4$ gave rise to nickel phyllosilicate formation, eventually resulting in large nickel particles after reduction. However, grafted $Ni(en)_2(H_2O)_2$ brought about isolated Ni^{2+} ions after calcination, resulting in very small particles after reduction. This was attributed due to the lack of free H_2O ligands in the adsorbed complex, so that it no longer reacted with other complexes or silicon containing species.[104]

Metal Distribution. Adsorption also plays a significant role on the metal distribution across macroscopic support grains or pellets. Although the pore filling with liquids of larger bodies occurs within a few seconds or minutes, adsorption on support sites often slows down penetration of the precursor significantly. After short equilibration times it is possible that metal precursor complexes are mostly adsorbed in the outer shell of the support body, resulting in an egg-shell distribution. The details of an egg-shell distribution will strongly depend on the equilibrium between adsorbed and solvated species. Longer equilibration time leads to diffusion of the metal complex towards the center of the catalyst body due to concentration gradients if the adsorption is at least to some extent reversible, so that eventually the system will converge to a homogeneous distribution. Addition of a second component that adsorbs more strongly than the precursor can result in egg-white or egg-yolk distributions (Figure 2.1). The additional component adsorbs in the outer shell leaving no sites available for the metal precursor complex, which diffuses inwards where more adsorption sites are available.[105,106] Although this has been known for a long time, the subsequent drying step is also reported to have a large impact on the distribution, and direct monitoring of the distribution during impregnation is now possible by advanced spectroscopic techniques that have recently been developed.[107]

Using Raman spectroscopy, the impregnation of 3 mm γ-Al_2O_3 pellets (PZC 9) with ammonium heptamolybdate (AHM) solutions at pH 5 or 9, leading to 15 wt.% Mo, was followed over time.[108] Because of the equilibrium between heptamolybdate and mono-molybdate, $Mo_7O_{24}^{6-}$ was the predominant species at pH 5 while at pH 9 mainly MoO_4^{2-} was found. Upon impregnation with the solution at pH 9, close to the PZC of the γ-Al_2O_3, the surface was minimally charged and almost no interaction took place between precursor and support, which led to a homogeneous MoO_4^{2-} distribution across the pellet after 10 minutes. With an impregnation solution of pH 5, the γ-Al_2O_3 was positively charged, and electrostatic adsorption of $Mo_7O_{24}^{6-}$ took place at the outer edges of the surface. At the same time, the buffering effect of γ-Al_2O_3 resulted in an increase in the pH and MoO_4^{2-} formation, which

more easily diffused towards the inside of the pellet. Moreover, $(NH_4)_3[Al(OH)_6Mo_6O_{18}]$ precipitated on the external surface, preventing a large part of the Mo to diffuse into the pellet altogether. When a γ-Al_2O_3 with a lower PZC of 8 was used, areas of high Mo concentrations were found throughout the pellet at long equilibration times with diagonally offset Raman spectroscopy and X-ray absorption tomography. [109,110] These were attributed to the formation of $Al(OH)_6Mo_6O_{18}^{3-}$ species throughout the support due to the lower buffering capacity of the alumina with PZC 8 instead of 9 as with the previous study. This was be mitigated by co-impregnation of a species that forms stable complexes with Mo^{6+}, such as citrate or H_3PO_4, which resulted in homogeneous distributions after sufficient time for equilibration.[108,110]

The concentration of the precursor has also been found important, which can be explained by the limited adsorption capacity of a support surface. For $Co(H_2O)_6^{2+}$ complexes impregnated on alumina, little interaction is expected between the positive complex and the protonated or neutral surface hydroxyls. Nonetheless, impregnation of a 3.85 mm γ-Al_2O_3 pellet with a low concentration of 0.2 M $Co(NO_3)_2$ took 4 hours for equilibration, as followed with ^{1}H MRI[111], while in a different study impregnation of a 3 mm γ-Al_2O_3 pellet with a 1.35 M $Co(NO_3)_2$ solution showed a homogeneous distribution already after 5 minutes.[112] Bergwerff *et al.* further studied the impregnation of 0.2 M Co^{2+} by varying the pH and citric acid concentration using ^{1}H MRI.[113] If no citric acid was added, a homogeneous distribution was obtained after 160 minutes at pH 1. Addition of citric acid at pH 1 did not lead to the formation of cobalt citrate complexes, so that competitive adsorption between $Co(H_2O)_6^{2+}$ and free citric acid resulted in more rapid transport of Co^{2+} to the center of the 3.85 mm pellet, producing egg-yolk catalysts after 90 minutes of equilibration (

Figure 2.11). At pH 5 and 9, cobalt citrate complexes formed which strongly adsorbed on the surface of the γ-Al_2O_3, resulting in egg shell distributions of varying degrees even after 48 hours. However, addition of extra citrate to these solutions again resulted in competitive adsorption, so that the Co^{2+} complexes migrated towards the center more rapidly.

Nickel combined with ethylenediamene (*en*) showed similar results. Upon impregnation of a 3 mm γ-Al_2O_3 pellet with 0.5 M $Ni(H_2O)_6^{2+}$ and *en* at different Ni/*en* molar ratios (0, 1, 2 and 3), homogeneous $Ni(H_2O)_6^{2+}$ and $Ni(en)_3^{2+}$ distributions were found after 5 minutes for Ni/*en* ratios of 0 and 3, respectively. At other ratios, $Ni(en)_x(H_2O)_{6-2x}^{2+}$ complexes formed which strongly adsorb, resulting in eggshell formations after 5 minutes, and a 2 hour equilibrium period was necessary to obtain homogeneous distributions.[114] On a 3.85 mm pellet, 5 minutes was not sufficient to obtain a homogeneous distribution upon impregnation of a 0.5 M $Ni(H_2O)_6^{2+}$ solution. This relatively slow equilibration of weakly interacting species was attributed to partial hydrolysis and subsequent re-dissolution of nickel nitrate.[115] While the PZC and surface area of this pellet was similar to the one used in the previous study, the difference might be attributed to the lower pore volume of the pellet, so that the amount of surface area per volume of impregnating solution doubled, allowing for more interaction with the support. Regardless, after 1 hour a homogeneous distribution was found. Combined with ethylenediamenetetraacetic acid (EDTA) at a molar ratio of Ni/EDTA of 6 at pH 1 or 6, slight

eggshell formations were found due to the formation and electrostatic adsorption of $Ni(EDTA)^{2-}$ and $Ni(EDTA\text{-}H)^{-}$ complexes in the external shell, while the remaining $Ni(H_2O)_6^{2+}$ was homogeneously distributed throughout the rest of the pellet. Equilibration was faster at pH 1, for which less hydrolysis of $Ni(H_2O)_6^{2+}$ species occurred.[115] This difference in equilibration time based on pH was even more pronounced for $Cr(H_2O)_6^{3+}$ complexes, where very defined eggshell profiles were formed at pH 4.5 due to hydrolysis of the precursor, while uniform distributions were obtained at pH 1.[116] When CrO_4^{2-} complexes were used as precursor, the roles were reversed. Strong electrostatic adsorption at low pH led to egg-white structures, while high pH led to limited interaction and therefore a homogeneous distribution. In this case, citric acid was found to limit hydrolysis of the Cr^{3+} complexes, while it also caused reduction of Cr^{6+} to Cr^{3+}, so that in most cases homogeneous distributions were obtained.

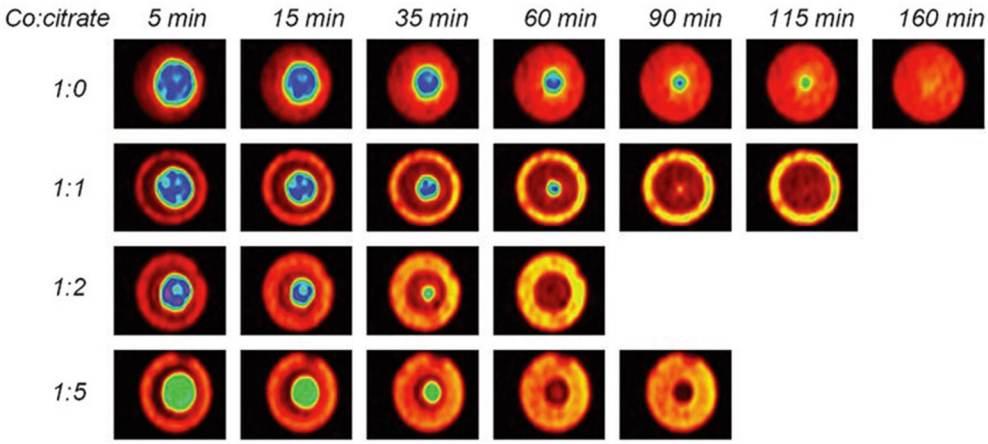

Figure 2.11. 2D 1H MRI images recorded on an Al_2O_3 extrudate after impregnation with 0.2 M $Co(NO_3)2$ (aq) at pH 1 with different molar ratios of cobalt/citrate. Blue color indicates low cobalt concentration, yellow indicates medium cobalt concentration, and red indicates high cobalt concentration. The higher the amount of citric acid, the faster cobalt migrated to the inside of the pellet, resulting in more concentrated egg-yolks, while the egg-shells with only medium cobalt concentrations (yellow) became larger. (Adapted with permission from ref 113. Copyright 2008 Wiley)

In the previous study, competitive adsorption was also studied using H_3PO_4. This led to egg-yolk catalysts upon co-impregnation with Cr^{6+} species.[116] Another example of competitive adsorption is Cl^- and $PdCl_4^{2-}$. 5 minutes after impregnation, all $PdCl_4^{2-}$ had hydrolyzed to $PdCl_2(OH)_2^{2-}$ at the edge of the γ-Al_2O_3 pellet due to the basic surface OH groups, regardless of Cl^- concentration and pH. After two hours, egg white distributions were obtained at pH 1 because many sites at the edge of the pellet were protonated followed by adsorption of Cl^-, so that the $PdCl_2(OH)_2^{2-}$ moved deeper into the pellet for adsorption on free sites. At pH 5, Cl^- adsorption was less favorable so that eggshell distributions were still detected. After 96 h each of the four main distributions (Figure 2.1) could be obtained depending on the conditions used. An egg-white distribution was obtained by strong and competitive Cl^- adsorption at low

pH, which was limited to the outer shell of the pellet at low Cl^- concentration, while at higher Cl^- concentration more competitive adsorption resulted in an egg-yolk profile. At higher pH and low Cl^- concentration, limited competitive adsorption resulted in an egg-shell catalyst, while increasing the Cl^- concentration resulted in a more homogeneous distribution.[117]

4.3 Drying

The drying step has long been known to have a strong influence on the final catalyst.[106,118] Drying can be separated into three main stages; the increasing rate, constant rate and falling rate periods. The increasing rate period concerns the time it takes for the system to attain the equilibrium drying temperature, which is slightly lower than the temperature set on the drying oven because evaporation is an endothermic process, but a pseudo steady state is generally achieved relatively rapidly. In the constant rate period, drying mainly occurs on the external surface of the drying grain or pellet. The system is in what is called a pendular state, whereby a continuous liquid exists throughout the particle, such that the solvent can be transported towards the external surface of the catalyst grain via capillary forces. If the precursor has a weak interaction with the support, it may be transported towards the external surface along with the solvent, resulting in a concentration buildup on the external rim of the support. As a consequence of the resulting concentration gradient, back diffusion towards the inside of the grain can occur. At a certain time, the amount of solvent has been reduced to such an extent that capillary flow towards the external surface of the catalyst grain can no longer keep up with the rate of drying, and the drying front moves inwards. As this happens, the drying rate slows down as transport via the vapor is slower than via the liquid, and the liquid inside the pores becomes discontinuous, called the funicular state, so that isolated patches of liquid can form and macroscopic redistribution at this stage becomes very limited.

As the solvent is removed during drying, the concentration of the precursor will rise and once it reaches the critical supersaturation, precipitation will take place. Moreover, a chemical change of the precursor induced by dehydration, temperature, or a gas atmosphere can result in precipitation. As systems likely go through severe macroscopic redistribution across the catalyst grain or pellet during drying, precipitation can be important for the final macroscopic distribution of the active phase. It should be noted that many organic molecules such as citric acid or ethylenediamene tetraacetic acid (EDTA) have previously been reported to change the viscosity of the impregnating solution.[119] This was recently shown in the preparation of 1-20 wt.% Fe catalysts on α-Al_2O_3 by Torres *et al.*, who compared the effect of iron nitrate and ammonium iron citrate on the iron distribution of the final catalysts. Iron particles of around 20 nm were found regardless of the precursor at loadings of 5 and 10 wt.% Fe. However, iron nitrate resulted in high local loadings while other parts of the support remained empty, whereas ammonium iron citrate led to a homogeneous distribution. This was attributed to the formation of a gel-like phase for the citrate precursor, thereby preventing redistribution.[120] Addition of ethylene glycol (EG) in the preparation of 20 wt.% Ni/MCM-41 catalysts prepared from nickel nitrate has been shown to prevent redistribution of nickel to the external

surface during thermal treatment, which happened to a great extend when EG was not co-impregnated.[121] However, few other recent studies have been performed on the effects of the viscosity, although the addition of organic molecules has been used extensively to obtain a higher metal dispersion, which is discussed in the section on activation (4.4).

Drying of Strongly or Weakly Adsorbing Species. Since drying concerns movement of solvated species on a large scale, it is important to consider the degree of adsorption of the metal species in solution. Recently, Liu *et al.* modelled the effects of drying on porous bodies with different metal profiles after impregnation. Although 0.25 M nickel nitrate was used as a case study, the developed methodology presented was not limited to specific active components or supports, and the interaction between the two could be parametrically varied. By varying the strength of adsorption of nickel nitrate to the support, and varying the nickel nitrate distribution after impregnation from homogeneous to egg-shell, the effect of drying was studied. For a high adsorption strength, drying had little effect on the distribution, so that the main determining factor for the distribution was the impregnation step. A homogeneous distribution after impregnation remained homogeneous after drying, while egg-shell distributions remained largely unchanged when the adsorption strength was high.

Recent improvements on spectroscopic techniques have enabled imaging of distributions after impregnation and drying, providing experimental evidence of the limited effect of drying on strongly adsorbing species. UV-Vis and IR microspectroscopy showed nickel ethylenediamene complexes (0.5 M) with 1 or 2 *en* ligands grafted on γ-alumina did not redistribute during drying, whereas non-adsorbing $Ni(en)_3^{2+}$ migrated towards the outside of the support.[114] Strongly adsorbing Pd species (0.1 M $PdCl_4^{1-}$ solution) on alumina were studied with UV-Vis microspectroscopy, and were also found to retain the distribution they had obtained during impregnation after drying.[117] Using magnetic resonance imaging, Cobalt nitrate at low concentration (0.2 M, pH 4) was found to adsorb sufficiently strongly to a y-alumina surface to retain its egg-shell distribution obtained during impregnation after drying.[122] Thus, these studies confirm that for strongly adsorbing species, the drying step does not alter the macroscopic distribution of the precursor to a large degree.

For weakly adsorbing species and high concentrations, convection and back-diffusion during the drying step become very important. In the model of Liu *et. al.*, when the adsorption strength of nickel nitrate was reduced to a moderate value and assuming a homogeneous distribution after impregnation, drying could result in severe redistribution of the 0.25 M nickel nitrate solution on γ-alumina depending on the conditions.[69] Drying at 70 °C resulted in an almost homogeneous distribution. However, increasing the drying temperature to 300 °C resulted in egg-shell distributions, because back-diffusion of nickel nitrate was not fast enough to compensate for the high drying rate. Similar results were obtained upon altering the humidity of the drying air; at 0.5% humidity, drying was relatively fast resulting in an egg-shell distribution, while drying in 10% humidity resulted in an almost homogeneous distribution. Finally, the size of the support pellet had a great influence on the distribution. A pellet diameter of 1 mm resulted in a moderate egg-shell distribution whereby the concentration of

nickel nitrate in the shell was 1.5 times higher than in the center of the pellet. For a 10 mm pellet, the concentration in the shell was almost 3 times higher compared to the center.[69] The model was recently extended to a 3 mm γ-alumina pellet impregnated with nickel nitrate concentrations ranging from 0.005 M to 4.0 M (Figure 2.12), and many of the results were compared to experimental data.[123,124] Very low nickel nitrate concentrations (0.005 M) resulted in homogeneous distributions after drying at 80 °C because most of the nickel nitrate remained adsorbed on the γ-alumina. At slightly higher concentrations (0.06 M), the amount of nickel nitrate exceeded the adsorption capacity of the support, and an egg-shell distribution was obtained due to convective redistribution towards the edge of the pellet. Although back-diffusion gave rise to partial mitigation of this redistribution, the system entered the falling-rate period relatively rapidly, so that film-breakage occurred and material was no longer transported across large distances. At even higher concentrations (3 M), the precursor was also initially transported towards the outer edge of the pellet, but the concentration was so high that film breakage did not occur, so that sufficient back-diffusion time resulted in a homogeneous distribution. It should be noted that in these model systems, only the solvent water was removed leaving the nickel nitrate hexahydrate, which melts in its own crystal water above 56 °C, intact. Nonetheless, good agreement was found between the model predictions and real experiments, suggesting macroscopic distribution occurs mainly during the removal of the solvent, not removal of the crystal water of metal nitrates.[123,124]

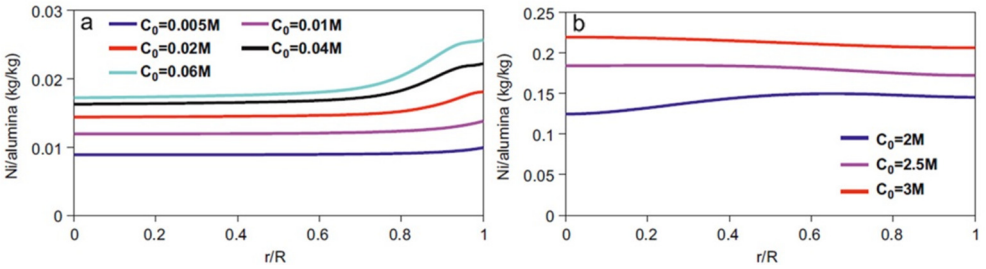

Figure 2.12. Simulated effect of the initial $Ni(NO_3)_2$ (aq) concentration on the final metal profile across a 3 mm γ-Al_2O_3 pellet after drying at 80 °C, starting from a homogeneous distribution after impregnation. (a) low metal loadings, (b) high metal loadings. The loading of nickel is plotted as a function of the normalized radial distance *r/R*, whereby *r* is the distance from the center of the pellet and *R* is the pellet radius. (Adapted with permission from ref 124. Copyright 2012 Elsevier)

An interesting consequence of these considerations is that precursor material present on the external surface of the catalyst grain or pellet does not necessarily mean it will be deposited there during drying. If material is on the outside after impregnation, capillary flow could pull it in when part of the pore volume becomes accessible again due to (partial) evaporation of the solvent, assuming the material on the outside is still dissolved or can be molten. The latter case closely resembles melt infiltration, which will be discussed in detail in section 5.1.

Other experimental evidence on redistribution of the precursor during drying has been reported in recent years. Impregnation of a basic ammonium heptamolybdate (AHM) solution (1.8 M, pH 9) onto gamma alumina resulted in little interaction with the support, so that redistribution towards the external of the pellet resulted in egg-shell distributions.[125] Alternatively, addition of H_3PO_4 to an impregnation of γ-alumina with AHM resulted in surface adsorption of PO_4^{3-}, so that the support surface was not significantly charged even at pH 2, together with complex formation of the form $H_xP_2Mo_5O_{23}^{6-x-}$. While normally AHM would adsorb to the alumina surface at this low pH, the negatively charged complex only weakly interacted with the PO_4 surface groups, so that redistribution of the complexes also resulted in egg-shell distributions.[110] As mentioned earlier, weakly interacting Ni(*en*)$_3$ complexes redistributed during drying resulting in egg-shell profiles.[114] Clearly, weakly interacting species can migrate over macroscopic distances during the drying step.

Metal Redistribution at the Nanoscale. Macroscopic distributions can be largely avoided by reducing the grain size of the support. This is often done in academia to rule out the effect of macroscopic distributions on the catalyst performance. However, even though support grains might be homogeneously distributed on the macroscale, inhomogeneities are frequently reported on the nanoscale. The active metal is often located in large clusters or aggregates, while a large part of the support remains empty. These aggregates can be much larger than the average pore diameter, and the nanoparticles often form an intricate network throughout the pore structure.[126] Moreover, the crystallites inside these aggregates have been observed to have an overall crystallographic alignment, suggesting they are closely linked to each other or were at some point during their synthesis.[127] Methods to prevent this include modification of the support or co-impregnating organic molecules.[128,129] However, recent studies revealed these inhomogeneous distributions can be circumvented by careful control of the drying step.

Using Stöber silica spheres impregnated with nickel nitrate solutions, Banerjee *et al.* used environmental TEM to study the distribution of the nickel phases during preparation. It was shown that inhomogeneous distributions obtained after *in-situ* drying of an aqueous solution largely remained after calcination and reduction, while use of ethanol as a solvent resulted in more homogeneous distributions, which was attributed to the lower surface tension of ethanol.[130] As described in chapter 4, Munnik *et al.* used a silica gel (38 - 75 μm grains) impregnated with a 4.2 M aqueous cobalt nitrate solution, close to saturation, and opted for drying in an N_2-flow in a fluidized bed reactor at different temperatures instead of often practiced stagnant drying in a muffle oven, followed by calcination at 350 °C in an N_2 flow.[12] While all of the samples displayed uniform cobalt distributions on the macroscale, drying at 25 °C followed by calcination resulted in 8 nm cobalt oxide particles clustered together in aggregates of 40 nm in size. Increasing the drying temperature gradually reduced the aggregate size until at 100 °C the 8 nm particles were homogeneously distributed over the support and no aggregates were found. However, further increase of the drying temperature to 150 °C resulted again in aggregate formation, which were up to 80 nm in size (Figure 2.13).[12]

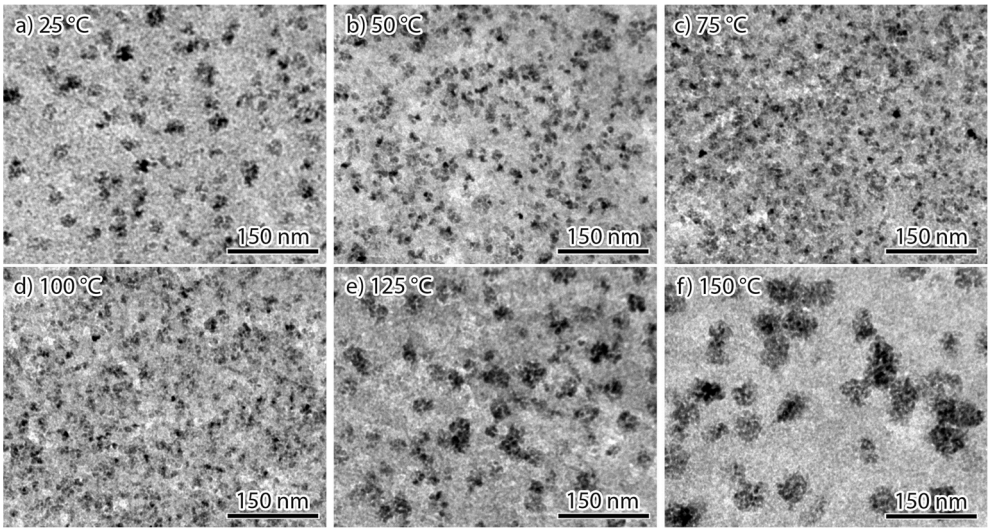

Figure 2.13. TEM of calcined Co_3O_4/SiO_2 after drying treatments in a N_2 fluidized bed at different temperatures. (a) 25 °C, (b) 50 °C, (c) 75 °C, (d) 100 °C, (e) 125 °C, (f) 150 °C. Different extent of cobalt aggregation (black) was observed located on the silica support (grey) depending on the drying temperature. The size of the primary cobalt oxide nanoparticles was ~9 nm in all cases. (Adapted with permission from ref 12. Copyright 2014 American Chemical Society)

This behavior was further studied by performing a calcination in a gas flow of 1% NO/N_2 after the drying treatment, which results in immobilization of the cobalt nitrate precursor via cobalt hydroxynitrate formation, so that further redistribution after drying was not possible.[131] As described in chapter 5, after drying at 25 °C and calcination in an NO/N_2 gas flow, 3 - 4 nm cobalt oxide particles were found in large irregularly shaped aggregates of up to 200 nm in size. Increasing the drying temperature reduced the size of the aggregates, until at 100 °C a homogeneous distribution of 3 - 4 nm cobalt particles was obtained. Further increase of the temperature resulted in 8 nm cobalt particles in increasingly large aggregates.[132] It was postulated that aggregation originated from two separate mechanisms. At low temperature, precipitation of a cobalt nitrate species occurred when the concentration reached the supersaturation. If the drying rate is low, nucleation of this species is relatively slow so that growth becomes very significant, resulting in large cobalt nitrate islands while other areas on the support become depleted. Raising the temperature increased the drying rate, so that the nucleation rate increased and smaller islands were formed, eventually resulting in a homogeneous distribution at 100 °C. This behavior shows resemblance to what is observed in the drying of colloidal wet films[133,134] and suggested that at low temperature aggregate formation was mainly a physical process. At temperatures above 100 °C, nucleation and growth of cobalt oxide due to decomposition of cobalt nitrate was found to occur during drying. As this mainly occurred still in the presence of a large amount of water, either in liquid or vapor

form, the cobalt nitrate was highly mobile and nucleation and growth of cobalt oxide resulted in increasingly larger aggregates.[132]

The effect of precursor support interactions was also investigated for a γ-alumina support. While stagnant drying in a muffle oven between 60 to 120 °C always resulted in 8 nm cobalt particles located in 30 - 60 nm aggregates after calcination in N_2 flow, drying in a fluidized bed between 25 and 100 °C resulted in the 8 nm particles uniformly distributed throughout the support after calcination. At 150 °C, aggregates of 30 - 40 nm were found, somewhat smaller than on silica. Thus, it appeared that the increased support-precursor interactions of the γ-alumina inhibited aggregate formation. Moreover, although drying in stagnant air always resulted in aggregates, drying using an N_2 flow resulted in uniform distributions, showing the importance of rapid removal of water during the drying process. It should be noted that fast drying can have a negative effect on the macroscopic distribution across catalyst grains when precipitation occurs without sufficient time for back-diffusion, as mentioned in the previous section and was observed for silica with larger pores of 23 nm.[132]

Aggregate formation due to a long retention time of water vapor has also been used for the synthesis of nanocast materials. Starting from iron nitrate, large iron oxide aggregates up to 2000 nm in size were synthesized on an ordered mesoporous silica support by covering up the sample container during a heat treatment to 150 °C. Similar results were found for cobalt, nickel, indium, manganese, cesium and chromium oxides when starting from the respective metal nitrates, showing the importance of the water pressure during drying and decomposition of metal nitrate hydrates in general.[135]

Alternative Drying Methods. While drying is most often performed in stagnant air in a regular muffle oven, other alternatives besides fluidized bed drying are available that alter the rate of drying or the drying process, and so influence the distribution of the active metal phase. In freeze-drying the precursor is frozen after impregnation, followed by sublimation of the immobilized solvent at reduced temperature and pressure. Eggenhuisen *et al.* performed freeze drying on SBA-15 impregnated with nickel or cobalt nitrate by freezing in liquid nitrogen and drying at -55 °C under reduced pressure. Using Cryo-TEM tomography to visualize the dried samples, it was shown that freeze drying resulted in homogeneous distributions of cobalt nitrate after drying, whereas inhomogeneous distributions were obtained after conventional drying at 60 °C (Figure 2.14). This difference in nanoscale distribution was largely maintained after performing a thermal activation, illustrating the drying step is highly important for the final metal distribution at the nanoscale.[73] As described in chapter 3, the method was also shown to work on a silica gel for cobalt nitrate and nickel nitrate.[20,136] However, freezing the precursor required great care. When a liquid is confined in nanometer sized pores, the freezing and melting point can be greatly depressed. While a 4.2 M cobalt nitrate solution froze at about -30 °C, confinement in a silica gel with 8 nm pores caused a freezing point depression to -90 °C. Thus, to properly freeze and dry the impregnated sample a temperature of -90 °C or lower should be applied. Therefore, although liquid nitrogen temperatures were sufficient to freeze the confined precursor, -45 °C was not sufficient to solidify the precursor and

redistribution was observed over the macroscopic catalyst grains, creating distinct egg-shell distributions.[136]

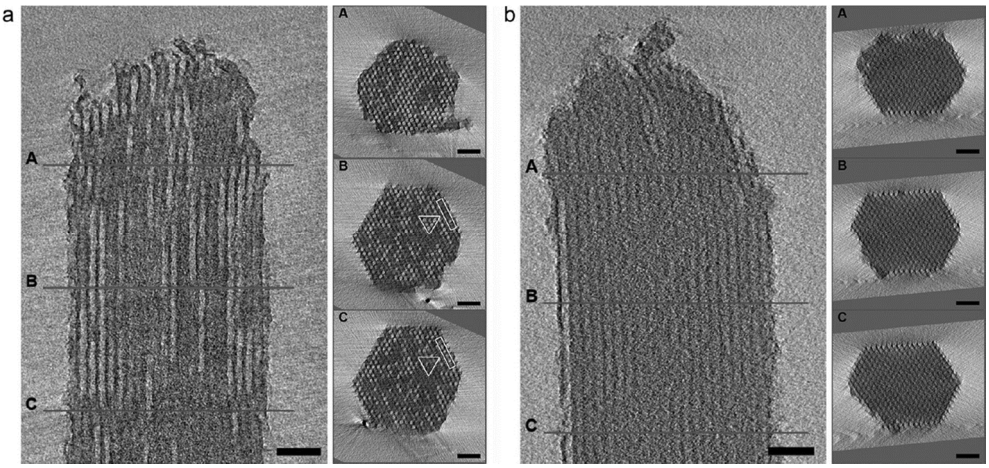

Figure 2.14. Cryo-TEM tomography results of $Co(NO_3)_2$ salt distribution in mesoporous SBA-15 after different drying treatments. (a) dried at 60 °C in a muffle oven, showing an inhomogeneous distribution after drying(trial and rectangle in B and C indicate examples of pores with inhomogeneous fillings), (b) dried by freeze-drying, showing a homogeneous distribution after drying. All scale bars are 50 nm. Lines A, B and C indicate the positions of the cross-sections. Bright dots and lines are empty pores; dark areas are filled pores. (Adapted with permission from ref 73. Copyright 2013 American Chemical Society)

Microwave drying provides another alternative since it has the potential to speed up drying drastically due to the volumetric heating of the material, removing the need for heat transport from the outer edge of the particle towards the center. Liu *et al.* studied microwave drying on 3 mm pellets impregnated with different concentrations of nickel nitrate solutions from 0.1 to 2 M.[124] In all cases, homogeneous macroscopic distributions across the pellet were obtained. Moreover, the drying step was completed in a relatively short amount of time. It was proposed that uniform drying reduced convection so that more homogeneous distributions were obtained.[124]

4.4 Activation

In the activation step the deposited metal precursor is converted into the active phase. Generally this is done by a calcination step, resulting in the metal oxides, followed by a reduction if metallic particles are required. Next to metals common active phases include metal oxides or metal sulfides. As the activation treatment leads to the formation of the nanoparticles, they often have a large influence on the final particle size. Moreover, although most treatments remain below the melting point of the active materials, the temperatures used can easily exceed the Hüttig temperature ($T_{Hüttig}$ = 0.3 T_{Melt}), around which defect sites on metal particles become mobile, or even the Tammann temperature ($T_{Tammann}$ = 0.5 T_{Melt}), whereby surface

atoms become mobile, which can lead to particle growth via migration and coalescence of the particles or via Ostwald ripening.

Although direct reduction of many precursors can lead to well dispersed catalysts, direct reduction is often highly exothermic and can lead to mixed metal-support phases. Moreover, it can produce a pyrophoric catalyst that needs to be passivated, often making it impractical for use on an industrial scale. Therefore, a calcination procedure is usually performed to form the pure metal oxide particles before further treatment such as reduction. Both the heating rate and air flow during calcination have been shown to be highly important for the preparation of 23 wt.% Co/γ-Al_2O_3 catalysts for the Fischer-Tropsch synthesis. Heating rates between 0.1 and 1 °C/min resulted in similarly active catalysts, however higher heating rates of 4 and 8 °C/min significantly reduced the activity when calcined to 250 °C. Air flows of 1 $m^3/(kg_{Co(NO3)2}·h)$, roughly corresponding to a gas hourly space velocity (GHSV) of 2000 h^{-1}, and higher during calcination resulted in similar catalysts with a cobalt surface area of 11 m^2/g, however at lower flows cobalt surface areas as low as 6 m^2/g were obtained.[137] In a separate study, flows higher than the above mentioned 1 $m^3/(kg_{Co(NO3)2}·h)$ were used to investigate the gas composition and calcination temperature in the synthesis of 20 wt.% Co/γ-Al_2O_3. Although calcination at temperatures between 150 and 500 °C for 10 h showed almost complete decomposition of the cobalt nitrate regardless of the temperature, dispersions of around 9% were found at 150 °C whereas at 400 °C this was slightly lower (7.5%). Upon testing gas composition, only 50% steam/air produced lower cobalt dispersions, whereas little difference was observed between N_2 and air.[138]

Sietsma *et al.* studied the calcination of nickel nitrate on SBA-15 (24 wt.% Ni). After drying at 120 °C, the precursor was found only inside the pores of the SBA-15 support, in the form of 9 nm crystallites of $Ni_3(NO_3)_2(OH)_4$, similar to the pore size of the support. Thermal decomposition of this phase in stagnant air resulted in severe redistribution and large particles on the external surface of the support (Figure 2.15). In a flow of air, the particle size was decreased, and a further improvement was obtained in a flow of He, suggesting decomposition in a flow and an O_2 free environment was beneficial for the metal dispersion. The highest dispersion was obtained in a flow of 1% NO/He, which resulted exclusively in small 4 nm NiO particles inside the mesopores of the support.[139] Further investigation on Ni/SBA-15 showed that addition of NO_2 or O_2 to the gas stream, both decomposition products of $Ni_3(NO_3)_2(OH)_4$, was detrimental for the metal dispersion and resulted in large particles and migration towards the external surface of the SBA-15 particles.[72] Moreover, NO concentrations as low as 0.1 %vol were already enough to reduce the NiO particle size from 11 to 4 nm at a gas hourly space velocity (GHSV) of 24,500 h^{-1}. Reduction of the GHSV at a concentration of 1 %vol NO showed little impact until a GHSV of 7000 h^{-1}, while further reduction resulted in gradually larger particles.[140] Additional IR, MS and isotopic labelling studies revealed that NO scavenges oxygen radicals from the nitrate during decomposition. It was proposed that when a nitrate group becomes unstable during the thermal treatment, NO reacts with the formed oxygen radical, thereby shifting the equilibrium toward NiO and so creating an NiO nucleus.

As this occurs at lower temperatures and because a larger number of nuclei are present, many small particles result, and extensive sintering or migration is prevented. If NO is not present during decomposition, oxygen radicals will combine to form O_2. This was proposed as the rate determining step, and moreover was postulated to be catalyzed by the formed NiO so that nucleation would start an autocatalytic process, causing the entire $Ni_3(NO_3)_2(OH)_4$ crystallite to rapidly decompose resulting in large particles.[141]

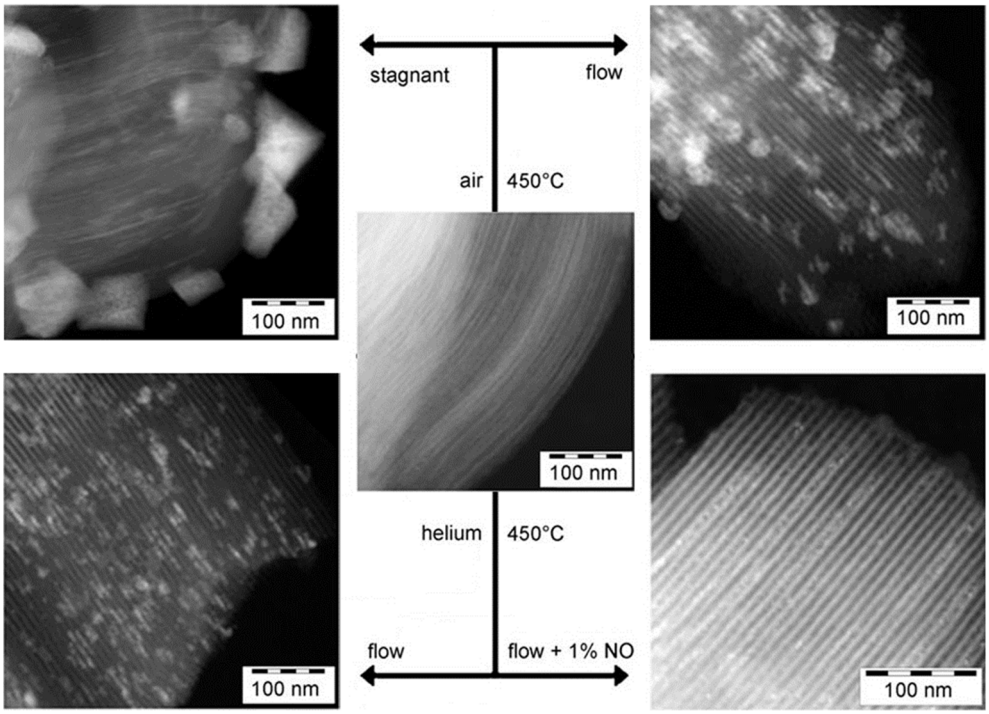

Figure 2.15. HAADF-STEM images of Ni/SBA-15 after drying at 120 °C (center) and after calcination in different gas atmospheres at 450 °C. After drying, nanowires of basic nickel nitrate were observed exclusively inside the mesopores of SBA-15. Calcination in stagnant air resulted in large NiO crystals on the external surface of the support particle. Calcination in in air or helium flow gave rise to smaller NiO particles while calcination in 1% NO led to very small particles of about 4 nm. (Adapted with permission from ref 139. Copyright 2007 Wiley)

Wolters *et al.* further investigated the decomposition of Sc, Mn, Fe, Co, Ni, Cu, and Zn nitrates impregnated onto silica gel and SBA-15 at metal loadings between 6 and 16 wt.%. After impregnation with the 3 M metal nitrate solution samples were dried in a dessicator at RT to prevent premature decomposition of the nitrates, followed by thermal treatment in Ar or 1% NO/Ar at 1 °C/min. For all metals, addition of NO was found to lower the decomposition temperature significantly by about 50 °C. However, for Sc, Mn, Fe and Zn, no crystalline phases were detected by XRD in either Ar or NO/Ar flow. For Co, Ni and Cu, addition of NO resulted in rapid hydrolysis of the metal nitrate to its respective metal hydroxynitrate,

which resulted in significantly lower metal oxide particle sizes of 5, 4 and 7 nm after decomposition, respectively, compared to averages of 10, 12 or 23 nm obtained in air.[142] By varying the pore size of the ordered mesoporous support between 2.5 and 10 nm, it was shown that the formed nickel hydroxynitrate crystallites obtained after drying were of a size similar to that of the pores, and that the size of the final NiO particles obtained after calcination depended on the original size of these crystallites.[143] Quick X-ray absorption spectroscopy on cobalt nitrate impregnated on silica at a Co loading of 10 wt.% also revealed rapid formation of cobalt hydroxynitrate below 100 °C in the presence of 5% NO/He, which further decomposed to Co_3O_4 between 110 and 170 °C.[144] Furthermore, temperature programmed calcination on cobalt nitrate melt infiltrated (see section 5.1) on γ-Al_2O_3, followed by drying at 85 °C in air revealed the hydrolysis of cobalt nitrate during an NO thermal treatment and subsequent improved particle size after decomposition also occurred on γ-Al_2O_3. However, the resulting increase in cobalt specific surface area of up to 33% for catalysts prepared using NO was less compared to the increase with silica.[145] Using TPR-XAFS, Jacobs *et al.* also observed that the effect of NO on the dispersion is larger on silica compared to γ-alumina, and attributed this to the strong interaction between γ-alumina and cobalt nitrate, which already results in relatively small particles. Therefore, it was postulated that the effect of NO would work best on supports such as silica that exhibit a weak interaction with the precursor.[146]

Further study on the decomposition of copper nitrate impregnated on SBA-15 and silica gel (18 wt.% Cu) confirmed the formation of copper hydroxynitrate at temperatures below 100 °C in the presence of 2%vol NO, which subsequently decompose directly into CuO at 200 °C leading to small 6 - 8 nm particles. However, when NO was not present, a higher copper dispersion was obtained in air flow with GHSV as low as 250 h^{-1}. Although large 30 nm CuO crystallites were detected by XRD, N_2O-chemisorption for the reduced catalyst revealed a relatively high Cu surface area of 90 m^2/g_{Cu}, indicating small particles dominated. From DRIFT measurements during calcination, it was concluded that the high dispersion originated from the mobilization of $Cu(NO_3)_2$ anhydride, which rapidly redispersed over the support surface anchored by silanol groups ultimately resulting in very small CuO particles. The large CuO particles were the result of a small amount of poorly dispersed copper hydroxynitrate which formed even in the absence NO.[147] Such premature hydrolysis during the initial stages of the thermal treatment may be largely avoided by vacuum-drying at room temperature. When this was performed on SBA-15 impregnated with a 4 M copper nitrate solution for 12 hours, no large crystallites were found after calcination at 500 °C in an N_2 flow (GHSV 1000 h^{-1}).[11]

Chelating Additives and other Organic-Containing Precursors. Organic precursors or additives are frequently used for the synthesis of supported catalysts, in particular for hydrodesulphurization (HDS) catalysts such as alumina-supported CoMoS, NiMoS, CoWS and NiWS. For these catalysts the active phase consists of MoS_2 or WS_2 slabs decorated with Co or Ni atoms located at the edges, which are commonly prepared by co-impregnation of the metal precursors followed by drying, calcination and sulfidation. However, during standard

conditions sulfidation of cobalt or nickel occurs prior to that of molybdenum or tungsten, resulting in undesired Co_9S_8 or Ni_2S_3 phases. Chelating agents are used amongst others to retard sulfidation of cobalt and nickel, so that they are only sulfidized after MoS_2 or WS_2 phases have formed and they efficiently deposit at the edges of the slabs. For CoMoS catalyst, a moderately strong chelating agent such as nitrilotriacetic acid (NTA) offers sufficient retardation,[148] whereas NiMoS catalysts require slightly stronger complexing agents such as ethylenediamenetetraacetic acid (EDTA).[149] Because tungsten is sulfidized at a higher temperature than molybdenum, formation of CoWS and NiWS catalysts generally requires even stronger complexing agents.[150,151]

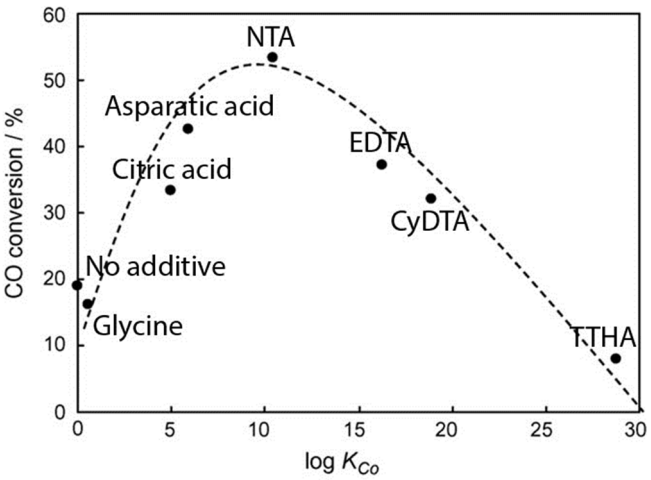

Figure 2.16. Relationship between the CO conversion in the Fischer Tropsch synthesis of reduced Co catalysts and the complex formation constant of the organic acids and chelating agents used during the catalyst preparation. The CO conversion was proportional to the dispersion after reduction, which exhibited a similar relationship with log K_{CO}. (Adapted with permission from ref 154. Copyright 2009 Elsevier)

More recently, research has focused on the use of chelating agents for the preparation of cobalt Fischer-Tropsch catalysts. In an extensive study 5 wt.% Co/SiO_2 catalysts were prepared by incipient wetness impregnation of cobalt nitrate and NTA, EDTA or *trans*-1,2-diaminocyclohexane-*N,N,N',N'*-tetraacetic acid (CyDTA) at equal nitrate/chelate molar ratios and a pH of 9 - 10 to ensure chelation of Co^{2+}(aq). After impregnation, samples were dried at 120 °C, calcined in stagnant air at 450 °C and reduced at 500 °C. When no chelate was used, a degree of reduction of 85% was found with 17 nm Co particles. Catalysts prepared with NTA exhibited a similar degree of reduction, but much smaller particles of 5.3 nm were obtained. However, although even smaller particles were formed with EDTA and CyDTA, the degree of reduction dropped to 12 and 8%, respectively. XPS revealed EDTA and CyDTA resulted in a mainly α-Co_2SiO_4-like phase after calcination, whereas a CoO_x with unknown stoichiometry was formed when NTA was used.[152] Glycine, citric acid, asparatic acid and triethylenetetraamine-*N,N,N',N',N'', N''*-hexa-acetic acid (TTHA) were also tested, but exhibited lower Co dispersion compared to NTA. Combining the results, the catalytic activity of Co was correlated to the complex formation constants of the organic additives with Co^{2+} in a volcano type plot (Figure 2.16), suggesting a moderately strong complexing agent offers the best compromise of obtaining small yet reducible particles.[153] Further investigation on NTA

showed a Co^{2+}/NTA molar ratio of 1 resulted in the highest dispersion, and that a calcination temperature of 450 °C was optimal.[154]

Due to the presence of chelating agents the concentration of the impregnation solution and thereby the resulting metal loading is relatively low. To cope with this challenge stepwise impregnation was proposed, whereby silica was first impregnated with the chelating agent (NTA or CyDTA) and dried at 120 °C, after which cobalt nitrate was impregnated with weight loadings between 5 and 20 wt.%. At 5 wt.% Co, corresponding to a Co/chelate molar ratio of 1, similar results were found as when co-impregnation was used. At Co loadings up to 20 wt.% (Co/chelate molar ratios up to 4), both NTA and CyDTA prepared catalysts exhibited very good and similar activities.[155] Further investigation of 20 wt.% Co catalyst with Co/chelate ratios of 4 showed only about one fourth of the CyDTA was complexed with Co^{2+} in the dried material, resulting in the suppressed particle growth of Co_3O_4 during calcination through stabilization of small cobalt clusters that served as nuclei.[156]

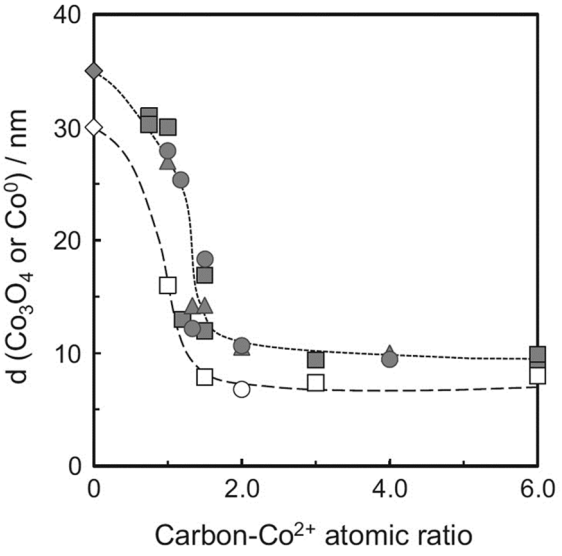

Figure 2.17. Impact of the amount of atomic carbon relative to Co^{2+} present in the impregnating solution for the preparation of 20 wt.% Co/SiO_2. Closed symbols represent Co3O4 measurements after calcination, open symbols metallic Co after reduction. Circles: EG, triangles: DEG, squares: TEG. (Adapted with permission from ref 159. Copyright 2011 Elsevier)

Glycols are a popular alternative to improve the dispersion of cobalt catalysts. Borg *et al.* prepared γ-alumina and α-alumina supported catalysts with Co loadings of 12, 20 and 30 wt.% by impregnation with cobalt nitrate and different ratios of water/ethylene glycol as solvent. After impregnation, samples were dried at 110 °C and calcined in air at 300 °C. On both supports, Co_3O_4 particles became smaller upon increasing the amount of ethylene glycol relative to water, from 16 nm to as low as 4 nm. Moreover, while samples without EG exhibited large aggregates of particles, addition of EG resulted in more uniform particle distributions. It was postulated by the authors that EG works as a surfactant resulting in better wetting of the support, although impact of EG on the drying and calcination steps was not excluded in this work.[129] This glycol method was subsequently used to prepare a wide range of particle sizes on γ, δ, θ, and α-aluminas.[157,158] Furthermore, the difference between straight

chains (ethylene glycol, diethylene glycol, triethylene glycol (TEG)) or branched (glycerol, pentaerythritol) glycols has been investigated for the preparation of 10 and 20 wt.% Co/SiO_2 catalysts at different Co/glycol molar ratios between 0 and 1. After impregnation, samples were dried at 120 °C and calcined in stagnant air at 450 °C. A reduction in crystallite size from 35 up to 10 nm was observed. Moreover, it was found that the resulting Co_3O_4 crystallite sizes did not depend on the specific glycol, but rather on the atomic ratio of carbon/Co^{2+} (Figure 2.17), while no further improvement was found above a carbon/Co ratio of 2. Further FTIR investigation of TEG samples suggested a polymer complex-like species was formed during calcination through ester polymerization of TEG with its derivatives, thereby preventing excessive grow of particles.[159,160]

Other additives and precursors have been used with mixed success. Co-impregnation of sorbitol for the preparation of 10 wt.% Co/SiO_2 samples with Co/sorbitol molar ratios between 2 and 10 showed an improvement in the particle size, going from 10 nm in the catalyst without sorbitol to 4 nm in the material with a ratio of 2. It was found that sorbitol caused the cobalt nitrate to decompose at higher temperatures, however the resulting material was much more difficult to reduce at 400 °C due to the formation of a large amount of cobalt silicates.[161] Addition of sucrose at molar ratios of 10 for the synthesis of 6 - 8 wt.% Co/SiO_2 also showed an increase in the decomposition temperature of the metal nitrate. In this case, 5 nm particles found after addition of sucrose exhibited a similar reducibility at 400 °C compared to the 12 nm particles that formed without sucrose. However, it should be noted Ru or Re was added as a reduction promoter here, which was not the case in the previous study.[162]

Cobalt nitrate and acetate have been compared for the preparation of 10 wt.% Co/SiO_2 catalysts by incipient wetness, dried at 90 °C and calcined at 400 °C. Cobalt nitrate exhibited endothermic calcination, favoring the formation of agglomerated 20 nm Co_3O_4 crystallites, while acetate decomposed exothermically during calcination, resulting in the formation of cobalt silicates, which hamper reduction.[163] Comparison of cobalt nitrate, acetate and chloride for the synthesis of 20 wt.% $Co/AlPO_4$ by impregnation, drying at 110 °C and calcination at 500 °C showed similar results; cobalt acetate mainly resulted in an amorphous phase that was not reduced at 400 °C, while, cobalt nitrate resulted in 15 nm particles with good reducibility. Cobalt chloride gave rise to 35 nm crystallites as determined by XRD, while H_2-chemisorption suggested particles were as large as 160 nm.[164] Nickel nitrate and acetate have been compared for the deposition of 1 or 5 wt.% Ni/MCM-41 by the two-solvent impregnation. After drying at 90 °C and calcination in an airflow at 500 °C, nickel acetate was shown to produce smaller NiO particles compared to nickel nitrate, while only a limited amount of nickel silicate was found.[76] Wet impregnated nickel glycinate on γ-alumina at a nickel loading of 15 or 28 wt.% resulted in 5 - 30 nm nickel particles after drying at 80 °C and calcination at 500 °C in an argon flow. Using the glycinate precursor both HCP and FCC Ni phases were detected, whereas normally FCC is the dominant phase.[165] Incipient wetness impregnation of γ-alumina has been performed with nickel ethylenediamine nitrate or nickel nitrate hexahydrate (14 - 15 wt.% Ni), followed by drying at 100 °C, calcination at 500 °C, and reduction at 500 °C. The

Ni(*en*) precursor resulted in a metallic nickel surface area of 13 $m^2/g_{cat,}$ whereas nickel nitrate resulted in 6 m^2/g_{cat}. Moreover, Ni(*en*) did not lead to formation of nickel aluminate, whereas this was found in significant amounts for nitrate samples.[166] These results show that although organic precursors can result in smaller particles, the conditions during thermal treatment and the nature of the support have a large influence on the formation of mixed metal support phases which are difficult to reduce, which was more severe for cobalt than for nickel precursors.

Plasma Activation. Although thermal activation treatments are conventionally used to decompose and reduce the metal precursors, cold plasma techniques are receiving increased attention. Especially glow discharge plasma is of interest, due to its ability to provide reduced catalysts when working with noble metal precursors without the need of a reducing agent. In glow discharge plasma, the sample is loaded in a special reactor, followed by evacuation of the reaction chamber to around 100 Pa. After this the gas is introduced, often H_2, Ar, or N_2, a voltage is applied to generate the plasma. Using this method, 2 - 3 wt.% Pt, Pd, Ag, or Au was prepared on TiO_2, γ-Al_2O_3 or HZSM-5 following impregnation with an aqueous solution of H_2PtCl_6, $PdCl_2$, $AgNO_3$, or $HAuCl_4$. Directly after impregnation, Ar glow discharge plasma was performed to produce the reduced materials. The treatment led to Pd, Pt and Ag particles of 2, 4 and 6 nm, respectively, a factor 2 to 3 smaller compared to samples reduced in H_2 at 300 °C. Systematic study on 2 wt.% Pt/TiO_2 revealed it took 60 minutes to fully reduce the sample, and even O_2 usage led to a net reducing plasma, although some oxides were also formed.[167] Ar Glow discharge plasma has also been used to produce 3.5 wt.% Pd/γ-Al_2O_3 after impregnation and drying at 110 °C. Compared to a regular calcination and reduction treatment at 500 °C, a factor of two smaller particles were obtained (3.2 vs 7.5 nm).[168] 1 wt.% Ir/γ-Al_2O_3 was prepared after impregnation with H_2IrCl_6 followed by Ar glow discharge plasma. Even after annealing at 600 °C in Ar, only 1 nm particles were found, while conventional reduction in H_2 resulted in 3 nm particles.[169] AuPd bimetallic particles on SBA-15 have also been prepared using this method by incipient wetness impregnation of $HAuCl_4$ and $Pd(NO_3)_2$ at a total metal loading of 4 wt.%. After impregnation, Ar glow discharge plasma was used to decompose the precursors. The resulting material exhibited nanoparticles with Pd rich shells and Au cores, whereas conventionally prepared samples contained homogeneous PdAu alloy particles, showing the potential for producing tailored bimetallics.[170]

Succession of N_2 and H_2 plasmas has also been used after impregnation and drying. Unpromoted and Pt promoted 15 wt.% Co/γ-Al_2O_3 catalysts were prepared by impregnation and drying at 100 °C. Even though a H_2 plasma was used, XANES and EXAFS data showed that the cobalt nitrate decomposed not into metallic Co but rather into Co_3O_4, suggesting the type of gas only plays a minor role, however no crystallinity was detected by XRD. Upon subsequent thermal reduction, 6 - 7 nm Co particles were obtained related to improved reducibility of the plasma treated sample as compared to a conventionally calcined sample that led to 10 nm particles.[171] Unpromoted and Ru promoted 10 wt.% Co/SiO_2 have also been prepared via this method after impregnation and drying at 90 °C. It was found that the

resulting Co_3O_4 particles depended on the power used during glow discharge. At 60 V, 8.5 nm particles formed, with good reducibility and performance in the Fischer-Tropsch reaction. Particles as small as 5.7 nm were found after treatment at 120 V, however this was accompanied by formation of cobalt silicate, which led to catalysts with lower activity. It was proposed that the plasma promotes crystal nucleation, so that a relatively high nucleation to growth ratio can be achieved resulting in relatively small particles.[172] Slightly smaller nickel particles have also been reported in 8 wt.% Ni/MgO-Al_2O_3 materials after impregnation and drying at 110 °C.[173]

Glow discharge plasma has also been used as an additional pretreatment step to improve catalysts. 5 wt.% Ni/γ-Al_2O_3 has been prepared by impregnation, drying at 110 °C, followed by decomposition in Ar plasma and a subsequent thermal calcination step. An improved stability was found during the dry reforming of methane, which was attributed to a stronger metal-support interaction induced by the plasma treatment.[174] A similar improved interaction was also suggested for the production of up to 2 wt.% Pt/TiO2 by including an Ar glow discharge plasma step in between drying and thermal calcination.[175]

Other cold plasma techniques have been investigated. Dielectric barrier discharge (DBD) plasma under atmospheric conditions was used in the synthesis of 20 wt.% Co/SiO_2 after incipient wetness impregnation and drying at 100 °C. However, the resulting catalyst exhibited similar activity in the Fischer-Tropsch synthesis compared to conventionally calcined catalysts, and TEM images showed 50 nm aggregates were formed in the DBD method.[176] Microwave plasma has been used for the preparation of 5 or 10 wt.% Ni/CeO_2 by wet impregnation and drying at 100 °C. Catalysts prepared with a power of 250 W exhibited a similar dispersion as samples conventionally prepared by calcination. The samples formed by microwave plasma exhibited a greatly increased stability, which was again attributed to enhanced metal support interactions. However, during the microwave treatment a large decrease in support surface area and a large increase in pore diameter were observed, which was more severe for higher microwave power, and did not occur during conventional thermal calcination. This was attributed to removal of residual carbon that remained after synthesis of the CeO_2 support. However, this may significantly influence the formed phase.[177]

5. EMERGING TECHNIQUES

5.1 Melt Infiltration

In melt infiltration, a metal or metal salt is physically mixed with the support structure, and subsequently heated above the melting temperature of the metal (salt). This results in the melt being pulled into the pores of the support by capillary forces, whereby an important condition is that the melt and decomposition temperatures should be sufficiently different. As such, this preparation method exhibits many similarities to impregnation and drying (section 4), and similar physical principles of support wetting and capillary pressure and flow are

extremely important.[178] In specific cases melt infiltration can provide an attractive alternative due to the relatively simple procedure and no need of solvent. Besides melt infiltration, the method is known by other names such as the solid-solid method, solid state impregnation, and the solvent-free method.

Table 2.3. Example of melting temperatures of several metal precursors.[179]

Precursor	T_{melt} (°C)[a]
$Co(NO_3)_2{\cdot}6H_2O$	55
$Ni(NO_3)_2{\cdot}6H_2O$	56
$Cu(NO_3)_2{\cdot}3H_2O$	114
$Cr(NO_3)_3{\cdot}9H_2O$	66
$Fe(NO_3)_3{\cdot}9H_2O$	47
$Ag(NO_3)$	210
$Fe(acac)_2$	190
$(NH_4)_2Cr_2O_7$	n/a[b]

[a]It is noted that many metal nitrates start to lose part of the crystal water at temperatures slightly above the melting temperature. [b]Decomposes before melting.

Melt infiltration for the synthesis of catalysts has been mostly performed with transition metal nitrate hydrates. These exhibit low melting points since melting occurs as dissolution in their own crystal water, generally between 50 and 100 °C (Table 2.3), while use of metal precursors without crystal water is generally less successful. For example, physical mixing of MCM-41 and nickel nitrate followed by heating to 500 °C caused infiltration of the nickel nitrate into the pores of the support, resulting in small NiO particles. However, when nickel acetate and MCM-41 were physically mixed, no infiltration was observed during thermal treatment, and all the acetate remained outside of the pores.[76] Care has to be taken to prevent decomposition of the precursor prior to entering the pores. Physical mixing of a hydrated $Fe(NO_3)_3$ salt (hydration not specified) and MCM-41, followed by heating to 400 °C at 5 °C/min and further heating to 700 °C resulted in sharp XRD patterns related to crystallites over 40 nm present the external surface of the MCM-41 primary particles. It is likely that the high temperature ramp applied caused decomposition of the iron nitrate before it completely filled the mesopores of the support. However, many small particles were also observed, indicating melt infiltration was partly successful.[180] 1 mmol $Co(NO_3)_2{\cdot}6H_2O$, $Ni(NO_3)_2{\cdot}6H_2O$, $Ce(NO_3)_3{\cdot}6H_2O$, or $Cr(NO_3)_3{\cdot}9H_2O$ physically mixed with 0.15 g SBA-15 or KIT-6 and heated to 500 °C at a rate of 1 °C/min resulted in large interconnected networks inside the pores of the support, which formed porous single crystal networks after removal of the silica. A similar procedure attempted with $Pb(NO_3)_2$ and $(NH_4)_2Cr_2O_7$ revealed these precursors did not infiltrate the silica supports, which was explained by decomposition of the precursor without melting.[181] Physical mixing of $Ce(NO_3)_3{\cdot}6H_2O$, $Ni(NO_3)_2{\cdot}6H_2O$, or

$Co(NO_3)_2{\cdot}6H_2O$ with SBA-15 at lower loadings (0.3 mmol for 0.1 g) followed by calcination to 450 °C did not result in large interconnected networks but rather in small 4 - 7 nm particles. This suggests the loading may be relevant for the formation of large crystals, or that there was a significant difference between the interconnectivity of the used SBA-15 supports.[182]

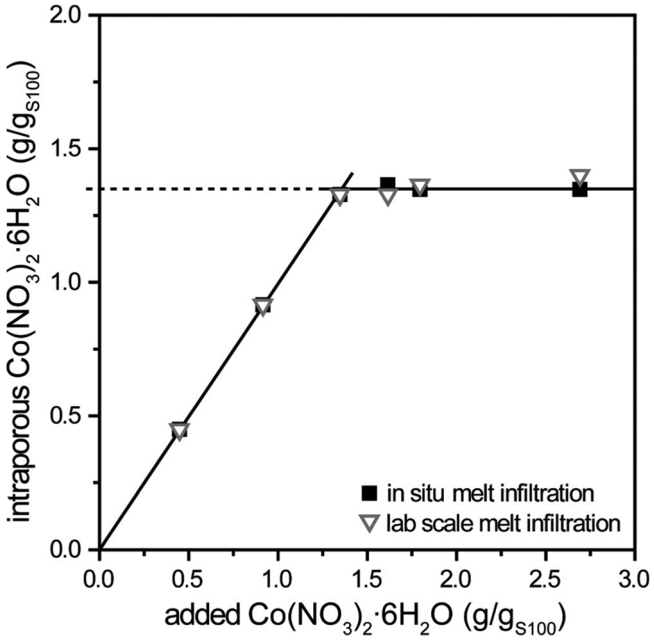

Figure 2.18. Amount of intraporous $Co(NO_3)_2{\cdot}6H_2O$ per gram of SBA-15 as a function of the amount added in the physical mixture. Squares were prepared in-situ in DSC measurement cups, while triangles were prepared ex-situ in a closed autoclave at 60 °C. Up to 1.4 g of added $Co(NO_3)_2{\cdot}6H_2O$, all was found inside the pores after melt infiltration, whereas further addition did not increase the intraporous loading. (Adapted with permission from ref 183. Copyright 2010 American Chemical Society)

In the previous studies, infiltration and decomposition of the metal nitrate hydrate precursors was performed in a single step. However, when decomposition starts while infiltration is still ongoing, it is possible material decomposes on the external surface of the support, or that the formed metal oxide nuclei are continuously supplied with additional metal nitrate hydrate, causing the grow of large crystals forming a network throughout the pores of the support. As this is undesirable for catalysis, the infiltration and decomposition step should ideally be separated. In a detailed study, three different SBA-15's, MCM-41 and a silica gel were melt infiltrated with $Co(NO_3)_2{\cdot}6H_2O$ by heating to 60 °C in a sealed Teflon lined autoclave for 24 h. Afterwards, XRD did not detect any crystalline material, suggesting all the $Co(NO_3)_2{\cdot}6H_2O$ was taken up by the pores of the support. In contrast, when the same procedure was performed in an open crucible, sharp $Co(NO_3)_2{\cdot}4H_2O$ peaks were observed indicative of partial decomposition of $Co(NO_3)_2{\cdot}6H_2O$, which then remained on the external surface of the support. After calcination in a flow of N_2, large Co_3O_4 particles were found on the external surface when an open crucible was used for infiltration, while no such particles were observed after melt infiltration in a closed autoclave.[183] Due to the difference in melting point between intraporous (5-20 °C) and extraporous (53 °C) $Co(NO_3)_2{\cdot}6H_2O$ the maximum loading was also studied by DSC. Up to a loading of 1.4 $g_{Co(NO3)2{\cdot}6H2O}/g_{SBA\text{-}15}$, only intraporous $Co(NO_3)_2{\cdot}6H_2O$ was observed, whereas above this both extraporous and intraporous

$Co(NO_3)_2{\cdot}6H_2O$ was found (Figure 2.18). This amount corresponded to a pore filling of 75% assuming the density of crystalline $Co(NO_3)_2{\cdot}6H_2O$. However, due to a lack of XRD signal, it was proposed that the $Co(NO_3)_2{\cdot}6H_2O$ was not crystalline but rather an amorphous phase with a lower density, so that a close to 100% filling was more likely.[183] This methodology of melt infiltration in an autoclave was subsequently utilized to produce a variety of highly loaded Co/SiO_2 (20 wt.%) and Ni/SiO_2 (21 wt.%) catalysts by using calcination in N_2 or 1% NO/N_2 gas flows,[20,136] and a similar method was used to form a bimetallic Co/Rh catalyst on γ-Al_2O_3 (20 and 1 wt.%, respectively).[145]

Cu-Ce bimetallic materials have also been synthesized using melt infiltration. $Cu(NO_3)_2{\cdot}2.5H_2O$ and $Ce(NO_3)_3{\cdot}6H_2O$ were first mixed at 120 °C in a closed vial, after which silica hollow spheres were added for infiltration at 120 °C in a closed system followed by calcination at 550 °C. The molar ratio between the copper-ceria nitrates was varied, while in each case the total salt volume was kept below the pore volume of the support. However, when Cu:Ce ratios higher than 1 were used, large $Cu(NO_3)_2{\cdot}2.5H_2O$ crystals were detected after infiltration, suggesting extraporous $Cu(NO_3)_2{\cdot}2.5H_2O$ was still present. This was also evidenced after calcination, where large 100 nm CuO crystallites were detected. When the ratios were reversed, no extraporous salt was found.[184] Another similar study successfully prepared Cu-Ce/SBA-15 using melt infiltration, which exhibited an increased interaction between copper and ceria compared to wet impregnation.[185]

Besides metal nitrates, acetylacetonate (acac) precursors have also been used for melt infiltration. $Mo(acac)_3$ and $Fe(acac)_3$ were used to prepare Fe/KIT-6, Mo/KIT-6 and Mo-Fe/KIT-6 at loadings between 0.3 and 1.5 wt.% by physically mixing the salt and support and heating to 500 °C for 5 h. However, this may have caused a large amount of pores to be blocked, as a reduction in BET surface area from 600 to 60 was observed accompanied by a reduction in pore volume from 0.8 to 0.15 mL/g, suggesting the melting point and decomposition temperature of these precursors are too close to each other for an efficient melt infiltration procedure.[186] $Pt(acac)_2$ has also been introduced into an Al-SBA-15 material by physical mixing, followed by a thermal treatment at 100 °C for 24 h, 180 °C for 0.5 h (5 °C/min) and 400 °C for 6 h (10 °C/min). A homogeneous distribution of the 1 wt.% Pt was obtained, with small 1 nm particles similar to preparation by wet impregnation. However, 180 °C is close to the boiling point of $Pt(acac)_2$, so that this form of solid state impregnation concerns vapor deposition rather than melt infiltration.[187]

Due to the absence of solvent that needs to be removed and the increased viscosity of molten metal salts compared to aqueous solutions, melt infiltration can have an effect on the distribution of the active phase during the loading step. For example, although the surface tension of a cobalt nitrate solution and a $Co(NO_3)_2{\cdot}6H_2O$ melt at 60 °C was found to be similar, the viscosity of the melt was over 10 times higher. Melt infiltration of a 2.7 mm silica pellet by $(NO_3)_2{\cdot}6H_2O$ at 60 °C for 30 seconds resulted in penetration of the outer 0.1 - 0.2 mm, whereas solution impregnation resulted in a homogeneous distribution.[188] Similarly, melt infiltration of $Ni(NO_3)_2{\cdot}6H_2O$ into a 3 mm alumina pellet for 2 - 5 min, followed by cooling

down to room temperature resulted in distinct egg-shells as determined by micro-XRF, while infiltration over 10 or 30 minutes, or an aging step at 65 °C, resulted in more homogeneous distributions. Some inhomogeneities did remain, attributed to the precipitation of nickel tetrahydrate on the alumina, which has a higher melting point.[189]

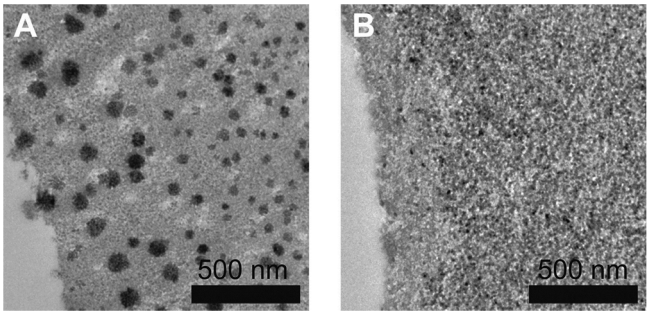

Figure 2.19. TEM of Co_3O_4/SiO_2 prepared via incipient wetness impregnation (a) or melt infiltration (b) followed by freeze drying at -45 °C and calcination in N_2 flow at 350 °C. The impregnated sample was not fully solidified resulting in severe aggregation and redistribution of the metal nitrate towards the external surface of the silica grain, whereas the melt infiltrated sample exhibited a homogeneous distribution due to the fully frozen precursor. (Adapted with permission from ref 136. Copyright 2013 Elsevier)

The absence of additional solvent can limit redistribution during subsequent thermal steps if enough time is allowed for a homogeneous distribution during melt infiltration. As mentioned in section 4.3 and described in detail in chapter 3, freeze-drying of a 4 M aqueous solution of cobalt nitrate inside the pores of the silica gel required temperatures below -90 °C to freeze. At -45 °C, the material was not completely frozen and extensive redistribution was observed in the form of egg-shell catalysts and large aggregates. However, when $Co(NO_3)_2{\cdot}6H_2O$ was melt infiltrated, a freezing temperature of only -20 °C was required to solidify the confined precursor. Thus, when freeze-drying was performed at -45 °C, a homogeneous distribution was obtained after melt infiltration (Figure 2.19).[136] As shown in appendix B, a more homogeneous distribution was also obtained after drying of Co/SiO_2 with large pores in a N_2 flow at 150 °C, which resulted in egg-shell catalysts after incipient wetness impregnation but in homogeneous distributions after melt infiltration.[132]

5.2 Colloidal Synthesis

Colloidal synthesis provides unique opportunities to control the size, shape and composition of nanoparticles in the liquid phase and has been reviewed earlier.[190,191] The nanoparticles are generally formed by stepwise induction of a change in conditions in an otherwise homogeneous solution of the metal precursor. This results in a nucleation burst, followed by growth of the nanoparticles from the remaining precursor in solution. Ligands present in the solution play an essential role to stabilize the nanoparticles against aggregation, coalescence and growth, while they may also influence the shape of the nanoparticles.[192] Even though the synthesis of colloidal nanoparticles has been studied extensively also for catalysis[193] (see also reviews on electrocatalysis[194], the oxygen reduction reaction[195], or size and shape

selectivity[196]), few studies focus on deposition of the preformed particles on a support, even though this step is crucial for obtaining active and stable heterogeneous catalysts. Here we do not repeat earlier reviews on nanoparticle synthesis but rather focus on recent studies that address the challenge of deposition on nanoparticles on a support.

Due to the relatively low nanoparticle concentrations in colloidal solutions necessary to prevent aggregation and precipitation, wet impregnation is commonly applied to deposit the colloids onto a support. However, diffusivity of colloidal nanoparticles is relatively slow so that it can take a long time for all particles to migrate into the pores of the support, which can be stimulated through use of sonication. When particles are not strongly bound to the support, the drying step can have a large influence in the distribution of the nanoparticles, as has been demonstrated for the drying of colloidal wet films.[134] Since evaporation of the solvent in porous bodies usually occurs on the external surface (see section 4.3), it is possible that significant redistribution towards the external surface of the grains occurs. Even so, few studies report on the distribution of nanoparticles at the nanoscale and even less on the macroscopic distribution across support grains. Co nanoparticles deposited on SBA-15 by wet impregnation followed by extensive washing resulted in aggregation of particles in some areas while other areas of the support remained empty.[197] Similarly, iron oxide particles of 2 - 10 nm deposited by wet impregnation on γ-Al_2O_3 showed similarly inhomogeneous distributions with particles aggregated and preferentially deposited on the external surface of the support. Particles deposited on MCM-41 with a pore size of 3 nm exhibited homogeneous distributions, but were exclusively deposited on the external surface, not surprisingly considering the relatively small pore size in relation to the nanoparticles.[198]

Deposition of nanoparticles often occurs through electrostatic interactions, Van der Waals interactions, or polar bonds involving the stabilizing ligands of the particles on the one hand, and the support surface groups on the other hand. Deposition of Pt and Pd particles has been shown to depend greatly on the surface of carbon nanofiber (CNF) supports. Pd colloids of 4 nm stabilized with polyvinylpyrrolidone (PVP) were found to be negatively charged between pH of 2 and 8. When deposited by a wet impregnation at pH 3 on differently treated CNFs with PZCs ranging from 2.2 to 7.7, it was found a maximum uptake (3.9 wt.%) occurred for CNFs with high PZC, whereas supports with a PZC around 2 - 3 exhibited almost no uptake (0.5 wt.%). This suggested electrostatic interactions played an important role during deposition of the particles, as supports with a low PZC and concomitant high surface oxygen content are negatively charged at pH 3, repelling the negatively charged colloids, whereas the high PZC carbon supports with low oxygen content attracted the colloids.[199] The uptake of PtO_2 colloidal particles stabilized by glycolate prepared by the polyol method has also been shown to greatly depend on the carbon support. Uptake of PtO_2 nanoparticles varied greatly from 1.5 to 19 wt.%. However, since deposition of the oxidic particles was performed at pH 9-10, electrostatic interaction was unlikely. It was proposed that the particles adsorbed preferentially on carbine-type or surface defect sites. Moreover, similar to the Pd metal

particles, uptake was improved by removing oxygen groups from the support, which were thought to weaken the adsorption strength.[200,201]

Adsorption of Pt particles stabilized with PVP has been shown to greatly depend on the chemical nature of the support. Kimura *et al.* found the adsorption capacity of TiO_2 to be very high, good for Al_2O_3 and MgO but poor on SiO_2. However, adsorption on TiO_2 was independent on the pH of the solution between pH 2 and 10, suggesting non-specific interactions (Van der Waals or polar) played an important role. At high loadings (10 wt.%), an increase in particle size was observed, suggesting the support did not directly bind with all particles at these high loadings, leading to aggregation.[202] Similar results have been reported for other Pd and Pt particles, which started to form aggregates at higher loadings. Moreover, extra addition of the used stabilizing agent hexadecyl(2-hydroxyethyl)dimethyl ammonium dihydrogenphosphate reduced the uptake of the metal nanoparticles likely due to competitive adsorption, suggesting the adsorption of ligands was competing with the surface deposition of nanoparticles.[203]

Immobilization of Au_{11}^{3+} particles with 0.8 nm diameter stabilized with triphenylphosphine (TPP) has been found to be greatly dependent on the solvent. The highest uptake was observed when pure dichloromethane was used, whereas a gradual decrease in uptake occurred upon mixing with ethanol. It was proposed that the binding with the TPP ligands occurred via weak interactive forces between the permanent dipole of the silica OH surface groups and the induced dipole within the ligand layer. At increasing ethanol concentration, the attractive force between the two became weaker due to the increased electrical permittivity caused by ethanol. However, although uptake was less when a DCM/ethanol mixture was used, smaller particle sizes were also obtained, which was attributed to a more homogeneous distribution due to the weaker interaction in the presence of ethanol.[204] Stability of Au particles has also been demonstrated to depend on the stabilizing ligand. When the electrostatic stabilizer tetrakis(hydroxypropyl)phosphonium chloride (THPC) was used, smaller particles were deposited on a carbon support compared to poly(vinyl alcohol) (PVA), a steric stabilizer. However, when Pd was subsequently added from a Na_2PdCl_4 solution in the presence of PVA and H_2, THPC stabilized particles exhibited more extensive growth compared to the PVA stabilized particles.[205]

The charge of the stabilizing agent also plays a large role. For the deposition of 10 nm Ag particles stabilized with 3-mercatopropionic acid (MPA) on γ-Al_2O_3, the final particle size greatly depended on the pH of the impregnating solution. At pH 3.7, MPA was negatively charged causing repulsion between nanoparticles, whereas attraction with the positively charged support caused direct deposition of the nanoparticles. However, at a pH of 2.9, MPA was almost negligibly charged, causing particles to assemble together due to hydrogen bonding and resulting in average particles of 26 nm after calcination at 550 °C (Figure 2.20).[206] Others have reported removing the stabilizing agent before deposition can be detrimental for the dispersion of 1 wt.% Cu/Al_2O_3 catalysts.[207] However, the stabilizing agent can also be difficult to remove after deposition. A low temperature treatment was not found to be sufficient to

remove a mixture of oleic acid, trioctylamine and trioctylphosphine from 5 nm Ni particles deposited on SiO_2, whereas high temperature treatments led to particle growth.[208]

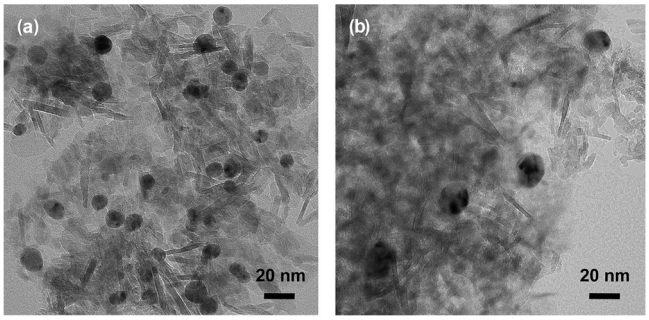

Figure 2.20. TEM of Ag particles deposited on γ-Al_2O_3 at different pH, followed by calcination at 550 °C and reduction at 200 °C. (a) pH 3.7, (b) pH 2.9. At pH 3.7, the originally 10 nm Ag colloids are unchanged after deposition due to the electrostatic repulsion of the MPA ligands, whereas at pH 2 severe sintering occurred due to the negligible charge of MPA at this pH. (Adapted with permission from ref 206. Copyright 2009 American Chemical Society)

Microemulsions provide a different way to produce finely dispersed colloidal nanoparticles, whereby nanoparticles are synthesized in the aqueous cores of the surfactant reverse micelles. Deposition of these nanoparticles can often be done by destabilizing the microemulsion in the presence of a support by addition of for example THF. However, the resulting supported metal dispersion can greatly suffer compared to that of the nanoparticles in solution. Moreover, synthesis of reverse micelle Co_3O_4 particles directly in contact with a γ-Al_2O_3 support resulted in large amounts of cobalt aluminate which gave rise to cumbersome catalyst activation.[209] A study on neutral (sodium bis(2-ethylhexyl) sulfosuccinate, AOT) or ionic (polyoxyethylene (8) octylphenyl ether, TT) surfactants for the production of Co_3O_4 particles showed the particle size was only slightly influenced by the surfactant. However, a great improvement in dispersion was observed when the silica support was first silylated. This resulted in a decrease in Co particle size from 16 to 6.5 nm (TT) or 15 to 5 nm (AOT), respectively, after reduction. It was concluded that the increased interaction between the hydrophobic silylated support and the micelles reduced the degree of aggregation in the liquid medium, thereby greatly improving the dispersion and possibly the distribution.[210]

Although investigation on the kinetics of particle formation is difficult and rarely attempted, Finke *et al.* elucidated the kinetics of Pt nanoparticle formation from an H_2PtCl_6 solution in the presence of γ-Al_2O_3 for the synthesis of 1 wt.% Pt/Al_2O_3. By using the hydrogenation activity of Pt, the nanoparticle formation was inferred from the simultaneous hydrogenation reaction of cyclohexene with hydrogen. Through use of a high precision pressure transducer, real-time information on the loss in H_2 pressure provided unique kinetic data on the nanoparticle formation, assuming the reaction was structure insensitive. H_2PtCl_6 was first impregnated using ethyl acetate as solvent, dried at room temperature in vacuum, and subsequently added to a solution of cyclohexene in ethanol. By applying a H_2 pressure at 22 °C, the Pt precursor was reduced to Pt(0), forming supported nanoparticles which immediately started to convert cyclohexane to cyclohexane. The rate determining step was assumed to be

formation of the growing nanoparticle, so that the catalyzed reaction was used as a probe for the rate of formation.[211] A sigmoidal growth behavior was observed that fit a two-step mechanism for nanoparticle formation of slow nucleation and autocatalytic surface growth first discovered for nanoparticle formation in solution.[212] Because of the good fit to the two-step mechanism, it was proposed that many of the insights obtained for nucleation and growth in solution also hold in the presence of a support.

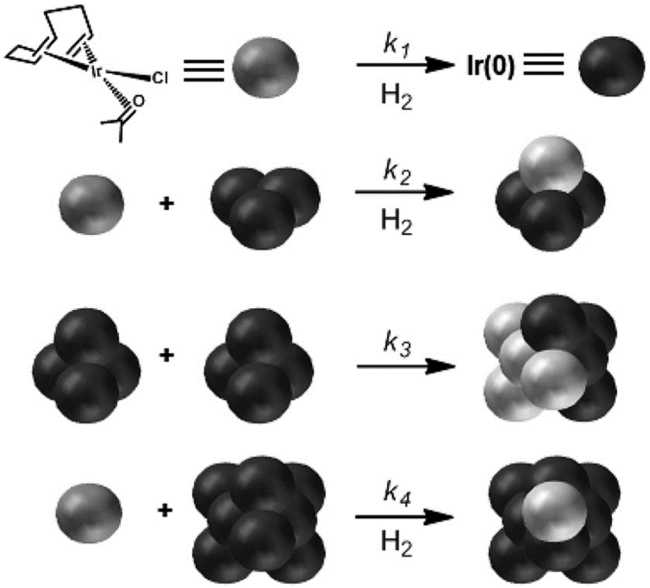

Figure 2.21. Schematic representation of the four-step mechanism for nanoparticle formation and agglomeration. Ir(1,5-COD)Cl is first reduced to Ir(0) nuclei, which subsequently grow autocatalytically by addition of more Ir(1,5-COD)Cl to form $Ir(0)_n$. Two such $Ir(0)_n$ clusters can aggregate to form one larger cluster, while further growth of such large clusters is limited to autocatalytic growth via addition of Ir(1,5-COD)Cl. (Adapted with permission from ref 216. Copyright 2014 American Chemical Society)

A more detailed study was subsequently performed for the synthesis of 1 wt.% Ir/γ-Al_2O_3 catalysts. Similarly, $[Ir(1,5\text{-}COD)Cl]_2$ was first deposited on γ-alumina using ethyl acetate and dried, followed by formation of the Ir nanoparticles in acetone at 22 °C under hydrogen pressure, which was monitored by the hydrogenation reaction of cyclohexene. Again, the system showed an excellent fit to the two-step mechanism of nucleation followed by autocatalytic surface growth, producing 3 nm iridium particles with a relatively narrow particle size distribution.[213] Further investigation showed nucleation occurred bimolecularly from precursor in solution, followed by rapid capture of the nuclei by the γ-Al_2O_3 surface and further autocatalytic growth of the supported particles.[214,215] However, when a five-fold decrease of the Ir(1,5-COD)Cl/γ-Al_2O_3 precatalyst was used a different growth behavior was observed, resulting in iridium particles of 1.7 nm with a relatively broad particle size distribution.[216] This led to the development of a new four-step mechanism, whereby Ir(0) nuclei are first formed, which subsequently either grow autocatalytically from additional precursor in solution to form larger $Ir(0)_n$ clusters, but can also aggregate. These larger aggregated clusters can again grow autocatalytically from precursor from solution, but will likely not aggregate with other nuclei due to their limited mobility when they are deposited on the support surface (Figure 2.21). The new model showed an excellent fit with experimental

data, however whether the individual steps occur in solution or on the support surface was not reported, and the reason for the change from a two-step to a four-step mechanism at lower concentration is subject to further research.[216]

Finally it is noted that in recent years colloidal techniques have been used for synthesizing a porous support shell around preformed nanoparticles. While these are highly interesting for catalysis and catalyst preparation, discussion of these is beyond the scope of the present review, and recent developments[217] as well as application of such nanostructured gold catalysts[218] have recently been reviewed.

5.3 Atomic Layer Deposition

Although conventional chemical vapor deposition generally does not offer adequate deposition control, atomic layer deposition (ALD) has shown increased used for the preparation of catalysts.[219] ALD, also known as atomic layer epitaxy (ALE) or molecular layering, is based on the irreversible and saturating reaction between a gas phase and a surface, so that a uniform monolayer is formed. In general, it entails reaction of a gas phase metal precursor with support surface groups such as terminal hydroxyls, followed by purging and a second reaction, often with oxygen or hydrides of the non-metal elements such as water, ammonia or hydrogen sulphide, for the formation of metals, metal oxides, nitrides or sulphides. This second reaction also regenerates surface sites, often in the form of hydroxyl groups, so that multiple ALD cycles can be performed successively to deposit more material in a layer by layer fashion to produce increasingly thick films.[220] The technique principally deposits sequential (mono)layers of material, however especially noble metals tend to agglomerate to form small particles even after one cycle due to the stable metal-metal bonds.

Early detailed studies on atomic layer deposition for catalyst preparation mainly concerned 2,2,6,6-tetramethyl-3,5-heptanedionato (thd) ligands for precursors such as $Cu(thd)_2$[221], $Pd(thd)_2$[221,222], and $Rh(thd)_2$,[222] while acetylacetonate (acac) precursors such as $Ni(acac)_2$[223], $Co(acac)_2$[224], $Co(acac)_3$[224,225], $Cr(acac)_3$[226], and $VO(acac)_2$[227] were also used. Selective adsorption on SiO_2 and Al_2O_3 surfaces occurred via an exchange reaction between surface OH groups and ligands, although recently steric hindrance was found to play a role in the deposition of $Co(acac)_2$ and $Co(acac)_3$.[228] The remaining ligands were decomposed in oxygen, hydrogen or water vapor. Multiple cycles were mainly used for Co and Ni, which exhibited a linear increase in metal loading along with an increase in particle size for increased number of cycles. Multiple cycles of $VO(OC_3H_9)_3$ on silica were less successful, because V catalyzed decomposition of the $VO(OC_3H_9)_3$ precursor complex caused uncontrolled deposition in later cycles.[229]

ALD can be an efficient deposition method for the production of finely dispersed metal particles for catalysis due to the self-limiting deposition reaction allowing for a homogeneous distribution even in highly porous and heterogeneous support bodies, which would not be possible with other, non-self-limiting methods. However the actual penetration depth of the gas is highly dependent on the support material and partial pressure of the precursor. For example, on a very low density silica aerogel, ZnO was deposited from $Zn(C_2H_5)_2$

homogeneously penetrating hundreds of micrometers,[230] while a copper layer formed by $[Cu(^{s}Bu\text{-}Me\text{-}amd)]_2$ penetrated only up to 10 microns due to the 2 order of magnitude lower partial pressure of the Cu precursor.[231] Similar results were also obtained for deposition of Pt on carbon aerogel from (Methylcyclopentadienyl)-trimethylplatinum ($MeCpPtMe_3$).[232] It was postulated that next to diffusion, adsorption-desorption equilibrium of the precursor and reaction product molecules also plays an important role depending on the support.

Feng *et al.* used silica with a grain size between 75 - 200 µm as a support for deposition of Pd. Prior to Pd deposition, the silica was first coated by a 0.5 nm thick layer of Al_2O_3 using trimethyl aluminium (TMA), or ZnO using diethyl zinc at 200 °C, while water was used to decompose the precursors. Subsequently, 1.5 - 2.5 wt.% Pd was deposited by 1 or 2 cycles of palladium hexafluoroacetylacetonate ($Pd(hfac)_2$) and formalin (formaldehyde and methanol in water). Based on a time-dependent deposition study, it was concluded that diffusion of the precursor into the support was the limiting step for these materials and conditions. On the Al_2O_3 coated silica, 1 - 2 nm Pd particles were found distributed uniformly across the support particles by SEM EDX, while no particles were detected on ZnO, suggesting an alloy formation.[233] Using up to 25 cycles, it was found that the Pd particle size increased almost linearly from 1.1 to 2.9 nm on Al_2O_3 coated silica.[234] Moreover, an induction time was observed for the uptake of Pd, which increased after several cycles. It was postulated that when $Pd(hfac)_2$ is deposited, Al(hfac)* species are formed which are not removed during subsequent formalin exposure, and thus are poisoning the surface.[235] The formalin treatment only removed hfac ligands on the Pd and replaced it with hydrogen adatoms, which formed new nucleation sites for further Pd cycles, resulting in an increased Pd uptake as particles became larger due to an increasing amount of nucleation sites for additional $Pd(hfac)_2$. A similar growth behavior was observed on MgO and TiO_2 layers, however no Pd particles were observed on pure silica, suggesting a limited reactivity of the Si-OH hydroxyl groups with $Pd(hfac)_2$.[234]

A study of the deposition of Pt on γ-Al_2O_3, TiO_2 and $SrTiO_3$ using $MeCpPtMe_3$ and H_2 or N_2 cycles showed the Pt precursor can be adsorbed on oxidic supports at temperatures as low as 100 °C, and is decomposed at 200 °C in H_2 or 300 °C in N_2 to form metallic Pt particles. Even though a prolonged time was necessary for adsorption of $MeCpPtMe_3$ at 100 °C, at 300 °C premature decomposition resulted in Pt deposition throughout the reactor. During decomposition of the precursor in H_2 or N_2, mobile Pt species formed that aggregated into small clusters, forming Pt particles of 1 - 2 nm. The hydroxyl groups during these treatments were also regenerated, so that additional cycles may be performed. It was observed that the $MeCpPtMe_3$ precursor preferentially adsorbs on surface hydroxyl groups and not on metallic Pt, and that the Pt particle size did not increase much upon subsequent cycles. When O_2 was used to decompose the precursor, PtO formed, which interacted with $MeCpPtMe_3$ via reductive adsorption, resulting in an increase in Pt particle size. However, this only occurred when $MeCpPtMe_3$ already occupied most of the surface hydroxyls, and was less noticeable for high surface area supports under the used conditions.[236] Pt on silica gel (30 - 75 µm grain size) has also been prepared while keeping the substrate at 325 °C. Even though the previous study

mentioned 300 °C as an upper temperature, homogeneous distributions were reported on cross-sectioned silica particles. 3, 5, or 10 cycles of Pt precursor and O_2 were used to deposit 1.6, 2.3 or 12 wt.% Pt, respectively, with particle sizes between 1 and 2.5 nm.[237]

Mixed PtRu particles on Al_2O_3 were synthesized using alternating cycles of $MeCpPtMe_3$ and 2,4-(dimethylpentadienyl)(ethylcyclopentadienyl) ruthenium (Ru(DER)), decomposing the precursor with oxygen in between. 2 cycles Ru(DER)/O_2 were followed by 1 cycle $MeCpPtMe_3/O_2$ and 1 cycle Ru(DER)/O_2 for a final 1:1 molar ratio, and resulted in 1 - 2 nm particles with good mixing of Ru and Pt as determined by EXAFS.[238] PtPd bimetallic particles have also been synthesized using ALD on SiO_2 covered with Al_2O_3 or TiO_2 supports, creating 1 - 2 nm particles. However, as soon as a reduction treatment was performed, the particles rearranged to a Pt core Pd shell nanostructure independent of the deposition sequence.[239]

Although most studies have been performed on noble metal nanoparticles, non-noble metal particles can also be synthesized. Co_3O_4 was deposited on Al_2O_3 coated and uncoated silica gel to 25 wt.% using bis(cyclopentadienyl)cobalt and ozone. Some samples were also promoted with Pt by ALD afterwards. Using ALD, the particle size was reduced 2 fold compared to incipient wetness impregnation, from 10 - 11 nm to 5 - 6 nm with ALD. However, IWI prepared catalysts were more active for the Fischer-Tropsch reaction. This was attributed to retarded reduction of Co_3O_4 to Co for catalyst prepared by ALD, which was mitigated somewhat by Pt addition.[240]

ALD for Nanoparticle Stabilization. Next to the active metal, a novel method was developed in which an additional support layer was deposited by an extra step during ALD, referred to as ABC atomic layer deposition. The nature of Pd deposition from $Pd(hfac)_2$ was especially suitable for this. In step A, $Pd(hfac)_2$ was adsorbed on Al_2O_3, whereby some (hfac) ligands dissociated and adsorbed on the alumina to prevent total coverage of Pd. Next, step B entailed ALD of tri methyl aluminum (TMA), which did not adsorb on the Pd precursor but did decompose the Al(hfac)* species, and deposited a new layer of alumina on the support. In step C, the adsorbed TMA was decomposed by water, creating new surface sites for Pd adsorption in the next ABC cycle while keeping the existing adsorbed Pd(hfac) intact, so that further growth of these was not possible (note $Pd(hfac)_2$ was decomposed by formalin, not water). This resulted in a very narrow size distribution of 1 nm particles for up to 15 cycles and 6.6 wt.% Pd.[234,241] However, this method is only possible if the precursor in step A does not adsorb on all sites, and reactants in step B and C do not react with the precursor from step A but do create new adsorption sites.

Deposition of a separate support layer after synthesis of the supported metal particles has been completed is also possible. Feng *et al.* deposited Pd by ALD on an Al_2O_3 covered silica gel, and subsequently coated this with additional Al_2O_3 by several ALD cycles using TMA and water at 200 °C. The resulting catalysts were tested in the decomposition of methanol, and showed significantly more active catalysts after 1 - 16 Al_2O_3 ALD cycles. This was attributed to more stable catalysts already after 1 cycle; whereas the uncoated catalyst exhibited particle growth from 1.4 to 2.3 nm, the Al_2O_3 coated catalysts did not exhibit any particle growth.

When more than 16 cycles were used, the activity greatly reduced, attributed to coverage of the entire Pd particle by Al_2O_3. It was found that initial Al_2O_3 cycles preferentially adsorbed on the Pd edge, step and corner sites, whereas the catalytic activity comes from Pd(111), which was left unchanged.[242] Further investigation showed that the Pd remained accessible because CH_3 species were adsorbed on Pd after the first ALD cycle, blocking it for further adsorption of TMA in the subsequent cycle, and so preventing formation of a monolayer (Figure 2.22).[243] One study showed that even after 45 ALD cycles with a resulting Al_2O_3 layer of 8 nm thickness, the Pd was still largely accessible and very resistant to coking and sintering in the dehydrogenation of ethane to ethylene at 650 °C.[244,245]

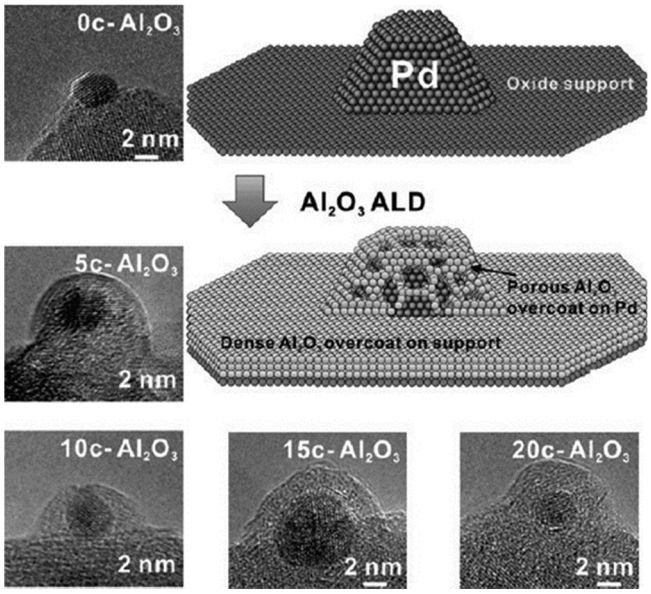

Figure 2.22. Schematic representation of the deposition of a porous alumina layer on Pd particles supported on an oxidic support, and TEM images of spherical alumina supported Pd particles with different numbers of Al_2O_3 layers deposited on top, represented by the number of cycles (#c). An increasingly thick layer was observed with increasing cycles, however the particles remained accessible for catalysis. (Adapted with permission from ref 243. Copyright 2012 American Chemical Society)

The principle of blocking part of the nanoparticle by adsorption of a specific molecule so that a porous rather than solid layer is formed was further investigated on Pd deposited on theta-Al_2O_3 by ALD. After investigating several blocking agents, octadecanethiol was chosen due to its relatively strong binding to the Pd particles and relatively large 2 nm length, while it does not react with TMA so should remain on the surface of the Pd nanoparticles during ALD deposition of Al_2O_3. CO adsorption after 21 cycles showed that Pd remained accessible when the blocking agent was used during ALD, whereas unprotected nanoparticles were completely covered in the sample prepared without octadecanethiol.[246]

Coating of 1.7 nm Pt particles deposited by ALD on mesoporous silica has also been performed. 10, 20, 30, or 40 cycles of TMA and ethylene glycol were performed for layers of 1, 2, 3, or 4 nm thickness, respectively. After 20 cycles, all Pt was found to be covered. However, an oxidation step at 400 °C in air created porosity in the Al_2O_3 layer. The resulting material had a Pt dispersion of 38%, significantly lower than the original material (65%). However,

when the materials were exposed to 800 °C, the uncoated Pt catalyst exhibited significant sintering and a reduced dispersion of 4%, whereas the Pt sample coated with 20 cycles of Al_2O_3 exhibited much better stability and 27% dispersion. When 40 cycles were used, sintering was even almost nil (Figure 2.23).[247]

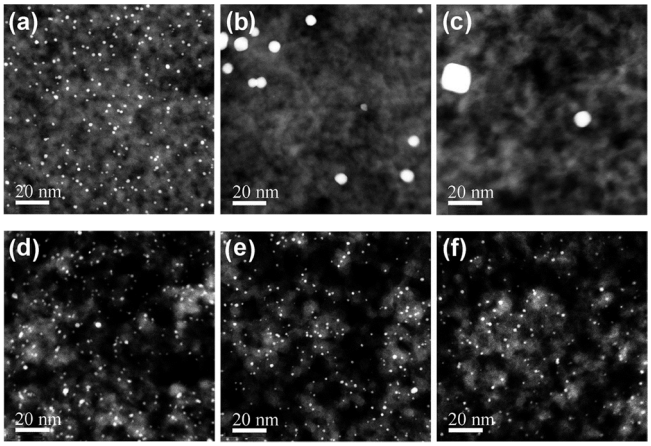

Figure 2.23. HAADF-STEM images of Pt/silica catalysts after calcination for 4 h at 400 (a,d), 600 (b,e) and 800 °C (c,f).The uncoated catalyst exhibited significant sintering, especially at higher temperatures (d,e,f), whereas the Al_2O_3 coated catalyst prepared using 40 ALD cycles exhibited negligible particle growth (a,b,c). (Adapted with permission from ref 247. Copyright 2011 American Chemical Society)

It should be noted that ALD of a stabilizing layer can also be realized on existing materials which have not been created by ALD. For example, ALD was used to deposit an Al_2O_3 layer on a 3 nm Cu/γ-Al_2O_3 catalyst prepared by incipient wetness impregnation of copper nitrate. After reduction, the catalyst exhibited 86 μmol/g surface Cu sites. After deposition of an Al_2O_3 layer by 45 cycles of TMA and water, no Cu surface sites were found. However, a thermal treatment at 700 °C in air created porosity in the layer, resulting in 23 μmol/g Cu surface sites. During the liquid phase hydrogenation of furfural, this catalyst did not exhibit any particle growth, whereas the uncoated catalyst showed particle growth from 3 to 5 nm after catalysis.[248] A similar improvement in nanoparticle stability was obtained for a Cu/SiO_2 material coated by application of 30 cycles of TMA and water, followed by calcination at 700 °C in air. Prior to the alumina coating, the catalyst displayed 34 μmol/g Cu surface sites. After coating, no sites were detected, whereas 15 μmol/g surface sites were recovered after accessibility was recreated by calcination at 700 °C.[249] To image the pores in the alumina overcoat, a layer of NbO_x was applied by 20 alternating ALD cycles of $Nb(OCH_2CH_3)_5$ and H_2O, which was previously shown to provide a uniform 1 nm thick niobia layer in the pores of SBA-15.[250] Using STEM-EELS, the penetration depth of NbO_x was found to be significantly larger after calcination of the overcoat at 700 °C, indicating the presence of pores before NbO_x deposition.[249] Similar deposition of a 0.2 nm thick Al_2O_3 layer by 2 ALD cycles has been performed to coat $LiCoO_2$ for lithium-ion battery electrodes, which also exhibited a greatly improved stability after extensive charge-discharge cycling compared to the untreated material.[251]

6. CONCLUSION AND OUTLOOK

In this chapter, we have reviewed the growth in the fundamental understanding of conventional techniques for the synthesis of supported catalysts that has been obtained in recent years. Detailed studies of coprecipitation have provided new insights in the precipitation mechanism and effect of subsequent thermal activation treatments, while alternative precursors, precipitating agents, and thermal treatments provide promising alternatives for 'greener' coprecipitation methods. Deposition precipitation is used to produce highly loaded metal catalyst, but is showing an increased usage for the preparation of low loaded, highly dispersed (noble) metal catalysts. However, research has revealed that the physicochemical processes that take place at low loadings resemble adsorption rather than precipitation.

Impregnation and drying remains the most used and studied preparation technique. Detailed study of impregnated ordered materials have shown complete pore filling with aqueous solutions and oxidic supports, and an enhanced understanding of adsorption on support surfaces has improved the ability to rationally synthesize well dispersed supported metal catalysts. The development of microspectroscopic tools enabled the study of (the development of) gradients and chemical speciation in macroscopic catalysts bodies during impregnation and drying processes, whereas models have been developed and experimentally verified that predict the distribution of the metal precursor across catalysts grains for both high and low precursor loadings. In addition, the development of the nanoscale metal distribution, which has been a long standing challenge in the synthesis of catalysts, was recently studied and controlled. Thermal decomposition of the metal salt precursor, in particular the role of the gas composition or use of chelating agents, have also been systematically studied to elucidate the effects on particle size and particle distribution.

Besides these, several new or rejuvenated approaches were noticed. First, melt infiltration is a promising and facile technique for the preparation of catalysts with high metal loadings that bears many similarities to impregnation and drying, and as such could benefit from the extensive knowledge obtained recently on this method. Second, the synthesis of colloids in solution leads to unique control over particle size, shape and composition and is based on extensive literature. However deposition of the formed colloids onto a support has been less studied but remains highly important for the synthesis of supported catalysts, and elicits further study. Third, the kinetics of particle growth in the presence of a support have been studied in real time for the first time using in situ catalytic measurements of the emerging catalyst. Fourth, atomic layer deposition is showing promise especially for deposition of nanoparticles, but also for deposition of a stabilizing layer onto supported catalysts, for which further insight in the stabilizing effect and ability to obtain porous layers are desired.

Based on the literature described in this review, it is clear that single (monometallic) particle properties can be largely controlled. To further advance the field of catalyst preparation, more detailed studies on the kinetics of particle formation[9] for each of the preparation methods, as well as systematic studies to control the collective properties of the

nanoparticles[11], and the controlled formation of bimetallic and core-shell particles[252] is greatly desired. To achieve this, the development of many *in-situ* spectroscopic and microscopic techniques will be critical. In particular, X-ray based techniques[253] and liquid-cell TEM[254] offer possibilities to study the genesis of particles in real time, while other advanced electron microscopy techniques such as Cryo-TEM[73] and electron tomography[255] offer information on the distribution of the precursor at different stages during preparation. Furthermore, surface science studies provide increased understanding of the influence of support hydroxylation and preparation method[256,257], while X-ray[258] and microbalance[259,260] techniques offer increasingly accurate information on the adsorption of complexes on flat surfaces. Model supports are also essential since 2D model supports provide an excellent platform to study morphological and compositional changes of nanoparticles,[261] while 3D model supports are excellent to study the synthesis[73], distribution, and stability[262] of metal nanoparticles in a more realistic environment. Combination of these and other techniques will provide key insights to further the rationalization of the synthesis of supported catalysts.

7. REFERENCES

(1) Behrens, M.; Studt, F.; Kasatkin, I.; Kühl, S.; Hävecker, M.; Abild-Pedersen, F.; Zander, S.; Girgsdies, F.; Kurr, P.; Kniep, B.-L.; Tovar, M.; Fischer, R. W.; Nørskov, J. K.; Schlögl, R. *Science.* **2012**, *336*, 893.

(2) Babich, I. V; Moulijn, J. A. *Fuel* **2003**, *82*, 607.

(3) Brown, D. E.; Edmonds, T.; Joyner, R. W.; McCarroll, J. J.; Tennison, S. R. *Catal. Letters* **2014**, *144*, 545.

(4) Torres Galvis, H. M.; Bitter, J. H.; Khare, C. B.; Ruitenbeek, M.; Dugulan, A. I.; de Jong, K. P. *Science.* **2012**, *335*, 835.

(5) Besson, M.; Gallezot, P.; Pinel, C. *Chem. Rev.* **2014**, *114*, 1827.

(6) Huber, G. W.; Iborra, S.; Corma, A. *Chem. Rev.* **2006**, *106*, 4044.

(7) Guo, X.; Fang, G.; Li, G.; Ma, H.; Fan, H.; Yu, L.; Ma, C.; Wu, X.; Deng, D.; Wei, M.; Tan, D.; Si, R.; Zhang, S.; Li, J.; Sun, L.; Tang, Z.; Pan, X.; Bao, X. *Science.* **2014**, *344*, 616.

(8) Schwarz, J. A.; Contescu, C.; Contescu, A. *Chem. Rev.* **1995**, *95*, 477.

(9) Mondloch, J. E.; Bayram, E.; Finke, R. G. *J. Mol. Catal. A Chem.* **2012**, *355*, 1.

(10) Bartholomew, C. H. *Appl. Catal.* **2001**, *212*, 17.

(11) Prieto, G.; Zečević, J.; Friedrich, H.; de Jong, K. P.; de Jongh, P. E. *Nat. Mater.* **2013**, *12*, 34.

(12) Munnik, P.; de Jongh, P. E.; de Jong, K. P. *J. Am. Chem. Soc.* **2014**, *136*, 7333.

(13) Van Santen, R. A. *Acc. Chem. Res.* **2009**, *42*, 57.

(14) Lundwall, M. J.; Mcclure, S. M.; Wang, X.; Wang, Z.; Chen, M.; Goodman, D. W. *J. Phys. Chem. C* **2012**, *116*, 18155.

(15) Bezemer, G. L.; Bitter, J. H.; Kuipers, H. P. C. E.; Oosterbeek, H.; Holewijn, J. E.; Xu, X. D.; Kapteijn, F.; van Dillen, J. A.; de Jong, K. P. *J. Am. Chem. Soc.* **2006**, *128*, 3956.

(16) Den Breejen, J. P.; Radstake, P. B.; Bezemer, G. L.; Bitter, J. H.; Frøseth, V.; Holmen, A.; de Jong, K. P. *J. Am. Chem. Soc.* **2009**, *131*, 7197.

(17) Farmer, J. A.; Campbell, C. T. *Science.* **2010**, *329*, 933.

(18) Cao, A.; Veser, G. *Nat. Mater.* **2010**, *9*, 75.

(19) Holby, E. F.; Sheng, W.; Shao-Horn, Y.; Morgan, D. *Energy Environ. Sci.* **2009**, *2*, 865.

(20) Munnik, P.; Velthoen, M.; de Jongh, P. E.; de Jong, K. P.; Gommes, C. J. *Angew. Chem. Int. Ed. Engl.* **2014**, Submitted.

(21) Li, W.; Yue, Q.; Deng, Y.; Zhao, D. *Adv. Mater.* **2013**, *25*, 5129.

(22) Corma, a; García, H.; Llabrés i Xamena, F. X. *Chem. Rev.* **2010**, *110*, 4606.

(23) Hiemstra, T.; Venema, P.; Riemsdijk, W. *J. Colloid Interface Sci.* **1996**, *184*, 680.
(24) Kosmulski, M. *J. Colloid Interface Sci.* **2011**, *353*, 1.
(25) Kaluza, S.; Schröter, M. K.; Naumann d'Alnoncourt, R.; Reinecke, T.; Muhler, M. *Adv. Funct. Mater.* **2008**, *18*, 3670.
(26) Kaluza, S.; Behrens, M.; Schiefenhövel, N.; Kniep, B.; Fischer, R.; Schlögl, R.; Muhler, M. *ChemCatChem* **2011**, *3*, 189.
(27) Villacampa, J. I.; Royo, C.; Romeo, E.; Montoya, J. A.; Del Angel, P.; Monzón, A. *Appl. Catal. A Gen.* **2003**, *252*, 363.
(28) Shroff, M. D.; Kalakkad, D. S.; Coulter, K. E.; Kohler, S. D.; Harrington, M. S.; Jackson, N. B.; Sault, A. G.; Datye, A. K. *J. Catal.* **1995**, *156*, 185.
(29) Behrens, M.; Schlögl, R. *Zeitschrift für Anorg. und Allg. Chemie* **2013**, *639*, 2683.
(30) Behrens, M.; Brennecke, D.; Girgsdies, F.; Kißner, S.; Trunschke, A.; Nasrudin, N.; Zakaria, S.; Idris, N. F.; Hamid, S. B. A.; Kniep, B.; Fischer, R.; Busser, W.; Muhler, M.; Schlögl, R. *Appl. Catal. A Gen.* **2011**, *392*, 93.
(31) Baltes, C.; Vukojevic, S.; Schuth, F. *J. Catal.* **2008**, *258*, 334.
(32) Zander, S.; Seidlhofer, B.; Behrens, M. *Dalton Trans.* **2012**, *41*, 13413.
(33) Behrens, M. *J. Catal.* **2009**, *267*, 24.
(34) Simson, G.; Prasetyo, E.; Reiner, S.; Hinrichsen, O. *Appl. Catal. A Gen.* **2013**, *450*, 1.
(35) Zhang, X.; Zhong, L.; Guo, Q.; Fan, H.; Zheng, H.; Xie, K. *Fuel* **2010**, *89*, 1348.
(36) Kowalik, P.; Konkol, M.; Kondracka, M.; Próchniak, W.; Bicki, R.; Wiercioch, P. *Appl. Catal. A Gen.* **2013**, *452*, 139.
(37) Budiman, A.; Ridwan, M.; Kim, S. M.; Choi, J.-W.; Yoon, C. W.; Ha, J.-M.; Suh, D. J.; Suh, Y.-W. *Appl. Catal. A Gen.* **2013**, *462-463*, 220.
(38) Li, Z.; Yan, S.; Fan, H. *Fuel* **2013**, *106*, 178.
(39) Behrens, M.; Kissner, S.; Girsgdies, F.; Kasatkin, I.; Hermerschmidt, F.; Mette, K.; Ruland, H.; Muhler, M.; Schlögl, R. *Chem. Commun.* **2011**, *47*, 1701.
(40) Prieto, G.; de Jong, K. P.; de Jongh, P. E. *Catal. Today* **2013**, *215*, 142.
(41) Burattin, P.; Che, M.; Louis, C. *J. Phys. Chem. B* **1998**, *102*, 2722.
(42) De Jong, K. P.; Geus, J. W. *Appl. Catal.* **1982**, *4*, 41.
(43) Lok, C. M. *Stud. Surf. Sci. Catal.* **2004**, *147*, 283.
(44) Bitter, J. H.; van der Lee, M. K.; Slotboom, A. G. T.; van Dillen, J. A.; de Jong, K. P. *Catal. Letters* **2003**, *89*, 139.
(45) Fang, B.; Chaudhari, N. K.; Kim, M.-S.; Kim, J. H.; Yu, J.-S. *J. Am. Chem. Soc.* **2009**, *131*, 15330.
(46) Kim, M.-S.; Lim, S.; Chaudhari, N. K.; Fang, B.; Bae, T.-S.; Yu, J.-S. *Catal. Today* **2010**, *158*, 354.
(47) Bezemer, G. L.; Radstake, P. B.; Koot, V.; van Dillen, J. A.; Geus, J. W.; de Jong, K. P. *J. Catal.* **2006**, *237*, 291.
(48) Eschemann, T. O.; Bitter, J. H.; de Jong, K. P. *Catal. Today* **2014**, *228*, 89.
(49) Moreau, F.; Bond, G. C. *Appl. Catal. A Gen.* **2006**, *302*, 110.
(50) Moreau, F.; Bond, G.; Taylor, A. *J. Catal.* **2005**, *231*, 105.
(51) Moreau, F.; Bond, G. C. *Catal. Today* **2007**, *122*, 215.
(52) Fang, W.; Chen, J.; Zhang, Q.; Deng, W.; Wang, Y. *Chemistry* **2011**, *17*, 1247.
(53) Martin, R.; Navalon, S.; Delgado, J. J.; Calvino, J. J.; Alvaro, M.; Garcia, H. *Chemistry* **2011**, *17*, 9494.
(54) Lim, S. H.; Phonthammachai, N.; Zhong, Z.; Teo, J.; White, T. J. *Langmuir* **2009**, *25*, 9480.
(55) Yazid, H.; Adnan, R.; Farrukh, M. A.; Hamid, S. A. *J. Chinese Chem. Soc.* **2011**, *58*, 593.
(56) Souza, K. R.; de Lima, A. F. F.; de Sousa, F. F.; Appel, L. G. *Appl. Catal. A Gen.* **2008**, *340*, 133.
(57) Zanella, R.; Giorgio, S.; Henry, C. R.; Louis, C. *J. Phys. Chem. B* **2002**, *106*, 7634.
(58) Cellier, C.; Lambert, S.; Gaigneaux, E. M.; Poleunis, C.; Ruaux, V.; Eloy, P.; Lahousse, C.; Bertrand, P.; Pirard, J.-P.; Grange, P. *Appl. Catal. B Environ.* **2007**, *70*, 406.
(59) Moreau, F.; Bond, G. C. *Catal. Today* **2007**, *122*, 260.
(60) Zanella, R.; Delannoy, L.; Louis, C. *Appl. Catal. A Gen.* **2005**, *291*, 62.

(61) Hugon, A.; Kolli, N. El; Louis, C. *J. Catal.* **2010**, *274*, 239.
(62) Hugon, A.; Delannoy, L.; Krafft, J.; Louis, C. *J. Phys. Chem. C* **2010**, *114*, 10823.
(63) Ward, T.; Delannoy, L.; Hahn, R.; Kendell, S.; Pursell, C. J.; Louis, C.; Chandler, B. D. *ACS Catal.* **2013**, *3*, 2644.
(64) Cárdenas-Lizana, F.; Gómez-Quero, S.; Hugon, A.; Delannoy, L.; Louis, C.; Keane, M. A. *J. Catal.* **2009**, *262*, 235.
(65) Murzin, D. Y.; Simakova, O. a.; Simakova, I. L.; Parmon, V. N. *React. Kinet. Mech. Catal.* **2011**, *104*, 259.
(66) Van Honschoten, J. W.; Brunets, N.; Tas, N. R. *Chem. Soc. Rev.* **2010**, *39*, 1096.
(67) Washburn, E. W. *Phys. Rev.* **1921**, *17*, 273.
(68) Haneveld, J.; Tas, N. R.; Brunets, N.; Jansen, H. V.; Elwenspoek, M. *J. Appl. Phys.* **2008**, *104*, 014309.
(69) Liu, X.; Khinast, J. G.; Glasser, B. J. *Chem. Eng. Sci.* **2008**, *63*, 4517.
(70) Imperor-Clerc, M.; Bazin, D.; Appay, M.; Beaunier, P.; Davidson, A. *Chem. Mater.* **2004**, *16*, 1813.
(71) Moreno, M. S.; Weyland, M.; Midgley, P. A.; Bengoa, J. F.; Cagnoli, M. V; Gallegos, N. G.; Alvarez, A. M.; Marchetti, S. G. *Micron* **2006**, *37*, 52.
(72) Sietsma, J. R. A.; Meeldijk, J. D.; Versluijs-Helder, M.; Broersma, A.; van Dillen, J. A.; de Jongh, P. E.; de Jong, K. P. *Chem. Mater.* **2008**, 2921.
(73) Eggenhuisen, T. M.; Friedrich, H.; Nudelman, F.; Zečević, J.; Sommerdijk, N. A. J. M.; de Jongh, P. E.; de Jong, K. P. *Chem. Mater.* **2013**, *25*, 890.
(74) Eggenhuisen, T. M.; van Steenbergen, M. J.; Talsma, H.; de Jongh, P. E.; de Jong, K. P. *J. Phys. Chem. C* **2009**, *113*, 16785.
(75) Cornu, C.; Bonardet, J. L.; Casale, S.; Davidson, A.; Ambramson, S.; Andre, G.; Porcher, F.; Grcic, I.; Tomasic, V.; Vujevic, D.; Koprivanac, N. *J. Phys. Chem. C* **2012**, *116*, 3437.
(76) Marceau, E.; Che, M.; Čejka, J.; Zukal, A. *ChemCatChem* **2010**, *2*, 413.
(77) Boubekr, F.; Davidson, A.; Casale, S.; Massiani, P. *Microporous Mesoporous Mater.* **2011**, *141*, 157.
(78) Van der Meer, J.; Bardez-Giboire, I.; Bart, F.; Albouy, P.; Wallez, G.; Davidson, A. *Microporous Mesoporous Mater.* **2009**, *118*, 183.
(79) Van der Meer, J.; Bardez-Giboire, I.; Mercier, C.; Revel, B.; Davidson, A.; Denoyel, R. *J. Phys. Chem. C* **2010**, *114*, 3507.
(80) Park, J.; Regalbuto, J. R. *J. Colloid Interface Sci.* **1995**, *175*, 239.
(81) Bourikas, K.; Kordulis, C.; Lycourghiotis, A. *Catal. Rev.* **2006**, *48*, 363.
(82) Hao, X.; Spieker, W. A.; Regalbuto, J. R. *J. Colloid Interface Sci.* **2003**, *267*, 259.
(83) Agashe, K.; Regalbuto, J. R. *J. Colloid Interface Sci.* **1997**, *185*, 174.
(84) Jiao, L.; Regalbuto, J. R. *J. Catal.* **2008**, *260*, 329.
(85) Jiao, L.; Regalbuto, J. R. *J. Catal.* **2008**, *260*, 342.
(86) Lambert, S.; Job, N.; Dsouza, L.; Pereira, M.; Pirard, R.; Heinrichs, B.; Figueiredo, J.; Pirard, J.; Regalbuto, J. R. *J. Catal.* **2009**, *261*, 23.
(87) Hao, X.; Barnes, S.; Regalbuto, J. R. *J. Catal.* **2011**, *279*, 48.
(88) Job, N.; Lambert, S.; Chatenet, M.; Gommes, C. J.; Maillard, F.; Berthon-Fabry, S.; Regalbuto, J. R.; Pirard, J.-P. *Catal. Today* **2010**, *150*, 119.
(89) Dsouza, L.; Jiao, L.; Regalbuto, J. R.; Miller, J.; Kropf, a. *J. Catal.* **2007**, *248*, 165.
(90) Dsouza, L.; Regalbuto, J. R.; Miller, J. *J. Catal.* **2008**, *254*, 157.
(91) Zhu, X.; Cho, H.; Pasupong, M.; Regalbuto, J. R. *ACS Catal.* **2013**, *3*, 625.
(92) Feltes, T. E.; Espinosa-Alonso, L.; Smit, E. De; D'Souza, L.; Meyer, R. J.; Weckhuysen, B. M.; Regalbuto, J. R. *J. Catal.* **2010**, *270*, 95.
(93) Feltes, T. E.; Zhao, Y.; Klie, R. F.; Meyer, R. J.; Regalbuto, J. R. *ChemCatChem* **2010**, *2*, 1065.
(94) Zhao, Y.; Feltes, T. E.; Regalbuto, J. R.; Meyer, R. J.; Klie, R. F. *Catal. Sci. Technol.* **2011**, *1*, 1483.
(95) Liu, J.; Tao, R.; Guo, Z.; Regalbuto, J. R.; Marshall, C. L.; Klie, R. F.; Miller, J. T.; Meyer, R. J. *ChemCatChem* **2013**, *5*, 3665.

(96) Petsi, T.; Panagiotou, G. D.; Garoufalis, C. S.; Kordulis, C.; Stathi, P.; Deligiannakis, Y.; Lycourghiotis, A.; Bourikas, K. *Chem. a Eur. J.* **2009**, *15*, 13090.
(97) Panagiotou, G. D.; Petsi, T.; Bourikas, K.; Kordulis, C.; Lycourghiotis, A. *J. Catal.* **2009**, *262*, 266.
(98) Panagiotou, G. D.; Petsi, T.; Bourikas, K.; Kalampounias, A. G.; Boghosian, S.; Kordulis, C.; Lycourghiotis, A. *J. Phys. Chem. C* **2010**, *114*, 11868.
(99) Petsi, T.; Panagiotou, G. D.; Bourikas, K.; Kordulis, C.; Voyiatzis, G. a.; Lycourghiotis, A. *ChemCatChem* **2011**, *3*, 1072.
(100) Bourikas, K.; Stavropoulos, J.; Garoufalis, C. S.; Kordulis, C.; Petsi, T.; Lycourghiotis, A. *Chem. a Eur. J.* **2011**, *17*, 1201.
(101) Bourikas, K.; Vakros, J.; Fountzoula, C.; Kordulis, C.; Lycourghiotis, A. *Catal. Today* **2007**, *128*, 138.
(102) Zacharaki, I.; Kontoyannis, C. G.; Boghosian, S.; Lycourghiotis, A.; Kordulis, C. *Catal. Today* **2009**, *143*, 38.
(103) Li, H.; Li, M.; Chu, Y.; Liu, F.; Nie, H. *Fuel* **2014**, *116*, 168.
(104) Sun, K.-Q.; Marceau, E.; Che, M. *Phys. Chem. Chem. Phys.* **2006**, *8*, 1731.
(105) Lee, S. Y.; Aris, R. *Catal. Rev. Sci. Eng.* **1985**, *27*, 207.
(106) Neimark, A. V; Kheifez, L. I.; Fenelonov, V. B. *Ind. Eng. Chem. Prod. Res. Dev.* **1981**, 439.
(107) Espinosa-Alonso, L.; Beale, A. M.; Weckhuysen, B. M. *Acc. Chem. Res.* **2010**, *43*, 1279.
(108) Bergwerff, J. A.; Visser, T.; Leliveld, B. R. G.; Rossenaar, B. D.; de Jong, K. P.; Weckhuysen, B. M. *J. Am. Chem. Soc.* **2004**, *126*, 14548.
(109) Zandbergen, M. W.; Jacques, S. D. M.; Weckhuysen, B. M.; Beale, A. M. *Angew. Chemie Int. Ed.* **2012**, *51*, 957.
(110) Gibson, E. K.; Zandbergen, M. W.; Jacques, S. D. M.; Biao, C.; Cernik, R. J.; Brien, M. G. O.; Michiel, M. Di; Weckhuysen, B. M.; Beale, A. M. *ACS Catal.* **2013**, *3*, 339.
(111) Bergwerff, J. A.; Lysova, A. A.; Espinosa-Alonso, L.; Koptyug, I. V; Weckhuysen, B. M. *Angew. Chemie Int. Ed.* **2007**, *46*, 7224.
(112) Van de Water, L. G. A.; Bezemer, G. L.; Bergwerff, J. A.; Versluijs-Helder, M.; Weckhuysen, B. M.; de Jong, K. P. *J. Catal.* **2006**, *242*, 287.
(113) Bergwerff, J. A.; Lysova, A. A.; Espinosa-Alonso, L.; Koptyug, I. V; Weckhuysen, B. M. *Chem. a Eur. J.* **2008**, *14*, 2363.
(114) Espinosa-Alonso, L.; de Jong, K. P.; Weckhuysen, B. M. *J. Phys. Chem. C* **2008**, *112*, 7201.
(115) Espinosa-Alonso, L.; Lysova, A. A.; de Peinder, P.; de Jong, K. P.; Koptyug, I. V; Weckhuysen, B. M. *J. Am. Chem. Soc.* **2009**, *131*, 6525.
(116) Zandbergen, M. W.; Beale, A. M.; Weckhuysen, I. B. M. *ChemCatChem* **2012**, *4*, 217.
(117) Espinosa-Alonso, L.; de Jong, K. P.; Weckhuysen, B. M. *Phys. Chem. Chem. Phys.* **2010**, *12*, 97.
(118) Lekhal, A.; Glasser, B. J.; Khinast, J. G. *Chem. Eng. Sci.* **2001**, *56*, 4473.
(119) Van Dillen, J. A.; Terorde, R.; Lensveld, D.; Geus, J.; de Jong, K. P. *J. Catal.* **2003**, *216*, 257.
(120) Torres Galvis, H. M.; Koeken, A. C. J.; Bitter, J. H.; Davidian, T.; Ruitenbeek, M.; Dugulan, A. I.; de Jong, K. P. *Catal. Today* **2013**, *215*, 95.
(121) Qiu, S.; Zhang, X.; Liu, Q.; Wang, T.; Zhang, Q.; Ma, L. *Catal. Commun.* **2013**, *42*, 73.
(122) Lysova, A. A.; Bergwerff, J. A.; Espinosa-Alonso, L.; Weckhuysen, B. M.; Koptyug, I. V. *Appl. Catal. A Gen.* **2010**, *374*, 126.
(123) Liu, X.; Khinast, J. G.; Glasser, B. J. *Ind. Eng. Chem. Res.* **2010**, *49*, 2649.
(124) Liu, X.; Khinast, J. G.; Glasser, B. J. *Chem. Eng. Sci.* **2012**, *79*, 187.
(125) Bergwerff, J. A.; Jansen, M.; Leliveld, B. R. G.; Visser, T.; de Jong, K. P.; Weckhuysen, B. *J. Catal.* **2006**, *243*, 292.
(126) Arslan, I.; Walmsley, J. C.; Rytter, E.; Bergene, E.; Midgley, P. A. *J. Am. Chem. Soc.* **2008**, *130*, 5716.
(127) Borg, Ø.; Walmsley, J. C.; Dehghan, R.; Tanem, B. S.; Blekkan, E. A.; Eri, S.; Rytter, E.; Holmen, A. *Catal. Letters* **2008**, *126*, 224.
(128) Loosdrecht, J. Van De; Datt, M.; Visagie, J. L. *Top. Catal.* **2013**, *57*, 430.

(129) Borg, Ø.; Dietzel, P. D. C.; Spjelkavik, A. I.; Tveten, E. Z.; Walmsley, J. C.; Diplas, S.; Eri, S.; Holmen, A.; Rytter, E. *J. Catal.* **2008**, *259*, 161.
(130) Banerjee, R.; Crozier, P. A. *J. Phys. Chem. C* **2012**, *116*, 11486.
(131) Wolters, M.; Munnik, P.; Bitter, J. H.; de Jongh, P. E.; de Jong, K. P. *J. Phys. Chem. C* **2011**, *115*, 3332.
(132) Munnik, P.; Krans, N. A.; de Jongh, P. E.; de Jong, K. P. *ACS Catal.* **2014**, in preparation.
(133) Stannard, A.; Martin, C. P.; Pauliac-Vaujour, E.; Moriarty, P.; Thiele, U. *J. Phys. Chem. C* **2008**, *112*, 15195.
(134) Stannard, A. *J. Phys. Condens. Matter* **2011**, *23*, 083001.
(135) Sun, X.; Shi, Y.; Zhang, P.; Zheng, C.; Zheng, X.; Zhang, F.; Zhang, Y.; Guan, N.; Zhao, D.; Stucky, G. D. *J. Am. Chem. Soc.* **2011**, *133*, 14542.
(136) Eggenhuisen, T. M.; Munnik, P.; Talsma, H.; de Jongh, P. E.; de Jong, K. P. *J. Catal.* **2013**, *297*, 306.
(137) Van de Loosdrecht, J.; Barradas, S.; Caricato, E. A.; Ngwenya, N. G.; Nkwanyana, P. S.; Rawat, M.; Sigwebela, B. H.; van Berge, P. J.; Visagie, J. L. *Top. Catal.* **2003**, *26*, 121.
(138) Borg, Ø.; Blekkan, E. A.; Eri, S.; Akporiaye, D.; Vigerust, B.; Rytter, E.; Holmen, A. *Top. Catal.* **2007**, *45*, 39.
(139) Sietsma, J. R. A.; Meeldijk, J. D.; den Breejen, J. P.; Versluijs-Helder, M.; van Dillen, J. A.; de Jongh, P. E.; de Jong, K. P. *Angew. Chemie Int. Ed.* **2007**, *46*, 4547.
(140) Sietsma, J. R. A.; Friedrich, H.; Broersma, A.; Versluijs-Helder, M.; Jos van Dillen, A.; de Jongh, P. E.; de Jong, K. P. *J. Catal.* **2008**, *260*, 227.
(141) Wolters, M.; Daly, H.; Goguet, A.; Meunier, F. C.; Hardacre, C.; Bitter, J. H.; de Jongh, P. E.; de Jong, K. P. *J. Phys. Chem. C* **2010**, *114*, 7839.
(142) Wolters, M.; Andrade, I. C. A. C.; Munnik, P.; Bitter, J. H.; de Jongh, P. E.; de Jong, K. P. *Stud. Surf. Sci. Catal.* **2010**, *175*, 69.
(143) Wolters, M.; van Grotel, L. J. W.; Eggenhuisen, T. M.; Sietsma, J. R. A.; de Jong, K. P.; de Jongh, P. E. *Catal. Today* **2011**, *163*, 27.
(144) Hong, J.; Marceau, E.; Khodakov, A. Y.; Griboval-Constant, A.; La Fontaine, C.; Briois, V. *Chem. a Eur. J.* **2012**, 2802.
(145) Becker, H.; Turek, T.; Güttel, R. *Catal. Today* **2013**, *215*, 8.
(146) Jacobs, G.; Ma, W.; Davis, B. H.; Cronauer, D. C.; Jeremy Kropf, a.; Marshall, C. L. *Catal. Letters* **2010**, *140*, 106.
(147) Munnik, P.; Wolters, M.; Gabrielsson, A.; Pollington, S. D.; Headdock, G.; Bitter, J. H.; de Jongh, P. E.; de Jong, K. P. *J. Phys. Chem. C* **2011**, *115*, 14698.
(148) Coulier, L.; Beer, V. H. J. De; Veen, J. A. R. Van; Niemantsverdriet, J. W. *Top. Catal.* **2000**, *13*, 99.
(149) Coulier, L.; de Beer, V. H. .; van Veen, J. a. .; Niemantsverdriet, J. . *J. Catal.* **2001**, *197*, 26.
(150) Kishan, G.; Veen, J. A. R. Van; Niemantsverdriet, J. W. *Top. Catal.* **2004**, *29*, 103.
(151) Kishan, G.; Coulier, L.; de Beer, V. H. J.; van Veen, J. a. R.; Niemantsverdriet, J. W. *J. Catal.* **2000**, *196*, 180.
(152) Mochizuki, T.; Hara, T.; Koizumi, N.; Yamada, M. *Appl. Catal. A Gen.* **2007**, *317*, 97.
(153) Mochizuki, T.; Hara, T.; Koizumi, N.; Yamada, M. *Catal. Letters* **2007**, *113*, 165.
(154) Koizumi, N.; Mochizuki, T.; Yamada, M. *Catal. Today* **2009**, *141*, 34.
(155) Mochizuki, T.; Hongo, D.; Satoh, T.; Koizumi, N.; Yamada, M. *Catal. Letters* **2008**, *121*, 52.
(156) Koizumi, N.; Ibi, Y.; Hongo, D.; Hamabe, Y.; Suzuki, S.; Hayasaka, Y.; Shindo, T.; Yamada, M. *J. Catal.* **2012**, *289*, 151.
(157) Rane, S.; Borg, Ø.; Yang, J.; Rytter, E.; Holmen, A. *Appl. Catal. A Gen.* **2010**, *388*, 160.
(158) Rane, S.; Borg, Ø.; Rytter, E.; Holmen, A. *Appl. Catal. A Gen.* **2012**, *437-438*, 10.
(159) Koizumi, N.; Suzuki, S.; Niiyama, S.; Ibi, Y.; Shindo, T.; Yamada, M. *Appl. Catal. A Gen.* **2011**, *395*, 138.
(160) Koizumi, N.; Suzuki, S.; Niiyama, S.; Shindo, T.; Yamada, M. *Catal. Letters* **2011**, *141*, 931.
(161) Hong, J.; Marceau, E.; Khodakov, A. Y.; Griboval-Constant, A.; La, C.; Briois, V.; Chernavskii, P. A. *Catal. Today* **2011**, *175*, 528.

(162) Girardon, J. S.; Quinet, E.; Gribovalconstant, a; Chernavskii, P.; Gengembre, L.; Khodakov, A. Y. *J. Catal.* **2007**, *248*, 143.
(163) Girardon, J. S.; Lermontov, A. S.; Gengembre, L.; Chernavskii, P. A. *J. Catal.* **2005**, *230*, 339.
(164) Bae, J. W.; Kim, S.-M.; Kang, S.-H.; Chary, K. V. R.; Lee, Y.-J.; Kim, H.-J.; Jun, K.-W. *J. Mol. Catal. A Chem.* **2009**, *311*, 7.
(165) Rodríguez-González, V.; Marceau, E.; Beaunier, P.; Che, M.; Train, C. *J. Solid State Chem.* **2007**, *180*, 22.
(166) Marceau, E.; Löfberg, A.; Giraudon, J.-M.; Négrier, F.; Che, M.; Leclercq, L. *Appl. Catal. A Gen.* **2009**, *362*, 34.
(167) Zou, J.-J.; Zhang, Y.; Liu, C.-J. *Langmuir* **2006**, *22*, 11388.
(168) Liang, X.; Liu, C.; Kuai, P. *Green Chem.* **2008**, *10*, 1318.
(169) Zhao, Y.; Pan, Y.; Xie, Y.; Liu, C. *Catal. Commun.* **2008**, *9*, 1558.
(170) Chen, Y.; Wang, H.; Liu, C.-J.; Zeng, Z.; Zhang, H.; Zhou, C.; Jia, X.; Yang, Y. *J. Catal.* **2012**, *289*, 105.
(171) Chu, W.; Wang, L. N.; Chernavskii, P. A.; Khodakov, A. Y. *Angew. Chemie Int. Ed.* **2008**, *47*, 5052.
(172) Hong, J.; Chu, W.; Chernavskii, P. A.; Khodakov, A. Y. *J. Catal.* **2010**, *273*, 9.
(173) Yu, X.; Zhang, F.; Wang, N.; Hao, S.; Chu, W. *Catal. Letters* **2013**, *144*, 293.
(174) Zhu, X.; Huo, P.; Zhang, Y.; Cheng, D.; Liu, C. *Appl. Catal. B Environ.* **2008**, *81*, 132.
(175) Zou, J.-J.; He, H.; Cui, L.; Du, H.-Y. *Int. J. Hydrogen Energy* **2007**, *32*, 1762.
(176) Huang, C.; Bai, S.; Lv, J.; Li, Z. *Catal. Letters* **2011**, *141*, 1391.
(177) Odedairo, T.; Chen, J.; Zhu, Z. *J. Phys. Chem. C* **2013**, *117*, 21288.
(178) De Jongh, P. E.; Eggenhuisen, T. M. *Adv. Mater.* **2013**, *25*, 6672.
(179) *Handbook of Chemistry and Physics*; 92nd ed.; CRC Press, 2012.
(180) Schüth, F.; Wingen, A.; Sauer, J. *Microporous mesoporous Mater.* **2001**, *45*, 465.
(181) Yue, W.; Zhou, W. *Chem. Mater.* **2007**, *19*, 2359.
(182) Tang, C.; Zhang, H.; Sun, C.; Li, J.; Qi, L.; Quan, Y.; Gao, F.; Dong, L. *Catal. Commun.* **2011**, *12*, 1075.
(183) Eggenhuisen, T. M.; den Breejen, J. P.; Verdoes, D.; de Jongh, P. E.; de Jong, K. P. *J. Am. Chem. Soc.* **2010**, *132*, 18318.
(184) Li, X.; Quek, X.-Y.; Michel Ligthart, D. A. J.; Guo, M.; Zhang, Y.; Li, C.; Yang, Q.; Hensen, E. J. M. *Appl. Catal. B Environ.* **2012**, *123-124*, 424.
(185) Tang, C.; Sun, J.; Yao, X.; Cao, Y.; Liu, L.; Ge, C.; Gao, F.; Dong, L. *Appl. Catal. B Environ.* **2014**, *146*, 201.
(186) Boulaoued, A.; Fechete, I.; Donnio, B.; Bernard, M.; Turek, P.; Garin, F. *Microporous Mesoporous Mater.* **2012**, *155*, 131.
(187) Medina-Mendoza, A. K.; Cortés-Jácome, M. A.; Toledo-Antonio, J. A.; Angeles-Chávez, C.; López-Salinas, E.; Cuauhtémoc-López, I.; Barrera, M. C.; Escobar, J.; Navarrete, J.; Hernández, I. *Appl. Catal. B Environ.* **2011**, *106*, 14.
(188) Iglesia, E.; Soled, S. L.; Baumgartner, J. E.; Reyes, S. C. *J. Catal.* **1995**, *153*, 108.
(189) Liu, X.; Khinast, J. G.; Glasser, B. J. *Ind. Eng. Chem. Res.* **2014**, *53*, 5792.
(190) Tao, A. R.; Habas, S.; Yang, P. *Small* **2008**, *4*, 310.
(191) Casavola, M.; Buonsanti, R.; Caputo, G.; Davide, P. *Eur. J. Inorg. Chem.* **2008**, 837.
(192) Park, J.; Joo, J.; Kwon, S. G.; Jang, Y.; Hyeon, T. *Angew. Chemie Int. Ed.* **2007**, *46*, 4630.
(193) Jia, C.-J.; Schüth, F. *Phys. Chem. Chem. Phys.* **2011**, *13*, 2457.
(194) You, H.; Yang, S.; Ding, B.; Yang, H. *Chem. Soc. Rev.* **2013**, *42*, 2880.
(195) Guo, S.; Zhang, S.; Sun, S. *Angew. Chemie Int. Ed.* **2013**, *52*, 8526.
(196) An, K.; Somorjai, G. A. *ChemCatChem* **2012**, *4*, 1512.
(197) Gross, A. F.; Diehl, M. R.; Beverly, K. C.; Richman, E. K.; Tolbert, S. H. *J. Phys. Chem. B* **2003**, *107*, 5475.
(198) Hondow, N.; Fuller, R. O. *J. Colloid Interface Sci.* **2014**, *417*, 396.
(199) Zhu, J.; Zhao, T.; Kvande, I.; Chen, D.; Zhou, X.; Yuan, W. *Chinese J. Catal.* **2008**, *29*, 1145.
(200) Kvande, I.; Zhu, J.; Zhao, T.-J.; Hammer, N.; Rønning, M.; Raaen, S.; Walmsley, J. C.; Chen, D. *J. Phys. Chem. C* **2010**, *114*, 1752.

(201) Muthuswamy, N.; de la Fuente, J. L. G.; Ochal, P.; Giri, R.; Raaen, S.; Sunde, S.; Rønning, M.; Chen, D. *Phys. Chem. Chem. Phys.* **2013**, *15*, 3803.
(202) Kimura, K.; Einaga, H.; Teraoka, Y. *Catal. Today* **2011**, *164*, 88.
(203) Witte, P. T.; Berben, P. H.; Boland, S.; Boymans, E. H.; Vogt, D.; Geus, J. W.; Donkervoort, J. G. *Top. Catal.* **2012**, *55*, 505.
(204) Liu, Y.; Tsunoyama, H.; Akita, T.; Tsukuda, T. *J. Phys. Chem. C* **2009**, *113*, 13457.
(205) Villa, A.; Wang, D.; Su, D.; Veith, G. M.; Prati, L. *Phys. Chem. Chem. Phys.* **2010**, *12*, 2183.
(206) Mori, K.; Kumami, A.; Tomonari, M.; Yamashita, H. *J. Phys. Chem. C* **2009**, *113*, 16850.
(207) Lin, J.-H.; Guliants, V. V. *ChemCatChem* **2011**, *3*, 1426.
(208) Rinaldi, R.; Porcari, A. D. M.; Rocha, T. C. R.; Cassinelli, W. H.; Ribeiro, R. U.; Bueno, J. M. C.; Zanchet, D. *J. Mol. Catal. A Chem.* **2009**, *301*, 11.
(209) Fischer, N.; Minnermann, M.; Baeumer, M.; van Steen, E.; Claeys, M. *Catal. Letters* **2012**, *142*, 830.
(210) Martínez, A.; Prieto, G. *Catal. Commun.* **2007**, *8*, 1479.
(211) Mondloch, J. E.; Yan, X.; Finke, R. G. *J. Am. Chem. Soc.* **2009**, *131*, 6389.
(212) Watzky, M. A.; Finke, R. G. *J. Am. Chem. Soc.* **1997**, *119*, 10382.
(213) Mondloch, J. E.; Wang, Q.; Frenkel, A. I.; Finke, R. G. *J. Am. Chem. Soc.* **2010**, *132*, 9701.
(214) Mondloch, J. E.; Finke, R. G. *J. Am. Chem. Soc.* **2011**, *133*, 7744.
(215) Mondloch, J.; Finke, R. G. *ACS Catal.* **2012**, *2*, 298.
(216) Kent, P.; Mondloch, J.; Finke, R. G. *J. Am. Chem. Soc.* **2014**, *136*, 1930.
(217) Li, G.; Tang, Z. *Nanoscale* **2014**, *6*, 3995.
(218) Ma, Z.; Dai, S. *ACS Catal.* **2011**, *1*, 805.
(219) Stair, P. C. *Top. Catal.* **2012**, *55*, 93.
(220) Miikkulainen, V.; Leskelä, M.; Ritala, M.; Puurunen, R. L. *J. Appl. Phys.* **2013**, *113*, 021301.
(221) Molenbroek, a. M.; Haukka, S.; Clausen, B. S. *J. Phys. Chem. B* **1998**, *102*, 10680.
(222) Lashdaf, M.; Hatanpää, T.; Krause, A. O. I.; Lahtinen, J.; Lindblad, M.; Tiitta, M. *Appl. Catal. A Gen.* **2003**, *241*, 51.
(223) Lindblad, M.; Peter, L.; Suntola, T. *Catal. Letters* **1994**, *27*, 323.
(224) Backman, L. .; Rautiainen, a; Lindblad, M.; Krause, a. O. . *Appl. Catal. A Gen.* **2000**, *191*, 55.
(225) Backman, L. B.; Rautiainen, A.; Krause, A. O. I.; Lindblad, M. *Catal. Today* **1998**, *43*, 11.
(226) Haukka, S.; Lakomaa, E.; Suntola, T. *Appl. Surf. Sci.* **1994**, *75*, 220.
(227) Keränen, J.; Auroux, a; Ek, S.; Niinistö, L. *Appl. Catal. A Gen.* **2002**, *228*, 213.
(228) Backman, L. B.; Rautiainen, a.; Lindblad, M.; Krause, a. O. I. *Appl. Catal. A Gen.* **2009**, *360*, 183.
(229) Keranen, J.; Guimon, C.; Iiskola, E.; Auroux, A.; Niinisto, L. *J. Phys. Chem. B* **2003**, *107*, 10773.
(230) Kucheyev, S. O.; Biener, J.; Wang, Y. M.; Baumann, T. F.; Wu, K. J.; van Buuren, T.; Hamza, a. V.; Satcher, J. H.; Elam, J. W.; Pellin, M. J. *Appl. Phys. Lett.* **2005**, *86*, 083108.
(231) Kucheyev, S. O.; Biener, J.; Baumann, T. F.; Wang, Y. M.; Hamza, A. V; Li, Z.; Lee, D. K.; Gordon, R. G. *Langmuir* **2008**, *24*, 943.
(232) King, J. S.; Wittstock, A.; Biener, J.; Kucheyev, S. O.; Wang, Y. M.; Baumann, T. F.; Giri, S. K.; Hamza, A. V; Baeumer, M.; Bent, S. F. *Nano Lett.* **2008**, *8*, 2405.
(233) Feng, H.; Elam, J. W.; Libera, J. A.; Setthapun, W.; Stair, P. C. *Chem. Mater.* **2010**, *22*, 3133.
(234) Lu, J.; Stair, P. C. *Langmuir* **2010**, *26*, 16486.
(235) Goldstein, D. N.; George, S. M. *Appl. Phys. Lett.* **2009**, *95*, 143106.
(236) Setthapun, W.; Williams, W. D.; Kim, S. M.; Feng, H.; Elam, J. W.; Rabuffetti, F. A.; Poeppelmeier, K. R.; Stair, P. C.; Stach, E. A.; Ribeiro, F. H.; Miller, J. T.; Marshall, C. L. *J. Phys. Chem. C* **2010**, *114*, 9758.
(237) Li, J.; Liang, X.; King, D. M.; Jiang, Y.-B.; Weimer, A. W. *Appl. Catal. B Environ.* **2010**, *97*, 220.
(238) Christensen, S. T.; Feng, H.; Libera, J. L.; Guo, N.; Miller, J. T.; Stair, P. C.; Elam, J. W. *Nano Lett.* **2010**, *10*, 3047.
(239) Lei, Y.; Liu, B.; Lu, J.; Lobo-Lapidus, R. J.; Wu, T.; Feng, H.; Xia, X.; Mane, A. U.; Libera, J. a.; Greeley, J. P.; Miller, J. T.; Elam, J. W. *Chem. Mater.* **2012**, *24*, 3525.

(240) Cronauer, D. C.; Elam, J. W.; Kropf, A. J.; Marshall, C. L.; Gao, P.; Hopps, S.; Jacobs, G.; Davis, B. H. *Catal. Letters* **2012**, *142*, 698.
(241) Lu, J.; Stair, P. C. *Angew. Chemie Int. Ed.* **2010**, *49*, 2547.
(242) Feng, H.; Lu, J.; Stair, P. C.; Elam, J. W. *Catal. Letters* **2011**, *141*, 512.
(243) Lu, J.; Liu, B.; Greeley, J. P.; Feng, Z.; Libera, J. a.; Lei, Y.; Bedzyk, M. J.; Stair, P. C.; Elam, J. W. *Chem. Mater.* **2012**, *24*, 2047.
(244) Lu, J.; Fu, B.; Kung, M. C.; Xiao, G.; Elam, J. W.; Kung, H. H.; Stair, P. C. *Science.* **2012**, *335*, 1205.
(245) Fu, B.; Lu, J.; Stair, P. C.; Xiao, G.; Kung, M. C.; Kung, H. H. *J. Catal.* **2013**, *297*, 289.
(246) Ray, N. a.; Van Duyne, R. P.; Stair, P. C. *J. Phys. Chem. C* **2012**, *116*, 7748.
(247) Liang, X.; Li, J.; Yu, M.; McMurray, C. N.; Falconer, J. L.; Weimer, A. W. *ACS Catal.* **2011**, *1*, 1162.
(248) O'Neill, B. J.; Jackson, D. H. K.; Crisci, A. J.; Farberow, C. a; Shi, F.; Alba-Rubio, A. C.; Lu, J.; Dietrich, P. J.; Gu, X.; Marshall, C. L.; Stair, P. C.; Elam, J. W.; Miller, J. T.; Ribeiro, F. H.; Voyles, P. M.; Greeley, J.; Mavrikakis, M.; Scott, S. L.; Kuech, T. F.; Dumesic, J. a. *Angew. Chem. Int. Ed. Engl.* **2013**, *52*, 13808.
(249) Alba-Rubio, A. C.; O'Neill, B. J.; Shi, F.; Akatay, C.; Canlas, C.; Li, T.; Winans, R.; Elam, J. W.; Stach, E. a.; Voyles, P. M.; Dumesic, J. a. *ACS Catal.* **2014**, *4*, 1554.
(250) Pagán-Torres, Y. J.; Gallo, J. M. R.; Wang, D.; Pham, H. N.; Libera, J. a.; Marshall, C. L.; Elam, J. W.; Datye, A. K.; Dumesic, J. a. *ACS Catal.* **2011**, *1*, 1234.
(251) Scott, I. D.; Jung, Y. S.; Cavanagh, A. S.; Yan, Y.; Dillon, A. C.; George, S. M.; Lee, S.-H. *Nano Lett.* **2011**, *11*, 414.
(252) Calderone, V. R.; Shiju, N. R.; Curulla-Ferré, D.; Chambrey, S.; Khodakov, A. Y.; Rose, A.; Thiessen, J.; Jess, A.; Rothenberg, G. *Angew. Chemie Int. Ed.* **2013**, *52*, 4397.
(253) Filez, M.; Poelman, H.; Ramachandran, R. K.; Dendooven, J.; Devloo-Casier, K.; Fonda, E.; Detavernier, C.; Marin, G. B. *Catal. Today* **2014**, *229*, 2.
(254) Evans, J. E.; Jungjohann, K. L.; Browning, N. D.; Arslan, I. *Nano Lett.* **2011**, *11*, 2809.
(255) Zečević, J.; de Jong, K. P.; de Jongh, P. E. *Curr. Opin. Solid State Mater. Sci.* **2013**, *17*, 115.
(256) Sterrer, M.; Freund, H.-J. *Catal. Letters* **2013**, *143*, 375.
(257) Xu, Y.; Yang, J.; Demura, M.; Hara, T.; Hirano, T.; Matsushita, Y.; Tanaka, M.; Katsuya, Y. *Appl. Catal. A Gen.* **2014**, *478*, 165.
(258) Park, C.; Fenter, P.; Sturchio, N.; Regalbuto, J. *Phys. Rev. Lett.* **2005**, *94*, 076104.
(259) Blanchard, J.; Hervier, A.; Costentin, G.; Regalbuto, J.; Louis, C.; Boujday, S. *Catal. Today* **2014**.
(260) Hervier, A.; Blanchard, J.; Costentin, G.; Regalbuto, J.; Louis, C.; Boujday, S. *Chem. Commun.* **2014**, *50*, 2409.
(261) Thüne, P. C.; Weststrate, C. J.; Moodley, P.; Saib, a. M.; van de Loosdrecht, J.; Miller, J. T.; Niemantsverdriet, J. W. *Catal. Sci. Technol.* **2011**, *1*, 689.
(262) Prieto, G.; Shakeri, M.; de Jong, K. P.; de Jongh, P. E. *ACS Nano* **2014**, *8*, 2522.

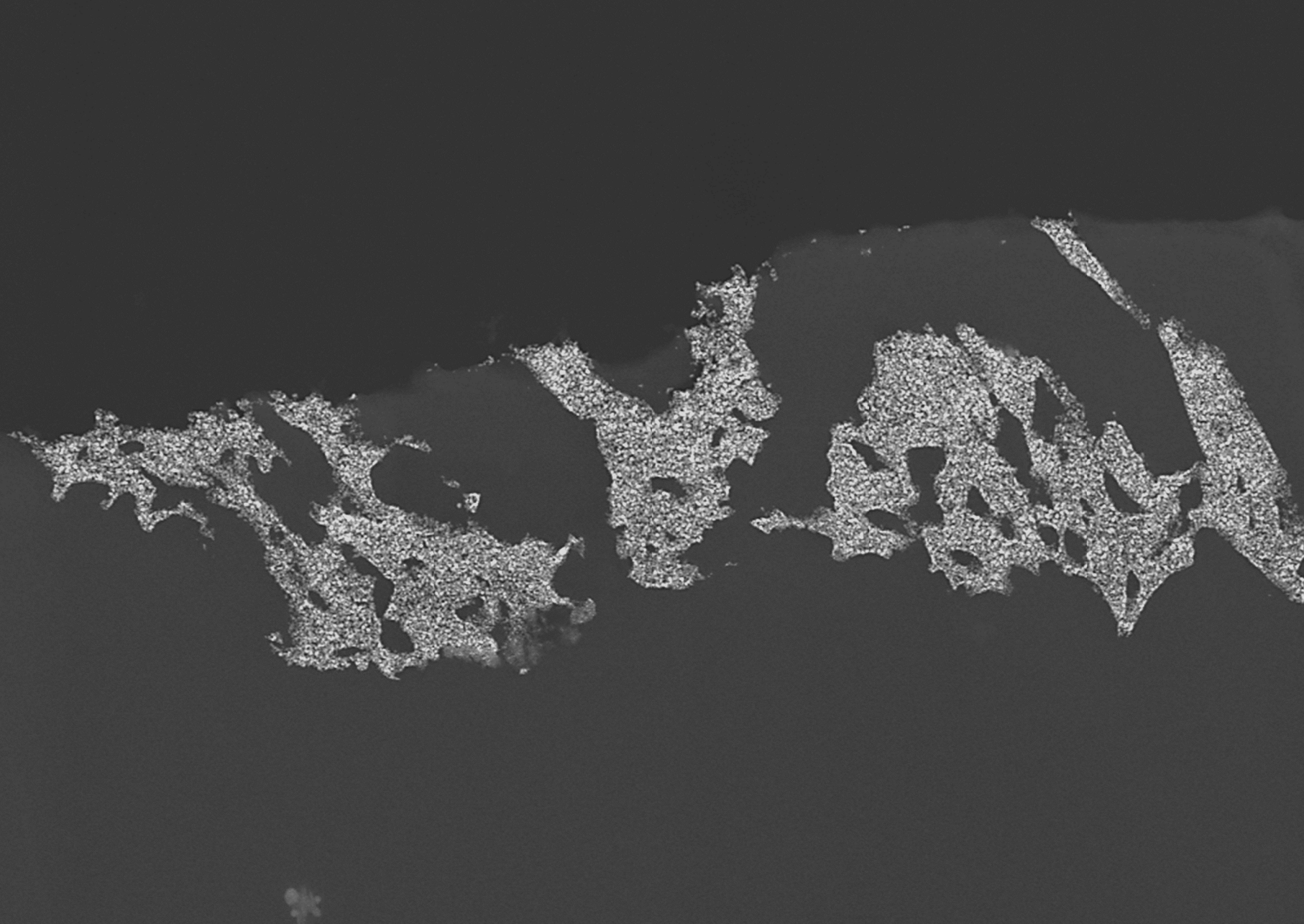

Chapter 3

Freeze-Drying for Controlled Nanoparticle Distribution in Co/SiO_2 Fischer-Tropsch Catalysts

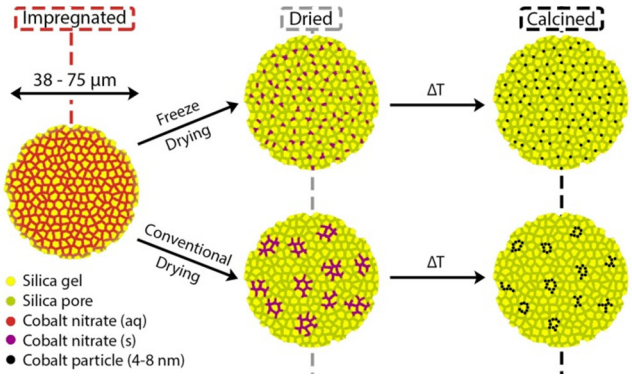

Controlling the nanoparticle distribution over a support is considered essential to arrive at more stable catalysts. By developing a novel freeze-drying method, the nanoparticle distribution was successfully manipulated for the preparation of Co/SiO_2 Fischer-Tropsch catalysts using a commercial silica-gel support. After loading the precursor via a solution impregnation or melt infiltration, differential scanning calorimetry was used to study the phase behavior of the confined cobalt nitrate precursor phases to ascertain suitable freeze-drying conditions. When a conventional drying treatment was utilized, catalysts showed inhomogeneous cobalt distributions, with 8 nm nanoparticles grouped in aggregates of up to 400 nm. In contrast, by utilizing freeze-drying starting at liquid nitrogen temperatures, homogeneous distributions of 4 to 6 nm nanoparticles were obtained. Raising the temperature at which the freeze drying process takes place resulted in either uniform or strongly non-uniform nanoparticle distributions across the catalyst support grains, depending on the specific conditions and precursor loading method. After reduction, all catalysts showed high activity for the Fischer-Tropsch reaction at 1 bar. The effective immobilization of freeze-drying emphasizes the importance of the drying step during the synthesis of supported catalysts.

Adapted with permission from: P. Munnik et al. *J. Catal.* **2013**, *297*, 306.
P. Munnik and T. M. Eggenhuisen contributed equally to this chapter therefore it is part of both PhD Theses.

INTRODUCTION

Migration and coalescence of nanoparticles is an irreversible deactivation pathway with detrimental effects on the activity and life time of supported catalysts.[1,2] Many innovative pathways have been developed to improve the stability of heterogeneous catalysts, such as encapsulation by a metal oxide shell around colloidal nanoparticles[3,4] or by a porous metal oxide layer covering supported nanoparticles,[5] and restriction of nanoparticle mobility by using cage-like support materials[6] or by alloying with a metal with a higher melting point.[7] Nevertheless, for supported nanoparticles maximizing nearest neighbor distances or, in other words, achieving a uniform nanoparticle distribution is essential to improve catalytic stability. Indeed, non-uniform nanoparticle distributions have been observed in many metal-support systems and showed to be prone to sintering.[8,9] On the other hand, a non-uniform distribution of the active phase over micrometers or even millimeters in macroscopic catalyst bodies may be preferred depending on the catalysis conditions.[10] For example, deposition of the active phase in the outer rim of a macroscopic support body, a so-called egg-shell configuration, is favorable for fast reactions combined with diffusion constrictions of substrates and products.[11] Therefore, active control over metal or metal oxide nanoparticle distribution on a support on different lengths scales is crucial to the rational synthesis of supported catalysts.

Impregnation and drying is a convenient catalyst preparation method and is commonly applied in industry and academia. With the use of highly soluble transition metal nitrate salts, waste streams are low and high metal loadings can be obtained in a single impregnation step. Nevertheless, controlling dispersion and distribution by this synthesis route has remained challenging.[12-15] Especially at high metal loadings[16] and low support-salt interactions,[17] agglomeration of nanoparticles after calcination is difficult to prevent. Drying has been recognized as a major influence on the distribution of the active phase over macroscopic bodies.[18-20] Although alternatives have been developed,[21-24] a method preserving the advantages of impregnation and drying is desirable. In this chapter, we will explore in detail the potential of freeze-drying for controlled nanoparticle distribution on an industrially relevant silica-gel support for the preparation of Co/SiO_2 Fischer-Tropsch catalysts.

Freeze-drying is a drying method often encountered in food-processing[25,26] as well as in the pharmaceutical industry,[27-29] usually for preservation purposes. By freeze-drying a solvent can be removed without exposing the matrix to tensile forces of a receding meniscus. Therefore, it is a suitable drying technique for the cryo-preservation of biological tissues[30,31] or to develop porous aerogels based on soft templates from polymeric materials.[32,33] For catalyst preparation, freeze-drying has been suggested to reduce precursor solution mobility during drying and therefore control the location of deposition of the precursor phase. Nevertheless, few applications have been reported.[34-37]

Freeze-drying generally consists of three steps: freezing, primary drying and secondary drying.[38,39] Freeze-drying processes for complex solutions most often result from experimentally based considerations and seems an art rather than a science.[40] Freezing is actually the most

important step, as it determines the ice crystalline structure, which is affected by the cooling rate, degree of supercooling and annealing.[41-43] During primary drying, ice sublimates due to the reduced pressure. The rate depends on the heat transfer determined mainly by the ice structure, pressure and temperature.[44] However, several experimental details have a large influence on this step, even the sample vial configuration.[45] Finally, non-freezing or amorphous water can be removed in the secondary drying step, during which the temperature is raised under reduced pressure.[46]

Due to its long history and industrial relevance, literature on freeze-drying of (bio)pharmaceutical formulations and food is extensive. In this chapter we aim to obtain the first fundamental insight into freeze-drying for the preparation of Co/SiO_2 Fischer-Tropsch catalysts. To develop a suitable freeze-drying method, The phase behavior of $Co(NO_3)_2$ (aq) solution and $Co(NO_3)_2{\cdot}6H_2O$ salt confined within a mesoporous silica matrix was studied with DSC. The phases present after freeze-drying were identified and compared to those resulting from conventional drying treatments. Detailed assessment of the distribution of the cobalt oxide nanoparticles after decomposition of the nitrates was done using ultramicrotomy and TEM. The fundamental insights on precursor phase behavior combined with freeze-drying led to control over the nanoparticle distribution on an industrially relevant silica gel support, emphasizing the importance of the drying step during catalyst preparation.

EXPERIMENTAL

Catalyst Synthesis. Co/SiO_2 catalysts were prepared using a commercially available silica gel as support (Davicat 1404, Grace-Davidson). The support was sieved to a grain size of 38 - 75 μm and the porous properties were characterized with N_2-physisorption at -196 °C (Tristar 3000, Micromeritics): V_p = 0.87 cm^3/g, S_{BET} = 443 m^2/g, d_p = 8 nm. Solution impregnation (SI) was performed to incipient wetness using a saturated $Co(NO_3)_2$ (aq) solution (4.2 M, $Co(NO_3)_2{\cdot}6H_2O$, >99% Sigma-Aldrich), leading to a nominal cobalt metal loading of 17 wt.%. For melt infiltration (MI), for example, 929 mg of $Co(NO_3)_2{\cdot}6H_2O$ and 754 mg of SiO_2-gel were physically mixed in a mortar with a pestle. The physical mixture was then heated overnight at 60 °C in a Teflon-lined steel autoclave (~6 mL). A nominal cobalt metal loading of 20 wt.% was obtained.

Different drying treatments were applied to the as-prepared SiO_2-SI and SiO_2-MI precursor loaded catalysts. Conventional drying (CD) for SiO_2-SI was performed in a crucible in a preheated muffle oven at 60 °C overnight, after which the sample was handled under ambient conditions. Melt infiltrated samples were used as-prepared. Freeze-drying (FD) was performed using a Sublimator 400 Freeze-dryer (Zirbus) and using the conditions summarized in Table 3.1. Samples were freeze-dried in 2 mL glass vials. The two freeze-drying procedures are denoted by their freezing temperature and the shelf temperature during the primary drying step. In the method FD(-45/-30), samples were frozen on the shelf by cooling to -45 °C (1 °C/min, 5 hours). Primary drying was started by reducing the chamber pressure, after which the shelf temperature was increased to -30 °C. For FD(LN_2/-45), quench freezing with liquid

N_2 was applied. The glass vials containing the samples were cooled down in a reservoir containing liquid nitrogen, after which the reservoir was placed on the precooled shelf at -45 °C in the freeze-dryer. Subsequently, the chamber pressure was reduced to start the primary drying step. Both methods included secondary drying by step-wise heating to 20 °C under reduced pressure. The condenser temperature was between -65 and -70 °C and the condenser chamber pressure was 0.02-0.03 mbar.

Calcination of all precursor loaded catalysts was performed by heating to 350 °C (1 °C/min, 1 hour) in a flow of N_2 or 1% v/v NO/N_2 at a gas hourly space velocity (GHSV) of 30000 h^{-1}. Freeze-dried pre-catalysts were transferred under dry nitrogen atmosphere to a fluidized-bed reactor.

Table 3.1. Summary of experimental freeze-drying conditions.

	FD(-45/-30)	FD(LN_2/-45)
Freezing temperature (time)	-45 °C (5 h)	~ -170 °C (15 min)
Shelf temperature primary drying (time)	-30 °C (82 h)	-45 °C (48 h)
Primary drying pressure	0.02 - 0.03 mbar	0.02 - 0.03 mbar
Shelf temperature secondary drying (time)	-10 °C (3 h), 20 °C	-30 °C (12 h), -15 °C (12 h), 20 °C
Secondary drying pressure	< 0.02 mbar	< 0.02 mbar

Catalyst Characterization. The phase behavior of cobalt nitrate present during the different stages of catalyst preparation was analyzed using differential scanning calorimetry (DSC, Q2000, TA Instruments). The temperature and heat flow were calibrated with a certified indium sample and measurements were performed with hermetically sealed aluminum pans (~40 µL, Tzero, TA Instruments) under a flow of N_2 (50 mL/min). Sample masses were typically between 5 - 15 mg and heat flows were recorded between -90 °C and 75 °C at a rate of 1 °C/min.

Thermogravimetric analysis (TGA, Q50 TA Instruments) was used to determine the residual water after different drying treatments by measuring the weight loss after heating to 500 °C for 30 min, at a heating rate 10 °C/min and an N_2 flow of 60 mL/min. The weight loss was corrected for the loss of water by condensation of silanol groups from the pristine silica gel, which was experimentally found to occur between 150 °C and 500 °C. Thus, the rest of the weight loss could be attributed to the loss of any residual water and the decomposition of $Co(NO_3)_2$ to Co_3O_4. The amount of residual water was calculated in moles H_2O/mole Co from the resulting corrected weight loss (m_{loss}).

Diffuse Reflectance Spectroscopy (DRS) was used to obtain the UV/VIS absorption spectra of dried samples. Measurements were obtained on a Varian Cary 500

spectrophotometer from 800 to 250 nm in diffuse reflectance mode. Samples were held in an air tight sample holder with a quartz window to prevent rehydration during measurements.

XRD patterns were recorded between 30 and 60 °2θ with a Bruker-AXS D2 Phaser X-ray Diffractometer using Co-$K_{\alpha 12}$ radiation (λ = 1.790 Å). The volume averaged Co_3O_4 crystallite size was determined using the Scherrer equation with a shape factor k = 0.9 and line broadening analysis on the (220), (311) and (400) peaks by a fitting procedure in Eva2 software (Bruker AXS).

The calined catalyst grains were embedded in a two component epoxy resin (Epofix, EMS) and cured at 60 °C overnight. The embedded catalysts were then cut into thin sections with a nominal thickness of 50 nm using a Diatome Ultra 35° diamond knife mounted on a Reichert-Jung Ultracut E microtome and collected on a TEM grid. Bright field TEM images were obtained on a Tecnai 12, operated at 120 keV. High angle annular dark field (HAAFD) STEM was performed on a Tecnai 20 equipped with a field emission gun and operated at 200 keV.

Catalytic Testing. Fischer-Tropsch synthesis was performed at 220 °C and 1 bar with a H_2/CO ratio of 2 v/v. Typically, a plug-flow reactor was loaded with 10 mg of catalyst diluted with 200 mg SiC (200 µm). The catalysts were reduced *in-situ* at 500 °C for 2 h (heating rate 5 °C/min) under a flow or H_2/Ar (20/40 mL/min). C_1-C_{15} products were analyzed by online gas chromatography (Varian 430 GC, CP sil-5). The catalytic activity, expressed as cobalt-time-yield (10^{-5} $mol_{CO}/g_{Co}/s$) and C_1/C_{5+} selectivity, expressed in wt.%, were determined after 20 h reaction time and a CO conversion of 2%.

RESULTS AND DISCUSSION

Freeze-Drying Methods. To develop suitable freeze-drying methods, the phase behavior of cobalt nitrate confined in the mesoporous silica gel support was studied with differential scanning calorimetry (DSC). Figure 3.1 shows the freezing and melting behavior observed for silica gel after solution impregnation (SI) with $Co(NO_3)_2$ (aq) and after melt infiltration (MI) with $Co(NO_3)_2{\cdot}6H_2O$. Different freezing and melting point depressions were observed for the confined cobalt nitrate solution and for the cobalt nitrate salt. For SiO_2-MI, a single freezing and a single melting event were detected, indicating a uniform composition and structure of the confined salt. Bulk $Co(NO_3)_2{\cdot}6H_2O$ melts at 55 °C, therefore, the confinement in the silica matrix caused a melting point depression of 35 °C. The solution impregnated on silica gel displayed more complex phase behavior with several crystallization and melting events. A saturated aqueous $Co(NO_3)_2$ solution melts at -31 °C. Therefore, the broad melting peak with a maximum at -35 °C was ascribed to residual extraporous solution. The melting peak with maximum at -54 °C was tentatively attributed to the confined solution, which would correspond to a melting point depression of 23 °C. The melting peak at 10 °C as well as the freezing peak at -30 °C were tentatively ascribed to melting and freezing of confined $Co(NO_3)_2{\cdot}6H_2O$, indicating that some phase separation of the solution occurred inside the pore system. The amount of water present in the sample has a huge impact on the absolute

freezing and melting point; comparing SI and MI shows a 55 °C difference which will be important for subsequent drying treatments.

Two freeze-drying conditions can be deduced from the DSC thermograms. Firstly, the closed arrows in Figure 3.1 indicate the minimum freezing temperature to solidify all cobalt nitrate. For SiO_2-SI, exotherm peaks are observed at -62 °C and -75 °C indicating that a freezing temperature of at least -85 °C is needed, while for SiO_2-MI -30 °C would suffice as freezing temperature. Second, the sample temperature during drying should not exceed the onset at which the precursor begins to melt. Therefore, as indicated by the open arrows, freeze-drying conditions should be chosen such that SiO_2-SI remains below -65 °C and SiO_2-MI below -10 °C.

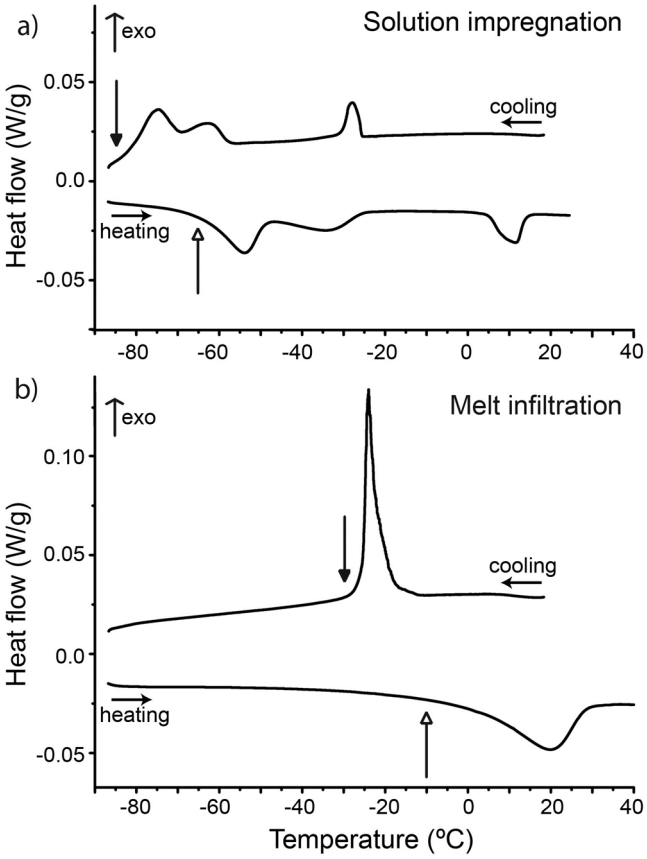

Figure 3.1. DSC thermograms recorded for precursor loaded silica gel prepared via (a) solution impregnation (SI) with $Co(NO_3)_2$ (aq) or (b) melt infiltration (MI) with $Co(NO_3)_2 \cdot 6H_2O$. Closed arrows indicate minimum freezing temperature, open arrows indicate maximum sample temperature during freeze-drying. Thermograms are offset for clarity.

Based on the results from DSC, two freeze-drying methods were developed within the boundaries set by experimental equipment. The first method, denoted by FD(LN_2/-45) involved quench freezing by liquid nitrogen, which should solidify both the confined cobalt nitrate solution (SI) as well as the salt (MI). Samples were then placed on a precooled shelf at -45 °C for the primary drying step. In the second freeze-drying method, FD(-45/-30) a higher freezing temperature (-45 °C) and a higher shelf temperature during primary drying (-30 °C)

were applied. By this method, the confined cobalt nitrate solution will not freeze, but the cobalt nitrate salt will. In both methods, the pressure range during primary drying was 0.02-0.03 mbar, which corresponds to an ice (I_h) equilibrium temperature of -55 °C to -53 °C. This temperature is low enough during primary drying in both methods to keep SiO_2-MI frozen. However, for SiO_2-SI the DSC data suggests this temperature is too high, and thus this sample will only remain frozen in FD(LN_2/-45) by self-cooling at sufficiently high freeze-drying rates. While it was not possible to measure the actual drying rate, an indirect indication is the resulting cobalt distribution over the support. A homogeneous distribution will indicate the drying rate was sufficiently high to keep the sample frozen, while an inhomogeneous distribution will indicate mobility of the precursor. In both methods, the heat for sublimation is provided by the shelf temperature, while the actual sample temperature is dependent on the rate of freeze-drying, the structure of the ice, the chamber pressure and the condenser temperature (see Table 3.1 for experimental details). Thus, the mobility of the precursor phase is expected to be restricted by FD(LN_2/-45) for both SiO_2-SI and SiO_2-MI. With FD(-45/-30), precursor immobilization is expected for SiO_2-MI, while for SiO_2-SI mobility of the solution is likely.

Precursor Phase after Drying. TGA, DSC and UV/VIS were measured after drying and the results are summarized in Table 3.2. The conventional drying was performed in a muffle oven to simulate the static nature of the freeze dryer. The drying was performed at 60 °C to prevent preliminary decomposition of the precursor. The residual water was quantified using TGA analysis. After conventional drying, 6 to 8 moles of H_2O per mole of cobalt remained. The samples were handled under ambient air conditions, and therefore rehydration of the salt could have occurred. Indeed, for SI-CD a sample transferred directly from the muffle oven at 60 °C to the drybox contained only 5 residual water molecules per mole of Co. Thus, some re-adsorption had occurred due to the hydrophilic nature of cobalt nitrate. However, this did not affect the final metal distributions as was observed with TEM. After melt infiltration, the water to cobalt ratio was slightly higher than for the $Co(NO_3)_2{\cdot}6H_2O$ from stock. This is partly due to the presence of physisorbed water in the silica gel, as the support was not dried prior to melt infiltration. After both freeze-drying treatments, water contents below 1 H_2O/Co were found in each case. Clearly, the different hydration states of cobalt nitrate depended on the drying method. This was also clearly observed in the derivative weight change profiles during decomposition, as shown in Figure 3.2. For Si-CD, decomposition occurred in two steps: dehydration and decomposition of the nitrate, as reported previously.[47] For the samples obtained after freeze-drying, dehydration was virtually absent and decomposition occurred in a single step.

Further information on the precursor phase after drying was deduced from the phase behavior observed with DSC. Figure 3.3 shows the melting behavior of the precursor loaded silica gel after the different drying treatments. SI-CD and MI showed a single melting peak at 20 °C, which has been ascribed to confined cobalt nitrate hexahydrate before.[48] Thus, both SI-CD and MI resulted in confined, liquid cobalt nitrate hexahydrate salt at room temperature.

No melting transitions were observed after freeze-drying. The hydration state was also studied by UV/VIS spectroscopy, as after conventional drying both SI and MI samples were pink, while after freeze-drying they had turned purple. Indeed, the main UV/VIS absorption band shifted from 510 nm, which corresponds to octahedral cobalt nitrate hexahydrate, to 540 nm for freeze-dried samples (Table 3.2). This suggests exchange of H_2O ligands for NO_3^- or a surface hydroxyl group, which both have a smaller ligand-field splitting parameter and therefore cause a shift of the absorption to lower energy.[49]

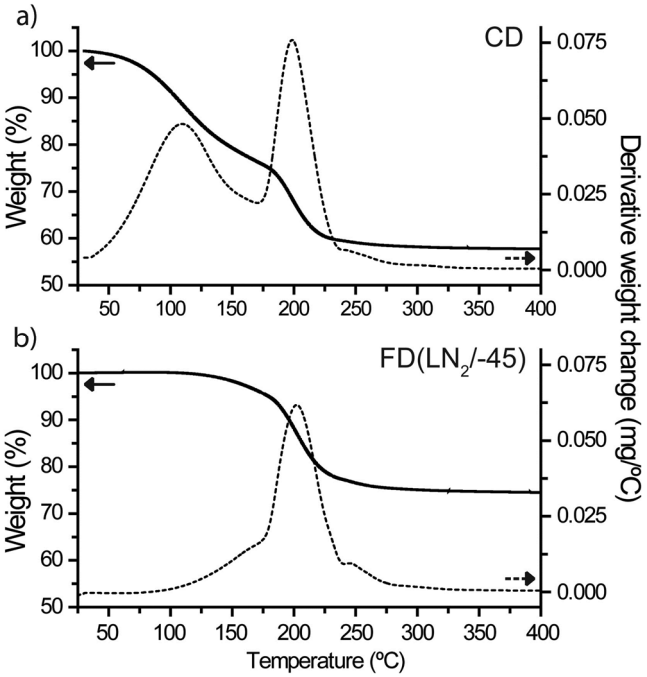

Figure 3.2. Weight loss determined with TGA for precursor loaded silica gel prepared via solution impregnation (SI) with $Co(NO_3)_2$ (aq). (a) After conventional drying at 60 °C (CD) and (b) after freeze-drying ($FD(LN_2/-45)$).

Table 3.2. Hydration state of precursor loaded silica gel prepared via solution impregnation (SI) with $Co(NO_3)_2$ (aq) and melt infiltration (MI) with $Co(NO_3)_2{\cdot}6H_2O$ after conventional drying (CD) or freeze-drying (FD).

Precursor loading	Drying method	Residual water[a] (moles H_2O /mole Co)	DSC melting peak maximum[b] (°C)	UV-VIS absorption maximum (nm)
SI	CD	6.5	19	514
SI	FD(-45/-30)	0.1	none	540
SI	$FD(LN_2/-45)$	0.7	none	538
MI	none	7.8	20	510
MI	FD(-45/-30)	0.9	none	539
MI	$FD(LN_2/-45)$	0.7	none	542

[a] determined by TGA, [b] maximum of melting point

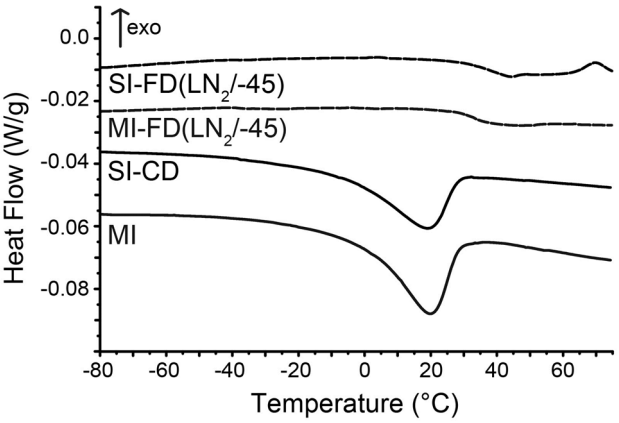

Figure 3.3. DSC thermograms recorded for precursor loaded silica gel prepared via solution impregnation (SI) with $Co(NO_3)_2$ (aq) and melt infiltration (MI) with $Co(NO_3)_2{\cdot}6H_2O$ after conventional drying at 60 °C (CD) and after freeze-drying (FD(LN_2/-45)).

Macroscopic Distribution. The effect of the drying method on the cobalt oxide distribution after calcination was imaged by TEM. Preparation of 50 nm thick slices by ultramicrotomy allowed detailed TEM analysis of nanoparticle size and distribution over the support. First, the macroscopic distribution of Co_3O_4 over the silica gel grains is discussed, while the next section addresses the dispersion and distribution of individual Co_3O_4 nanoparticles on the nanometer scale.

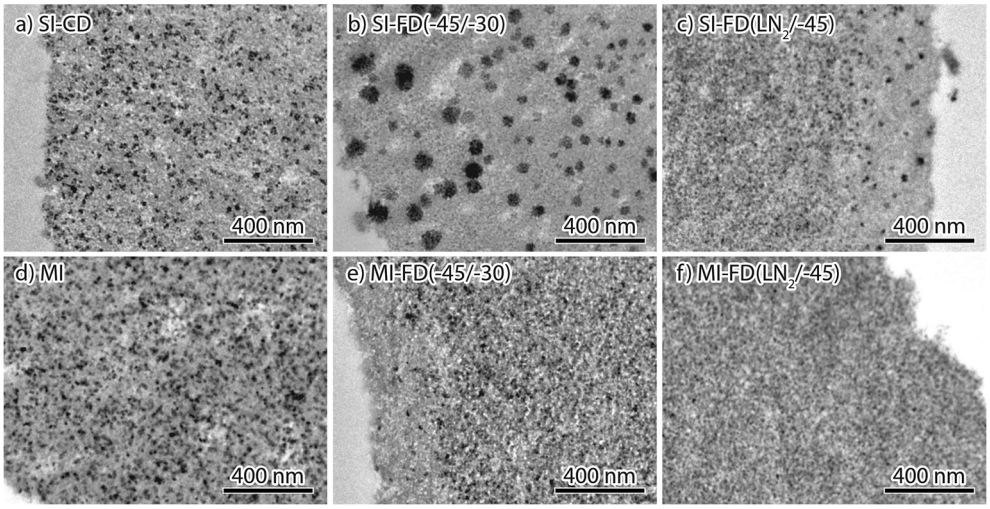

Figure 3.4. TEM micrographs of ultramicrotomed slices of Co_3O_4/SiO_2 prepared via different drying treatments followed by calcination in a flow of N_2 prepared via solution impregnation (SI, top row) or melt infiltration (MI, bottom row) and conventional drying (left column, CD), freeze-drying (middle column, FD(-45/-30)) and freeze-drying (right column, FD(LN_2/-45)).

Figure 3.4 shows micrographs recorded for catalysts prepared by different drying treatments followed by calcination in a flow of N_2. In most cases aggregates were observed with

sizes ranging from 10 to 40 nm. Note that the aggregates appeared to consist of a (large) number of individual nanoparticles of about 8 nm in size (vide infra). Three types of cobalt oxide distributions over the support grains were identified. After conventional treatment of both SI and MI (Figure 3.4a and d), 40 nm clusters were distributed homogeneously over the whole support. Second, freeze-drying by liquid nitrogen freezing (Figure 3.4c and f) as well as FD(-45/-30) for MI (Figure 3.4e) led to a homogeneous distribution of very small Co_3O_4 aggregates below 20 nm. Last, by solution impregnation and FD(-45/-30) shown in Figure 3.4b, aggregates up to 140 nm were observed. Surprisingly, an egg-shell configuration was apparent for this catalyst at lower magnification and cobalt aggregates were only observed in the 5 µm outer rim, while the body of the support grain was mostly empty (Figure 3.5). Thus, FD(-45/-30) caused extensive redistribution of the cobalt nitrate solution to the surface of the macroscopic support grain, while for the sample melt infiltrated with $Co(NO_3)_2{\cdot}6H_2O$ this drying method led to a homogeneous distribution after calcination.

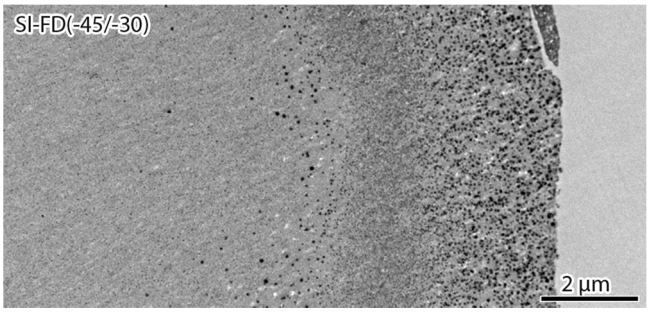

Figure 3.5. TEM micrograph of ultramicrotomed slice of Co_3O_4/SiO_2 prepared via solution impregnation (SI) and freeze-drying (FD(-45/-30)) followed by calcination in a flow of N_2.

The different distributions are attributed to the mobility of the precursor and the rate of drying. During conventional drying at 60 °C, the precursor is liquid (either in solute state or molten) allowing for mobility and redistribution, resulting in an inhomogeneous distribution. However, the drying rate at this temperature will be relatively high, limiting the timespan in which redistribution occurs and causing limited agglomeration. For SI-FD(-45/-30), a similar principle holds: if the precursor is not frozen mobility is expected. However, the drying rate will be relatively low due to the low vapor pressure, and redistribution can occur over a substantially longer period of time. We tentatively propose that due to the low support-precursor interactions and low drying rate, the precursor moved towards a drying front at the surface of the support grain, resulting in an egg-shell distribution. For SI-FD(LN_2/-45), a homogeneous distribution was observed throughout the particle. This confirms that the precursor was completely immobilized during freezing, and that the drying rate was sufficiently high to keep the precursor frozen. The MI samples respond in a similar way to the drying procedures. However, the infiltrated cobalt nitrate hexahydrate of the MI samples has a higher freezing and melting point than the SI samples. Therefore, in the case of MI-FD(-45/-30) a temperature of -45 °C was enough to solidify and thereby immobilize the precursor, preventing redistribution.

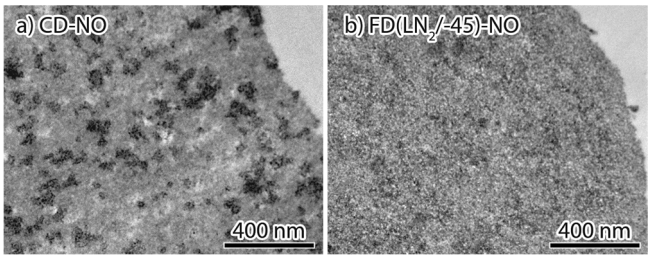

Figure 3.6. TEM micrographs of ultramicrotomed slices of Co_3O_4/SiO_2 prepared via solution impregnation (SI) and different drying treatments followed by calcination in a flow of 1% NO/N_2: (a) conventional drying (CD) or (b) freeze-drying ($FD(LN_2/-45)$).

By calcination in a flow of N_2, mobility of cobalt during decomposition is expected.[50] By the addition of 1% v/v NO during calcination, aggregation is mostly prevented during decomposition of hydrated transition metal nitrates.[13,51] Here NO calcination was applied to confirm the footprint of the salt distribution obtained after different drying treatments. TEM showed that the Co_3O_4 aggregate distribution followed the same general trend as was observed after calcination in N_2 flow. Both SI and MI resulted in similar cobalt oxide aggregate distributions after conventional drying or very homogeneous distributions after freeze-drying starting at liquid nitrogen temperatures. By FD(-45/-30), solution impregnation again led to an egg-shell configuration, while melt infiltration resulted in a homogeneous distribution. This similarity shows that the cobalt distribution on the macroscale was mainly determined by the precursor phase distribution after drying. Only the aggregate sizes after conventional drying differ; Figure 3.6a shows aggregates obtained after NO calcination can be substantially larger compared to those obtained after calcination in an N_2 flow, however this is in line with previous results.[52,53] Regardless, it is clear that after conventional drying the cobalt distribution is very inhomogeneous. In contrast, freeze-drying starting at liquid nitrogen temperatures (Figure 3.6b) again led to a homogeneous distribution of cobalt oxide.

Table 3.3. Average crystallite size determined with XRD and average particle size determined with HAADF STEM for catalysts after calcination in a flow of N_2 or a flow of 1% NO/N_2, prepared via solution impregnation (SI) with $Co(NO_3)_2$ (aq) and melt infiltration (MI) with $Co(NO_3)_2{\cdot}6H_2O$ and conventional drying at 60 °C (CD) or after freeze-drying (FD).

Catalyst Preparation	Calcination in N_2		Calcination in 1% NO/N_2	
	d_{XRD} (nm)	d_{TEM} (nm)	d_{XRD} (nm)	d_{TEM} (nm)
Co_3O_4/SiO_2-SI-CD	8.0	7.9 ± 1.9	5.4	6.4 ± 1.7
Co_3O_4/SiO_2-SI-FD(-45/-30)	7.9	7.4 ± 1.8	4.7	5.5 ± 1.5
Co_3O_4/SiO_2-SI-FD(LN_2/-45)	7.8	6.6 ± 1.5	4.4	4.2 ± 0.8
Co_3O_4/SiO_2-MI	7.9	6.8 ± 1.5	6.2	6.0 ± 1.3
Co_3O_4/SiO_2-MI-FD(-45/-30)	7.9	7.3 ± 1.5	6.0	5.0 ± 1.1
Co_3O_4/SiO_2-MI-FD(LN_2/-45)	7.9	6.8 ± 1.4	4.2	4.6 ± 1.1

Nanoscale Distribution. For a more detailed analysis of the nanoparticle size and local distribution, micrographs at higher magnifications are shown in Figure 3.7 for catalysts prepared by solution impregnation. In this case, the cobalt nanoparticles were imaged in dark field mode, and appear as light spots on the darker background of the silica matrix. Furthermore, Table 3.3 shows the results for average crystallite size as determined by XRD and average particle size from analysis of high angle annular dark field (HAADF) STEM images. After calcination in a flow of N_2, SI-CD led to the formation of 10-40 nm large aggregates as can be seen in Figure 3.7a. However, the aggregates appeared to consist 8 nm nanoparticles, which corresponded to the average crystallite size from XRD. After calcination in 1% NO/N_2, larger aggregates up to 400 nm were formed by SI-CD (Figure 3.6b). However, in Figure 3.7c it is clear that the large aggregates consisted of smaller, 6 nm individual nanoparticles. By freeze-drying (Figure 3.7b and d), nanoparticles were found distributed uniformly over the support. Furthermore, by both calcination methods smaller Co_3O_4 nanoparticles formed after freeze-drying, i.e. 7 nm by N_2 calcination and 4 nm by NO calcination.

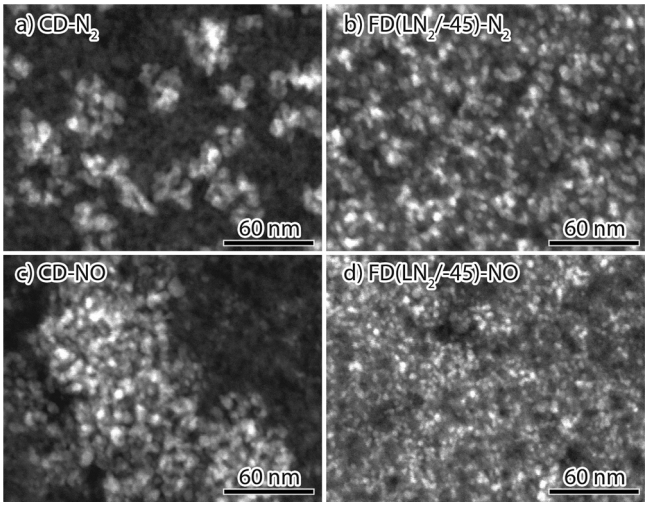

Figure 3.7. HAADF-STEM micrographs of ultramicrotomed slices of Co_3O_4/SiO_2 prepared via solution impregnation (SI) and conventional drying (left column) or freeze-drying (right column) followed by calcination in a flow of N_2 (top row) or a flow of 1% NO/N_2 (bottom row): (a) CD-N_2, (b) FD(LN_2/-45)-N_2, (c) CD-NO, (d) FD(LN_2/-45)-NO.

Fischer-Tropsch Catalysis. The Co_3O_4/SiO_2 catalysts prepared by different drying methods were tested for the Fischer-Tropsch synthesis. Table 3.4 shows the results of the catalytic tests at 1 bar and 2% conversion. The catalysts prepared by calcination in N_2 were activated by reduction at 450 °C. The smaller particles obtained after calcination in NO/N_2 were reduced at 550 °C, as these are more difficult to reduce than larger particles.[54,55] They showed catalytic activities comparable to earlier reported highly active catalysts treated at the same reduction temperature.[55] The N_2 calcined catalysts exhibited a slightly lower Fischer-Tropsch activity, which is ascribed to the larger Co_3O_4 nanoparticle size.[56] The freeze-dried catalysts showed slightly higher activity as compared to the catalysts prepared by conventional drying. This indicates that the cobalt oxides formed after calcination and different drying treatments had similar reducibility and excludes the formation of large amounts of cobalt

(hydro)silicates. Due to the mild reaction conditions catalyst deactivation during reaction was not significant. Therefore, industrially relevant reaction conditions, i.e. pressures of 20 bar and high conversions should be applied to study the effect of the Co_3O_4 nanoparticle distribution on deactivation by sintering.

Table 3.4. Catalytic activity for the Fischer-Tropsch synthesis at 220 °C and 1 bar of various catalysts prepared by solution impregnation (SI) and conventional drying (CD) or freeze-drying (FD) and calcination in different gas flows.

Catalyst Preparation	Calcination atmosphere	Reduction temperature (°C)	CTY[a,b] (10^{-5} $mol_{CO}/g_{Co}/s$)	C_1[a,c] (wt.%)	C_{5+}[a,c] (wt.%)
SI-CD	N_2	450	3.70	19.9	51.5
SI-FD(LN_2/-45)	N_2	450	4.09	23.0	44.9
SI-CD	NO/N_2	550	5.20	20.9	49.9
SI-FD(LN_2/-45)	NO/N_2	550	6.20	23.3	44.0

[a]catalytic properties were determined after 20 hrs time-on-stream, [b]cobalt-time-yield, [c]selectivity.

CONCLUSION

The cobalt oxide nanoparticle distribution in Co/SiO_2 Fischer-Tropsch catalysts was successfully manipulated by varying the drying treatments. More specifically, this was achieved for a system with weak support-precursor interaction and at high metal loadings, using a commercially available silica-gel support and cobalt nitrate as precursor. Freeze-drying was applied to restrict precursor mobility during the drying step. Based on the different freezing point depressions of confined cobalt nitrate solution and cobalt nitrate hexahydrate salt, two freeze-drying methods were developed. DSC showed that by freezing at liquid nitrogen temperatures, both solution and salt solidified, while by freezing at -45 °C only the confined cobalt nitrate salt crystallized.

The Co_3O_4 distribution after decomposition of the nitrate largely represented the distribution of the precursor phase obtained by drying. Conventional drying led to the formation of aggregates of individual nanoparticles, while freeze-drying starting at liquid nitrogen temperatures led to a uniform distribution of nanoparticles over the support. An egg-shell catalyst was obtained after solution impregnation and freeze-drying starting at -45 °C, which is above the crystallization temperature of confined cobalt nitrate solution. An average particle size of 8 nm was obtained after calcination in a flow of N_2 and 4 - 6 nm particles were obtained by decomposition in 1% NO/N_2. All catalysts showed high activity for the Fischer-Tropsch reaction at 1 bar, showing similar reducibility of the oxides formed after the different drying treatments and calcination. The effect of freeze-drying on the macroscale and nanoscale distributions of cobalt nanoparticles emphasizes the importance of the drying step in the synthesis of supported catalysts.

ACKNOWLEDGMENTS

T.E. Eggenhuisen contributed equally to this work. Mr. M. van Steenbergen (Utrecht University) is acknowledged for technical support and useful discussions on freeze-drying as well as thermal analysis. Dr. H. de Waard (University of Groningen) and Dr. Foppe Bakker (MSD) are acknowledged for providing access to freeze-drying equipment and sharing their expertise. Ms. E. van Donselaar (Utrecht University) is acknowledged for ultramicrotomy instructions. The Electron Microscopy Unit at Utrecht University is acknowledged for their excellent facilities.

REFERENCES

(1) Bartholomew, C. H. *Appl. Catal. A* **2001**, *212*, 17.
(2) Forzatti, P.; Lietti, L. *Catal. Today* **1999**, *52*, 165.
(3) Arnal, P. M.; Comotti, M.; Schuth, F. *Angew. Chemie Int. Ed.* **2006**, *45*, 8224.
(4) Joo, S. H.; Park, J. Y.; Tsung, C. K.; Yamada, Y.; Yang, P. D.; Somorjai, G. A. *Nat. Mater.* **2009**, *8*, 126.
(5) Yan, W. F.; Mahurin, S. M.; Pan, Z. W.; Overbury, S. H.; Dai, S. *J. Am. Chem. Soc.* **2005**, *127*, 10480.
(6) Li, L. Y.; King, D. L.; Liu, J.; Huo, Q. S.; Zhu, K. K.; Wang, C. M.; Gerber, M.; Stevens, D.; Wang, Y. *Chem. Mater.* **2009**, *21*, 5358.
(7) Cao, A.; Veser, G.; *Nat. Mater.* **2010**, *9*, 75.
(8) Soled, S. L.; Malek, A. ; Miseo, S.; Baumgartner, J.; Kliewer, C.; Afeworki, M.; Stevens, P. A. *Scientific Bases for the Preparation of Heterogeneous Catalysts, Proceedings of the 9th International Symposium* **2006**, *162*, 103.
(9) Saib, A. M.; Moodley, D. J.; Ciobica, I. M.; Hauman, M. M.; Sigwebela, B. H.; Weststrate, C. J.; Niemantsverdriet, J. W.; van de Loosdrecht, J. *Catal. Today* **2010**, *154*, 271.
(10) Neimark, A. V.; Kheifez, L. I.; Fenelonov, V. B. *Ind. Eng. Chem. Prod. Res. Dev.* **1981**, *20*, 439.
(11) Iglesia, E.; Soled, S. L.; Baumgartner, J. E.; Reyes, S. C. *J. Catal.* **1995**, *153*, 108.
(12) Borg, O.; Walmsley, J. C.; Dehghan, R.; Tanem, B. S.; Blekkan, E. A.; Eri, S.; Rytter, E.; Holmen, A. *Catal. Lett.* **2008**, *126*, 224.
(13) Sietsma, J. R. A.; Meeldijk, J. D.; den Breejen, J. P.; Versluijs-Helder, M.; van Dillen, A. J.; de Jongh, P. E.; de Jong, K. P. *Angew. Chemie Int. Ed.* **2007**, *46*, 4547.
(14) Martinez, A.; Lopez, C.; Marquez, F.; Diaz, I. *J. Catal.* **2003**, *220*, 486.
(15) van der Meer, J.; Bardez, I.; Bart, F.; Albouy, P. A.; Wallez, G.; Davidson A. *Micropor. Mesopor. Mat.* **2009**, *118*, 183.
(16) Arslan, I.; Walmsley, J. C.; Rytter, E.; Bergene, E.; Midgley, P. A. *J. Am. Chem. Soc.* **2008**, *130*, 5716.
(17) Marceau, E.; Che, M.; Cejka, J.; Zukal, A. *ChemCatChem* **2010**, *2*, 413.
(18) Lekhal, A.; Glasser, B. J.; Khinast, J. G. *Chem. Eng. Sci.* **2001**, *56*, 4473.
(19) Liu, X.; Khinast, J. G.; Glasser, B. J. *Ind. Eng. Chem. Res.* **2010**, *49*, 2649.
(20) Komiyama, M.; Merrill, R. P.; Harnsberger, H. F. *J. Catal.* **1980**, *63*, 35.
(21) Che, M.; Cheng, Z. X.; Louis, C. *J. Am. Chem. Soc.* **1995**, *117*, 2008.
(22) Chu, W.; Wang, L. N.; Chernavskii, P. A.; Khodakov, A. Y. *Angew. Chemie Int. Ed.* **2008**, *47*, 5052.
(23) van Dillen, A. J.; Terorde, R. J. A. M.; Lensveld, D. J.; Geus, J. W.; de Jong, K. P. *J. Catal.* **2003**, *216*, 257.
(24) Zheng, N. F.; Stucky, G. D. *J. Am. Chem. Soc.* **2006**, *128*, 14278.
(25) Reyes, A.; Vega, R.; Bustos, R.; Araneda, C. *Dry. Technol.* **2008**, *26*, 1272.
(26) Kirmaci, V.; Usta, H.; Menlik, T. *Dry. Technol.* **2008**, *26*, 1570.
(27) Chen, G. H.; Wang, W. *Dry. Technol.* **2007**, *25*, 29.
(28) Chen, C. J.; Han, D. D.; Cai, C. F.; Tang, X. *J. Control. Release* **2010**, *142*, 299.
(29) Wang, W. *Int. J. Pharm.* **2000**, *203*, 1.

(30) Portner, D. C.; Leuschner, R. G. K.; Murray, B. S. *Cryobiology* **2007**, *54*, 265.
(31) Schwab, C.; Vogel, R.; Ganzle, M. G. *Cryobiology* **2007**, *55*, 108.
(32) Qian, L.; Zhang, H. *J. Chem. Technol. Biotechnol.* **2010**, *86*, 172-184.
(33) Kraiwattanawong, K.; Sano, N.; Tamon, H. *Carbon* **2011**, *49*, 3404.
(34) Vergunst, T.; Kapteijn, F.; Moulijn, J. A. *Appl. Catal. A* **2001**, *213*, 179.
(35) Xi, X. L.; Nie, Z. R.; Jiang, Y. B.; Xu, X. Y.; Zuo, T. Y. *Powder Technol.* **2009**, *191*, 107.
(36) Kim, H. J.; Choi, S. M.; Nam, S. H.; Seo, M. H.; Kim, W. B. *Appl. Catal. A* **2009**, *352*, 145.
(37) Carrier, X.; Lambert, J. F.; Kuba, S.; Knozinger, H.; Che, M. *J. Mol. Struct.* **2003**, *656*, 231.
(38) Mellor, J. D. *Fundamentals of Freeze-Drying* Academic Press, London New York San Fransisco, **1978**.
(39) Flosdorf, E. W. *Freeze-Drying. Drying by Sublimation* Reinhold Publishing corporation, New York, **1949**.
(40) Tang, X. L.; Pikal, M. J. *Pharm. Res.* **2004**, *21*, 191.
(41) Kasper, J. C.; Friess, W. *Eur. J. Pharm. Biopharm.* **2011**, *78*, 248.
(42) Beirowski, J.; Inghelbrecht, S.; Arien, A.; Gieseler, H. *J. Pharm. Sci.* **2011**, *100*, 1958.
(43) Searles, J. A.; Carpenter, J. F.; Randolph, T. W. *J. Pharm. Sci.* **2001**, *90*, 872.
(44) Malmstrom, B. G. *Exp. Cell Res.* **1951**, *2*, 688.
(45) Gan, K. H.; Bruttini, R.; Crosser, O. K.; Liapis, A. I. *Dry. Technol.* **2004**, *22*, 1539.
(46) Pikal, M. J.; Shah, S.; Roy, M. L.; Putman, R. *Int. J. Pharm.* **1990**, *60*, 203.
(47) Wolters, M.; Contreras Andrade, I. C. A.; Munnik, P.; Bitter, J. H.; de Jongh, P. E.; de Jong, K. P. *Stud. Surf. Sci. Catal.* **2010**, *175*, 69-76.
(48) Eggenhuisen, T. M.; den Breejen, J. P.; Verdoes, D.; de Jongh, P. E.; de Jong, K. P. *J. Am. Chem. Soc.* **2010**, *132*, 18318.
(49) Vakros, J.; Bourikas, K.; Perlepes, S.; Kordulis, C.; Lycourghiotis, A. *Langmuir* **2004**, *20*, 10542.
(50) Sietsma, J. R. A.; Friedrich, H.; Broersma, A.; Versluijs-Helder, M.; van Dillen, A. J.; de Jongh, P. E.; de Jong, K. P. *J. Catal.* **2008**, *260*, 227.
(51) Wolters, M.; Munnik, P.; Bitter, J. H.; de Jongh, P. E.; de Jong, K. P. *J. Phys. Chem. C* **2011**, *115*, 3332.
(52) Friedrich, H.; Sietsma, J. R. A.; de Jongh, P. E.; Verkleij, A. J.; de Jong, K. P. *J. Am. Chem. Soc.* **2007**, *129*, 10249.
(53) Munnik, P.; Wolters, M.; Gabrielsson, A.; Pollington, S. D.; Headdock, G.; Bitter, J. H.; de Jongh, P. E.; de Jong, K. P. *J. Phys. Chem. C* **2011**, *115*, 14698.
(54) Jacobs, G.; Das, T. K.; Zhang, Y. Q.; Li, J. L.; Racoillet, G.; Davis, B. H. *Appl. Catal. A* **2002**, *233*, 263.
(55) den Breejen, J. P.; Sietsma, J. R. A.; Friedrich, H.; Bitter, J. H.; de Jong, K. P. *J. Catal.* **2010**, *270*, 146.
(56) den Breejen, J. P.; Radstake, P. B.; Bezemer, G. L.; Bitter, J. H.; Froseth, V.; Holmen, A.; de Jong, K. P. *J. Am. Chem. Soc.* **2009**, *131*, 7197.

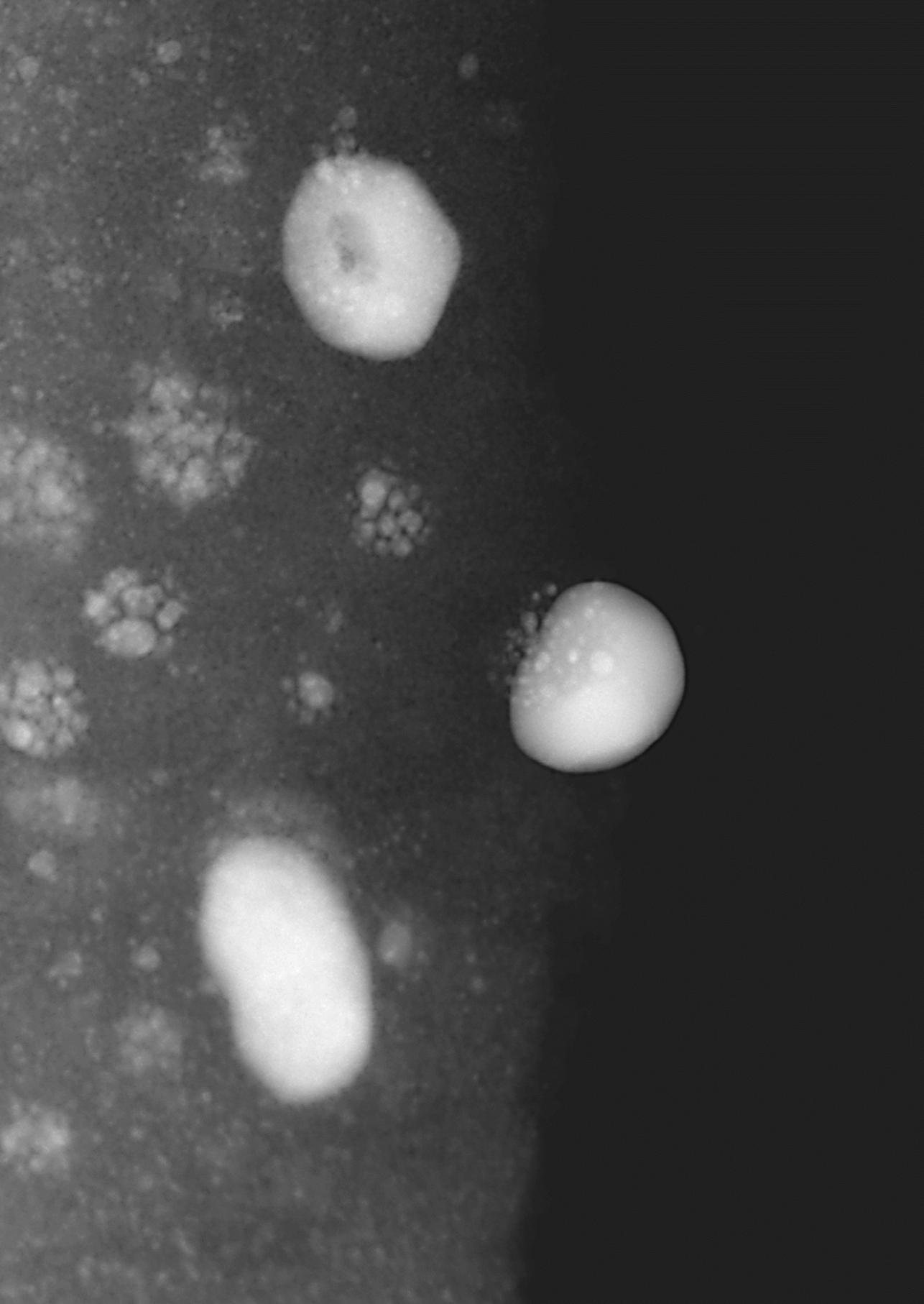

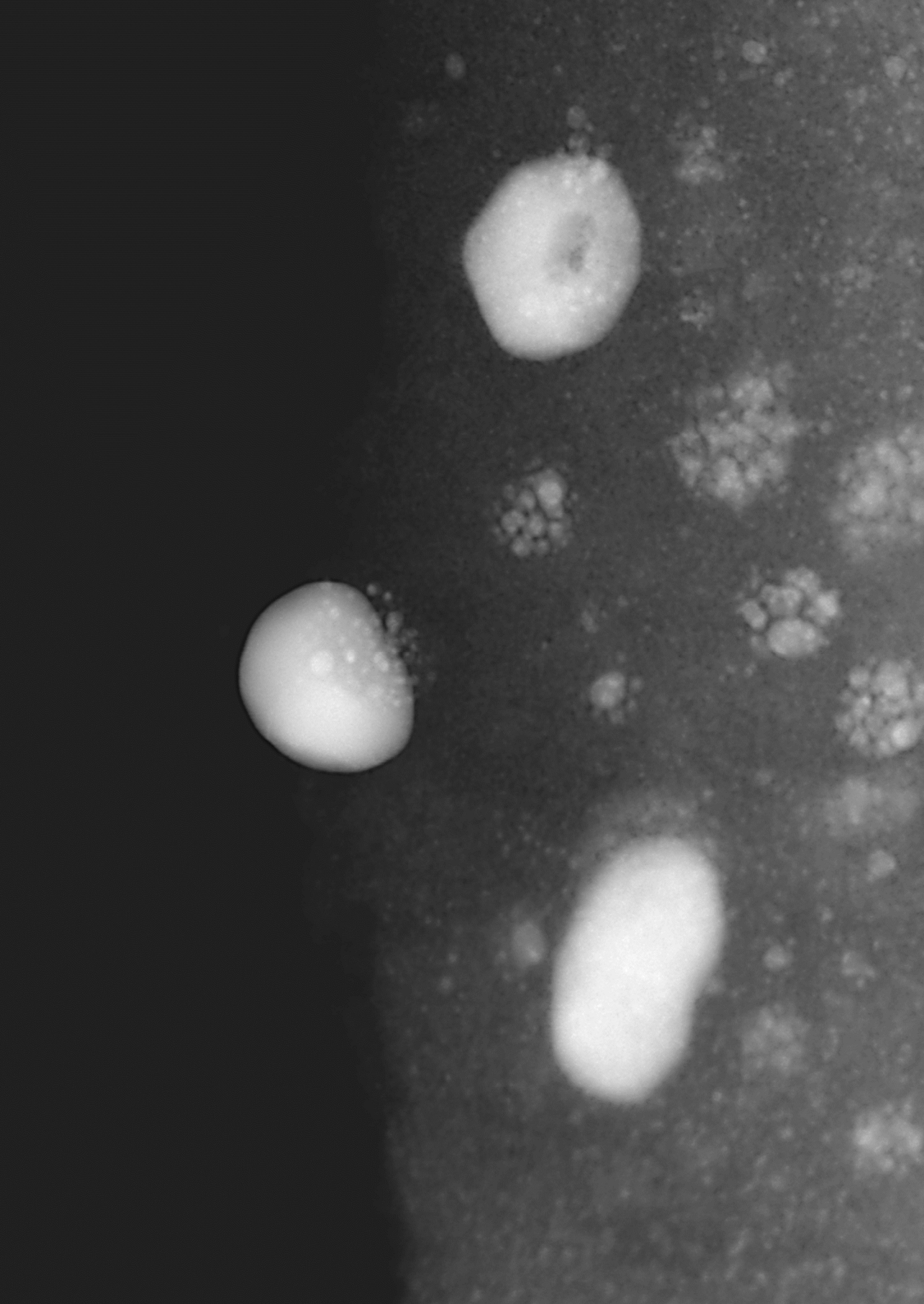

Chapter 4

Control and Impact of the Nanoscale Distribution of Supported Cobalt Particles in Fischer-Tropsch Catalysts

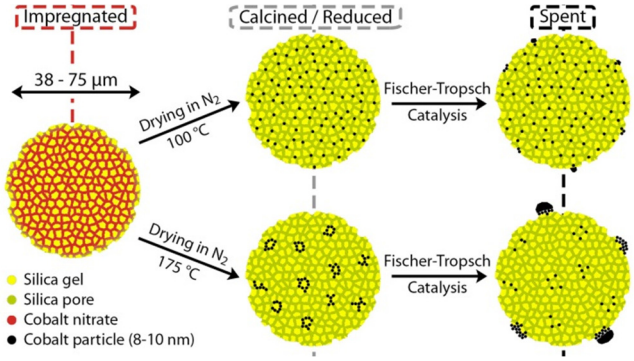

Short interparticle distances may affect the stability of supported metal catalysts and often arise during catalyst preparation by formation of aggregates. The cause of aggregation of cobalt nanoparticles during the synthesis of highly loaded silica-supported catalysts was found to originate from the drying process after impregnation of the silica grains with an aqueous cobalt nitrate precursor. Maximal spacing of the Co_3O_4 nanoparticles was obtained by fluid-bed drying at 100 °C in an N_2 flow. Below this temperature, redistribution of liquid occurred before and during precipitation of a solid phase, leading to aggregation of the cobalt particles. At higher temperatures, nucleation and growth of Co_3O_4 occurred during the drying process also giving rise to aggregation. Fischer-Tropsch catalysis performed under industrially relevant conditions for unpromoted and Pt-promoted cobalt catalysts revealed that the size of aggregates (13 - 80 nm) of Co particles (size ~ 9 nm) had little effect on activity. Larger aggregates of Co particles gave rise to extensive migration of cobalt (up to 75%) to the external surface of the macroscopic catalyst grains (38 – 75 µm). Although particle size did not increase inside the silica support grains, migration of cobalt to the external surface partly led to particle growth, thus causing a loss of activity. This cobalt migration over macroscopic length scales was suppressed by maximizing the distance between nanoparticles over the support. Clearly, the nanoscale distribution of particles is an important design parameter of supported catalysts.

Adapted with permission from: P. Munnik et al. *J. Am. Chem. Soc.* **2014**, *136*, 7333.

INTRODUCTION

Supported metal nanoparticles are at the center of many existing as well as new and more sustainable processes, such as energy conversion and storage, nanoelectronics and the catalytic production of fuels and chemicals.[1–3] Unfortunately, degradation of these functional nanomaterials during usage is a major concern. Small metal particles often grow to larger crystals, either via particle migration and coalescence or through Ostwald ripening, whereby monomeric species are transported from small to large particles.[4–7] In specific cases crystal growth may be moderated by tuning properties of the nanoparticles such as their size[8], composition[9] and interaction with the support.[10] Particles being close together may lead to increased deactivation[11], and recently, the interparticle distance was shown to have a large effect on the stability of copper catalysts for methanol synthesis.[12] However, the nanoscale distribution of particles is rarely studied and difficult to control. It has been noted that many materials, used both in academic and industrial context, exhibit non-uniform distributions of metal particles grouped together on the support as s0-called aggregates or clusters of nanoparticles.[13–15]

Aggregates are often formed during the synthesis of the desired supported nanoparticles. Here we consider a widely used method of synthesis; impregnation of macroscopic support grains followed by drying and subsequent thermal decomposition. Research has focused on circumventing the formation of aggregates through the choice of precursor[16–18], addition of organic additives[19–22] and changing the solvent.[23,24] However, systematic knowledge of aggregate formation of nanoparticles is lacking. The drying step has long been known to have a large impact on the macroscale distribution[25,26], while recently it was also shown to have a large impact on the nanoscale distribution by studying conventional drying versus freeze drying, as discussed in Chapter 3.[27–29]

Cobalt catalysts are often used for Fischer-Tropsch synthesis, whereby CO and H_2 are converted into long chain alkanes for the production of ultra-clean transportation fuels. For industrial applications, the deactivation of these catalysts is a large problem.[30–35] However, the role of aggregation of nanoparticles on performance in general, and stability in particular, is not well known. Changes in selectivities to long chain alkanes have been reported for catalysts with different degrees of aggregation, but this was always accompanied by a change in cobalt particle size[36,37], support pore size[38], support type[39] or promoter addition[40], factors which can also influence the selectivity. In this chapter, we use silica-supported cobalt catalysts as a case study, elucidate the cause for nanoparticle aggregation by an extensive study of the drying step, show how to control the extent of aggregation, and report the effect on Fischer-Tropsch catalysis.

EXPERIMENTAL

Catalyst Synthesis. Co/SiO_2 catalysts were prepared using a commercially available silica gel as support (Davicat 1404, Grace-Davidson). The support grains were sieved to a fraction of

38 - 75 μm and the porosity was characterized with N_2-physisorption at -196 °C (Tristar 3000, Micromeritics): V_p = 0.87 cm^3/g, S_{BET} = 443 m^2/g, d_p = 8 nm. Solution impregnation was performed to incipient wetness using a 4.2 M $Co(NO_3)_2 \cdot 6H_2O$ (Sigma-Aldrich, >99%) (aq) solution leading to a nominal cobalt metal loading of 16.2 wt%. Pt promoted samples were impregnated with a 4.2 M $Co(NO_3)_2 \cdot 6H_2O$, 0.03 M $(NH_3)_4Pt(NO_3)_2$ (Alfa Aesar, 99.99%) (aq) solution to obtain 0.5 wt% Pt and 16.2 wt% Co.

Different drying treatments were applied by transferring 100 or 400 mg of the impregnated grains into an upflow fluidized bed reactor (internal diameter of 1 or 2 cm, respectively). After the oven reached the drying temperature the reactor was placed in the oven and an N_2 flow with a gas hourly space velocity (GHSV) of 5000 h^{-1} was applied. Catalysts were dried at 25, 50, 75, 100, 125 and 150 °C for 48, 24, 16, 3, 3 and 2 hours, respectively. Calcination of all dried catalysts was performed by further heating the fluidized bed reactor to 350 °C (1 °C/min, 1h) in a flow of N_2 (GHSV 30000 h^{-1}).

Catalyst Characterization. The phase behavior of cobalt nitrate present during the different stages of catalyst preparation was analyzed using differential scanning calorimetry (DSC, Q2000, TA Instruments). The temperature and heat flow were calibrated with a certified indium sample and measurements were performed with hermetically sealed aluminum pans (~40 μL, Tzero, TA Instruments) under a flow of N_2 (50 mL/min). Sample masses were typically between 5 - 15 mg and heat flows were recorded between -90 °C and 120 °C at a rate of 1 °C/min.

Thermogravimetric analysis (TGA, Q50 TA Instruments) was used to determine the residual water content after different drying treatments by measuring the weight loss after heating to 500 °C for 30 min (10 °C/min) under a 60 mL/min N_2 flow. The weight loss was corrected for the loss of water by condensation of silanol groups from the pristine silica gel, which was experimentally found to occur between 150 and 500 °C. The rest of the weight loss was attributed to residual water, or the decomposition of $Co(NO_3)_2$ to Co_3O_4 after drying at 125 and 150 °C as was evident from the black color of the samples.

The degree of reduction was measured using TGA (Pyris 1 TGA, Perkin Elmer) in a flow of 10% H_2/He. 10 Mg of sample was heated at 2 °C/min to 350 or 500 °C for the Pt promoted and unpromoted samples, respectively, and held there for three hours. While this was shorter compared to the reduction prior to catalysis experiments, no significant weight loss was observed after this time.

H_2-Chemisorption measurements were performed on a Micromeretics ASAP 2020 instrument. Samples were dried at 100 °C for 1 h in dynamic vacuum followed by a reduction in H_2 at 350 or 500 °C (5 h, 2 °C/min). Isotherms were measured at 150 °C. Apparent cobalt surface areas were calculated assuming H:Co = 1 and an atomic cross-section of 0.0662 nm^2. The corrected particle sizes were deduced from the cobalt surface areas using the amount cobalt per gram of catalysts multiplied by the degree of reduction.

XRD patterns were recorded between 20 and 90° 2θ with a Bruker-AXS D2 Phaser X-ray Diffractometer using Co-$K_{\alpha 12}$ radiation (λ = 1.790 Å). The volume averaged Co_3O_4 crystallite

size was determined using the Scherrer equation with a shape factor k = 0.9 and line broadening analysis on the (220), (311) and (400) peaks by a fitting procedure in Eva2 software (Bruker AXS).

N_2-physisorption isotherms were measured at -196 °C using a Micromeritics Tristar 3000 apparatus. Prior to analysis, samples were dried in He flow for 16 hours at 200 °C. For the spent catalysts, several samples were measured before and after heat treatment in a muffle oven at 500 °C in air to remove all the waxes present in the pores.

Catalyst grains were embedded in a two component epoxy resin (Epofix, EMS) and cured at 60 °C overnight. The embedded catalysts were then cut into thin sections with a nominal thickness of 50 nm using a Diatome Ultra 35° diamond knife mounted on a Ultracut E microtome (Reichert-Jung) and collected on a TEM grid. Bright field TEM images were obtained on a Tecnai 12 (FEI), operated at 120 keV.

Dark field images were taken to study the crystallinity of the aggregates at 80 KeV by tilting the incoming electron beam 1.2°. The smallest objective aperture was used so that only diffracted electrons in a small rotational range were selected, allowing for the imaging of crystallites which were crystallographically aligned. The incoming electron beam was then rotated 10° for each subsequent image so that a semicircle of 180° was measured.

EDX analysis was used to measure the cobalt weight loading of the spent catalysts in a Technai 20-FEG (FEI) electron microscope operating at 200 keV. For each sample, EDX was performed on large areas (>100 μm^2) of the microtomed sections of 5 – 10 catalyst grains to measure the average Co/Si atomic ratio of the grains.

Low-resolution SEM was performed on a PHENOM SEM (Phenom World) equipped with a backscatter detector operated at 5 keV. For high resolution SEM, samples were coated with a thin layer of Pt, after which the measurements were performed on a XL30SFEG (FEI).

Catalytic Testing. Catalysis was performed on a Flowrence (Avantium) 16 parallel reactor unit. 50 mg or 70 mg of the Pt-promoted or unpromoted catalyst (38 - 75 μm), respectively, was mixed with 200 mg SiC (100 - 200 μm) and loaded into a stainless steel reactor. Catalysts were reduced in-situ in 25 vol.% H_2/He by going to 350 or 500 °C, respectively, at 1 °C/min and held for 8 hours. Afterwards, the reactors were cooled to 180 °C at which the pressure was increased to 20 bar under H_2. Next, the feed was changed to an H_2/CO ratio of 2.0 with 5 vol.% He, which functioned as internal standard for the on-line GC (Agilent 7890A). After 1 hour, the temperature was increased to the reaction temperature of 220 °C at 1 °C/min. All catalysts started at a CO conversion around 80%. After 240 hours on-stream at high CO conversion levels, the catalysts were flushed with argon, and subsequently the reactors were re-pressurized to 20 bar under H_2 at 180 °C, after which syngas was reintroduced and the temperature was returned to 220 °C. Next, the conversion was lowered by increasing the GHSV, to measure the selectivity of all catalysts at a CO conversion of 65% after 10 h. The C_{5+} selectivity was calculated by subtracting the amount of CO used for the formation of C_1 to C_4 products, as determined via on-line GC using He as an internal standard, from the total amount of CO converted.

RESULTS AND DISCUSSION

Effect of Drying. Co/SiO_2 catalysts with a 16 wt.% Co loading were synthesized by incipient wetness impregnation of silica gel grains with a saturated $Co(NO_3)_2{\cdot}6H_2O$ solution. Subsequently, N_2 fluidized bed drying treatments were applied at six different temperatures to different batches of the impregnated catalysts, followed by calcination at 350 °C in N_2 flow. Table 4.1 shows the Co_3O_4 crystallite size after drying and calcination obtained from XRD, averaging around 8.5 nm regardless of the drying treatment. This is close to the average pore diameter of the support, and suggests particles grew in confinement of the pores, as has been reported before.[41]

Figure 4.1 shows TEM micrographs of the same catalysts. Drying at 25 °C resulted in cobalt aggregates with an average size of 25 nm. These aggregates became smaller as the drying temperature increased, until at 100 °C most of the crystallites were isolated instead of aggregated. Further increase in temperature resulted in an increase in aggregate size, as large as 50 nm after drying at 150 °C.

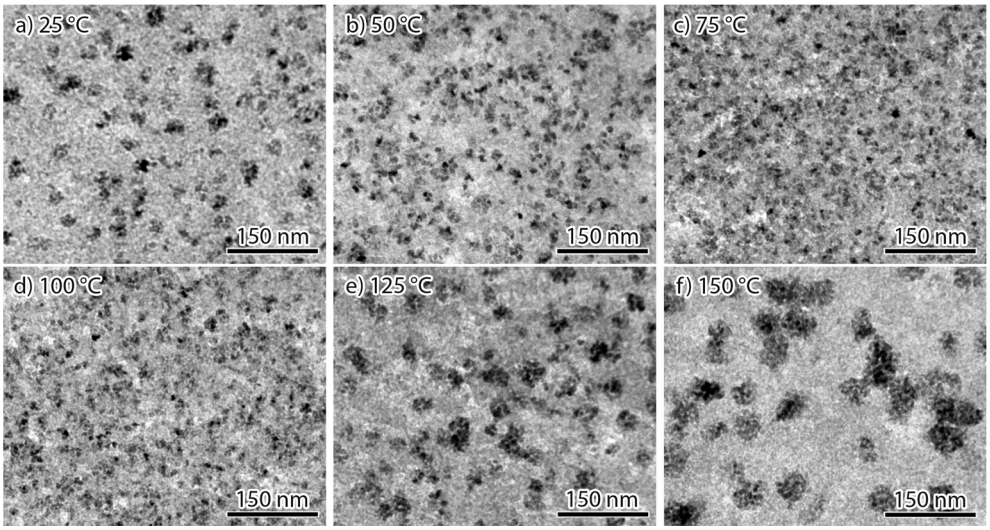

Figure 4.1: TEM of calcined Co_3O_4/SiO_2 after different drying treatments, showing different aggregate sizes (black) on the silica support (grey) depending on the drying temperature. (a) Dried at 25 °C, (b) 50 °C, (c) 75 °C, (d) 100 °C, (e) 125 °C, (f) 150 °C.

Figure 4.2 shows dark field (DFTEM) analysis of the catalyst dried at 150 °C and subsequently calcined, which allows imaging of electrons diffracted by only a specific Co_3O_4 lattice plane depending on the orientation of the crystallite. Many aggregates were observed as a single color or not at all, suggesting they consisted of a single crystalline domain of multiple nanocrystals. These crystalline domains likely grew around the support grains, as has previously been observed for cobalt on γ-alumina[39,42], and which was confirmed by removing the silica,

leaving aggregated cobalt particles with the size of the aggregates with well-defined pores (see Appendix A, Figure A.5).

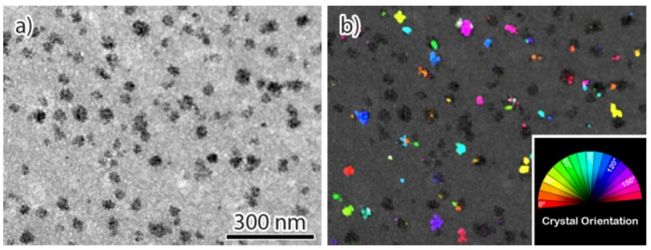

Figure 4.2. DFTEM of Co_3O_4/SiO_2 dried at 150 °C, followed by calcination. (a) Bright field image, showing large cobalt oxide aggregates (black). (b) Superposition of 18 dark field images separated by a beam orientation of 10° each. The crystal lattice orientation of the aggregates is represented by different colors (inset).

TGA was performed to study the water content of the catalyst precursor after drying (Table 4.1). After drying at 25 °C, 4 mol H_2O/mol Co remained. Higher drying temperatures resulted in less residual water, and at 100 °C the sample was almost completely dehydrated. Temperatures above 100 °C resulted in partial conversion of cobalt nitrate into cobalt oxide during drying. At 150 °C, 55% of the cobalt nitrate was decomposed during the drying treatment. Phase analysis was performed for each sample after drying by DSC, however no melting peaks were observed between -90 and +120 °C for any of the samples, suggesting the remaining precursor had precipitated as solid cobalt nitrate or cobalt oxide species. These results, along with samples obtained by varying the drying time and gas hourly space velocity and the subsequent temperature ramp during calcination (see Appendix A, Figures A.1-A.3), allowed us to tentatively propose two different mechanisms for the formation of cobalt oxide aggregates.

Table 4.1: Precursor properties obtained after drying and after calcination of the cobalt nitrate impregnated silica grains

Drying Temperature (°C)	H2O content after drying (mol_{H2O}/mol_{Co})[a]	$Co(NO_3)_2$ converted to Co_3O_4 during drying[a]	Co_3O_4 crystallite size (XRD) after calcination (nm)	Aggregate size (TEM) after calcination (nm)
25	4.5	0%	8.7	25 (± 6)
50	1.4	0%	8.5	18 (± 4)
75	0.6	0%	7.8	14 (± 2)
100	0.4	0%	8.5	11 (± 2)
125	0	17%	8.7	26 (± 6)
150	0	55%	9.4	44 (± 10)

[a]Determined by TGA after drying.

At temperatures below 100 °C aggregation is attributed to the slow drying process. At a certain point during drying, the water content becomes so low that a solid cobalt nitrate phase precipitates. When such a transition is slow, severe redistribution of remaining liquid may take place on a nanoscale, as is well known for the drying of colloidal films.[43] Nucleation of the precipitated phase combined with extensive growth could result in the formation of cobalt nitrate rich and poor areas, the sizes of which depend on the mobility of the precursor while still in solution and the allowed time for redistribution. These cobalt nitrate rich areas are then the basis to form Co_3O_4 aggregates upon further heat treatment. Thus, at 25 °C, when drying takes long and the transition is presumed to be slow, aggregation was observed, whereas increasing the temperature to 100 °C gradually reduced the aggregation. Macroscopically, the drying rate was recently shown to influence the distribution of low melting point metal nitrates at high concentration.[44] However, by utilizing ultramicrotomy, the distribution for each catalyst was verified to be uniform throughout the 38 - 75 μm catalyst grains, suggesting our system was not sensitive to macroscopic redistribution effects under the used conditions.

The most uniform distribution at the nanoscale obtained after drying at 100 °C is explained from fast drying that restricts redistribution of viscous liquids.[44] Above 100 °C, nucleation and growth of Co_3O_4 from cobalt nitrate becomes possible. This already occurs before the sample is completely dried, while cobalt nitrate has not yet precipitated and due to reduced viscosity has high mobility. Indeed, a high water partial pressure during high temperature drying, or insufficient removal of water during calcination, is known to result in severe agglomeration.[45–47] We postulate that this interplay between temperature, viscosity and water partial pressure leads to the formation of the observed aggregates, whereby growth from capturing cobalt from solution is favorable over nucleation of Co_3O_4, leading to large aggregates of crystallographically-aligned cobalt oxide particles which originate from a single nucleation point.[48]

Reduced Catalysts. To study the effect of aggregation on Fischer-Tropsch catalysis, catalysts with four aggregate sizes between 10 and 80 nm were synthesized using four drying temperatures between 100 and 175 °C, indicated after the D in the sample name. In one set of catalysts, 0.5 wt.% Pt was added as a reduction promoter.[49] Table 4.2 shows the average aggregate size of each catalyst as determined by TEM, as well as the Co surface area, degree of reduction and corrected cobalt metal particle size.

To ensure a high degree of reduction, the unpromoted catalysts were reduced at 500 °C while the Pt promoted catalysts were reduced at 350 °C. This resulted in an average degree of reduction of 80% and average cobalt surface area of 55 m^2/g_{Co} for the unpromoted catalysts, while the promoted catalysts showed almost complete reduction and averaged around 80 m^2/g_{Co} regardless of aggregate size. Consequently, the particle sizes of all catalysts were similar, between 8 and 10 nm, close to the support pore diameter (Table 4.2).

TEM on reduced and passivated CoPt catalysts (Figure A.4) showed that the aggregates were still present, but now also distinct Co particles within the aggregates were observed. DFTEM (Figure 4.3) showed many particles in a single aggregate to have different crystal

orientations. This indicated that after reduction the aggregates had broken up into smaller non-aligned crystallites, similar to what was previously reported for large cobalt oxide particles in model systems.[50,51] Thus, during the initial stages of catalysis the aggregates consisted of many individual particles with very small but finite interparticle distances.

Table 4.2. Catalyst aggregate size, properties after reduction and catalytic activity, selectivity and deactivation rate constant obtained after 240 hours on stream at 20 bar, 220 °C, H_2/CO 2.0; activity and selectivity reported at 65% CO conversion

Catalyst	Aggregate size (nm)	Co surface area (m^2/g_{Co})	Degree of reduction (%)	Corrected Co particle size (nm)	TOF (10^{-2} s^{-1})	CTY (10^{-5} $mol_{CO}g_{Co}^{-1}$ s^{-1})	C_1 (wt.%)	C_{5+} (wt.%)	$k_{D,2}$ (10^{-4} h^{-1})[a]
Co D100	13 (± 3)	57	78%	9.2	4.6	6.5	8.6	83.3	14.7
Co D125	22 (± 6)	55	76%	9.3	4.1	5.8	8.5	83.5	16.0
Co D150	37 (± 9)	55	83%	10.1	4.4	5.6	8.5	84.1	17.3
Co D175	77 (± 18)	55	84%	10.3	3.9	5.3	8.4	84.5	19.3
CoPt D100	11 (± 4)	80	105%	8.4	3.9	7.9	9.5	82.9	5.3
CoPt D125	18 (± 5)	74	103%	9.1	4.5	8.2	8.9	83.6	9.4
CoPt D150	38 (± 10)	85	96%	8.0	4.3	8.9	8.6	83.6	11.0
CoPt D175	74 (± 18)	75	93%	8.3	4.3	8.2	7.9	85.0	13.6

[a]The deactivation rate constant was defined as $a_{norm}^{1-n} = (n\text{-}1)\cdot k_D \cdot t + 1$ whereby a_{norm} is a measure for the normalized activity assuming first order kinetics so that a is proportional to $-ln(1 - conversion_{CO})$ and $n = 2$ (see Appendix A).

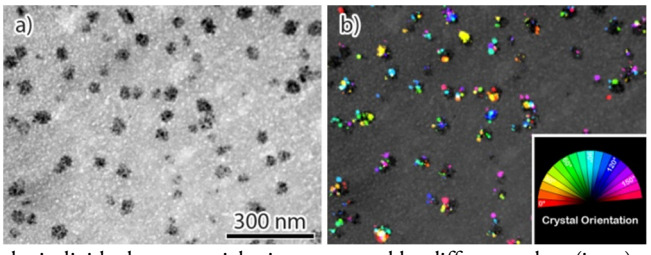

Figure 4.3. DFTEM of CoPtD150 after reduction and passivation. (a) Bright field image, showing large cobalt aggregates. (b) Superposition of 18 dark field images separated by a beam orientation of 10° each. The crystal lattice orientation of the individual nanoparticles is represented by different colors (inset).

Fischer-Tropsch Catalysis. The catalysts were tested at 220 °C, 20 bar and an H_2/CO ratio of 2.0. Table 4.2 shows the catalytic data after 240 h on-stream. An average TOF of $4.2 \cdot 10^{-2}$ s^{-1} was found with no significant difference between the promoted and unpromoted samples, as expected for cobalt particles larger than 6 nm.[52] Consequently, the promoted catalysts were 40% more active on average (CTY, see Table 4.2), due to their slightly smaller cobalt particles and higher degree of reduction. Little effect of aggregation on activity was found. Only for the unpromoted catalysts an effect of the aggregate size was observed, the most uniformly distributed catalyst being 25% more active compared to the highly aggregated catalyst. Also an increasing C_{5+} selectivity for increasing aggregate size was apparent, accompanied by a decrease in the methane selectivity (Table 4.2). An increase in olefin production was also observed for catalysts with larger aggregates (see Appendix A, Figure A.8a). This suggests that enhanced formation, re-adsorption and secondary chain growth of olefins inside aggregates is the cause of the increased selectivity. The olefin production for all Pt promoted catalysts was lower than for the corresponding unpromoted catalysts, attributed to the additional hydrogenation activity of the platinum.

All catalysts were observed to deactivate (Figure A.7a) and second-order deactivation rate constants, which are a measure of the decrease in activity per hour (see Appendix A), are shown in Table 4.2 and Figure 4.4. CoPtD100 exhibited the lowest deactivation rate constant of 5.3 10^{-4} h^{-1}, which increased up to 13.6 10^{-4} h^{-1} for CoPtD175. All unpromoted catalysts had higher deactivation constants, ranging from 14.7 to 19.3 10^{-4} h^{-1} for CoD100 and CoD175, respectively. Thus, two effects were found to influence the stability of the catalysts. First, introducing Pt lowered the deactivation rate for each catalyst, and catalysts containing larger aggregates of cobalt particles were found to deactivate faster.

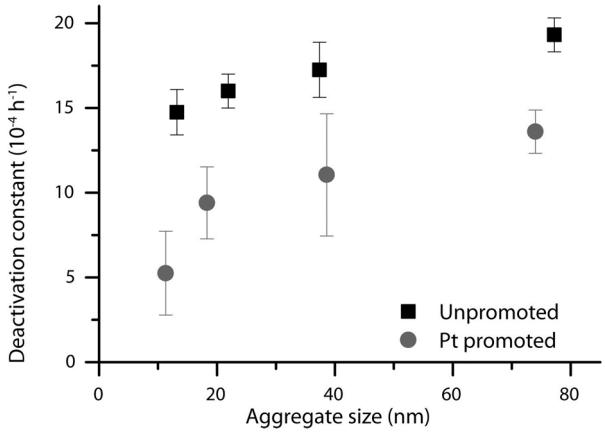

Figure 4.4. Deactivation rate constants measured during 240 hours of Fischer-Tropsch activity as a function of the cobalt aggregate size in Co/SiO_2 (black squares) and $Co/Pt/SiO_2$ (grey circles) catalysts.

Catalyst Deactivation. Deactivation in Fischer-Tropsch catalysts can occur via several different pathways, such as poisoning, carbon deposition and particle growth, often occurring simultaneously to some degree.[30] In addition, a high steam pressure, such as found at the bottom of the reactor, could affect the SiO_2 support. N_2-physisorption experiments (see

Appendix A, Table A.1) excluded the latter as significant for the conditions and time frame studied, and no evidence of large amounts of cobalt silicates was found in TEM micrographs of spent catalysts.[53] Carbon deposition has previously been reported to cause long term deactivation, and is difficult to avoid.[54] Noble metal promoters can prevent extensive formation of polymeric carbon,[55–57] which could explain the difference in deactivation between unpromoted and Pt promoted catalysts observed in Figure 4.4. The particles within aggregates have very short interparticle distances, so that particle growth likely contributed to deactivation.

Figure 4.5 shows TEM images of CoPtD100 and CoD175 after reduction and after catalysis from the top half and bottom half of the reactor respectively. Aggregates of cobalt nanoparticles were found to have fragmented into more isolated nanoparticles upon catalysis, as shown, for example, by comparison of Figures 4.5d with 4.5e and 4.5f. This breakup of aggregates was more apparent for larger aggregates and had occurred more extensively in the bottom of the reactor where the CO conversion was highest (see also Appendix A, Figure A.12). Surprisingly, the cobalt particles did not exhibit a significant increase in size, as shown by TEM histogram analysis (see Appendix A, Table A.2).

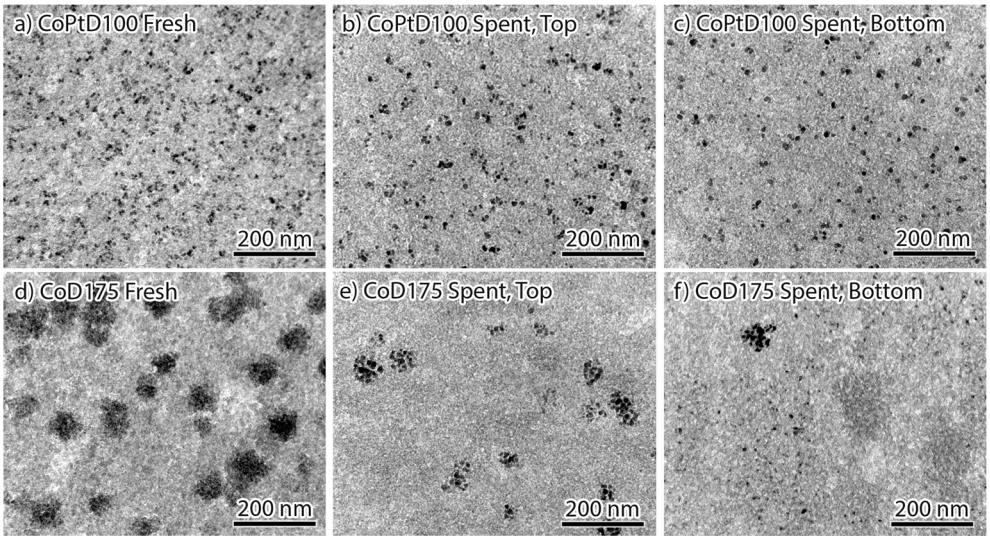

Figure 4.5. TEM comparison of fresh and spent Co/SiO_2 catalysts. (a) CoPtD100 after reduction, (b) CoPtD100 after reaction from the top half and (c) CoPtD100 from the bottom half of the reactor. (d) CoD175 after reduction, (e) CoD175 after reaction from the top half and (f) CoD175 after reaction from the bottom half of the reactor.

Although no increase in cobalt particle size was observed after catalysis, a decrease in particle density on the support is apparent from Figure 4.5. EDX analysis of the Co/Si atomic ratio of the microtomed sections of the spent catalysts was used to investigate this apparent cobalt mass loss. Fresh catalysts showed to have a weight loading of 16.2 wt.%, whereas all

spent catalysts contained less cobalt. A correlation was found between the loss of cobalt inside of the catalyst grains and the loss in activity (Figure 4.6); the higher the loss in cobalt, the higher the loss in activity. The cobalt loading inside the catalyst grains could be as low as 4wt.% for CoD175 after catalysis, 75% less than the nominal loading. However, the activity decreased only by about 30%, less than half of what was expected given the observed loss in cobalt and the similar particle size. Clearly, the question comes up – what is the fate of the cobalt that is lost from the interior of the catalyst grains?

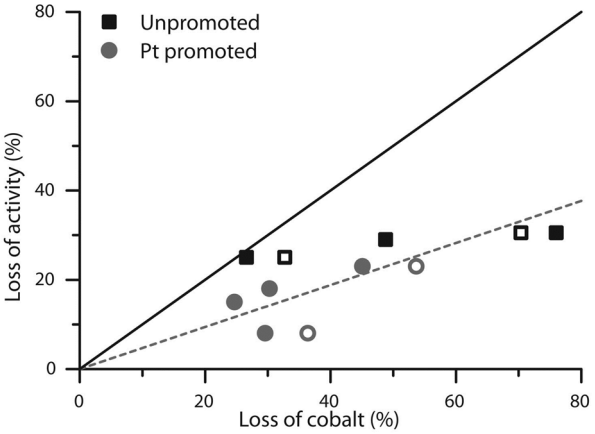

Figure 4.6. Loss of cobalt (from EDX) inside promoted and unpromoted Co/SiO_2 catalyst grains after catalysis taken from the top half (open symbol) or bottom half (closed symbol) of the reactor, related to the loss in activity of the corresponding catalyst assuming first-order kinetics. The black line illustrates the expected activity loss if the cobalt was lost from the reactor or sintered into very large particles.

SEM images of macroscopic catalyst grains before and after catalysis are shown in Figure 4.7a and 4.7b. Before catalysis, no cobalt was observed on the external surface of CoD175 (Figure 4.7a). However after reaction large cobalt rich areas were found on the exterior surfaces of catalyst grains (Figure 4.7b). This was observed for each catalyst, whereby the largest amount of cobalt was observed on the exterior surface of catalysts originally with the largest aggregates, such as CoD175 and CoPtD175, while CoD100 and CoPtD100, the catalysts with homogeneously distributed nanoparticles, had much less cobalt on the outer surface (see Appendix A, Figure A.15). Thus, it was concluded that the difference in deactivation between homogeneously distributed and aggregated catalysts coincided with the migration of cobalt over macroscopic distances to the outside of the catalyst grains.

HAADF-STEM tomography revealed that aggregates on the external surface of the grains consisted of large solid particles of ~ 300 nm in size on top of small particles (Figure 4.7c, d and e). See the Supporting Information of the published article for movies of the full tomogram and tilt series. Histogram analysis on the small particles showed the average particle size within these aggregates was 9.7 nm (± 2.2), identical to the size of the fresh and spent catalysts (Figure A.14). Thus, the cobalt that migrated to the external surface was deposited as many small particles that still contributed to the catalytic activity, however sintering also occurred on the external surface, forming huge particles. This explains the difference between the observed loss of cobalt and loss of activity in Figure 4.6.

Migration of cobalt over macroscopic distances has been previously observed on γ-Al_2O_3 by Khodakov *et al.* and attributed to high temperature effects or low H_2/CO ratios and low gas flow rates.[58,59] However, here we show for the first time that the degree of redistribution on the macroscale was greatly influenced by the nanoscale cobalt distribution. The exact mechanism for this long-range migration is as yet unknown. Because the cobalt particles found inside the catalyst grains and those that migrated towards external surface were similar in size, Ostwald ripening is an unlikely candidate, since this concerns transport from small to larger particles. Partial oxidation during Fischer-Tropsch conditions and migration of entire particles has been proposed as a mechanism for sintering by Khodakov et al.[60], and evidence for (surface) oxidation of cobalt particles has been observed in some studies.[61–63] Catalysts with a low deactivation rate exhibited a relatively high hydrogenation activity, as observed from the propene/propane ratio, which could support this mechanism (see Appendix A, Figure A.8). However, calculations based on literature data[60,64,65] suggest classical random-walk diffusion of (oxidized) Co particles over the surface of the support can be excluded for transport over macroscopic distances. The diffusion coefficient of nanoparticles in a colloidal state is orders of magnitude higher, so that diffusion of the particles in liquid phase is a possible transport mechanism. Moreover, because particles are collected in aggregates at the external surface we tentatively propose entrainment of particles by reaction products to be responsible for the observed migration. At high conversion, confinement in the small silica pores and the presence of a hydrophobic liquid phase of long-chain alkanes, could lead water vapor to condense into small droplets. Droplets expelled to the outside surface of the catalyst particle by the formation of new reaction products will transport the cobalt particles in the liquid phase by entrainment. If the water droplets evaporate on the outside of the catalyst grains once no longer confined, deposition of the entrained cobalt particles at the external surface takes place.

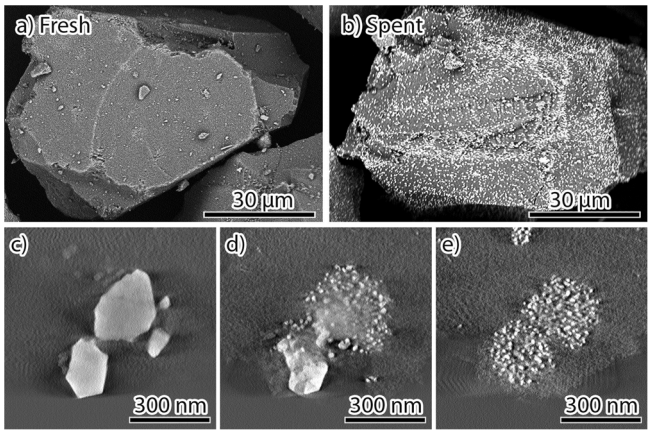

Figure 4.7. (a, b) SEM comparison of the external surface of Co/SiO_2 grains from CoD175 after reduction (a) and after catalysis (b). Before catalysis, little cobalt was observed on the external surface of the grains, whereas after catalysis a huge amount of cobalt was observed indicated by the bright spots. (c, d, e) Slices from an HAADF-STEM Tomography reconstruction of an aggregate at the external surface of a grain of the spent CoD175, separated by 75 nm in the z direction, illustrating the aggregate consisted of large solid cobalt particles of 100 - 300 nm (c), on top of many smaller cobalt particles of about 10 nm (d,e).

CONCLUSION

Aggregation of supported metal nanoparticles during the synthesis of *ex-nitrate* catalysts was strongly affected by the drying step after impregnation of a silica support with a metal nitrate precursor solution. At low temperatures, aggregation occurred as dissolved metal nitrate species were given ample time to redistribute before and during precipitation of the solid phase. At high temperatures, aggregation was caused by decomposition of the metal nitrate into the metal oxide during the drying process, which was aggravated by the mobile precursor at high water vapor pressures. At intermediate temperature (100 °C), aggregation could be largely prevented and by utilization of a fluid bed drying process isolated nanoparticles on the support were obtained.

After calcination, the aggregates consisted mainly of crystallographically aligned nanoparticles throughout the porous network. During reduction these aggregated crystallites fragmented into smaller particles with small interparticle spacing. Large aggregates of cobalt nanoparticles exhibited somewhat higher C_{5+} selectivities in Fischer Tropsch catalysis, attributed to higher olefin formation, re-adsorption and consecutive chain growth. A difference in deactivation between unpromoted and platinum promoted catalysts could indicate carbon deposition as a relevant deactivation mehanism. Moreover, an additional form of deactivation occurred not via direct nanoparticle growth, but via the migration over macroscopic distances of cobalt nanoparticles to the external surface of the catalyst grains. Only once on the surface of the catalyst grains, particles could sinter together into very large cobalt particles. This migration likely resulted from nanoparticles being entrained over distances of many micrometers from their original location, and was found to be more extensive for large initial aggregate sizes. By creating more uniformly dispersed catalysts, the degree of migration to the external surface of the catalyst grains was greatly reduced. These results are not only highly important for the rational design of supported cobalt catalysts, but point to the general relevance of nanoparticles distribution and spacing as an important design criterion of functional nanomaterials.[66–69]

ACKNOWLEDGMENTS

Mr. M. van Steenbergen and Dr. H. Talsma (Utrecht University) are acknowledged for their help with the DSC and TGA measurements on dried samples. Mr. H. Meeldijk (Utrecht University) is acknowledged for EDX analysis and tomography. Ms. M. Versluis-Helder (Utrecht University) is acknowledged for the TGA-reduction measurements and high resolution SEM. Ms. E. van Donselaar (Utrecht University) is acknowledged for ultramicrotomy instructions. Mr. J.H. den Otter (Utrecht University) is acknowledged for H_2-chemisorption and N_2-physisorption measurements. The Electron Microscopy Unit at Utrecht University is acknowledged for their excellent facilities.

REFERENCES

(1) Galeano, C.; Meier, J. C.; Peinecke, V.; Bongard, H.; Katsounaros, I.; Topalov, A. a; Lu, A.; Mayrhofer, K. J. J.; Schüth, F. *J. Am. Chem. Soc.* **2012**, *134*, 20457.

(2) Torres Galvis, H. M.; Bitter, J. H.; Khare, C. B.; Ruitenbeek, M.; Dugulan, A. I.; de Jong, K. P. *Science* **2012**, *335*, 835.

(3) Bezemer, G. L.; Bitter, J. H.; Kuipers, H. P. C. E.; Oosterbeek, H.; Holewijn, J. E.; Xu, X. D.; Kapteijn, F.; van Dillen, J. A.; de Jong, K. P. *J. Am. Chem. Soc.* **2006**, *128*, 3956.

(4) Wynblatt, P.; Gjostein, N. A. *Prog. Solid State Chem.* **1975**, 21.

(5) Ouyang, R.; Liu, J.-X.; Li, W.-X. *J. Am. Chem. Soc.* **2013**, *135*, 1760.

(6) Parkinson, G. S.; Novotny, Z.; Argentero, G.; Schmid, M.; Pavelec, J.; Kosak, R.; Blaha, P.; Diebold, U. *Nat. Mater.* **2013**, *12*, 724.

(7) Hansen, T. W.; Delariva, A. T.; Challa, S. R.; Datye, A. K. *Acc. Chem. Res.* **2013**, *46*, 1720.

(8) Campbell, C. T.; Parker, S.; Starr, D. *Science* **2002**, *298*, 811.

(9) Cao, A.; Veser, G. *Nat. Mater.* **2010**, *9*, 75.

(10) Farmer, J. A.; Campbell, C. T. *Science* **2010**, *329*, 933.

(11) Soled, S. L. *Synthesis of Solid Catalysts*; de Jong, K. P., Ed.; WILEY-VCH Verlag GmbH& Co. KGaA: Weinheim, 2009.

(12) Prieto, G.; Zečević, J.; Friedrich, H.; de Jong, K. P.; de Jongh, P. E. *Nat. Mater.* **2013**, *12*, 34.

(13) Friedrich, H.; Sietsma, J. R. A.; de Jongh, P. E.; Verkleij, A. J.; de Jong, K. P. *J. Am. Chem. Soc.* **2007**, *129*, 10249.

(14) Jiao, L.; Regalbuto, J. R. *J. Catal.* **2008**, *260*, 342.

(15) Den Breejen, J. P.; Frey, A. M.; Yang, J.; Holmen, A.; Schooneveld, M. M.; Groot, F. M. F.; Stephan, O.; Bitter, J. H.; de Jong, K. P. *Top. Catal.* **2011**, *54*, 768.

(16) Bae, J. W.; Kim, S.-M.; Kang, S.-H.; Chary, K. V. R.; Lee, Y.-J.; Kim, H.-J.; Jun, K.-W. *J. Mol. Catal. A Chem.* **2009**, *311*, 7.

(17) Girardon, J. S.; Lermontov, A. S.; Gengembre, L.; Chernavskii, P. A. *J. Catal.* **2005**, *230*, 339.

(18) Panpranot, J.; Kaewkun, S.; Praserthdam, P.; Goodwin, J. G. *Catal. Letters* **2003**, *91*, 95.

(19) Rane, S.; Borg, Ø.; Rytter, E.; Holmen, A. *Appl. Catal. A Gen.* **2012**, *437-438*, 10.

(20) Borg, Ø.; Dietzel, P. D. C.; Spjelkavik, A. I.; Tveten, E. Z.; Walmsley, J. C.; Diplas, S.; Eri, S.; Holmen, A.; Rytter, E. *J. Catal.* **2008**, *259*, 161.

(21) Hong, J.; Marceau, E.; Khodakov, A. Y.; Griboval-Constant, A.; La, C.; Briois, V.; Chernavskii, P. A. *Catal. Today* **2011**, *175*, 528.

(22) Dumond, F.; Marceau, E.; Che, M. *J. Phys. Chem. C* **2007**, *111*, 4780.

(23) Zhang, Y.; Liu, Y.; Yang, G.; Sun, S.; Tsubaki, N. *Appl. Catal. A Gen.* **2007**, *321*, 79.

(24) Kok, E.; Cant, N.; Trimm, D.; Scott, J. *Catal. Today* **2011**, *178*, 79.

(25) Neimark, A. V; Kheifez, L. I.; Fenelonov, V. B. *Ind. Eng. Chem. Prod. Res. Dev.* **1981**, 439.

(26) Lekhal, A.; Glasser, B. J.; Khinast, J. G. *Chem. Eng. Sci.* **2001**, *56*, 4473.

(27) Bogdanchikova, N. E.; Tretyakov, V. V. *Preparation of Catalysts V*; Poncelet, G.; Jacobs, P. A.; Grange, P.; Delmon, B., Eds.; Elsevier: Amsterdam, 1991; pp. 647–652.

(28) Eggenhuisen, T. M.; Friedrich, H.; Nudelman, F.; Zečević, J.; Sommerdijk, N. A. J. M.; de Jongh, P. E.; de Jong, K. P. *Chem. Mater.* **2013**, *25*, 890.

(29) Eggenhuisen, T. M.; Munnik, P.; Talsma, H.; de Jongh, P. E.; de Jong, K. P. *J. Catal.* **2013**, *297*, 306.

(30) Tsakoumis, N. E.; Rønning, M.; Borg, Ø.; Rytter, E.; Holmen, A. *Catal. Today* **2010**, *154*, 162.

(31) Saib, A. M.; Moodley, D. J.; Ciobîc, I. M.; Hauman, M. M.; Sigwebela, B. H.; Weststrate, C. J.; Niemantsverdriet, J. W.; van de Loosdrecht, J. *Catal. Today* **2010**, *154*, 271.

(32) Karaca, H.; Safonova, O. V.; Chambrey, S.; Fongarland, P.; Roussel, P.; Griboval-Constant, A.; Lacroix, M.; Khodakov, A. Y. *J. Catal.* **2011**, *277*, 14.

(33) Karaca, H.; Hong, J.; Fongarland, P.; Roussel, P.; Griboval-Constant, A.; Lacroix, M.; Hortmann, K.; Safonova, O. V; Khodakov, A. Y. *Chem. Commun.* **2010**, *46*, 788.

(34) Das, T. K.; Jacobs, G.; Davis, B. H. *Catal. Letters* **2005**, *101*, 187.
(35) Bezemer, G. L.; Remans, T. J.; van Bavel, A. P.; Dugulan, A. I. *J. Am. Chem. Soc.* **2010**, *132*, 8540.
(36) Borg, Ø.; Eri, S.; Blekkan, E. A.; Storsæter, S.; Wigum, H.; Rytter, E.; Holmen, A. *J. Catal.* **2007**, *248*, 89.
(37) Roy, M.; Marion, M. US Patent: 6235798B1, 2001.
(38) Saib, A. M.; Claeys, M.; van Steen, E. *Catal. Today* **2002**, *71*, 395.
(39) Borg, Ø.; Walmsley, J. C.; Dehghan, R.; Tanem, B. S.; Blekkan, E. A.; Eri, S.; Rytter, E.; Holmen, A. *Catal. Letters* **2008**, *126*, 224.
(40) Feller, A.; Claeys, M.; van Steen, E. *J. Catal.* **1999**, *185*, 120.
(41) Wolters, M.; van Grotel, L. J. W.; Eggenhuisen, T. M.; Sietsma, J. R. A.; de Jong, K. P.; de Jongh, P. E. *Catal. Today* **2011**, *163*, 27.
(42) Arslan, I.; Walmsley, J. C.; Rytter, E.; Bergene, E.; Midgley, P. A. *J. Am. Chem. Soc.* **2008**, *130*, 5716.
(43) Vancea, I.; Thiele, U.; Pauliac-Vaujour, E.; Stannard, A.; Martin, C. P.; Blunt, M.; Moriarty, P. *Phys. Rev. E* **2008**, *78*, 1.
(44) Liu, X.; Khinast, J. G.; Glasser, B. J. *Chem. Eng. Sci.* **2012**, *79*, 187.
(45) Sun, X.; Shi, Y.; Zhang, P.; Zheng, C.; Zheng, X.; Zhang, F.; Zhang, Y.; Guan, N.; Zhao, D.; Stucky, G. D. *J. Am. Chem. Soc.* **2011**, *133*, 14542.
(46) Sietsma, J. R. A.; Meeldijk, J. D.; den Breejen, J. P.; Versluijs-Helder, M.; van Dillen, J. A.; de Jongh, P. E.; de Jong, K. P. *Angew. Chemie Int. Ed.* **2007**, *46*, 4547.
(47) Wolters, M.; Munnik, P.; Bitter, J. H.; de Jongh, P. E.; de Jong, K. P. *J. Phys. Chem. C* **2011**, 3332.
(48) Castner, D. G.; Watson, P. R.; Chan, I. Y. *J. Phys. Chem.* **1989**, *93*, 3188.
(49) Jacobs, G.; Das, T. K.; Zhang, Y.; Li, J.; Racoillet, G.; Davis, B. H. *Appl. Catal. A Gen.* **2002**, *233*, 263.
(50) Weststrate, C. J.; Hauman, M. M.; Moodley, D. J.; Saib, A. M.; van Steen, E.; Niemantsverdriet, J. W. *Top. Catal.* **2011**, 811.
(51) Dehghan, R.; Hansen, T. W.; Wagner, J. B.; Holmen, A.; Rytter, E.; Borg, Ø.; Walmsley, J. C. *Catal. Letters* **2011**, *141*, 754.
(52) Den Breejen, J. P.; Radstake, P. B.; Bezemer, G. L.; Bitter, J. H.; Frøseth, V.; Holmen, A.; de Jong, K. P. *J. Am. Chem. Soc.* **2009**, *131*, 7197.
(53) Kiss, G. *J. Catal.* **2003**, *217*, 127.
(54) Moodley, D. J.; van de Loosdrecht, J.; Saib, A. M.; Overett, M. J.; Datye, A. K.; Niemantsverdriet, J. W. *Appl. Catal. A Gen.* **2009**, *354*, 102.
(55) Bae, J. W.; Kim, S.; Park, S.; Prasad, P. S. S.; Lee, Y.; Jun, K. **2009**, 3228.
(56) Park, S.-J.; Bae, J. W.; Lee, Y.-J.; Ha, K.-S.; Jun, K.-W.; Karandikar, P. *Catal. Commun.* **2011**, *12*, 539.
(57) Balakrishnan, N.; Joseph, B.; Bhethanabotla, V. R. *Appl. Catal. A Gen.* **2013**, *462-463*, 107.
(58) Peña, D.; Griboval-Constant, A.; Diehl, F.; Lecocq, V.; Khodakov, A. Y. *ChemCatChem* **2013**, *5*, 728.
(59) Chambrey, S.; Fongarland, P.; Karaca, H.; Piché, S.; Griboval-Constant, A.; Schweich, D.; Luck, F.; Savin, S.; Khodakov, A. Y. *Catal. Today* **2011**, *171*, 201.
(60) Sadeqzadeh, M.; Hong, J.; Fongarland, P.; Curulla-Ferré, D.; Luck, F.; Bousquet, J.; Schweich, D.; Khodakov, A. Y. *Ind. Eng. Chem. Res.* **2012**, 11955.
(61) Schanke, D.; Hilmen, A.; Bergene, E.; Kinnari, K. *Catal. Letters* **1995**, *34*, 269.
(62) Schanke, D.; Hilmen, A.; Bergene, E. *Energy & Fuels* **1996**, *10*, 867.
(63) Krishnamoorthy, S.; Tu, M.; Ojeda, M. P.; Pinna, D.; Iglesia, E. *J. Catal.* **2002**, *211*, 422.
(64) Sehested, J.; Carlsson, A.; Janssens, T. V. W.; Hansen, P. L.; Datye, A. K. *J. Catal.* **2001**, *197*, 200.
(65) Richardson, J. T.; Crump, J. G. *J. Catal.* **1979**, *57*, 417.
(66) Neouze, M.-A. *J. Mater. Sci.* **2013**, *48*, 7321.
(67) Xin, H. L.; Mundy, J. A.; Liu, Z.; Cabezas, R.; Hovden, R.; Kourkoutis, L. F.; Zhang, J.; Subramanian, N. P.; Makharia, R.; Wagner, F. T.; Muller, D. A. *Nano Lett.* **2012**, *12*, 490.
(68) Wickman, B.; Seidel, Y. E.; Jusys, Z.; Kasemo, B.; Behm, R. J. *ACS Nano* **2011**, *5*, 2547.
(69) Seidel, Y.; Jusys, Z.; Wickman, B.; Kasemo, B.; Behm, R. J. *ECS Transitions* **2010**, *25*, 91.

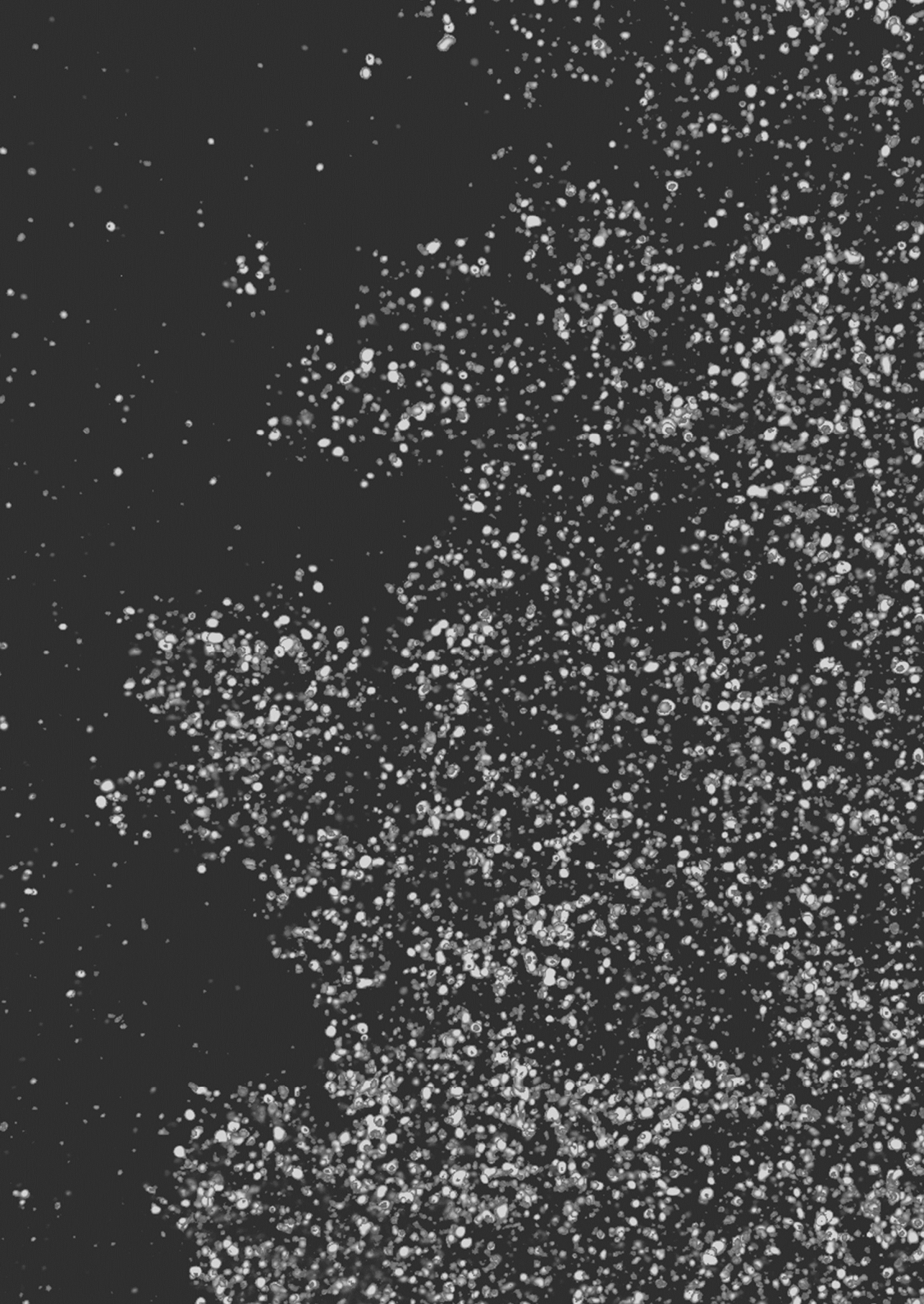

Chapter 5

Effects of Drying Conditions on the Synthesis of Co/SiO_2 and Co/Al_2O_3 Fischer-Tropsch Catalysts

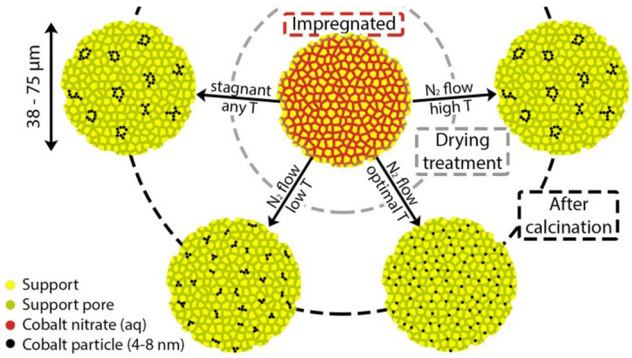

The nanoscale distribution of the supported metal phase is an important property for highly active, selective and stable catalysts. Here, the nanoscale redistribution and aggregate formation of cobalt nitrate during the synthesis of supported cobalt catalysts were studied. Drying over a range of temperatures in stagnant air resulted in cobalt particles (8 nm) present in large aggregates (30 - 150 nm). However, drying in an N_2 flow resulted in cobalt nanoparticles distributed either in aggregates or uniformly on various SiO_2 and γ-Al_2O_3 supports, critically dependent on the drying temperature. The mechanism of aggregation was studied through chemical immobilization of the precursor on a silica support after drying in an N_2 flow. The aggregation behavior upon drying in a gas flow at temperatures below 100 °C showed a remarkable similarity to distributions obtained upon the dewetting of colloidal films, suggesting a physical process. Alternatively, by inducing decomposition of the cobalt nitrate above 100 °C before drying was complete, aggregation was brought about through a chemical process that occurred both in stagnant and flowing gas. A γ-alumina support exhibited increased precursor-support interactions and displayed little cobalt aggregation upon drying in a gas flow, but extensive aggregation upon drying in stagnant air. The aggregation behavior was further studied on silica supports with pore sizes between 3 to 15 nm and tested under industrially relevant Fischer-Tropsch conditions, which revealed that uniform cobalt nanoparticle distributions were up to 50% more active compared to aggregated systems. Thus, hydrodynamics and temperature of the gas phase are critical parameters to control nanoscale distributions during drying of functional nanomaterials such as supported catalysts.

Adapted with permission from: P. Munnik et al. *ACS Catal.* **2014**, *4*, 3219.

INTRODUCTION

Supported transition metal nanoparticles are used as catalysts in many industrial processes. The size, composition and chemical environment of these particles as well as their distribution over the support greatly influences the activity, selectivity and stability of the catalysts.[1–4] Therefore, control over the synthesis of these nanomaterials is of utmost importance.[5–7] However, although the number of fundamental studies on catalyst preparation is increasing, the physiochemical processes that take place during synthesis are often not understood.

A facile and cost-effective preparation method is the impregnation of a metal precursor solution onto a porous support, such as alumina, silica or titania. The impregnation can be done to incipient wetness, whereby the impregnating volume is equal to the pore volume of the support, eliminating the need for a filtration step. Evaporation of the solvent, followed by decomposition of the precursor via a thermal treatment, leads to supported metal oxides. Metal nitrates precursors are often used, as their high solubility allows for high metal loadings in a single impregnation step. However, poor metal oxide dispersions and inhomogeneous distributions of the metal oxide are frequently obtained. Many studies report on improvement by changing the solvent or precursor[8–15], co-impregnation with organic molecules[7,16–19] or modifying the drying or calcination procedure.[20–28] However, fundamental knowledge on, and control over, inhomogeneous metal oxide distributions and precursor redistribution is lacking.

The drying step has long been known to have a large impact on the macroscopic distribution of the active phase, especially for impregnations with diluted precursor solutions.[29,30] Recently, models have shown that at high nickel nitrate concentrations, homogeneous macroscopic distributions can be obtained after impregnation and drying.[31] In chapter 3, using freeze-drying it was shown that the drying step can also have a large influence on the nanometer scale distribution of cobalt nitrate on silica gel supports.[32,33] In chapter 4, the nanoscale redistribution was further controlled by drying in an N_2 fluidized bed reactor at different temperatures.[34] Both low and high drying temperatures resulted in the formation of agglomerates, and an optimum temperature of 100 °C was found whereby homogeneous distributions were obtained.

When silica is used as a support, the low point of zero charge (PZC), generally between a pH of 3 to 4, results in little electrostatic interaction between the support and cobalt ions of the metal nitrate precursor solution, which has a similar pH. In contrast, electrostatic interactions[5,35] could start to play a role in the drying and agglomeration process on γ-alumina, also a widely used support in academia and industry but which has a higher PZC of 8-9. Alternatively, metal nitrates can be immobilized through the use of nitric oxide (NO), which stimulates the hydrolysis of several metal nitrates at low temperature, leading to the formation of metal hydroxynitrate phases ($M_x(OH)_y(NO_3)_z$, whereby M=Cu, Ni or Co).[23,28,36,37] This phase is immobile, and further heat treatment leads to oxygen scavenging by NO during the decomposition of cobalt (hydroxy)nitrate and the formation of small cobalt oxide particles.[20,23,38]

In this chapter, we further study the mechanism and compounds involved in the nanoscale redistribution of cobalt nitrate during drying. We first show that the formation of cobalt hydroxynitrate is possible for an impregnated and dried $Co(NO_3)_2/SiO_2$ sample with low water content. This precursor immobilization technique was subsequently used to study the drying imprint on the nanoscale distribution of cobalt on silica gel at different temperatures. Next, a γ-alumina support was studied, and finally the effect of pore size on the nanoscale distribution was studied using different silica gels, as well as the impact of the cobalt nanoscale distribution on the activity and selectivity in the Fischer-Tropsch synthesis.

EXPERIMENTAL

Catalyst Synthesis. Commercially available silica gels (SG) and γ-alumina (GA) were used as supports (Table 5.1. Davicat, Grace-Davidson and Puralox, Sasol). Before precursor loading the support was sieved to a grain size of 38 - 75 μm. Solution impregnation was performed to incipient wetness using a saturated $Co(NO_3)_2$ (aq) solution (4.2 M, $Co(NO_3)_2{\cdot}6H_2O$, >99% Sigma-Aldrich) at room temperature under static vacuum.

Table 5.1. Physical properties of the supports and final cobalt loading for the corresponding catalysts.

Support[a]	BET surface area (m^2/g)	Pore volume (P/P_0 = 0.93) (mL/g)	Average pore diameter (nm)	Co loading (wt.%)
SG3	720	0.5	3	10
SG8	500	0.9	8	16
SG15	330	1.2	15	21
GA9	250	0.5	9	17

*SG = silica gel, GA = γ-alumina; number refers to the average pore size (nm).

Different drying treatments were applied to 100 - 400 mg of the impregnated grains in a fluidized bed reactor. The oven was first brought to a temperature of 25, 50, 75, 100, 125 or 150 °C after which the sample was introduced and an N_2 flow was applied with a gas hourly space velocity (GHSV) of 5000 h^{-1} for 48, 24, 16, 3, 3 or 2 hours, respectively. As reported previously, these drying times were sufficient to induce precipitation of the precursor, while greatly extended drying times did not alter the nanoscale distributions of the final catalysts.[34] Alternatively, the sample was cooled to -45 °C for 5 hours under N_2 and drying was performed at -30 °C at reduced pressure (0.02 - 0.03 mbar) for 3 days,[32] or drying was performed at room temperature in a dynamic vacuum (~50 mbar) or in a muffle oven at 90 °C for 1 day or 8 hours, respectively. Calcination of all dried catalysts was performed by transfer to or further heating of the fluidized bed reactor to 350 °C (1 °C/min, 1 hour) in a flow of pure N_2 or 1% v/v NO/N_2 (GHSV 30000 h^{-1}). In this study, NO was used to immobilize the precursor after drying by formation of cobalt hydroxynitrate. However, this also led to very small particles, which can be difficult to image and are undesirable for the Fischer-Tropsch synthesis. Because

calcination in an N_2 flow results in somewhat larger particles, it was used for the γ-alumina samples and the samples that were used for catalysis. For γ-alumina, after calcination the sample was impregnated, dried and calcined a second time to increase the metal loading.

Catalyst Characterization. N_2-Physisorption measurements were performed at -196 °C using a Micromeritics Tristar 3000 apparatus. Prior to analysis, samples were dried in He flow for 16 hours at 200 °C. Average pore diameter was calculated using the BJH desorption isotherm.

Thermogravimetric analysis (TGA, Q50 TA Instruments) was used to determine the residual water content of impregnated samples after different drying treatments by measuring the weight loss after heating to 500 °C for 30 min (10 °C/min) under a 60 mL/min N_2 flow. The weight loss was corrected for the loss of water by desorption and condensation of silanol groups from the pristine silica gel, which was experimentally found to occur between 150 and 500 °C. The rest of the weight loss was attributed to the loss of any residual water and the decomposition of $Co(NO_3)_2$ to Co_3O_4.

TGA-MS was measured on a Pyris 1 TGA, (Perkin Elmer). 10 Mg of the impregnated silica was heated at 5 °C/min to 800 °C. Above 300 °C, no significant weight loss or MS signals were detected.

In-situ diffuse reflectance infrared Fourier transform spectroscopy (DRIFTS) measurements were performed on a Bruker Tensor 27 apparatus utilizing a HVC-DRP-3 diffuse reflectance reaction chamber with CaF_2 windows and a high-sensitivity liquid N_2-cooled MCT detector. To minimize temperature gradients the bottom of the bed was filled with SiC, which was separated from the sample by a grid. 1% v/v NO in N_2 or pure N_2 was flown through 10 mg of sample at 10 ml/min from top to bottom while the chamber was heated to 300 °C at 2 °C/min. Spectra were taken at a resolution of 4 cm^{-1} at 2 min intervals.

X-ray diffraction (XRD) patterns were recorded between 20 and 90 °2θ with a Bruker-AXS D2 Phaser X-ray Diffractometer using Co-$K_{\alpha 12}$ radiation (λ = 1.790 Å). The volume averaged Co_3O_4 crystallite size was determined using the Scherrer equation with a shape factor k = 0.9 and line broadening analysis on the (220), (311) and (400) peaks by a fitting procedure in Eva2 software (Bruker AXS).

The catalyst grains were embedded in a two component epoxy resin (Epofix, EMS) and cured at 60 °C overnight. The embedded catalysts were then cut into thin sections with a nominal thickness of 50 nm using a Diatome Ultra 35° diamond knife mounted on a Reichert-Jung Ultracut E microtome and collected on a copper grid. Bright field transmission electron microscopy (TEM) images were obtained on a Tecnai 12, operated at 120 keV. High angle annular dark field (HAAFD) STEM was performed on a Tecnai 20 equipped with a field emission gun operated at 200 keV.

Catalytic Testing. Fischer-Tropsch synthesis was performed on a Flowrence (Avantium) 16 parallel reactor unit. Each stainless steel reactor was loaded with the same amount of cobalt, resulting in a weight loading of 80, 50 or 40 mg for catalysts made from SG3, SG8 or SG15, respectively. Catalysts were mixed with 200 mg SiC, and reduced in-situ in 25 vol.% H_2/He at

500 °C for 8 hours (1 °C/min). Afterwards, the reactors were cooled down to 180 °C at which the pressure was increased to 20 bar under H_2. Next, the feed was changed to a H_2/CO ratio of 2.0 with 5 vol.% He, which functioned as internal standard for the on-line GC (Agilent 7890A). After 1 hour, the temperature was increased to the reaction temperature of 220 °C at 1 °C/min. After 100 hours on-stream, the conversion was lowered by increasing the gas hourly space velocity (GHSV) so that the performance of all catalysts could be reported at 30 - 35% conversion, eliminating effects of conversion on selectivity.

RESULTS AND DISCUSSION

Hydroxynitrate Formation. To study the cobalt nitrate distributions on a silica gel with 8 nm pores (SG8) after different drying treatments, samples were subjected to a thermal treatment in 1% v/v NO/N_2 after drying. This treatment is known to induce the formation of cobalt hydroxynitrate,[23,28,36,37] an immobile phase that prevents further redistribution upon thermal decomposition into cobalt oxide. NO-assisted decomposition of cobalt nitrate also results in smaller particles compared to decomposition in stagnant air or an N_2 flow.[20] To ensure hydrolysis of cobalt nitrate did occur after drying, an *In-situ* Diffuse Reflectance Infrared Fourier Transform Spectroscopy (DRIFTS) study was performed in 1% v/v NO/N_2 on a cobalt nitrate loaded SG8 sample impregnated and dried at 100 °C in N_2. Figure 5.1 shows the spectrum evolution during heat treatment. The initial broad -OH stretching vibration band between 3100 and 3600 cm^{-1} accompanied by a sharp H-O-H bending vibration band at 1630 cm^{-1} indicated some water was still present after drying. These bands gradually decreased, and at 150 °C a sharp -OH band formed at 3585 cm^{-1}, accompanied with a shift in the -O-N-O_2 stretching vibration band from the nitrate group from 1580 to 1540 cm^{-1}. These bands were previously attributed to cobalt hydroxynitrate species,[23,36] and disappeared simultaneously above 200 °C, when Co_3O_4 was formed.

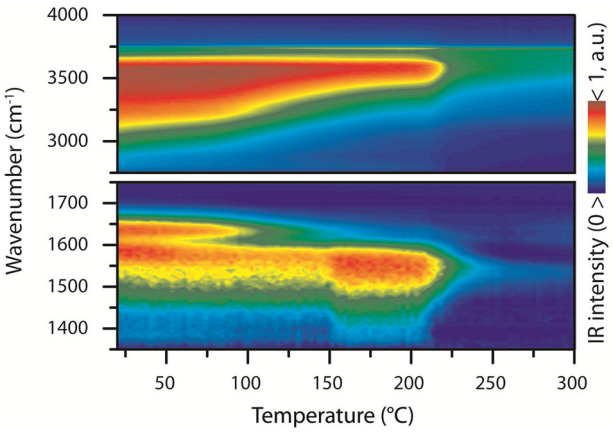

Figure 5.1. *In-situ* DRIFTS of cobalt nitrate loaded SG8 during calcination in 1% NO after impregnation and drying at 100 °C in N_2. Formation of an OH^- peak at 3585 cm^{-1} combined with an NO_3^- peak at 1540 cm^{-1} is characteristic of the formation of cobalt hydroxynitrate. Above 200 °C, the peaks disappear in a single step, indicating direct decomposition to Co_3O_4.

The mass loss upon heating was investigated by Thermogravimetric Analysis (TGA). The SG8 sample after impregnation and drying at 100 °C in N_2 showed a remaining water content of about 0.4 $mol_{H2O}/mol_{Co(NO3)2}$. This suggests a phase with an OH:Co ratio of at most 0.5 was formed ($Co_2OH(NO_3)_3$), whereas previous studies reported hydroxynitrates with higher hydroxyl content ($Co_3(OH)_4(NO_3)_2$ or $Co_2(OH)_3NO_3$).[23,28] However, TGA results might underestimate the remaining water content, and it is possible that surface hydroxyl groups of the silica or strongly adsorbed water contributed to the formation. Moreover, the formation of cobalt hydroxynitrate need not be quantitative. Regardless, it was clear that even after drying, hydroxynitrates were formed via the NO assisted hydrolysis of cobalt nitrate.

Precursor Immobilization. The nanoscale distributions of six SG8 supported Co_3O_4 catalysts calcined in 1% NO at 350 °C with a ramp of 1 °C/min are shown in Figure 5.2. The drying temperature before calcination was varied between 25 and 150 °C. The sample dried at 25 °C exhibited cobalt as small 3 to 4 nm particles in large irregular aggregates. These nanoparticle aggregates were 100 to 200 nm long and 50 to 100 nm wide, many times the average support pore size of 8 nm. Increasing the drying temperature resulted in gradually smaller aggregates until at 100 °C a homogeneous distribution of similarly sized 3 to 4 nm cobalt crystallites was observed. Drying at 125 °C resulted in a bimodal distribution of the small homogeneously distributed particles and aggregates of 15 - 20 nm, consisting of 8 nm particles. After drying at 150 °C most of the cobalt was located as 8 nm particles in 50 nm spherical aggregates, whereas few small particles were found.

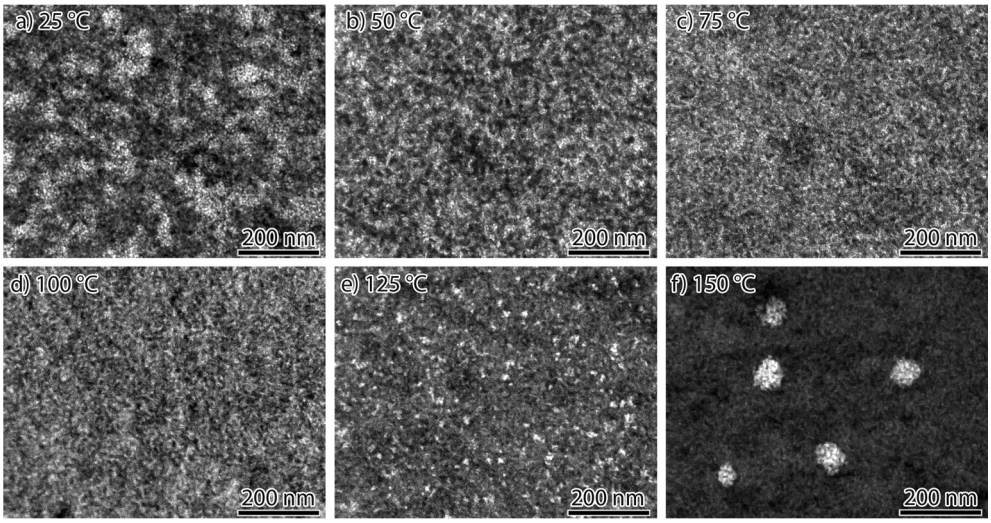

Figure 5.2. HAADF-STEM images of SG8 supported Co_3O_4 catalysts after calcination in 1% NO at 350 °C, whereby the drying temperature in an N_2 flow (before calcination) was varied between 25 and 150 °C. Different aggregates of cobalt nanoparticles (white) were found on the silica SG8 support (black) depending on the drying temperature. (a): Dried at 25 °C (b): 50 °C, (c): 75 °C, (d): 100 °C, (e): 125 °C, (f): 150 °C.

These results illustrate the two possible ways of aggregate formation previously postulated.[34] At temperatures between 25 °C and 100 °C, a difference in the drying rate resulted in a different degree of aggregation during the precipitation of cobalt nitrate species. This aggregation occurred in the form of irregular domains as large as 200 nm, more than 20 times the size of the average pore. During the subsequent heat treatment in 1% NO, this precipitated phase was converted into cobalt hydroxynitrate, which decomposed into small cobalt oxide nanoparticles at higher temperatures. Since one immobile phase was converted into another, little redistribution occurred, so that the resulting patterns are the imprint of where the cobalt nitrate precipitated during drying.

At drying temperatures above 100 °C, part of the cobalt nitrate started to decompose into Co_3O_4 during the drying process. Previously it was shown that 20% of the cobalt nitrate decomposed into Co_3O_4 during drying at 125 °C.[34] This decomposition occurred in the absence of NO, but in the presence of H_2O, which induces mobility and leads to larger particles and aggregation,[20,23,39] forming small (15 – 20 nm) aggregates of 8 nm particles. The remaining 80% of the cobalt nitrate which did not decompose during drying was subsequently exposed to NO during further heat treatment which resulted in small (3 – 4 nm) nanoparticles, explaining the bimodal distribution. At a drying temperature of 150 °C, more cobalt nitrate decomposed during drying, resulting in many 8 nm particles located in 50 nm spherical aggregates that formed during drying, while little unreacted cobalt nitrate remained to form 3 – 4 nm cobalt particles via NO-assisted decomposition. Although drying can affect the macroscopic distribution across pellets or grains, homogeneous distributions were observed on these larger length scales.

Similar patterns to those observed after drying between 25 and 100 °C have been found in different fields of physics and chemistry, most noticeably in the drying of colloidal wet films.[40–44] The drying of colloidal systems has been extensively studied, and models have been proposed that explain the patterns found experimentally for a wide variety of colloids, solvents and substrates. In those models, the drying temperature, and so the drying rate, was found to be key in obtaining differently sized aggregates and patterns. At a high drying rate, solvent evaporation is thought to occur throughout the entire film within a very short time window, called spinodal dewetting, resulting in deposition of the colloids close to where they were in solution. At lower rates, dewetting does not occur homogeneously or as rapidly, so that colloids can move and gather in patches, which increase in size with decreasing temperature. Despite the fact that a colloidal dispersion on a flat surface is very different from a dissolved salt in a 3D porous network, such as in the present work, the similar temperature dependency is remarkable. (For an example, compare the results obtained here after drying at 25 and 50 °C with the 3rd and 4th column of Figure 1 in reference 43). It appears that in both cases, redistribution of the liquid phase, which is determined by the rate of drying determines the final distribution of particles.

At very low drying rates, the colloidal dewetting models predict the formation of large cellular networks, whereby the cell walls are made up of colloids whereas the cell bodies are

empty. Very slow drying is thought to lead to isolated gas bubbles that nucleate and subsequently grow, entraining the colloidal rich phase along in the meniscus surrounding the growing gas bubble. Deposition of colloids occurs when two menisci meet, at which point all the material is deposited in the thin strands forming the cell walls, enclosing mostly empty cells where the gas bubble used to be. A similar mechanism could be envisioned in porous media, whereby growing gas bubbles inside the impregnated support[45] force the dissolved precursor into increasingly concentrated areas, until the menisci of two bubbles meet and the salt concentration suddenly exceeds the supersaturation, causing precipitation. To investigate this, cobalt nitrate impregnated on silica gel (SG8) was dried at -30 °C under reduced pressure, followed by calcination in 1% NO. It should be noted that this drying temperature was previously found to be insufficient to freeze the precursor, such that redistribution was possible.[32] The resulting material exhibited a cellular network whereby the cells were made up of empty silica, while the cell walls were cobalt rich and connected to other cells (Figure 5.3a). It is remarkable that a relatively simple 2D model of colloidal particles in a liquid film behaves very similar to a complicated 3D system in which a salt precursor precipitates from a solution.

An alternative explanation may be found in capillary flow phenomena. Capillary flow can lead to inhomogeneous distributions, especially in supports with bi- or multimodal pore size distributions, whereby the meniscus at the drying front recedes from larger to smaller pores, entraining the dissolved precursor with it.[29] Figure B.4 shows the pore size distributions of all support materials, which were relatively narrow and monomodal. Nonetheless, for drying at low temperatures such as at 25 °C, capillary flow may be significantly faster than the drying rate, so that capillary flow could play a role in the redistribution of the precursor phase. At higher temperatures, drying may be faster relative to capillary flow, especially if highly viscous cobalt nitrate tetra- or di-hydrates form, so that redistribution may be limited. Regardless of the mechanism, it is clear that aggregate formation at 100 °C can be limited by applying an N_2 flow leading to a fast drying rate based on physical processes.

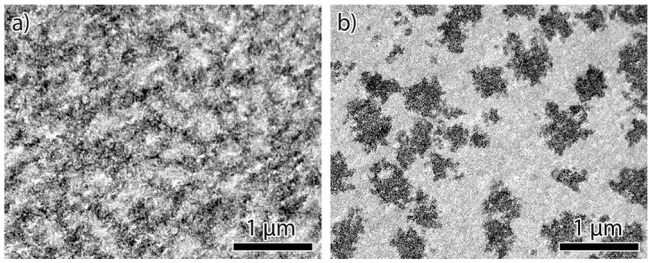

Figure 5.3. Bright field TEM images of two Co_3O_4 (in black) catalysts on SG8 created by heat treatment in a 1% NO atmosphere. (a) Dried at -30 °C in vacuum, whereby a cellular network was formed, followed by calcination in NO. (b) Directly calcined in an NO/N_2 flow without prior drying in an N_2 flow, resulting in large nanoparticle islands.

Drying at higher temperatures showed aggregation can also occur via a chemical process, through nucleation and growth of cobalt oxide from a cobalt nitrate solution. To explore whether a similar effect could be created at lower temperatures, a sample was directly dried and heat treated in a 1% NO/N_2 flow after impregnation, without a drying step in an N_2 flow.

Figure 5.3b shows this led to the formation of large islands of a few hundred nanometers, separated by large empty areas. This behavior is understood by the nucleation and growth of a hydroxynitrate phase from a liquid precursor. As soon as nucleation of the precipitate occurs, further growth resulted in large cobalt hydroxynitrate patches, which are subsequently converted to small cobalt oxide particles at higher temperature. These patches could even become several micrometers in size (see Appendix B, Figure B.1). Thus, although aggregate formation can occur through a physical process, whereby it is mainly dependent on the drying rate, the chemistry of the system remains highly relevant and can dominate aggregate formation.

γ-Alumina Support. Compared to silica, which has a PZC of 3 - 4, γ-alumina shows a stronger interaction with the precursor solution of pH 3 because of its high PZC (8 - 9). This could affect the impregnation and drying step, and adsorption of Co^{2+} complexes onto the support via a ligand exchange between water and surface hydroxyl groups has been observed.[46–48] To investigate whether such support precursor interactions influence the aggregation behavior of cobalt nitrate, a γ-alumina with 9 nm pores (GA9) was impregnated and dried at different temperatures. Again, heat treatment in 1% NO/N_2 after drying resulted in very small particles, as is known from literature.[37,49] However, these particles were very difficult to image, even after a double impregnation to increase the loading from 9 to 17 wt.% (see Appendix B, Figure B.2). For this reason, the heat treatment after drying was performed in N_2 rather than NO. In an N_2 flow, hydroxynitrates do not form despite the high pH of the support, so that larger particles were obtained that allowed clear visualization of the spatial distribution.

On γ-alumina, aggregate formation is often reported in the context of Fischer-Tropsch catalysts.[50,51] Attempts to avoid the formation of aggregates include modification of the support[52] or co-impregnation with organic molecules.[16] However, these strategies only apply in specific cases. Conventional synthesis of such catalysts includes drying the impregnated material in stagnant air, often between 60 and 120 °C, before performing a calcination treatment. Figure 5.4a shows a sample dried at 90 °C in stagnant air followed by calcination in N_2. Cobalt particles of 8 nm were observed in irregularly shaped aggregates between 30 - 60 nm throughout the sample, similar to what is described in literature. Drying at 60 and 120 °C showed comparable results, and drying at 150 °C resulted in even larger aggregates of 100 - 150 nm (see Appendix B, Figure B.3).

A large difference was observed upon drying in an N_2 fluidized bed. After drying at 25 and 100 °C, no aggregates were found at all (Figure 5.4b-c); the 7 - 8 nm sized particles were homogeneously distributed throughout the support. Even drying at 150 °C in an N_2 flow only resulted in small 20 - 30 nm aggregates (Figure 5.4d). Thus, although aggregates formed upon drying in stagnant air regardless of temperature on γ-alumina, a procedure whereby the sample was dried in an N_2 fluidized bed reactor completely prevented aggregation when a temperature between 25 and 100 °C was used, resulting in uniform nanoparticle distributions.

Upon comparing γ-alumina with silica, discussed in the previous section, the homogeneous distribution observed on γ-alumina after drying at 25 °C is remarkable, and

suggests the increased precursor-support interactions suppressed the formation of aggregates at low temperatures. Although N_2 was used during heat treatment, so that some redistribution might be expected, previous results on SiO_2 heat treated in N_2 showed aggregation were also present at low temperature on SiO_2,[34] so that the difference cannot be explained by the alternative heat treatment. Even at 150 °C, aggregates were smaller than those found on SiO_2. However, removing the gas flow during drying greatly increased the size of the aggregates (see Appendix B), underlining the importance of a gas flow regardless of the temperature.

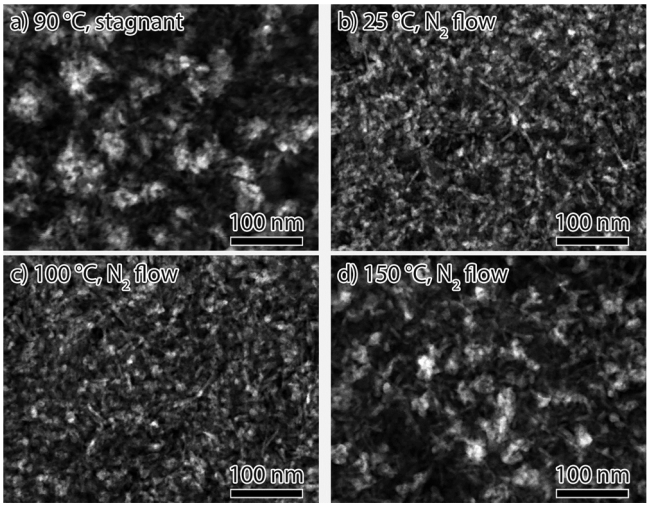

Figure 5.4. HAADF-STEM images of Co_3O_4 (white) on γ-alumina (GA9) using different drying treatments, followed by calcination at 350 °C in an N_2 flow. (a) dried at 90 °C without a gas flow. (b) dried in N_2 fluidized bed at 25 °C, (c) 100 °C and (d) 150 °C.

Influence of Pore Size. To further investigate aggregate formation, three different silica supports with pore sizes of 3, 8 and 15 nm were impregnated and dried in a N_2 flow at 25, 100 and 150 °C. To study the effect of drying on Fischer-Tropsch catalysis, subsequent calcination was performed in N_2 rather than NO to form larger 7 - 11 nm sized particles, which are more favorable for the Fischer Tropsch synthesis.[53–55] Figure 5.5 shows the nanoscale cobalt distribution of silica with 3 nm pores (SG3, top row), 8 nm pores (SG8, middle row) and 15 nm pores (SG15, bottom row). For each silica, drying at 25 °C led to the formation of medium sized aggregates (left column), drying at 100 °C resulted in homogeneous distributions (middle column) while after drying at 150 °C (right column) large aggregates were observed. The average sizes of the aggregates and average Co_3O_4 crystallite sizes as determined by TEM and XRD, respectively, are shown in Table 5.2. For the catalysts dried at 25 °C, a trend towards smaller aggregate sizes for larger pore sizes was observed, while this trend is less evident after drying at 150 °C. The Co_3O_4 crystallite sizes ranged from 8 to 12 nm regardless of pore size, even for SG3. While this could indicate extensive deposition of cobalt on the external surface, this was not observed. Thus, it appeared cobalt was either preferentially deposited in larger pores or the growth of Co_3O_4 crystallites deformed or locally broke up the silica structure.

The decrease in aggregate size for larger pore silicas obtained after drying at 25 °C indicated that also the support pore structure played an important role in the formation of

aggregates when the drying rate was low. This is tentatively attributed to the increased drying rate that is possible for larger pore silicas[45], thereby reducing the extent of redistribution. At 100 °C, this effect was less noticeable because a relatively fast drying rate was already achieved. Since drying at 150 °C concerned aggregate formation via decomposition, it was not affected significantly by the pore size. Finally, we note that a larger silica pore size (23 nm) exhibited macroscopic redistribution effects upon drying (Figures B.5 and B.6). This could be suppressed by using melt infiltration rather than solution impregnation (Figure B.7), so that a reduced amount of solvent limited redistribution.

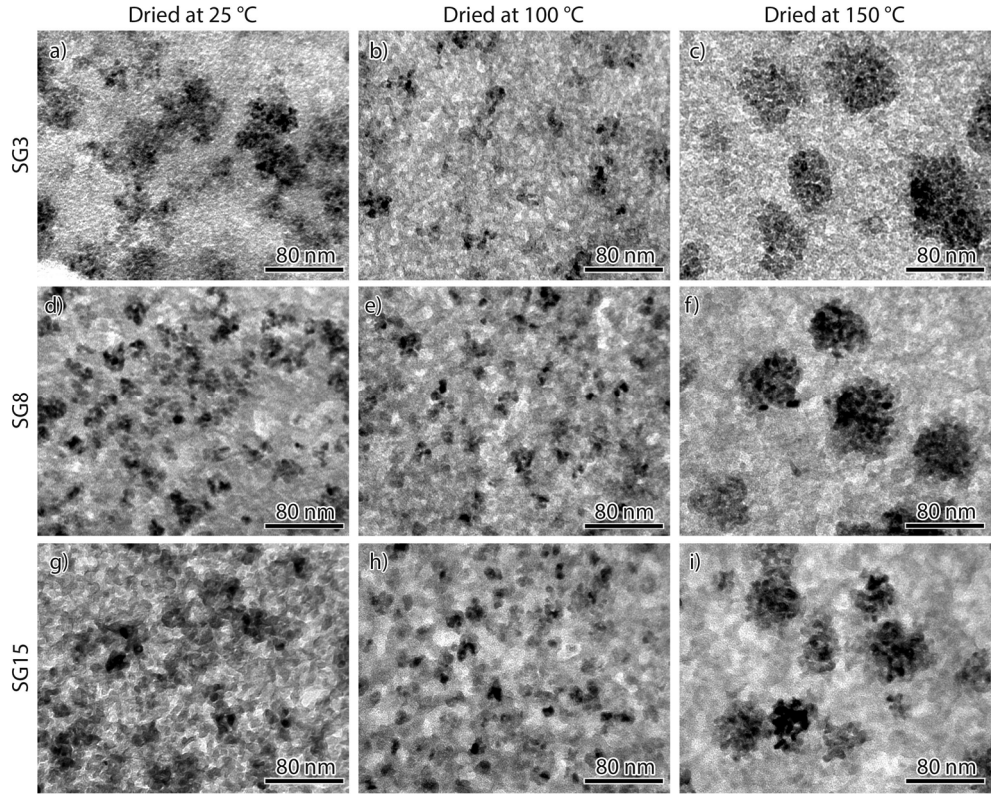

Figure 5.5. TEM of *Ex-nitrate* cobalt catalysts synthesized using 3 different silica gels and 3 different drying temperatures, followed by calcination in N_2. Top row) silica gel with 3 nm pores. Middle row) silica gel with 8 nm pores. Bottom row) silica gel with 15 nm pores. Left column) dried at 25 °C. Middle column) dried at 100 °C, right column) dried at 150 °C.

Catalysis. To investigate the influence of the interplay between pore size and spatial distribution on catalytic performance, the nine catalysts shown in Figure 5.5 were tested in the Fischer-Tropsch synthesis reaction, whereby hydrogen and carbon monoxide are converted into long chain hydrocarbons, at industrially relevant conditions (20 bar, H_2/CO ratio of 2.0, 220 °C). After 100 hours, the gas flow was adapted such that for each catalyst the CO

conversion was between 30 and 35%. The results are summarized in Table 2. Although the degree of aggregation is also known to affect the stability of the catalysts, this has been described in detail in a separate paper.[34] The cobalt-weight based activities varied between 4.3 and 7.7 (10^{-5} $mol_{CO} \cdot g_{Co}^{-1} \cdot s^{-1}$), while the selectivity to long hydrocarbons chains with 5 carbons or more (C_{5+}) varied between 75 and 85 wt.%. Comparison of the most homogeneous (obtained after drying at 100 °C) and the most aggregated (obtained at 150 °C) catalysts shows that in each case the uniform catalyst was most active, while the aggregated catalyst was most selective. Catalysts prepared by drying at 25 °C, which had intermediate aggregate sizes, generally lay in between these values. The catalysts based on SG3 showed the lowest activity and selectivity, averaging around 4.5 and 75.5 wt.%, respectively, with little variation caused by the degree of aggregation. For SG8, medium activities and selectivities were found. The homogeneously distributed catalyst was 10% more active compared to the aggregated one, which in turn showed a 2% higher selectivity, similar to what was reported previously.[34] With SG15, the highest activities and selectivities, and largest influence of the degree of aggregation was found. The homogeneously distributed catalyst was 50% more active than the aggregated one, which was 4% more selective.

Table 5.2. Catalyst properties after calcination and catalytic results during Fischer-Tropsch synthesis, measured after 100 h on-stream at 20 bar, H_2/CO ratio of 2.0, 220 °C, 30 - 35% CO conversion.

Silica support	Drying Temperature (°C)	Crystallite size (XRD) (nm)	Aggregate size (TEM) (nm)	CTY (10^{-5} $mol_{CO} \cdot g_{Co}^{-1} \cdot s^{-1}$)	C_1 (wt.%)	C_{5+} (wt.%)
	25	8	50	4.3	13.1	75.5
SG3	100	8	-	4.6	13.8	74.9
	150	7	65	4.7	13.1	75.9
	25	8	20	5.2	10.0	81.5
SG8	100	8	-	5.6	10.1	81.5
	150	9	60	5.0	8.9	83.3
	25	10	16	7.2	9.1	84.1
SG15	100	10	-	7.7	10.9	81.6
	150	11	55	5.2	8.6	85.2

It is clear that in general a larger pore size was favorable for the Fischer-Tropsch reaction, as has been studied and explained in detail before.[56–59] However, for the first time we show that the larger the pore size, the more important the role of the nanoscopic distribution in determining the activity and selectivity of the catalyst. Whereas the nanoscopic distribution in SG3 and SG8 only caused a maximum difference in activity of 10%, this difference could become as high as 50% in SG15. Although a comprehensive understanding of these effects would require more thorough investigation of the reduced catalysts, it is clear that the

distribution of the metal oxide plays a large role in determining the final activity, selectivity and stability.[34]

CONCLUSION

The mechanism of the nanoscale redistribution and aggregate formation of cobalt nitrate during the synthesis of supported cobalt catalysts was studied. On silica gel, heat treatment in a 1% NO gas flow was used after drying in an N_2 flow to immobilize cobalt nitrate via the formation of cobalt hydroxynitrates. Upon drying the impregnated sample in a nitrogen gas flow at 25 °C, small particles (3 - 4 nm) were located in large irregularly shaped aggregates (100 - 200 nm), many times the size of the pore diameter of the support (8 nm). Increasing the drying temperature in a gas flow reduced the size of the aggregates found after calcination in an NO-containing gas flow, until at 100 °C homogeneously distributed cobalt particles (3 - 4 nm) were found. This aggregation behavior greatly resembled the patterns observed in literature for the dewetting of colloidal films. This similarity was extended towards very slow drying at -30 °C, resulting in the formation of a cellular network type distribution, whereby small particles (3 - 4 nm) made up the walls of large (200 - 500 nm) cells empty of cobalt. Moreover, although a relatively narrow support pore size distribution was used, capillary flow could play a role in the formation of aggregates. Regardless of the mechanism, these results strongly suggest aggregate formation at these temperatures is the result of physical processes. Large cobalt aggregates (100 - 1000 nm) could also be formed by chemical processes at temperatures above 100 °C, which caused the deposition of Co_3O_4 from solution, or by hydroxynitrates precipitation during a heat treatment in a 1% NO flow without prior drying in N_2.

The role of the chemical nature of the support on the aggregation of cobalt nitrate was investigated using a γ-alumina, which exhibits stronger support-precursor interactions. Drying in stagnant air between 60 and 120 °C resulted in medium sized cobalt aggregates (30 - 60 nm) after calcination in N_2, similar to what is often found in literature. However, drying at 25 and 100 °C in an N_2 flow resulted in homogeneous distributions, showing the importance of using a flow during drying and suggesting that increased precursor-support interactions suppressed the formation of aggregates. Even at 150 °C, only small aggregates (20 - 30 nm) were found upon drying in an N_2 flow, whereas drying in stagnant air at 150 °C resulted in large aggregates (100 - 150 nm), underlining the importance of drying in an N_2 flow regardless of the temperature.

The role of pore size on the aggregate formation upon drying in an N_2 flow was studied using silica gels with 3, 8 and 15 nm pores. Larger pores resulted in slightly smaller aggregates, possibly related to faster drying rates in larger pores. Testing these catalysts under industrially relevant Fischer-Tropsch conditions revealed that homogeneously distributed catalysts could be up to 50% more active compared to aggregated catalysts. Thus, the hydrodynamics of the gas phase and temperature during the drying process are critical for controlling the nanoscale distribution during the synthesis of nanomaterials, and supported catalysts in particular.

ACKNOWLEDGMENTS

Mr. H. Meeldijk (Utrecht University) is acknowledged for HAADF-STEM measurements. Ms. M. Versluis-Helder (Utrecht University) is acknowledged for the TGA-MS measurements. Ms. E. van Donselaar (Utrecht University) is acknowledged for ultramicrotomy instructions. Mr. J.H. den Otter (Utrecht University) is acknowledged for N_2-physisorption measurements. The Electron Microscopy Unit at Utrecht University is acknowledged for their excellent facilities.

REFERENCES

(1) Farmer, J. A.; Campbell, C. T. *Science* **2010**, *329*, 933.
(2) Torres Galvis, H. M.; Bitter, J. H.; Khare, C. B.; Ruitenbeek, M.; Dugulan, A. I.; de Jong, K. P. *Science* **2012**, *335*, 835.
(3) Prieto, G.; Zečević, J.; Friedrich, H.; de Jong, K. P.; de Jongh, P. E. *Nat. Mater.* **2013**, *12*, 34.
(4) Cao, A.; Veser, G. *Nat. Mater.* **2010**, *9*, 75.
(5) Zhu, X.; Cho, H.; Pasupong, M.; Regalbuto, J. R. *ACS Catal.* **2013**, *3*, 625.
(6) Calderone, V. R.; Shiju, N. R.; Curulla-Ferré, D.; Chambrey, S.; Khodakov, A. Y.; Rose, A.; Thiessen, J.; Jess, A.; Rothenberg, G. *Angew. Chemie Int. Ed.* **2013**, *52*, 4397.
(7) Rane, S.; Borg, Ø.; Rytter, E.; Holmen, A. *Appl. Catal. A Gen.* **2012**, *437-438*, 10.
(8) Girardon, J. S.; Quinet, E.; Gribovalconstant, a; Chernavskii, P.; Gengembre, L.; Khodakov, A. Y. *J. Catal.* **2007**, *248*, 143.
(9) Girardon, J. S.; Lermontov, A. S.; Gengembre, L.; Chernavskii, P. A. *J. Catal.* **2005**, *230*, 339.
(10) Bae, J. W.; Kim, S.-M.; Kang, S.-H.; Chary, K. V. R.; Lee, Y.-J.; Kim, H.-J.; Jun, K.-W. *J. Mol. Catal. A Chem.* **2009**, *311*, 7.
(11) Kok, E.; Cant, N.; Trimm, D.; Scott, J. *Catal. Today* **2011**, *178*, 79.
(12) Rodríguez-González, V.; Marceau, E.; Beaunier, P.; Che, M.; Train, C. *J. Solid State Chem.* **2007**, *180*, 22.
(13) Marceau, E.; Löfberg, A.; Giraudon, J.-M.; Négrier, F.; Che, M.; Leclercq, L. *Appl. Catal. A Gen.* **2009**, *362*, 34.
(14) Zhang, L.; Dong, L.; Yu, W.; Liu, L.; Deng, Y.; Liu, B.; Wan, H.; Gao, F.; Sun, K.; Dong, L. *J. Colloid Interface Sci.* **2011**, *355*, 464.
(15) Marceau, E.; Che, M.; Čejka, J.; Zukal, A. *ChemCatChem* **2010**, *2*, 413.
(16) Borg, Ø.; Dietzel, P. D. C.; Spjelkavik, A. I.; Tveten, E. Z.; Walmsley, J. C.; Diplas, S.; Eri, S.; Holmen, A.; Rytter, E. *J. Catal.* **2008**, *259*, 161.
(17) Hong, J.; Marceau, E.; Khodakov, A. Y.; Griboval-Constant, A.; La, C.; Briois, V.; Chernavskii, P. A. *Catal. Today* **2011**, *175*, 528.
(18) Dumond, F.; Marceau, E.; Che, M. *J. Phys. Chem. C* **2007**, *111*, 4780.
(19) Qiu, S.; Zhang, X.; Liu, Q.; Wang, T.; Zhang, Q.; Ma, L. *Catal. Commun.* **2013**, *42*, 73.
(20) Sietsma, J. R. A.; Meeldijk, J. D.; den Breejen, J. P.; Versluijs-Helder, M.; van Dillen, J. A.; de Jongh, P. E.; de Jong, K. P. *Angew. Chemie Int. Ed.* **2007**, *46*, 4547.
(21) Munnik, P.; Wolters, M.; Gabrielsson, A.; Pollington, S. D.; Headdock, G.; Bitter, J. H.; de Jongh, P. E.; de Jong, K. P. *J. Phys. Chem. C* **2011**, *115*, 14698.
(22) Van de Loosdrecht, J.; Barradas, S.; Caricato, E. A.; Ngwenya, N. G.; Nkwanyana, P. S.; Rawat, M.; Sigwebela, B. H.; van Berge, P. J.; Visagie, J. L. *Top. Catal.* **2003**, *26*, 121.
(23) Wolters, M.; Munnik, P.; Bitter, J. H.; de Jongh, P. E.; de Jong, K. P. *J. Phys. Chem. C* **2011**, *115*, 3332.
(24) Huang, C.; Bai, S.; Lv, J.; Li, Z. *Catal. Letters* **2011**, *141*, 1391.
(25) Boubekr, F.; Davidson, A.; Casale, S.; Massiani, P. *Microporous Mesoporous Mater.* **2011**, *141*, 157.
(26) Huang, X.; Dong, W.; Wang, G.; Yang, M.; Tan, L.; Feng, Y.; Zhang, X. *J. Colloid Interface Sci.* **2011**, *359*, 40.

(27) Imperor-Clerc, M.; Bazin, D.; Appay, M.; Beaunier, P.; Davidson, A. *Chem. Mater.* **2004**, *16*, 1813.

(28) Hong, J.; Marceau, E.; Khodakov, A. Y.; Griboval-Constant, A.; La Fontaine, C.; Briois, V. *Chem. a Eur. J.* **2012**, 2802.

(29) Neimark, A. V; Kheifez, L. I.; Fenelonov, V. B. *Ind. Eng. Chem. Prod. Res. Dev.* **1981**, 439.

(30) Lekhal, A.; Glasser, B. J.; Khinast, J. G. *Chem. Eng. Sci.* **2001**, *56*, 4473.

(31) Liu, X.; Khinast, J. G.; Glasser, B. J. *Chem. Eng. Sci.* **2012**, *79*, 187.

(32) Eggenhuisen, T. M.; Munnik, P.; Talsma, H.; de Jongh, P. E.; de Jong, K. P. *J. Catal.* **2013**, *297*, 306.

(33) Eggenhuisen, T. M.; Friedrich, H.; Nudelman, F.; Zečević, J.; Sommerdijk, N. A. J. M.; de Jongh, P. E.; de Jong, K. P. *Chem. Mater.* **2013**, *25*, 890.

(34) Munnik, P.; de Jongh, P. E.; de Jong, K. P. *J. Am. Chem. Soc.* **2014**, *136*, 7333.

(35) Hao, X.; Spieker, W. A.; Regalbuto, J. R. *J. Colloid Interface Sci.* **2003**, *267*, 259.

(36) Wolters, M.; Andrade, I. C. A. C.; Munnik, P.; Bitter, J. H.; de Jongh, P. E.; de Jong, K. P. *Stud. Surf. Sci. Catal.* **2010**, *175*, 69.

(37) Becker, H.; Turek, T.; Güttel, R. *Catal. Today* **2013**, *215*, 8.

(38) Wolters, M.; Daly, H.; Goguet, A.; Meunier, F. C.; Hardacre, C.; Bitter, J. H.; de Jongh, P. E.; de Jong, K. P. *J. Phys. Chem. C* **2010**, *114*, 7839.

(39) Sun, X.; Shi, Y.; Zhang, P.; Zheng, C.; Zheng, X.; Zhang, F.; Zhang, Y.; Guan, N.; Zhao, D.; Stucky, G. D. *J. Am. Chem. Soc.* **2011**, *133*, 14542.

(40) Kletenik-Edelman, O.; Ploshnik, E.; Salant, a.; Shenhar, R.; Banin, U.; Rabani, E. *J. Phys. Chem. C* **2008**, *112*, 4498.

(41) Kletenik-Edelman, O.; Sztrum-Vartash, C. G.; Rabani, E. *J. Mater. Chem.* **2009**, *19*, 2872.

(42) Stannard, A. *J. Phys. Condens. Matter* **2011**, *23*, 083001.

(43) Stannard, A.; Martin, C. P.; Pauliac-Vaujour, E.; Moriarty, P.; Thiele, U. *J. Phys. Chem. C* **2008**, *112*, 15195.

(44) Vancea, I.; Thiele, U.; Pauliac-Vaujour, E.; Stannard, A.; Martin, C. P.; Blunt, M.; Moriarty, P. *Phys. Rev. E* **2008**, *78*, 1.

(45) Geus, J. W. In *Catalyst Preparation: Science and Engineering*; Regalbuto, J. R., Ed.; CRC Press, 2007; pp. 341–372.

(46) Vakros, J.; Bourikas, K.; Perlepes, S.; Kordulis, C.; Lycourghiotis, A. *Langmuir* **2004**, *20*, 10542.

(47) Ataloglou, T.; Fountzoula, C.; Bourikas, K.; Vakros, J.; Lycourghiotis, A.; Kordulis, C. *Appl. Catal. A Gen.* **2005**, *288*, 1.

(48) Van de Water, L. G. A.; Bezemer, G. L.; Bergwerff, J. A.; Versluijs-Helder, M.; Weckhuysen, B. M.; de Jong, K. P. *J. Catal.* **2006**, *242*, 287.

(49) Jacobs, G.; Ma, W.; Davis, B. H.; Cronauer, D. C.; Jeremy Kropf, a.; Marshall, C. L. *Catal. Letters* **2010**, *140*, 106.

(50) Borg, Ø.; Walmsley, J. C.; Dehghan, R.; Tanem, B. S.; Blekkan, E. A.; Eri, S.; Rytter, E.; Holmen, A. *Catal. Letters* **2008**, *126*, 224.

(51) Saib, A. M.; Moodley, D. J.; Ciobîc, I. M.; Hauman, M. M.; Sigwebela, B. H.; Weststrate, C. J.; Niemantsverdriet, J. W.; van de Loosdrecht, J. *Catal. Today* **2010**, *154*, 271.

(52) Loosdrecht, J. Van De; Datt, M.; Visagie, J. L. *Top. Catal.* **2013**, *57*, 430.

(53) Bezemer, G. L.; Bitter, J. H.; Kuipers, H. P. C. E.; Oosterbeek, H.; Holewijn, J. E.; Xu, X. D.; Kapteijn, F.; van Dillen, J. A.; de Jong, K. P. *J. Am. Chem. Soc.* **2006**, *128*, 3956.

(54) Den Breejen, J. P.; Radstake, P. B.; Bezemer, G. L.; Bitter, J. H.; Frøseth, V.; Holmen, A.; de Jong, K. P. *J. Am. Chem. Soc.* **2009**, *131*, 7197.

(55) Prieto, G.; Martínez, A.; Concepción, P.; Moreno-Tost, R. *J. Catal.* **2009**, *266*, 129.

(56) Borg, Ø.; Hammer, N.; Eri, S.; Lindvag, O. A.; Myrstad, R.; Blekkan, E. A.; Ronning, M.; Rytter, E.; Holmen, A. *Catal. Today* **2009**, *142*, 70.

(57) Saib, A. M.; Claeys, M.; van Steen, E. *Catal. Today* **2002**, *71*, 395.

(58) Prieto, G.; Martínez, A.; Murciano, R.; Arribas, M. A. *Appl. Catal. A Gen.* **2009**, *367*, 146.

(59) Iglesia, E. *Appl. Catal. A Gen.* **1997**, *161*, 59.

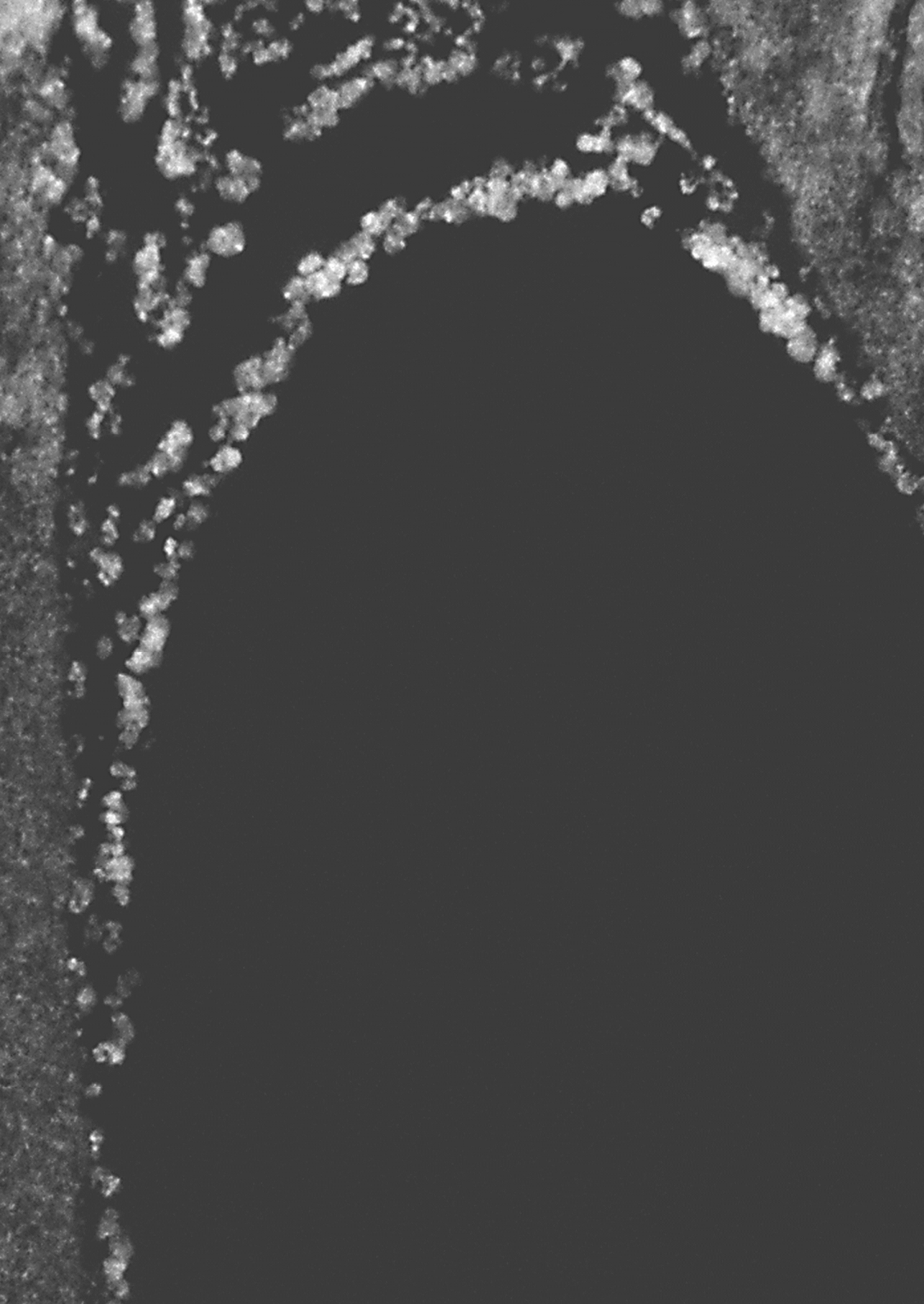

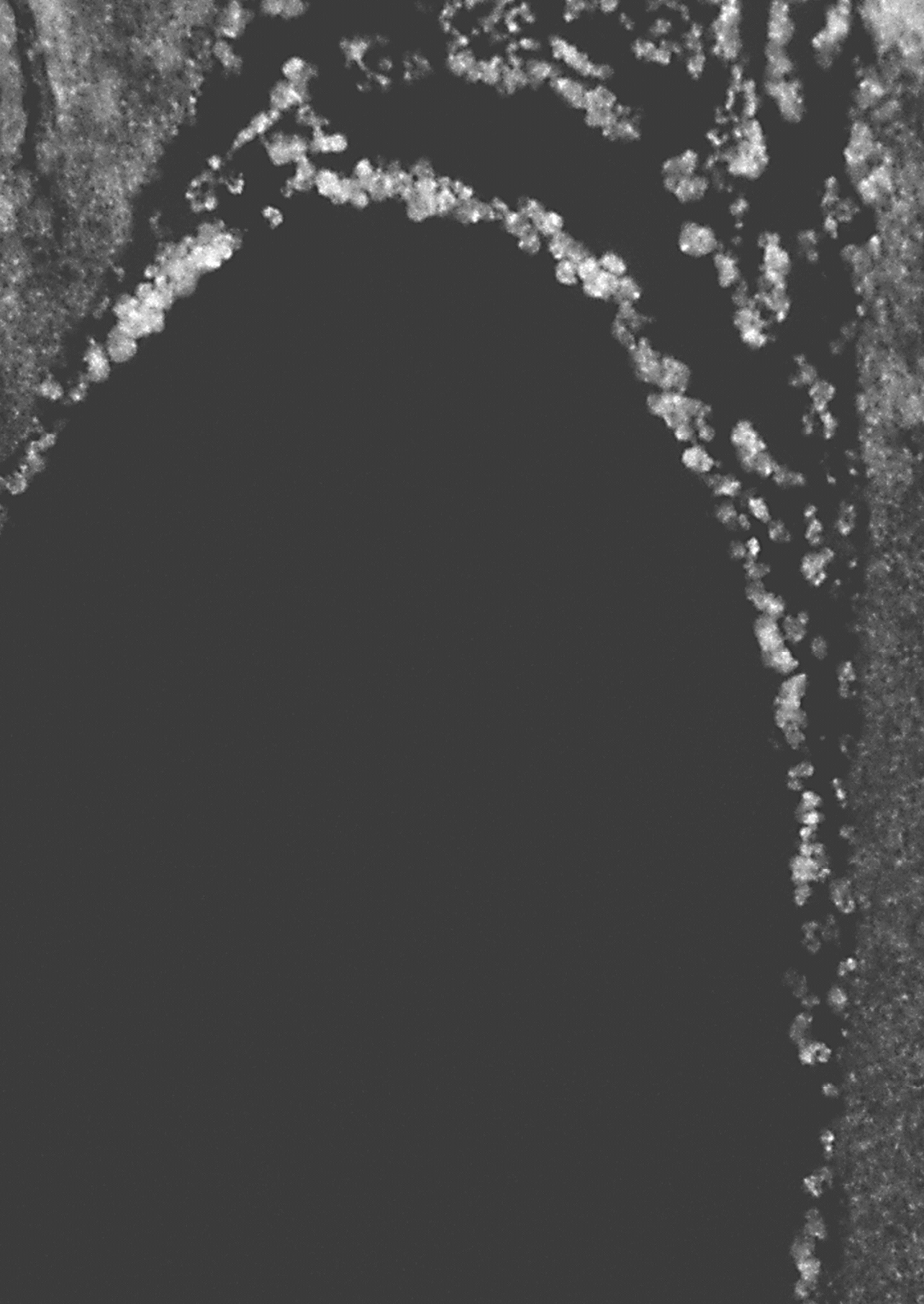

Chapter 6

Nanoparticle Growth in Supported Nickel Catalysts during Methanation Reaction – Larger is Better

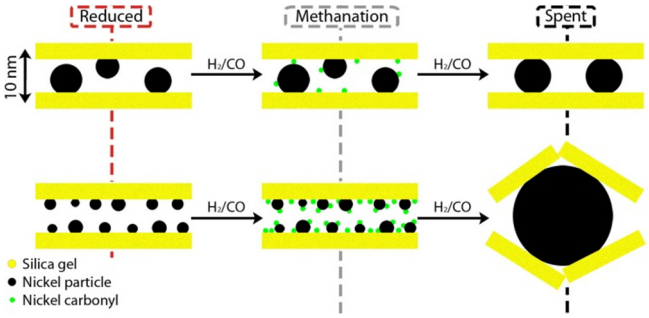

A major cause of supported metal catalyst deactivation is particle growth via Ostwald ripening. Nickel catalysts, used in the methanation reaction, may suffer greatly from this via the formation of $Ni(CO)_4$. By analyzing catalysts with various particle sizes and spatial distributions, the interparticle distance was found to have little effect on the stability, because formation and decomposition of nickel carbonyl rather than diffusion was rate limiting. Small particles (3 - 4 nm) were found to grow very large (20 - 200 nm), involving local destruction of the support, which was detrimental to the catalyst stability. However, medium sized particles (8 nm) remained confined by the pores of the support displaying enhanced stability, and an activity 3 times higher than initially small particles after 150 h. Physical modeling suggests that the higher $Ni(CO)_4$ supersaturation in catalysts with smaller particles enabled them to overcome the mechanical resistance of the support. Understanding the interplay of particle size and support properties related to the stability of nanoparticles offers the prospect of novel strategies to develop more stable nanostructured materials, also for applications beyond catalysis.

Adapted with permission from: P. Munnik et al. *Angew. Chemie Int. Ed.* **2014**, *53*, 9493. Detailed information on the mathematical model used in this work can be found in the Supporting Information of the published article.

INTRODUCTION

Supported metal catalysts are of great importance for many processes related to the more sustainable production of fuels and chemicals.[1–6] Because the catalytic reactions take place on the surface of the active metal, the latter is generally dispersed in the form of nanoparticles, the size, shape and composition of which controls the activity and selectivity of the catalysts.[7–9] Much less is known about the relationship between a catalyst structure and its stability, even though it is pivotal to understand and to abate its irreversible deactivation.

A major cause of catalyst deactivation is nanoparticle growth, a process thermodynamically driven by the surface energy of the active metal. Nanoparticles may migrate over the support and coalesce to form larger particles. Alternatively Ostwald ripening may occur, whereby monoatomic species or small clusters diffuse from small to large particles.[10–13] Reactive gasses such as H_2, CO and H_2O, present in many industrial reactions, can accelerate growth of metal particles such as Pt, Pd, Co and Ni by lowering the diffusion barrier of whole particles through surface modification, or via the formation of mobile species such as metal carbonyls.[14–17] Recently, maximizing the distance between copper particles was shown to greatly stabilize catalysts for the synthesis of methanol.[18] Other factors that affect nanoparticle growth include the size, the composition as well as the metal-support interaction.[19–21] In this contribution, we study how the particle spatial distribution and particle size affect the stability of supported nickel catalysts for methanation.

Nickel catalysts are often used for hydrogenation reactions such as that of CO into CH_4 and H_2O, for the production of synthetic methane or to remove CO from feed gasses of industrial ammonia plants.[22] In this process deactivation can occur by deposition of carbon on the active metal surface and by Ostwald ripening via the formation of $Ni(CO)_4$ species.[23–27] The influence of the nickel particle size and spatial distribution on the nanoparticle stability remains poorly understood, which hampers the optimization of these catalysts. In this chapter, we study the effect of nickel particle size and spatial distribution through use of four catalysts with a nickel loading of ~20 wt.% that were synthesized on a silica gel support using the knowledge obtained in the previous chapters and previously reported in literature.[28–32]

EXPERIMENTAL

Catalyst Synthesis. Loading the nickel nitrate precursor for Ni-D8, Ni-C4 and Ni-C3 was performed via melt-infiltration by taking 0.5 g silica gel (Grace-Davidson, V_p = 0,87 cm^3/g, d_p = 8 nm, grain sieve fraction 38 - 75 μm), which was mixed with 0.66 g of $Ni(NO_3)_2{\cdot}6H_2O$ and transferred to a Teflon-lined steel autoclave of 25 ml. The sample was heated in the closed autoclave to 60 °C and kept overnight to allow capillary forces to suck the molten $Ni(NO_3)_2{\cdot}6H_2O$ into the pores of the support, leading to a nickel loading of 21 wt.%.

Ni-D8 and Ni-C3 were freeze-dried as per the method described in chapter 3 to get a homogeneous distribution of the active metal phase. Briefly, the melt infiltrated sample was

flash-frozen in liquid nitrogen, and subsequently transferred onto a precooled shelf at -45 °C in a Zirbus Sublimator 400 Freeze-dryer. The pressure was immediately reduced to 0.02 mbar for 72 h, followed by a steps at -30 °C for 24 h and at -15 °C for 12 h. Before removal, the chamber was filled with nitrogen and the samples were sealed to prevent readsorption of ambient water. Ni-C4 was not dried prior to calcination. DSC measurements on melt infiltrated samples were performed to ensure the freeze-drying temperatures were sufficient to freeze the confined precursor (see Appendix C, Figure C.1).

The precursor was subsequently decomposed by transferring 200 mg of the sample to a fluidized bed reactor, in which calcination was carried out at 350 °C for 1 hour (1 °C/min). Calcination either was done in a 100 mL/min N_2 (Ni-D8) flow or in 100 mL/min 1% v/v NO/N_2 flow (Ni-C4 and Ni-C3). By employing an NO flow, smaller particles were obtained, which became even smaller when preceded by freeze drying. By not drying the sample prior to the NO calcination, inhomogeneous distributions were obtained of still relatively small particles. Alternatively, for Ni-C9 the silica gel was prepared via solution-impregnation to incipient wetness with a 4.2 M $Ni(NO_3)_2$ (aq) solution and dried at 60 °C in stagnant air to get a highly aggregated system after calcination in a flow of N_2 (Ni loading 16.6 wt.%).

Reduction was done *in-situ* in the methanation setup at 500 °C for 2 hours (1 °C/min) in a flow of 60 mL/min 33% v/v H_2/He after mixing 10 mg of catalyst with 200 mg SiC. The high temperature of 500 °C was used to ensure complete reduction of the nickel oxide phase.

Catalyst Characterization. To study the behavior of the $Ni(NO_3)_2$ during freeze drying, the samples were analyzed using differential scanning calorimetry (DSC; Q2, TA Instruments) with hermetically sealed aluminum pans (~40 µL, Tzero, TA Instruments) under a flow of N_2 (50 mL/min). Sample masses were typically between 10 - 15 mg and heat flows were recorded between -90 °C and 80 °C at a rate of 1 °C/min.

Catalyst grains were embedded in a two component epoxy resin (Epofix, EMS), which was subsequently cured at 60 °C overnight. Samples were then cut in sections with a nominal thickness of 50 nm using a Diatome Ultra 35° diamond knife mounted on a Reichert-Jung Ultracut E microtome. The 50 nm sections were collected on a TEM grid and bright field TEM micrographs were obtained with the use of a Tecnai 12 operating at 120 keV. EDX on large areas of the sliced support grains was measured with the use of a Technai 20-FEG operating at 200 keV.

XRD patterns were recorded between 20 and 90° 2θ with a Bruker-AXS D2 Phaser X-ray Diffractometer using Co-$K\alpha_{12}$ radiation (λ= 1.790 Å). The average crystallite size of NiO was determined using the Scherrer equation with a shape factor k = 0.9 and line broadening analysis on the (220), (111) and (200) peaks in Eva2 software (Bruker AXS).

N_2-Physisorption measurements were performed at -196 °C using a Micromeritics Tristar 3000 apparatus. Prior to analysis, samples were dried in He flow for 14 hours at 300 °C.

Catalytic Testing. Methanation was studied in a fixed bed reactor at 230 °C and an H_2:CO volume ratio of 2:1 (6 mL(STP)/min total flow, resulting in a GHSV of 18000 h^{-1}) at 1 bar total pressure for either 15 or 150 hours. 10 Mg of catalyst was mixed with 200 mg SiC

and reduced *in-situ* (see above). The reactor had an internal diameter of 2 mm, resulting in a bed length of 1.5 cm. A thermocouple was inserted in the middle of the catalyst bed, and the local temperature was controlled within 1 °C. The C_1-C_5 products were analyzed by on-line GC analysis (Varian CP 3800 GC, CP sil-5 column). The degree of conversion was maintained low (< 1%) to ensure differential and isothermal conditions.

RESULTS AND DISCUSSION

Catalyst Synthesis. The four nickel catalysts Ni-D8, Ni-C9, Ni-C4 and Ni-C3 were named by their volume-averaged Ni particle size of 7.5, 9.0, 4.2 and 3.2 nm, respectively, after reduction (Figure 6.1 and Table 6.1). The difference in particle size was obtained through varying the calcination method. Ni-D8 and Ni-C9 were calcined in N_2, resulting in 7 to 9 nm nickel oxide particles, while Ni-C4 and Ni-C3 were calcined in 1% NO/N_2, so that 3 to 4 nm nickel oxide particles were obtained.

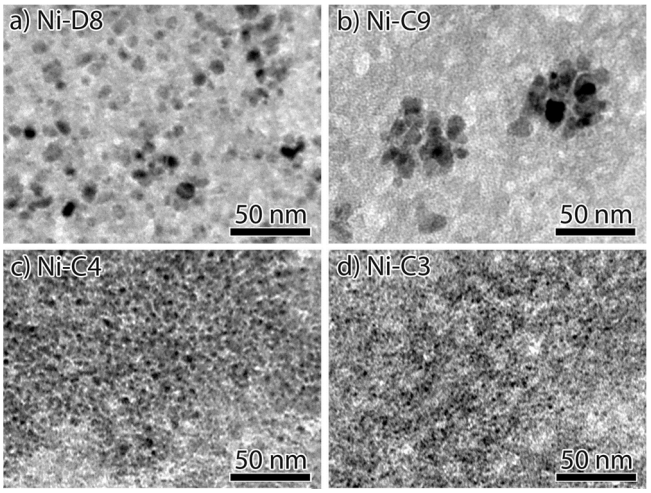

Figure 6.1. Bright Field TEM of 50 nm thick slices of Ni/SiO_2 catalysts after reduction: (a) Ni-D8, (b) Ni-C9, (c) Ni-C4 and (d) Ni-C3.

The difference in spatial distribution was obtained by different drying methods, and was characterized quantitatively in terms of the percentage of support that was covered by nickel particles using low-magnification TEM (Figure 6.2). The coverage varied between 95% for Ni-D8 to 15% for Ni-C9, resulting in different surface-to-surface interparticle distances. For Ni-D8, Freeze-drying resulted in well dispersed particles (indicated with a D) with an average distance of 16 nm between nearest neighbors. For Ni-C9 and Ni-C4, conventional drying at 60 °C in a muffle oven or not drying at all resulted in similarly sized particles being very close together (indicated with a C), with interparticle distances of 7 nm. For Ni-C3, freeze-drying again resulted in homogeneously distributed particles, however due to their small size the interparticle distance was nonetheless 7 nm (see also Appendix C, Table C.1).

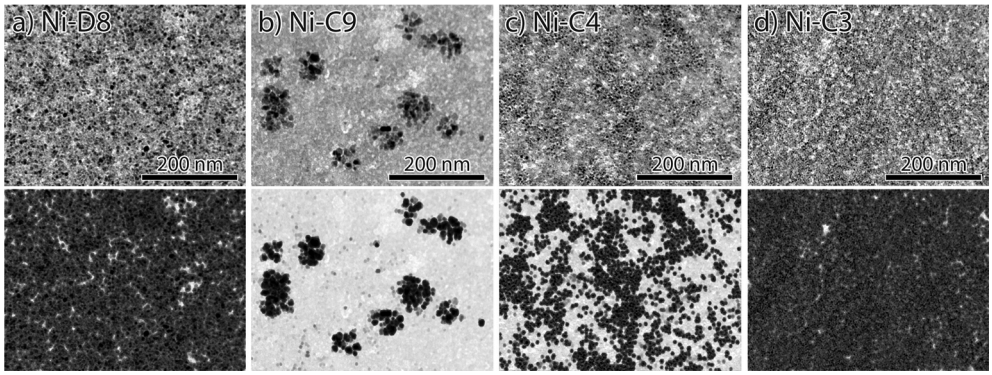

Figure 6.2. Low magnification bright-field TEM images of microtomed catalyst particles after reduction showing the distribution and coverage of nickel over the support. (a) Ni-D8, (b) Ni-C9, (c) Ni-C4 and (d) Ni-C3. Bottom row shows digital contrast versions of the original images. Dark areas represent support covered with nickel particles, white areas represent silica devoid of nickel.

Table 6.1. Structural and catalytic properties of silica-supported nickel catalysts.

	NiO size[a]	Ni size	Nickel coverage[c]	particle distance[d]	Initial activity	Activity at 150 h	Deactivation constant[e]
	(nm)	(nm)	(%)	(nm)	(10^{-5} mol_{CO} g_{Ni}^{-1} s^{-1})		(10^{-2} h^{-1})
Ni-D8	7.7	7.5	95 (±5)	16.0	1.1	0.46	2.5
Ni-C9	8.7	9.0	15 (±5)	7.1	1.0	0.35	2.7
Ni-C4	3.9	4.3	55 (±5)	6.9	1.5	0.12	9.0
Ni-C3	3.2	3.2	95 (±5)	6.8	2.2	0.14	29

[a]Volume average crystallite size from XRD after calcination. [b]Volume average particle size from TEM histogram analysis after reduction. [c]Percentage of support covered with nickel particles (Figure 6.2). [d]Nearest surface-to-surface distance calculated from the nickel loading, particle size, pore volume and nickel coverage assuming hexagonal packing. [e]Second-order deactivation rate constant (see Appendix C).

Each catalyst was tested for the methanation reaction (230 °C, H_2:CO = 2:1, 1 bar). The gas hourly space velocity and the temperature were chosen such to keep the conversion below 1%, ensuring differential and isothermal conditions, and to prevent significant loss of nickel from the reactor.[26,27] The conservation of the nickel loading was also confirmed by EDX and calculations (see Appendix C and Table C.1). Note that under these reaction conditions the rate determining step of the methanation is the hydrogenation of surface carbon species and that the reaction is structure insensitive.[24,33,34]

Figure 6.3 shows the nickel weight-based activities of the catalysts. The initial activity, the activity after 150 hours and the second-order deactivation rate constants are summarized in Table 6.1. The initial activities of the four catalysts were proportional to the surface area of the metal, with an average turnover frequency (TOF) of $4 \cdot 10^{-3}$ s^{-1} (Figure 6.4). After 150 h, Ni-C9

and Ni-D8 both lost 60 - 65% of their activity with similar deactivation rate constants, despite different interparticle distances. On the other hand, Ni-C4 and Ni-C3 both lost 90 - 95% of their initial activity. It therefore appeared that the deactivation was controlled by the particle size rather than by the interparticle distance. After 150 h, the activity of the catalysts with small particles was three times lower than that of the catalysts with medium sized particles, which were more active in the long term. The observation that interparticle distance has no effect on the deactivation suggests that Ostwald ripening is the dominant mechanism for particle growth rather than migration and coalescence. This is in line with earlier observations that in presence of CO, migration and coalescence is significant only at temperatures above 500 °C, where nickel carbonyl species are unstable.[35–37]

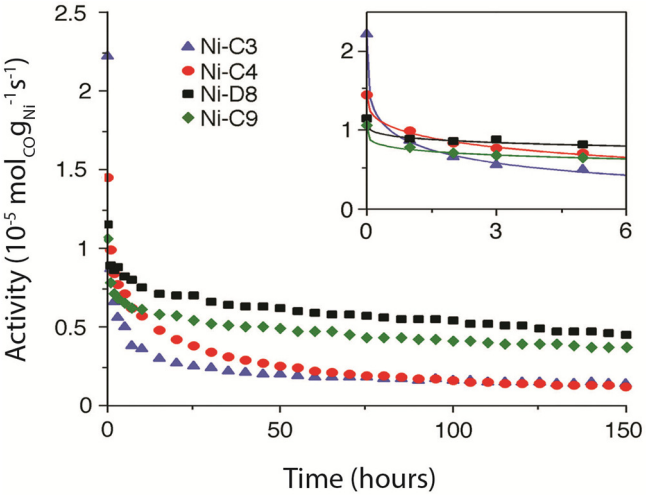

Figure 6.3. Nickel weight-based activity during 150 hours on-stream at 230 °C with a H_2/CO feed ratio of 2:1. The inset shows a close-up of the first 6 hours. Although Ni-C4 and Ni-C3 start very active, they rapidly deactivate and cross the activity curves of Ni-D8 and Ni-C9.

The main intermediate species in Ostwald ripening is nickel carbonyl, which may exists both as an adspecies and as a gaseous molecule.[27] Independently of its dominant physical form, the equilibrium pressure of the carbonyl depends on the particle radius R via the following Kelvin-like equation

$$P_{Ni(CO)4} = K_0 e^{\lambda/R} P_{CO}^4 \qquad \text{(Equation 6.1)}$$

where K_0 is the equilibrium constant over a flat nickel surface, P_{CO} is the partial pressure of CO, and λ = 3.9 nm under the reaction conditions (see Appendix C). Using these values and a conservative estimate for the diffusion coefficient of $Ni(CO)_4$ between two nanoparticles, the lifetime of 3 to 9 nm particles was found to be of the order of milliseconds to seconds, much shorter than the observed deactivation time. Thus, it is not diffusion but the formation and decomposition of the nickel carbonyl that controls the rate of Ostwald ripening. This explains why the spatial distribution of the nanoparticles only played a minor role in the deactivation and justifies using a mean-field approximation, in which the nickel carbonyl concentration is uniform throughout the catalyst.[12,17,38]

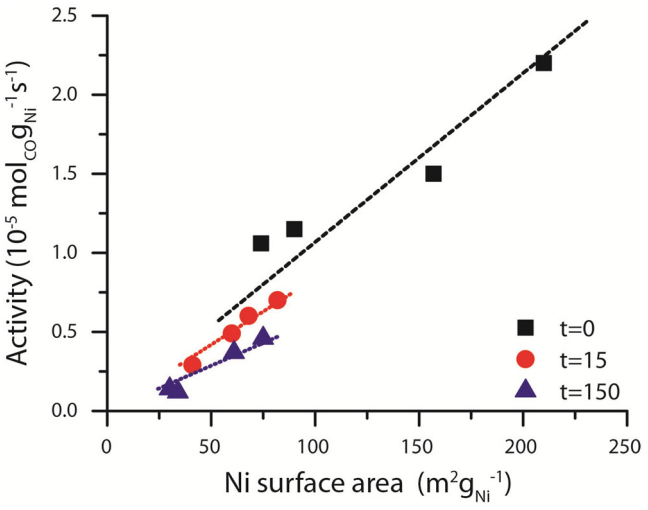

Figure 6.4. Nickel weight-based activity plotted against the calculated nickel surface area from TEM particle size distributions. Dotted lines show the linear fits for different times on-stream. The slope of these lines corresponds to the TOF of the catalysts. No dependency of TOF on particle size was observed. However, the slopes of the fits become lower for longer times on stream, suggestive of carbon buildup.

From metallurgy, the decomposition of nickel carbonyl is known to proceed via competitive adsorption of carbonyl and carbon monoxide on the nickel surface, followed by the successive chemisorption of the carbonyl groups on neighboring empty surface sites.[39] From transition-state theory, the time-evolution of the radius of a spherical nickel particle obeys

$$\frac{dR}{dt} = v(S - \mathrm{e}^{\lambda/R}) \qquad \text{(Equation 6.2)}$$

where v is a velocity that depends on the kinetic constants of the reaction as well as the partial pressure of CO, which was estimated at v = 0.87 nm/h from literature data[40] (for more information on the mathematical model, see the Supporting Information of the published article). S is the nickel carbonyl supersaturation ratio defined as $P_{Ni(CO)4}/(K_0 P_{CO}^4)$. Equation 6.2 assumes unhindered growth, so that the particles are free to grow larger than the pores of the support, which has been observed for noble metals in zeolites.[41,42]

Figure 6.5 compares the experimental activities of Ni-C3 and Ni-D8 with the predictions of Equation 6.2, assuming an activity proportional to the surface area of the nanoparticles with the TOF measured on the fresh catalysts (solid grey lines) or on the spent catalysts (dashed grey lines). The deactivation of Ni-C3 was well accounted for by the unhindered Ostwald ripening model, limited by the rate of formation and decomposition of nickel carbonyl. Interestingly, in the case of Ni-D8, the experimental deactivation was much slower than predicted by the present model. Similar conclusions hold when comparing Ni-C4 to Ni-C9 (Figure C.10).

Figure 6.6 shows TEM of the catalysts after 150 h on-stream, and the particle size distributions derived from TEM are presented in Figure C.4. A remarkable feature of Ni-C4 and Ni-C3 is the presence of particles that can be as large as 100 nm (Figure C.4). In both cases, the volume-averaged particle size is around 20 nm (Table C.1), much larger than the 10

nm average pore size of the support. Studying a Ni/SBA-15 catalyst with 4 nm initial Ni particles for comparison, electron tomography confirmed that similar large nickel particles had grown much larger than the pores of the support, locally breaking up the silica walls to do so (Figure C.5). These results show that the unhindered growth mechanism is a valid assumption for catalyst with initially small particles. By contrast, Ni-D8 and Ni-C9 exhibited only a minor increase in particle size, from 7.5 to 9.0 nm and 9.0 to 11.1 nm, respectively, suggesting that the particles were confined in the pores (Figure C.4).

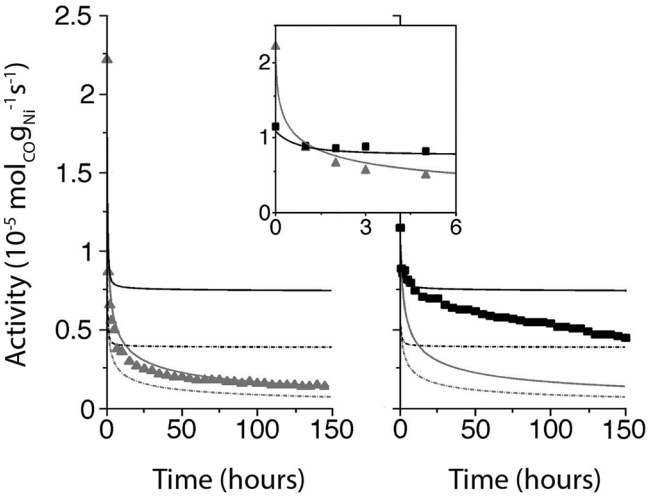

Figure 6.5. Modelling the deactivation of catalysts Ni-C3 (left, grey triangles) and Ni-D8 (right, black squares). The symbols represent the experimental data, the lines the model predictions: unhindered particle growth (grey) and confined growth (black). The solid and dashed lines are obtained using the TOF of the fresh and spent catalysts, respectively. In the inset, the unhindered growth model is used for Ni-C3 and the confined model for Ni-D8.

The conditions for a growing nanoparticle to break a pore wall or to stay confined is a problem familiar to engineers interested in the weathering of construction materials.[43] The quantitative criteria depend on the specific microstructure of the material, its mechanical properties, and the surface energies of the interfaces.[44] Qualitatively, however, the criterion is universal: if the supersaturation of the reservoir from which the nanoparticle grows is high enough, the free energy released by the growth is sufficient to overcome the mechanical resistance of the confining material. In the present context, the supersaturation is controlled by the particle size via the area-weighted average of $e^{\lambda/R}$. The values calculated from the experimental size distributions of the fresh catalysts are S = 19 and 8 for Ni-C3 and Ni-C4, and S = 3 and 2.5 for Ni-D8 and Ni-C9. The absence of very large particles in Ni-D8 and Ni-C9 suggests that the critical value of the supersaturation for the silica gels used in the present work lies between 3 and 8.

To further test the confinement of particles in Ni-C8 and Ni-D9, Equation 6.2 was solved again while limiting the growth of particles to the pore size, approximately 10 nm. The results are plotted as black lines in Figure 6.5. By contrast to Ni-C3, the activity of Ni-D8 was well accounted for by the confined growth model. The agreement was almost quantitative for short times, but the activity progressively dropped below the prediction of the confined model over 150 h. This was explained by carbon buildup on the nickel surface. Although the TOF did not

depend on particle size, an approximately 50% reduction in TOF was apparent for all catalysts over 150h (Figure 6.4). This suggests that unreactive carbon coated half of the nickel surface, in line with previous studies.[24,27,37] Using the initial and final TOF as upper and lower bounds (solid and dashed lines in Figure 6.5), the deactivation of Ni-C3 and Ni-D8 were well described by Equation 6.2; unhindered growth was dominant in the former, while confined growth applied to the latter.

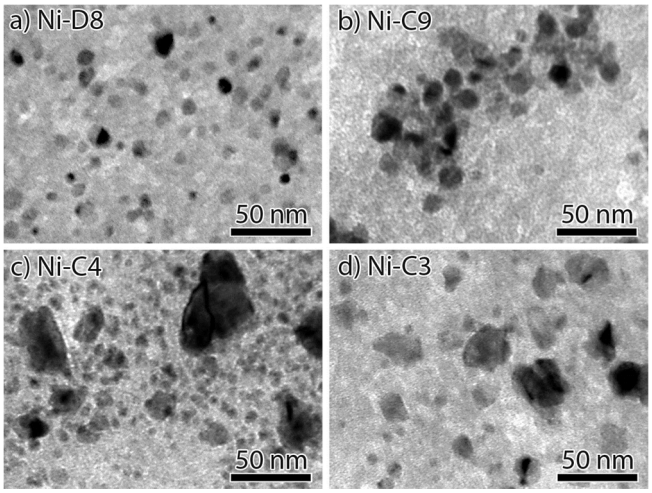

Figure 6.6. TEM of microtomed 50 nm slices of catalyst particles after 150 hours on-stream. (a) Ni-D8, (b) Ni-C9, (c) Ni-C4 and (d) Ni-C3.

A similar observation was made when considering the particle size distributions (Figures C.4 and C.9). The unhindered model was in fair agreement with the experimental particle size distributions of Ni-C3 and Ni-C4, but only the confined growth model could account for the particle stability in Ni-C9 and Ni-D8. Interestingly, the very large particles in Ni-C3 and Ni-C4 coexisted with smaller particles that were not predicted by the unhindered growth model (Figure 6.4 and C.4). These results suggest that unhindered growth applied only for a short time during which the supersaturation was sufficiently high (Figure C.10). This was followed by a hybrid regime where the particles smaller than the pores remained confined, while the larger particles grew unhindered. After a few hours, the average particle size of Ni-C3 reached the same value as Ni-D8 resulting in identical activities (inset of Figure 6.5). However, the presence of the few particles that broke early though the pores was responsible for the faster and more extensive deactivation of Ni-C3.

CONCLUSION

The stability of Ni/SiO_2 catalysts with different particle sizes and interparticle distances was studied during the methanation reaction. The distance between neighboring particles was found to have only a minor influence on the stability. The deactivation via Ostwald ripening was limited not by diffusion but by the formation and decomposition of nickel carbonyl on the

metal surface. The main determinant of the catalyst stability was the particle size. Catalysts with smaller particles deactivated faster and to a larger extent than catalysts with medium sized particles. This counter-intuitive finding resulted from qualitatively different mechanisms. In the case of small particles, the nickel carbonyl supersaturation was sufficiently high for the particles to break the pore walls, resulting in very large nanoparticles. By contrast, the supersaturation was low in catalysts with medium sized nanoparticles, which limited the possible extent of their growth to the pore diameter. The large difference in stability between particles that differ only by a few nanometers in size is very relevant not only for durable catalysis, but also for other fields such as that of nanostructured materials for energy conversion and storage devices.[45]

ACKNOWLEDGMENTS

Mr. M. van Steenbergen (Utrecht University) is acknowledged for technical support and useful discussions on freeze-drying. Ms. E. van Donselaar (Utrecht University) is acknowledged for ultramicrotomy instructions. The Electron Microscopy Unit at Utrecht University is acknowledged for their excellent facilities.

REFERENCES

(1) Román-Leshkov, Y.; Barrett, C. J.; Liu, Z. Y.; Dumesic, J. A. *Nature* **2007**, *447*, 982.
(2) Guo, S.; Zhang, S.; Sun, S. *Angew. Chemie Int. Ed.* **2013**, *52*, 8526.
(3) Calderone, V. R.; Shiju, N. R.; Curulla-Ferré, D.; Chambrey, S.; Khodakov, A. Y.; Rose, A.; Thiessen, J.; Jess, A.; Rothenberg, G. *Angew. Chemie Int. Ed.* **2013**, *52*, 4397.
(4) Torres Galvis, H. M.; Bitter, J. H.; Khare, C. B.; Ruitenbeek, M.; Dugulan, A. I.; de Jong, K. P. *Science* **2012**, *335*, 835.
(5) Galeano, C.; Meier, J. C.; Peinecke, V.; Bongard, H.; Katsounaros, I.; Topalov, A. a; Lu, A.; Mayrhofer, K. J. J.; Schüth, F. *J. Am. Chem. Soc.* **2012**, *134*, 20457.
(6) Aricò, A. S.; Bruce, P. G.; Scrosati, B.; Tarascon, J.-M.; van Schalkwijk, W. *Nat. Mater.* **2005**, *4*, 366.
(7) Den Breejen, J. P.; Radstake, P. B.; Bezemer, G. L.; Bitter, J. H.; Frøseth, V.; Holmen, A.; de Jong, K. P. *J. Am. Chem. Soc.* **2009**, *131*, 7197.
(8) Simonsen, S. B.; Chorkendorff, I.; Dahl, S.; Skoglundh, M.; Meinander, K.; Jensen, T. N.; Lauritsen, J. V.; Helveg, S. *J. Phys. Chem. C* **2012**, *116*, 5646.
(9) Studt, F.; Abild-Pedersen, F.; Bligaard, T.; Sørensen, R. Z.; Christensen, C. H.; Nørskov, J. K. *Science* **2008**, *320*, 1320.
(10) Hansen, T. W.; Delariva, A. T.; Challa, S. R.; Datye, A. K. *Acc. Chem. Res.* **2013**, *46*, 1720.
(11) Newton, M. A. *Chem. Soc. Rev.* **2008**, *37*, 2644.
(12) Ouyang, R.; Liu, J.-X.; Li, W.-X. *J. Am. Chem. Soc.* **2013**, *135*, 1760.
(13) Benavidez, A. D.; Kovarik, L.; Genc, A.; Agrawal, N.; Larsson, E. M.; Hansen, T. W.; Karim, A. M.; Datye, A. K. *ACS Catal.* **2012**, *2*, 2349.
(14) Parkinson, G. S.; Novotny, Z.; Argentero, G.; Schmid, M.; Pavelec, J.; Kosak, R.; Blaha, P.; Diebold, U. *Nat. Mater.* **2013**, *12*, 724.
(15) Horch, S.; Lorensen, H.; Helveg, S.; Laegsgaard, E.; Stensgaard, I.; Jacobsenk, K. W.; Norskov, J. K.; Besenbacher, F. *Nature* **1999**, *398*, 134.

(16) Sadeqzadeh, M.; Hong, J.; Fongarland, P.; Curulla-Ferré, D.; Luck, F.; Bousquet, J.; Schweich, D.; Khodakov, A. Y. *Ind. Eng. Chem. Res.* **2012**, 11955.
(17) Challa, S. R.; Delariva, A. T.; Hansen, T. W.; Helveg, S.; Sehested, J.; Hansen, P. L.; Garzon, F.; Datye, A. K. *J. Am. Chem. Soc.* **2011**, *133*, 20672.
(18) Prieto, G.; Zečević, J.; Friedrich, H.; de Jong, K. P.; de Jongh, P. E. *Nat. Mater.* **2013**, *12*, 34.
(19) Campbell, C. T.; Parker, S.; Starr, D. *Science* **2002**, *298*, 811.
(20) Cao, A.; Veser, G. *Nat. Mater.* **2010**, *9*, 75.
(21) Farmer, J. A.; Campbell, C. T. *Science* **2010**, *329*, 933.
(22) Kopyscinski, J.; Schildhauer, T. J.; Biollaz, S. M. a. *Fuel* **2010**, *89*, 1763.
(23) Mihaylov, M.; Hadjiivanov, K.; Knözinger, H. *Catal. Letters* **2001**, *76*, 59.
(24) Agnelli, M.; Swaan, H. M.; Marquez-Alvarez, C.; Martin, G. A.; Mirodatos, C. *J. Catal.* **1998**, *128*, 117.
(25) Goldberger, W. M.; Othmer, D. F. *Ind. Eng. Chem. Proc. DD* **1963**, *2*, 202.
(26) Shen, W. M.; Dumesic, J. A.; Hill, C. G. *J. Catal.* **1981**, *165*, 152.
(27) Agnelli, M.; Kolb, M.; Mirodatos, C. *J. Catal.* **1994**, *148*, 9.
(28) Eggenhuisen, T. M.; Munnik, P.; Talsma, H.; de Jongh, P. E.; de Jong, K. P. *J. Catal.* **2013**, *297*, 306.
(29) Sietsma, J. R. A.; Meeldijk, J. D.; den Breejen, J. P.; Versluijs-Helder, M.; van Dillen, J. A.; de Jongh, P. E.; de Jong, K. P. *Angew. Chemie Int. Ed.* **2007**, *46*, 4547.
(30) Eggenhuisen, T. M.; den Breejen, J. P. *J. Am. Chem. Soc.* **2010**, 18318.
(31) Eggenhuisen, T. M.; Friedrich, H.; Nudelman, F.; Zečević, J.; Sommerdijk, N. A. J. M.; de Jongh, P. E.; de Jong, K. P. *Chem. Mater.* **2013**, *25*, 890.
(32) Bogdanchikova, N. E.; Tretyakov, V. V. *Preparation of Catalysts V*; Poncelet, G.; Jacobs, P. A.; Grange, P.; Delmon, B., Eds.; Elsevier: Amsterdam, 1991; pp. 647–652.
(33) Andersson, M. P.; Abild-Pedersen, F.; Remediakis, I. N.; Bligaard, T.; Jones, G.; Engbæk, J.; Lytken, O.; Horch, S.; Nielsen, J. H.; Sehested, J. *J. Catal.* **2008**, *255*, 6.
(34) Alstrup, I. *J. Catal.* **1995**, *151*, 216.
(35) Sehested, J.; Gelten, J. A. P.; Helveg, S. *Appl. Catal. A Gen.* **2006**, *309*, 237.
(36) Vogelaar, B. M.; van Langeveld, a. D.; Kooyman, P. J.; Lok, C. M.; Bonné, R. L. C.; Moulijn, J. a. *Catal. Today* **2011**, *163*, 20.
(37) Agnelli, M.; Mirodatos, C. *J. Catal.* **2000**, *192*, 204.
(38) Bredmose, S.; Chorkendorff, I.; Dahl, S.; Skoglundh, M.; Sehested, J.; Helveg, S. *J. Catal.* **2011**, *281*, 147.
(39) Garratt, A. P.; Thompson, H. W. *J. Chem. Soc.* **1934**, 1822.
(40) Carlton, H. E.; Oxley, J. H. *AIChE J.* **1967**, *13*, 86.
(41) Zečević, J.; van der Eerden, A. M. J.; Friedrich, H.; de Jongh, P. E.; de Jong, K. P. *ACS Nano* **2013**, *7*, 3698.
(42) Gallezot, P.; Alarcon-Diaz, A.; Dalmon, J. A.; Renouprez, A. J.; Imelik, B. *J. Catal.* **1975**, *39*, 334.
(43) Coussy, O. *Mechanics and Physics of Porous Solids*; Wiley, 2010.
(44) Scherer, G. *Cem. Concr. Res.* **1999**, *29*, 1347.
(45) Holby, E. F.; Sheng, W.; Shao-Horn, Y.; Morgan, D. *Energy Environ. Sci.* **2009**, *2*, 865.

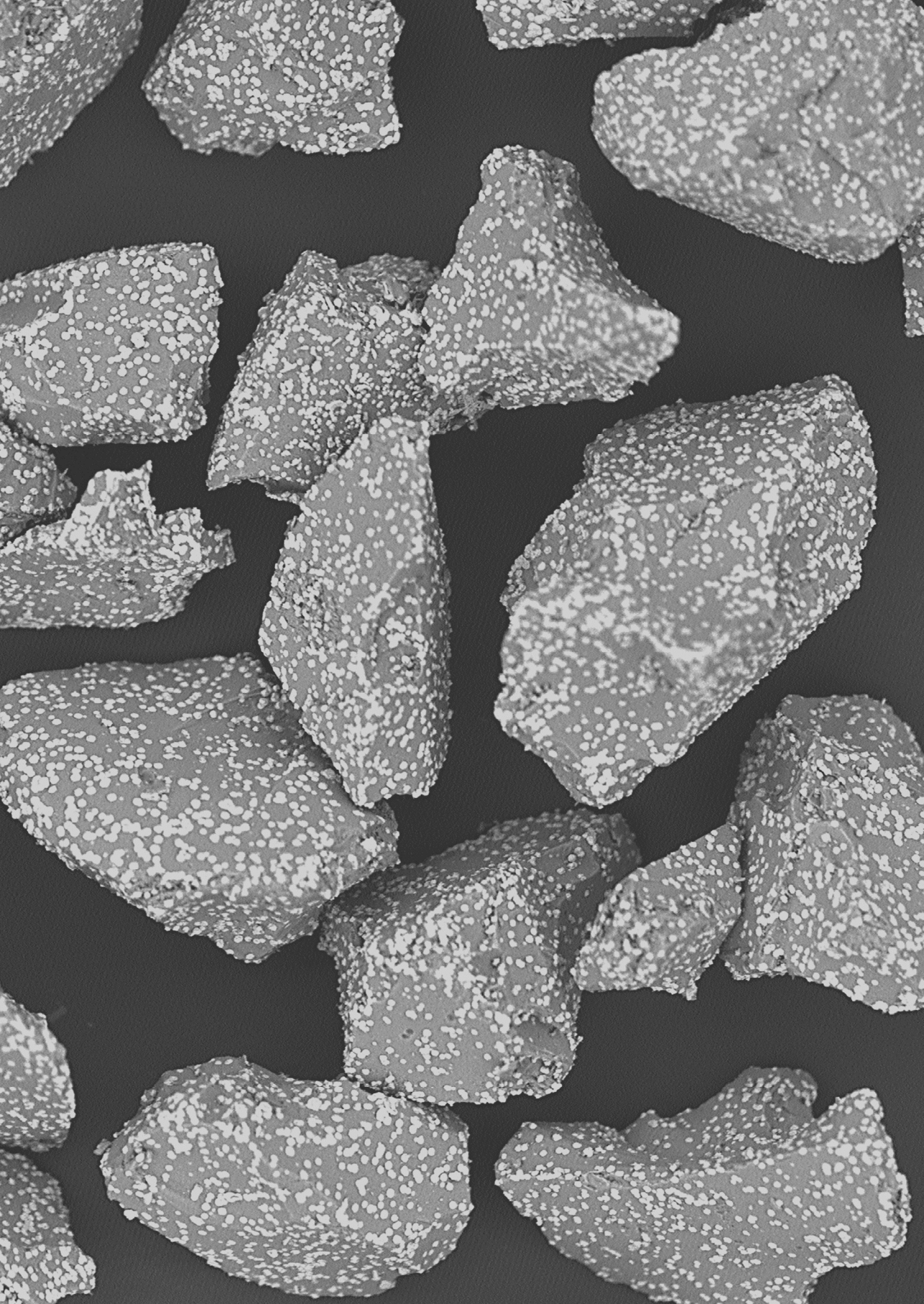

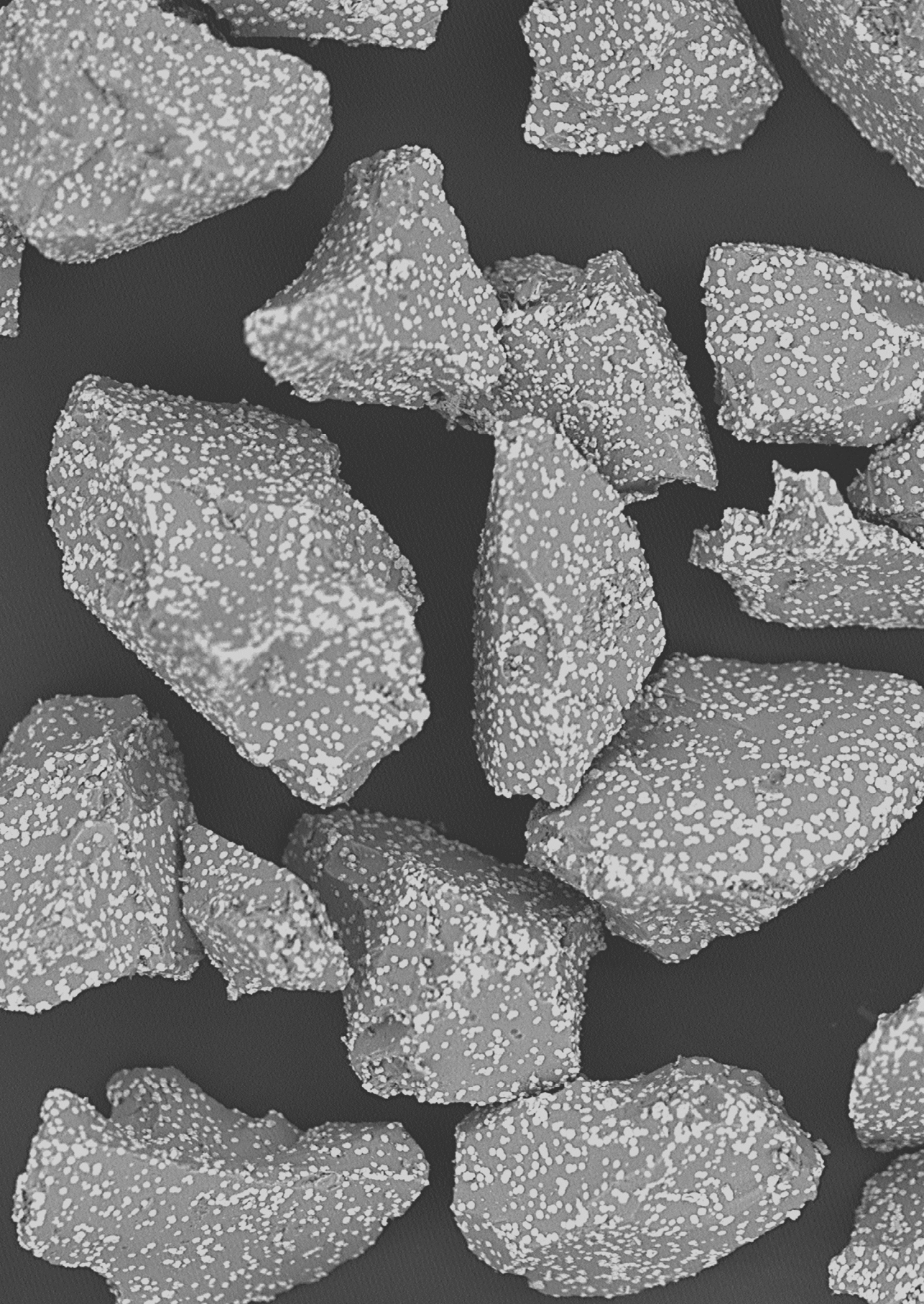

Chapter 7a

Summary, Concluding Remarks and Outlook

SUMMARY

Supported metal nanoparticles are at the center of many existing as well as new and more sustainable processes, such as energy conversion and storage, nanoelectronics and the catalytic production of fuels and chemicals. For rational development of these materials, a comprehensive understanding of the processes that play a role during their synthesis is of utmost importance. Moreover, degradation of such materials by growth of nanoparticles under process conditions is detrimental for their functionality. Therefore, understanding the method of degradation and devising strategies to prevent these is paramount.

One group of nanomaterials, heterogeneous catalysts, consists of many metal nanoparticles, supported on highly porous, mechanically strong and chemically inert supports. Because the catalyzed reaction occurs on the surface of the metal, typically 1 - 20 nm particles are desired to maximize the activity of the often expensive metals. The support provides a structure to help keep the particles separated from each other. Nonetheless, deactivation occurs via the growth of particles, causing a loss of metal surface area and thereby often a loss of activity.

In general, two mechanisms can be distinguished for particle growth. Entire particles can migrate over the surface of the support, and coalesce when they meet to form one bigger particle. Alternatively, monomers and clusters can detach from one particle and deposit on another, so that large particles grow larger at the expense of smaller ones. Methods to reduce these mechanisms include changing reaction conditions or modifying the catalyst by adding additional compounds, or altering the support material. However, these strategies can also have undesirable consequences for the activity and selectivity of the catalysts. The initial particle size and interparticle distance also have an influence on the stability, although these effects are less well known and difficult to control during catalyst preparation.

The synthesis of catalysts can be done in many different ways. However, the more complicated the technique, the more difficult and expensive they become to perform on a large scale, which is necessary if the catalyst is ever to be used on an industrial scale. Because of this, the method of impregnation and drying is often preferred, whereby a metal precursor dissolved in water is impregnated onto a premade porous support, which is subsequently dried to remove the solvent and calcined to decompose the precursor into the desired metal (oxide). Because metal nitrates have a high solubility in water, high loadings can be easily obtained in a single step. Moreover, by impregnating only the pores of the support, no filtration or waste water is produced. Unfortunately, the resulting size and distribution of the metal nanoparticles are often difficult to control, for example as large particles or small particles clumped together into large aggregates.

Catalysts that often suffer from aggregation are those used in the conversion of syngas, a mixture of H_2 and CO, to more useful products. In Fischer-Tropsch synthesis, syngas is converted into long hydrocarbon chains for the production of clean and more sustainable transportation fuels and lubricants from feedstocks other than crude oil. Cobalt is often the

desired metal for Fischer-Tropsch synthesis, and is commonly prepared on an industrial scale via impregnation of a porous support with cobalt nitrate solution. However, aggregates of cobalt nanoparticles are often reported, although their effect on the activity, selectivity and stability of the catalyst performance is not well understood. Alternatively, syngas can be converted into methane known as the methanation reaction, used to clean up the hydrogen feed for industrial ammonia plants and for the production of synthetic natural gas. This reaction is performed over nickel catalysts, which exhibit a high activity but suffer from Ostwald ripening via nickel carbonyl species, leading to rapid deactivation.

The present work focuses on the synthesis of cobalt and nickel catalysts from their respective metal nitrate precursors via impregnation. Of main interest was to achieve control over the degree of aggregation and the particle size by studying the synthesis, in particular the drying step, and to elucidate the effects of particle size and nanoscale distribution on the performance of the Fischer-Tropsch and methanation reactions.

Chapter 2 provides a review on the aspects and recent developments of important catalyst synthesis methods. Deposition precipitation is showing an increased use in the preparation of gold catalysts, while greener coprecipitation techniques are sought after to make the technique more viable on a large scale. Upcoming synthesis methods include melt infiltration, whereby the metal precursor is molten and taken up by the support without the need of a solvent. Colloidal methods can produce nanoparticles with almost any size and shape, but depositing them on a support material needs further research. Preparation via impregnation and drying is still one of the most discussed and used methods in both academia and industry. An intricate interplay exists between impregnation, adsorption of solvated species, redistribution during drying on a nano- and macroscale, and thermal treatment of the metal precursor.

In **chapter 3**, freeze drying is used to study the effect of the drying step on nanoscale aggregation of cobalt nitrate impregnated onto silica gel. The phase behavior of a concentrated cobalt nitrate solution confined in the pores of the mesoporous silica was investigated using differential scanning calorimetry (DSC). Based on the resulting freezing and melting points, two freeze drying methods were developed, and compared to a regular drying method in a muffle oven at 60 °C. While the latter resulted in cobalt aggregates between 40 to 200 nm, freeze drying starting from liquid nitrogen temperatures resulted in uniform distributions for all catalysts. However, drying at -45 °C was insufficient to freeze a solution impregnated catalyst, resulting in severe redistribution of the active phase towards the outside of the support grains during the drying step, creating an egg-shell catalyst. To circumvent this, melt infiltration was used, which led to a higher melting and freezing temperature due to a lower water content, so that the precursor could be frozen at -45 °C. This led to uniformly distributed catalysts with both freeze drying methods. To control the particle size, a heat treatment was performed in either N_2 or NO, which resulted in 8 or 5 nm particles, respectively. The resulting catalysts were highly active for the Fischer-Tropsch synthesis at 1 bar. Thus, through the use of freeze drying it was shown that the drying step in the preparation of supported metal catalysts is of utmost importance in regulating the degree of aggregation.

The drying step was further studied in **chapter 4**. Silica gel impregnated with a concentrated cobalt nitrate solution was dried in an N_2 gas flow in a fluidized bed at different temperatures. Two different mechanisms for aggregate formation were found. At temperatures below 100 °C, aggregation occurred during the precipitation of a cobalt nitrate species. At a low drying rate, caused by a low N_2 flow or low temperature, larger aggregates were formed. At temperatures above 100 °C, direct decomposition of cobalt nitrate to cobalt oxide during drying led to the nucleation and growth of large aggregates. An optimum was found by drying at 100 °C in an N_2 flow, whereby a uniform distribution of nanoparticles was obtained.

The effect of aggregation was studied in the Fischer-Tropsch synthesis under industrially relevant conditions at 20 bar pressure. All aggregate sizes exhibited similar activities and selectivities, attributed to the similarity in particle size for all samples. However, significant differences in the deactivation behavior were observed. Although particle growth inside the pores of the support was not apparent, particles could move tens of micrometers towards the external surface of the catalyst grains, where they were deposited into large aggregates and some coalesced into large solid cobalt particles. This migration was found to occur much more extensively for catalysts with larger initial aggregates. Thus, the degree of aggregation was found to play a large role in the stability of Fischer-Tropsch catalysts.

Fundamental insights in the mechanisms of aggregation are provided in **chapter 5**. Using an NO atmosphere during the heat treatment after drying, the cobalt nitrate was hydrolyzed to cobalt hydroxynitrate, which was immobile, so that the distribution after drying could be imaged. Aggregates that formed by drying between -45 and 100 °C strongly resembled those obtained by the drying of colloidal films, suggesting redistribution originates form a physical process. Drying at higher temperatures, or performing a direct heat treatment in NO without a previous drying step, resulted in aggregates via the chemical deposition of cobalt oxide or cobalt hydroxynitrate, respectively, from solution. Thus, under these conditions, chemistry dominated aggregate formation.

On γ-alumina, which exhibited higher precursor-support interactions compared to silica gel, aggregation via a physical process was greatly reduced. By using a fluidized bed drying process, no aggregates were found between 25-100 °C, whereas conventional drying in stagnant air resulted in large aggregates regardless of temperature also for alumina. No major impact of pore size was found for the nanoscale distribution of cobalt oxide on silica. However, studying these catalysts in the Fischer-Tropsch reaction under industrially relevant conditions revealed homogeneous catalysts were up to 50% more active compared to aggregated ones.

In **chapter 6**, nickel catalysts with different particle sizes and particle distributions were used by combining freeze-drying, regular drying, melt infiltration, solution impregnation, N_2 calcination and NO calcination. Catalysts were tested for the methanation reaction, which suffers greatly from Ostwald ripening via nickel carbonyl species. Two catalysts with similar particle sizes but different interparticle distances revealed that the nanoparticle distribution was of only minor influence for this reaction. Formation and decomposition rather than diffusion

of nickel carbonyl was rate limiting, so that the distance between particles was of little importance.

The initial nickel particle size played a large role in the deactivation behavior. Starting with small particles resulted in rapid and extensive deactivation, with particles growing up to 100 nm in size, many times larger than the pores of the silica gel support. Alternatively, when starting out with medium sized particles, only minor particle growth occurred; particles remained of a size similar to the support pores, resulting in more stable catalysts. Modeling revealed that the nickel carbonyl supersaturation in catalysts with medium sized particles was relatively low, so that the crystallization pressure of the growing particles did not exceed the mechanical strength of the support, keeping the particles confined. For small particles, the supersaturation was so high that growing particles could break the support, becoming much larger and leading to extensive deactivation.

CONCLUDING REMARKS AND OUTLOOK

The implications of this work are numerous. Metal nitrates are often used in both academia and in industry, not only for cobalt or nickel but for many other metals, so many of the results obtained here could apply to a broader range of metals and supports.

Freeze drying is a well-known technique in the pharmaceutical and food processing industries. Therefore, knowledge on process optimization and upscaling of this technique is available and could be integrated into catalyst synthesis by an interdisciplinary approach. Application of freeze-drying for the synthesis of many different catalysts could be possible regardless of the precursor and support, although rational synthesis via investigation of the melting and freezing point of the confined precursor is necessary to prevent the redistribution of the precursor material on a macroscopic scale and to arrive at realistic rates of drying.

More generally, since the aggregation mechanism during drying in a gas flow at temperatures below 100 °C was mainly the result of a physical process, it is likely this also plays an important role in the aggregation of other metal nitrates. The exact temperature behavior will depend on the specifics of the metal nitrate, such as the temperature at which decomposition starts, and needs further investigations. When drying in a fluidized bed, an optimal distribution is expected at a temperature that allows rapid drying without altering the chemical nature of the precursor. It is also possible that other metal precursors, such as metal chlorides, behave in a similar manner.

Because of the physical nature of aggregate formation, a similar behavior is also expected on other supports that exhibit a relatively low interaction with the precursor. However, care should be taken that macroscopic drying effects do not start to play a dominant role. For silica gel with 23 nm pores, egg-shell catalysts were obtained upon drying in fluidized bed due to redistribution of the material on a macroscopic scale. This could be mitigated by applying melt infiltration instead of solution impregnation to load the cobalt nitrate precursor, which reduced the time available for macroscopic migration due to a lack of solvent.

Fluidized bed drying was used extensively in this research, which might not be the preferred method of drying on an industrial scale, where larger grain sizes or other reasons might make fluidized beds impractical. However, most important is the efficient removal of water during the drying process for a fast drying rate. Thus, while this can be efficiently done by drying in fluidized bed, this might also be achieved in a different apparatus, such as a rotary kiln with a gas flow going through, which might be easier to apply on a large scale.

These ways to create uniform nanoparticle distributions on both the macro and nanoscale could contribute to highly stable catalysts and other nanomaterials whereby the distance between particles is of importance. In addition, the new insights in catalysts deactivation could aid in creating more efficient catalysts.

The large scale migration of cobalt towards the outside of the catalysts grains has almost never been reported. By the use of ultramicrotomy, we could efficiently show the extent of this aggregation. However, the method by which these particles migrate to the outer surface is yet unclear and elicits further investigation. Regardless, the fact that a homogeneous distribution resulted in less migration is of great importance to the catalysis and nanomaterials communities.

Moreover, the fact that medium sized particles deactivated much less than small particles is highly important for nanomaterials in general. While we always strive for the smallest possible particles to obtain the highest possible activity, this shows it can be highly beneficial to produce slightly larger particles, so that they can remain confined in the pores of the support material.

Chapter 7b

Nederlandse Samenvatting

SAMENVATTING

Metaaldeeltjes met afmetingen van enkele nanometers zijn erg belangrijk voor een groot aantal processen en technologieën, en worden onder andere gebruikt bij de opslag van energie, in de nano-elektronica, en als katalysator voor de productie van een breed scala aan chemicaliën. Voor elke toepassing zijn er specifieke en unieke eisen waaraan het materiaal moet voldoen. Hierdoor is kennis van de processen die spelen tijdens de synthese van de materialen essentieel. Bovendien verliezen nanodeeltjes bij gebruik veelal langzaam hun functionaliteit, ook wel deactivatie genoemd, wat erg onwenselijk is en vaak voorkomen kan worden door beter inzicht in de synthese en het gebruik. Het is dan ook cruciaal om er achter te komen hoe de deactivatie verloopt, waardoor die veroorzaakt wordt en hoe dit voorkomen kan worden.

Een belangrijke groep nanomaterialen zijn diegene die functioneren als katalysator. Deze worden gebruikt om chemische reacties sneller te laten verlopen en bestaan uit een groot aantal nanodeeltjes, meestal van metaal, die afgezet zijn op een dragermateriaal. De drager heeft veelal een hoge porositeit en is mechanisch sterk maar levert geen bijdrage aan het versnellen van de reactie. Nanodeeltjes met een grootte tussen de 1 tot 20 nm zijn vaak gewenst omdat de gekatalyseerde reactie plaatsvindt aan het oppervlak van het veelal dure metaal en er zo maximaal gebruik van wordt gemaakt. Het is dan ook belangrijk de deeltjes uit elkaar te houden tijdens gebruik van de katalysator voor behoud van activiteit, waarbij het dragermateriaal een grote rol speelt. Toch vindt deactivatie vaak plaats via groei van nanodeeltjes zodat het metallisch oppervlak per gram metaal afneemt.

Er zijn twee mechanismen bekend die zorgen voor de groei van nanodeeltjes. Deeltjes kunnen in hun geheel migreren over het oppervlak van het dragermateriaal. Als deeltjes met elkaar in contact komen kunnen ze samensmelten tot één groter deeltje. Ook kunnen monomeren of kleine clusters van atomen van het ene deeltje naar het andere migreren, zodat de grote deeltjes groeien ten koste van de kleine. Welk mechanisme het belangrijkst is hangt sterk af van het metaal en de reactie (condities). Soms is deeltjesgroei tegen te gaan door andere reactiecondities te kiezen of de katalysator te modificeren met andere metalen of moleculen. Echter zijn deze methoden vaak gecompliceerd en kunnen ook negatieve consequenties hebben voor de activiteit en selectiviteit. Minder bekend is het effect van deeltjesgrootte en de afstand tussen deeltjes op de stabiliteit van de katalysator, mede omdat deze parameters vaak moeilijk te sturen zijn tijdens de synthese van de katalysator.

Er bestaan veel verschillende manieren om katalysatoren te synthetiseren. Hierbij geldt vaak dat hoe gecompliceerder de techniek, hoe moeilijker en duurder het is uit te voeren op industriële schaal. Hierdoor is het juist een relatief eenvoudig uit te voeren techniek die het meest gebruikt wordt zowel in academia als in de industrie. In deze techniek, die vaak “impregnatie en drogen” genoemd wordt, begint men met een poreus dragermateriaal waarvan de poriën gevuld worden met een oplossing van een metaalzout, meestal een metaalnitraat vanwege de hoge oplosbaarheid in water. Het oplosmiddel wordt vervolgens verdampt in een droogstap, waarna het metaalnitraat wordt omgezet in het bijbehorende metaaloxide in een

calcinatiebehandeling gevolgd door reductie met waterstof tot het betreffende metaal. Hoewel deze methode eenvoudig is in de uitvoering, zijn de resulterende materialen vaak ver van optimaal. De gevormde nanodeeltjes zijn soms groter dan beoogd of variëren onderling erg veel in grootte en zijn vaak niet homogeen verspreid over het dragermateriaal maar bevinden zich in groepjes of aggregaten.

Aggregaten van nanodeeltjes komen veel voor bij katalysatoren die gebruikt worden bij het omzetten van synthesegas, een mengsel van H_2 en CO, naar brandstoffen of chemicaliën. Zo worden kobaltkatalysatoren, gemaakt vanuit impregnatie met een oplossing van kobaltnitraat in water, veel gebruikt voor de Fischer-Tropsch synthese. Hierbij wordt het synthesegas omgezet in lange koolstofketens, die gebruikt kunnen worden voor ultraschone dieselbrandstof van hoge kwaliteit. Hoewel deze katalysatoren op industriële schaal gebruikt worden, zijn er vele voorbeelden in de literatuur te vinden van katalysatoren waarbij voornamelijk aggregaten van kobaltnanodeeltjes op de drager voorkomen, en is de invloed van deze aggregaten op de prestatie van de katalysatoren nog niet bekend.

Synthesegas kan ook worden gebruikt in de methanatie reactie, waarbij het wordt omgezet naar methaan. Dit wordt veel gebruikt om H_2-gas verontreinigd met CO te zuiveren voordat het gebruikt wordt in de synthese van ammoniak. De reactie kan ook gebruikt worden om synthetisch aardgas te produceren. Deze reactie wordt veelal uitgevoerd met gebruik van nikkelkatalysatoren, waarbij deeltjesgroei plaats vindt via de vorming van nikkelcarbonylen die zich kunnen verplaatsen van kleine naar grote deeltjes.

Dit proefschrift richt zich op de synthese van nikkel- en kobaltkatalysatoren door middel van impregnatie van een dragermateriaal, voornamelijk silica, met kobaltnitraat of nikkelnitraat. Hierbij is in detail gekeken naar de oorzaak van aggregatie en hoe dit gestuurd kan worden tijdens de synthese, in het bijzonder tijdens de droogstap. Ook zijn de effecten van aggregatie en deeltjesgrootte bestudeerd voor de Fischer-Tropsch en methanatie reacties.

Een literatuuroverzicht van belangrijke aspecten en recente ontwikkelingen in de synthese van heterogene katalysatoren is beschreven in **hoofdstuk 2**. Bekende methoden ondergaan continu ontwikkeling door wetenschappelijk onderzoek. Precipitatie van een precursor op het dragermateriaal vanuit een oplossing wordt steeds vaker gebruikt voor het afzetten van edelmetalen met een hoge dispersie. Bij precipitatie van het gewenste metaal en het dragermateriaal in één stap zijn de vele parameters die een rol spelen tijdens synthese uitvoerig onderzocht, alsook manieren om milieuvriendelijkere precipitatiemethodes te ontwikkelen. Nieuwe en innovatieve methodes worden steeds verder ontwikkeld, zoals smeltinfiltratie, waarbij het metaal of een precursor daarvan door middel van smelten direct opgenomen wordt in de poriën van het dragermateriaal zonder toevoegen van een oplosmiddel. Echter de meest gebruikte methode blijft impregnatie en drogen. Hoewel de uitvoering hiervan in de basis eenvoudig is, spelen veel fysisch chemische aspecten een belangrijke rol, zoals precursoradsorptie, herverdeling tijdens drogen en decompositie in samenspel met migratie van de precursor tijdens calcinatie, waardoor het verkrijgen van een goed inzicht niet eenvoudig is maar er in de laatste tien jaar een veel beter begrip is opgebouwd.

In **hoofdstuk 3** is vriesdrogen gebruikt om het effect van de droogstap te bestuderen op de verdeling van kobaltnitraatprecursors over een commercieel gebruikte silica drager. Van groot belang was het fasegedrag van de gedragen precursor, dat werd bestudeerd met differentiële scanning calorimetrie (DSC). Op basis van deze gegevens werden twee vriesdroogmethodes ontwikkeld, die werden vergeleken met een standaard droogmethode waarbij gedroogd werd op 60 °C in een elektrische heteluchtoven. Waar de standaardmethode na calcinatie resulteerde in kobaltnanodeeltjes gelokaliseerd in aggregaten van tussen de 40 en 200 nm, resulteerde vriesdrogen, waarbij ingevroren werd op -196 °C, in homogene distributies. -45 °C was echter niet voldoende om een ge-impregneerde kobaltnitraatoplossing in te vriezen, zodat tijdens de droogstap een grote herverdeling van het materiaal naar de randen van de macroscopische deeltjes van het dragermateriaal plaatsvond. Dit kon vermeden worden door het kobaltnitraat op het dragermateriaal af te zetten door middel van smelt-infiltratie, waarbij het smelt- en vriespunt van het gedragen zout hoger lag wegens gebrek aan oplosmiddel.

De deeltjesgrootte werd gevarieerd door verschillende thermische behandelingen toe te passen na drogen. Door het kobaltnitraat te laten ontleden in een gasstroom van N_2 ontstonden 8 nanometer deeltjes, en bij ontleding in een gasstroom van 1% NO/N_2 werden 5 nm deeltjes verkregen. De katalysatoren vertoonden allemaal een hoge activiteit in de Fischer-Tropsch synthese bij 1 bar gasdruk. Met het gebruik van deze vriesdroogtechniek is duidelijk laten zien dat de droogstap van groot belang is voor de vorming van aggregaten en hoe dit kan worden verminderd.

De droogstap werd nader bestudeerd in **hoofdstuk 4**. Dit werd gedaan door silicagel na impregnatie met een kobaltnitraatoplossing te drogen in een N_2 gasstroom bij verschillende temperaturen. Hierbij werden twee oorzaken gevonden voor de aggregatie van kobaltnanodeeltjes. Onder de 100 °C kon aggregatie plaats vinden tijdens de precipitatie van een vorm van kobaltnitraat. Door de langzame precipitatie kon een groot deel van de oplossing zich herverdelen, resulterend in grote aggregaten. Bij temperaturen boven de 100 °C ontleedde kobaltnitraat in kobaltoxide tijdens de droogstap terwijl het grootste deel van het kobaltnitraat nog in vloeibare vorm was. Doordat de groeiende kiemen gevoed werden door de oplossing konden ook hier grote kobaltaggregaten vormen. Een optimum werd gevonden bij 100 °C, waarbij een hoge droogsnelheid bereikt kon worden zonder dat ontleding van kobaltnitraat voortijdig plaatsvond.

Het effect van de grootte van de aggregaten werd bestudeerd voor de Fischer-Tropsch reactie onder industrieel relevante condities. Alle aggregaten vertoonden een gelijke activiteit en selectiviteit, wat te verklaren was door de gelijke grootte van de grootte van de primaire kobaltdeeltjes van ~10 nm in alle katalysatoren. Een groot verschil werd echter geobserveerd in de deactivatiesnelheid. Deactivatie gebeurde niet door de groei van kobaltdeeltjes in de poriën van de silicadrager, maar door de migratie van nanodeeltjes over tientallen micrometers, waarbij deze zich verzamelden aan het extern oppervlak van de macroscopisch deeltjes (circa 0.07 mm) van het dragermateriaal en pas daar soms groeiden tot deeltjes van circa 300 nanometer maar veelal tot opnieuw aggregaten van dezelfde afmeting. De migratie van

nanodeeltjes kon deels voorkomen worden door de nanodeeltjes homogeen te verdelen over het intern oppervlak van het dragermateriaal. Dit laat zien dat de verdeling van de nanodeeltjes op de nanoschaal en de grootte van de aggregaten een belangrijke rol speelt bij het verkrijgen van stabiele katalysatoren.

Meer fundamenteel inzicht in de vorming van aggregaten tijdens drogen werd verkregen in **hoofdstuk 5**. Door een thermishe behandeling in een gasstroom van 1% NO/N_2 na het drogen werd kobaltnitraat gehydroliseerd naar kobalthydroxynitraat, een vaste stof die niet mobiel is tijdens verdere behandeling en direct ontleedt naar kobaltoxide, zodat de distributie van kobaltnitraat na drogen in beeld kon worden gebracht. De aggregaten die werden gevormd tijdens drogen bij temperaturen tussen de -45 en 100 °C vertoonden overeenkomst met aggregaten die verkregen werden door het drogen van een dunne laag vloeistof met colloïden, wat suggereert dat deze vorm van aggregatie voortkomt uit een fysisch proces. Bij drogen op hogere temperatuur veroorzaakte een chemisch proces juist de vorming van aggregaten.

Op γ-alumina werd aggregatie via dit fysische proces onderdrukt door een hogere interactie tussen de kobaltnitraatprecursor en hydroxylgroepen van het alumina-oppervlak. Door gebruik te maken van een N_2 gasstroom tijdens het drogen werden uitzonderlijk homogene verdelingen van de nanodeeltjes verkregen bij 25 en 100 °C, terwijl drogen op de conventionele manier in stilstaande lucht op 60, 90 en 120 °C resulteerde in aggregaten. De poriegrootte van verschillende silicagels had echter weinig invloed op de grootte van de aggregaten. Wanneer de katalysatoren getest werden voor de Fischer-Tropsch reactie onder industrieel relevante condities werd duidelijk dat homogeen verdeelde katalysatoren tot 50% meer actief konden zijn in vergelijking met katalysatoren met grote aggregaten, afhankelijk van de poriegrootte.

In het onderzoek beschreven in **hoofdstuk 6** werden nikkelkatalysatoren gemaakt met verschillende deeltjesgroottes en -distributies door middel van verschillende combinaties van vriesdrogen, conventioneel drogen, smeltinfiltratie, impregnatie en verschillende calcinatiemethodes. De katalysatoren werden getest voor de methanatiereactie, waarbij deactivatie via Ostwaldrijping door nikkelcarbonyl veelvuldig voorkomt. Twee katalysatoren met gelijke deeltjesgrootte maar verschillende afstanden tussen de deeltjes vertoonden vergelijkbare deactivatie, wat suggereerde dat de afstand tussen deeltjes niet belangrijk is voor deze reactie. Dit wordt verklaard doordat de formatie en decompositie van nikkelcarbonyl de snelheidsbepalende stap is in plaats van diffusie van de monomeren.

De initiële grootte van de nikkeldeeltjes was zeer belangrijk voor de deactivatie. Katalysatoren met kleine deeltjes van 3-4 nm aan het begin van de reactie deactiveerden snel en verloren bijna 95% van hun activiteit na 150 uur. Dit kwam door de groei van sommige deeltjes tot wel 100 nm groot, veel groter dan de poriegrootte van het dragermateriaal. Wanneer er met middelgrootte deeltjes van 8-9 nm werd begonnen deactiveerde de katalysatoren minder snel. Na 150 uur waren deze katalysatoren een factor drie actiever vergeleken met katalysatoren met initieel kleine deeltjes, en de groei van de deeltjes was beperkt tot 10-11 nm, vergelijkbaar met de poriegrootte van het dragermateriaal. Het modelleren van

de reactie toonde aan dat de concentratie van nikkelcarbonyl in katalysatoren met middelgrote deeltjes relatief klein was, terwijl deze in katalysatoren met initieel kleine deeltjes exponentieel hoger was. Hierdoor was er een groot verschil in de druk die door de groeiende nikkeldeeltjes werd uitgeoefend op de poriën van de silicagel. Deze druk was veel groter was voor kleine deeltjes, waardoor deze de poriën konden openbreken en zo ongehinderd konden groeien. Als echter met middelgrote deeltjes werd begonnen, was de druk niet hoog genoeg om het dragermateriaal open te breken en bleven de deeltjes van een grootte gelijk aan de poriegrootte, wat leidde tot stabiele katalysatoren.

VOORUITBLIK

Er kan veel uit dit werk worden afgeleid. Niet alleen kobalt- en nikkelnitraat, maar vele andere metaalnitraten worden vaak gebruikt voor de bereiding van katalysatoren in zowel academisch onderzoek als de industrie. Veel van de huidige conclusies zijn dan ook toepasbaar op een breed scala aan materialen.

Vriesdrogen is een techniek die op grote schaal gebruikt wordt in de farmaceutische- en voedselindustrie. Er is veel kennis over het opschalen van vriesdroogprocessen, en samenwerking met deze sectoren is cruciaal voor optimaliseren van deze techniek voor katalysatorbereiding. De techniek is potentieel toepasbaar op veel verschillende soorten katalysatoren, ongeacht de metaalprecursor en dragermateriaal. Hierbij zijn de faseovergangen van de precursor die geïmpregneerd wordt in het dragermateriaal van groot belang en zullen van te voren bestudeerd moeten worden om herverdeling door een niet-bevroren precursor te voorkomen.

Omdat het mechanisme van aggregatie tijdens drogen onder de 100 °C in een gasstroom een fysisch proces betreft, zou dit ook kunnen spelen bij andere metaalnitraten. Hoe het metaalnitraat zich exact gedraagt zal mede afhangen van de temperatuur waarbij deze ontleedt en eventuele nevenreacties. In het algemeen kan een optimale distributie verwacht worden bij een zo hoog mogelijke temperatuur, waarbij ontleding van het metaalnitraat nog niet plaatsvindt. Ook zouden andere metaalprecursors, bijvoorbeeld metaalchloriden, een soortgelijk gedrag kunnen vertonen.

Het proces van aggregatie zou ook voor andere dragers kunnen gelden, mits er een relatief kleine interactie bestaat tussen het dragermateriaal en het metaalnitraat. Er moet echter wel rekening gehouden worden met macroscopische droogeffecten, die afhankelijk van de specificaties van het dragermateriaal een belangrijke rol kunnen spelen. Voor een silicagel met 23 nm poriën gebeurde dit door middel van migratie van de precursor tijdens drogen naar de buitenste schil van de macroscopische silicageldeeltjes. Dit zou ook kunnen gebeuren als grotere dragerdeeltjes worden gebruikt. Voor de silicagel met 23 nm poriën kon macroscopische migratie worden voorkomen door smeltinfiltratie te gebruiken in plaats van impregnatie, waarbij de kleinere hoeveelheid oplosmiddel herverdeling tijdens de droogstap verminderde.

In dit werk is uitvoerig gebruik gemaakt van wervelbedreactoren, waarbij een gas van onderaf door het dragermateriaal (een poeder) wordt geleid, zodanig dat de deeltjes gaan bewegen (wervelen) en eigenschappen vertonen die gelijk zijn aan een vloeistof. Deze techniek is niet altijd praktisch voor alle soorten deeltjes of op grote schaal en is niet noodzakelijkerwijs essentieel. Het behalen van een hoge droogsnelheid en een vlotte afvoer van water en decompositieproducten zijn de belangrijkste factoren, welke ook behaald zouden kunnen worden door gebruik te maken van alternatieve reactoren, zoals een zogeheten "rotary kiln" reactor, waarbij gassen horizontaal kunnen stromen door een reactor die om een horizontale as draait, zodat het materiaal continu in beweging is.

Deze nieuwe inzichten in het sturen van de aggregatie van metalen op een dragermateriaal tijdens katalysatorpreparatie zijn essentieel bij het verkrijgen van stabiele katalysatoren en andere nanomaterialen waarbij de afstand tussen metaalnanodeeltjes belangrijk is. Ook zijn de nieuwe inzichten die zijn behaald op het gebied van katalysatordeactivatie van groot belang.

De migratie van kobaltnanodeeltjes over vele micrometers naar het extern oppervlak van het dragermateriaal is zelden gerapporteerd. Door middel van ultramicrotomie kon het resultaat van deze migratie op zowel de nano- als de macroschaal uitvoerig bestudeerd worden. Echter is de exacte reden voor deze migratie vooralsnog onbekend en vereist verder onderzoek. Desalniettemin is de conclusie dat een homogene distributie voor significant minder migratie zorgde een belangrijke vinding.

Ten slotte is de bevinding dat middelgrote nikkeldeeltjes stabieler waren voor methanering vergeleken met kleine deeltjes erg belangrijk voor nanomaterialen in het algemeen. Het laat duidelijk zien dat, hoewel er vaak gestreefd wordt naar de kleinst mogelijke deeltjes, iets grotere deeltjes in sommige gevallen stabieler kunnen zijn.

Appendix A

Control and Impact of the Nanoscale Distribution of Supported Cobalt Particles in Fischer-Tropsch Catalysts

ADDITIONAL DRYING EXPERIMENTS

Flow and Ramp Variation. During synthesis, the rate of drying could also be controlled by changing the gas space velocity, allowing further control of the degree of aggregation. Drying at 150 °C in a 6 times higher flow reduced the aggregate size significantly, while drying in stagnant air increased the aggregate size (Figure A.1). It should be noted that a higher GHSV could also translate to a lower temperature due to the 'wet bulb effect'; a higher flow has a higher capacity of water removal per unit of time, so more evaporative cooling could take place keeping the sample at a lower temperature. Regardless, this illustrates the significance of the drying rate.

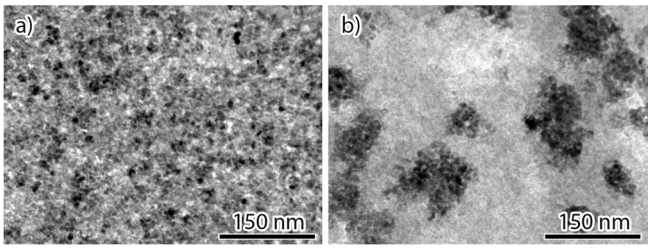

Figure A.1. TEM of calcined Co_3O_4/SiO_2 after drying at 150 °C under different flows. (a) GHSV of 30000 h^{-1} and (b) GHSV of 0 h^{-1}. While no flow resulted in large aggregates, a high flow greatly reduced the aggregate sizes.

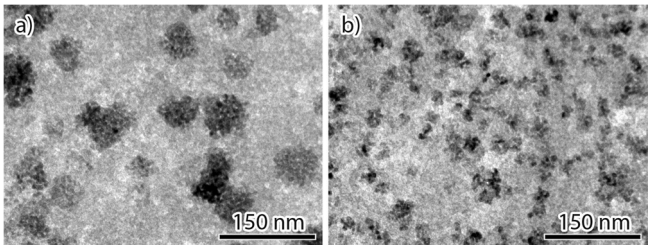

Figure A.2. TEM of Co_3O_4/SiO_2 calcined with a temperature ramp of 10 °C/min after different drying treatments. (a) Dried at 25 °C and (b) 100 °C. A high temperature ramp led to larger aggregates.

Increasing the rate at which the temperature was increased during calcination further increased the aggregate size (Figure A.2). This shows careful control of the calcination is also highly important. The drying time was not found to be of influence, as long as enough time had passed for a solid cobalt nitrate species to precipitate (Figure A.3). Thus, it is the drying rate that is the most important factor in controlling the nanoscale distribution of cobalt.

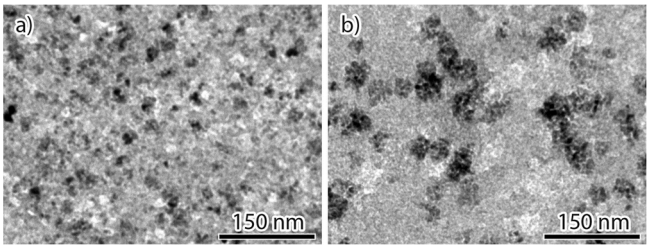

Figure A.3. TEM of calcined Co_3O_4/SiO_2 after different drying treatments at longer drying times. a) Dried at 100 °C for 72 h and b) 150 °C for 8 h. These samples are similar to those found at shorter drying times (see Figure 6.1), showing the drying time is of little influence to the aggregation.

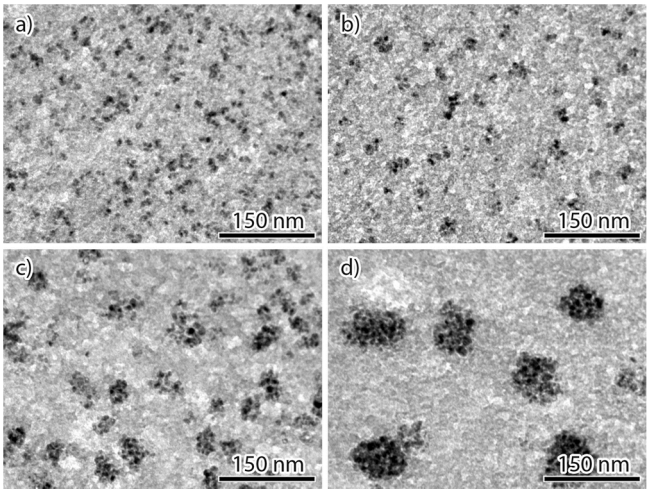

Figure A.4. TEM of reduced and passivated $CoPt/SiO_2$ after different drying treatments. (a) Dried at 100 °C, (b) 125 °C, (c) 150 °C and (d) 175 °C. Aggregates were observed to fragment into small individual nanoparticles 8-10 nm in size.

Aggregate Structure. To investigate the structure of the aggregates after calcination, the silica of one sample with 50 nm aggregates was removed by 2M NaOH treatment at room temperature overnight. The sample was subsequently washed and centrifuged, leaving 50 nm cobalt oxide particles, the same size as the original cobalt oxide aggregates were in the catalyst body (Figure A.5a). Taking a slice from the middle of an electron tomogram, reconstructed from 13 images with tilts between -55 and 45°, the inner structure was observed to be porous (Figure A.5b) while dark field imaging showed large parts or entire aggregates could still consist of single crystal domains (Figure A.5c).

N_2-physisorption showed a well-defined adsorption/desorption isotherm (Figure A.5d) with an exceptionally large pore volume (0.5 mL/g) and high BET surface area (170 m^2/g) for such nanocast materials, and a bimodal pore system consisting of primary pores of 5 nm

located inside the Co_3O_4 particles and larger mesopores of up to 40 nm located between the particles (Figure A.5e). At the same time, XRD before and after silica removal showed to be almost identical with the exception of the missing broad amorphous SiO_2 band, with corresponding Co_3O_4 crystallite sizes of 8.4 and 8.7 nm, respectively, much smaller than the size of the particles but close to that of the original pore size of the silica template (Figure A.5f). These results show the cobalt oxide grew to confinement of the pores creating large 50 nm aggregates of crystallographically aligned Co_3O_4 nanocrystals growing around and throughout the silica support structure.

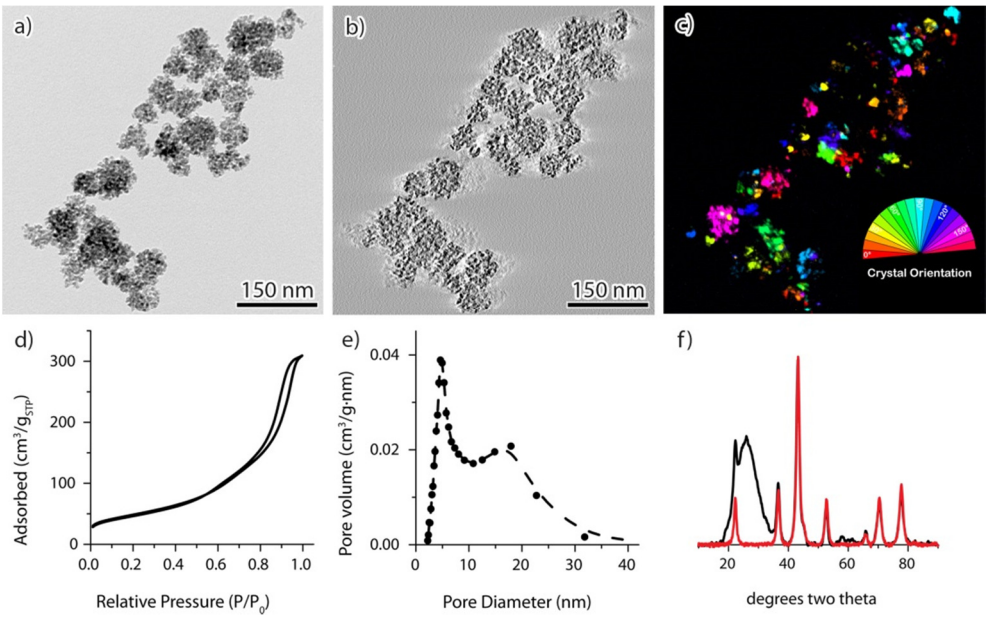

Figure A.5. Analysis of aggregates after removal of the silica support. (a) Bright field image, (b) slice from the middle of tomogram reconstruction, (c) superposition of 18 dark field images separated by a beam orientation of 10° each, using a different color for each orientation (inset), (d) N_2-physisorption isotherm, (e) BJH desorption pore size distribution, (f) XRD before (black) and after (red) silica removal, showing the Co_3O_4 crystallites do not change upon removal.

CATALYSIS

Initial Activity Loss. Each catalyst showed a high apparent drop in activity in the first 25 hours. To investigate this, the catalysts were flushed with argon for two hours after 240 hours on-stream. The reactors were subsequently re-pressurized to 20 bar under H_2 at 180 °C, after which syngas was reintroduced and the temperature was returned to 220 °C at t = 255 h (Figure A.6). After this, an increased activity was observed compared to before the reactors were flushed, but it rapidly dropped back to the baseline level it was at before the treatment. A

difference between the initial activity at t = 0 and t = 255 h was observed, which was similar to the loss in activity found between t = 25 and t = 240 h. Thus, the initial drop in activity was attributed to the filling of the catalyst pore structure with waxes rather than any form of structural deactivation. After t=25 h, it was assumed the pores were filled and any further deactivation was attributed to a different process.

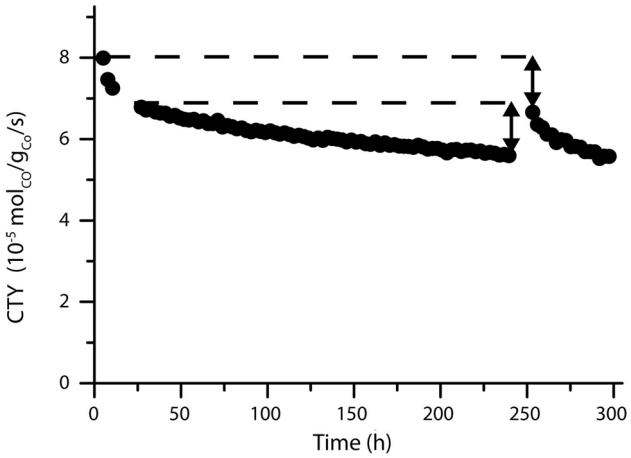

Figure A.6. Catalytic activity of CoD150. An initial drop in activity is observed in the first 25 hours. This could be recovered after removal and reintroduction of syngas, without any regeneration treatment. Permanent deactivation was observed over the course of 240 hours (arrowed lines). All catalysts behaved similarly.

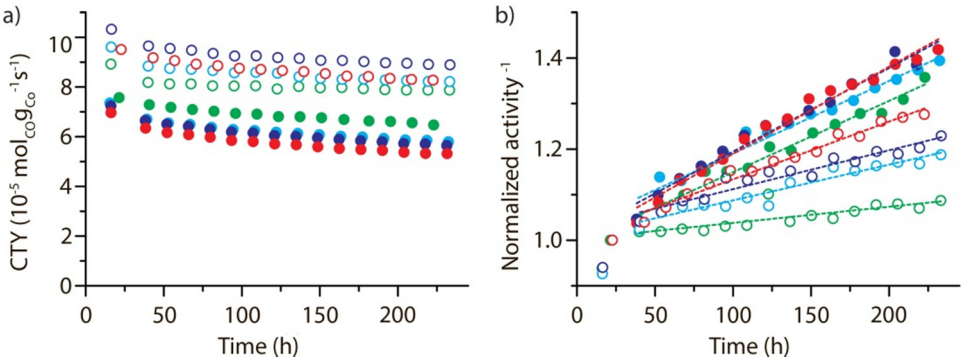

Figure A.7. (a) Catalyst activity plotted as a function of time on-stream. Green: dried at 100 °C, cyan: 125 °C, blue: 150 °C, red: 175 °C. Closed symbols: unpromoted catalysts, open symbols: Pt promoted catalysts. (b) CO conversion (*a(t) proportional to -ln 1 - x (t)*) normalized at t = 25 h as a function of time on-stream, fitted with a PLE (Equation A.2) with n = 2, showing a good fit from which the deactivation constants were obtained.

Deactivation. The activity of each catalyst as a function of time on-stream is shown in Figure A.7a. The experimental activities were fitted with a Power Law Expression (PLE) of the form[1]:

$$da/dt = -k_D \cdot a(t)^n \qquad \text{(Equation A.1)}$$

where $a(t)$ is the normalized activity as a function of the time-on-stream, k_D is the deactivation rate constant and the exponent n usually ranging from 2 to 10. Simple first-order kinetics were assumed such that $a(t)$ is proportional to the first order rate constant - ln (1 - $x(t)$), whereby $x(t)$ is the CO conversion. Equation A.1 can be integrated and rewritten to yield a linear relationship between the normalized activity $a(t)$ and time-on-stream:

$$a(t)^{1-n} = (n - 1) \cdot k_D \cdot t + 1 \qquad \text{(Equation A.2)}$$

such that the slope of a^{1-n} gives the deactivation rate constant. Catalyst activities were normalized at t = 25 h, at which time a steady decline of activity was observed. Figure A.7b shows this relation plotted assuming a second-order deactivation for each catalyst so that n = 2.

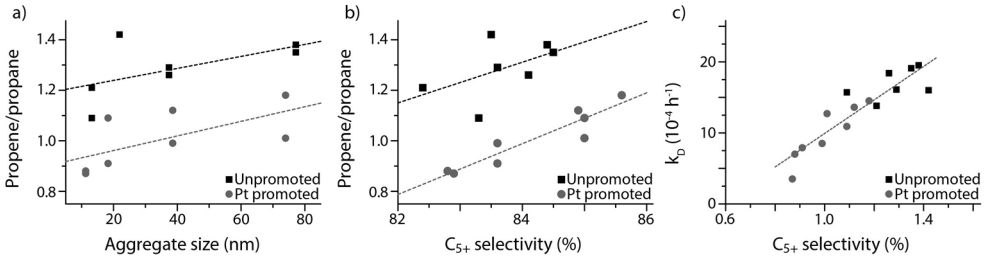

Figure A.8. (a) Propene/propane ratio as a function of aggregate size for the unpromoted (black squares) and Pt promoted (grey circles) samples, showing Pt reduces the propene/propane ratio for all aggregates sizes. (b) Propene/propane ratio related to C_{5+} selectivity, illustrating the reported reduction in (a) is not related to the selectivity. (c) Deactivation constant of promoted and unpromoted Co/SiO_2 catalysts related to the propene/propane ratio, showing a linear correlation.

Figure A.9. C_{5+} selectivity as a function of CO conversion for each catalyst. An increase in selectivity is observed for increasing CO conversion, while the difference between catalysts remains similar throughout the entire CO conversion range.

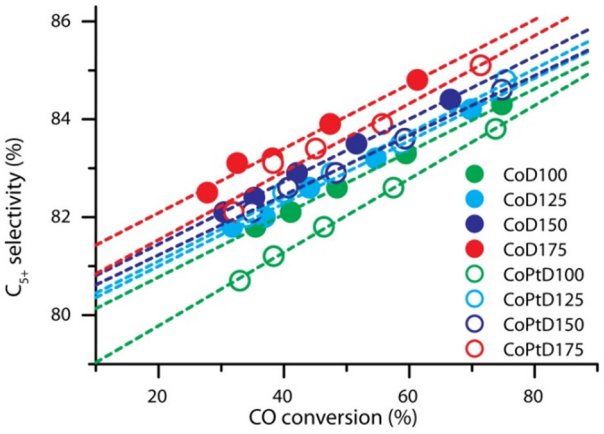

Selectivity Dependency on Conversion. After the 240 h deactivation test, the CO conversion was varied between 30 and 80% by varying the GHSV. For every CO conversion in the range studied, larger aggregates resulted in higher C_{5+} selectivities (Figure A.9). In general, higher CO conversions resulted in higher C_{5+} conversions for each catalyst, as has been reported before.[2] However, this increase appeared unrelated to the aggregate size, as can be observed by the similarities in the slopes of the linear fits (dashed lines). No significant difference in activity was found by changing the conversion.

ANALYSIS ON SPENT CATALYSTS

Large Scale Aggregates. To further investigate aggregates during the Fischer-Tropsch catalysis, catalysts with very large aggregates of about 1000 nm were synthesized by drying an impregnated sample at 150 °C in a closed environment (Figure A.10a).[44] The catalyst was transferred into a stainless steel reactor in layers (SiC, 10 mg catalyst, SiC, 80 mg catalyst, SiC, 10 mg catalyst, SiC) so that the top and bottom catalyst layers could be easily separated after reaction while a total conversion of about 80% was achieved at 240 °C.

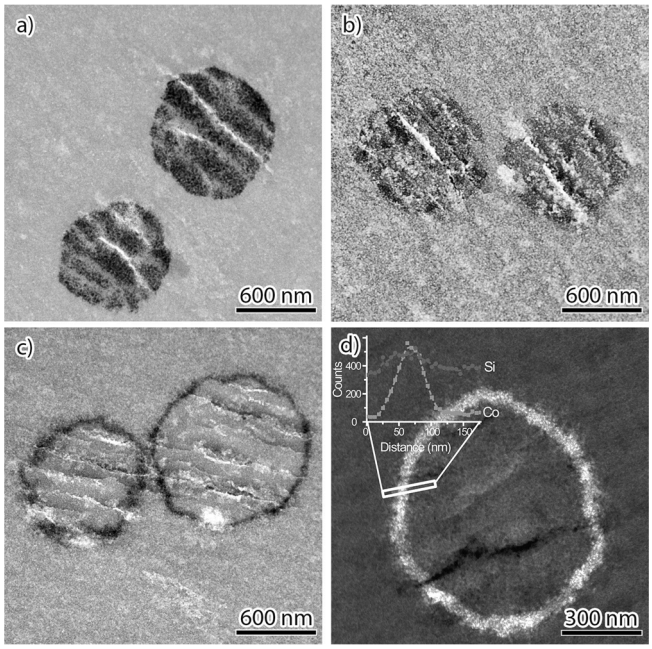

Figure A.10. TEM of microtomed catalysts with 1000 nm sized aggregates. (a) After reduction and passivation, (b) after reaction from the top of the reactor and (c) from the bottom of the reactor. (d) HAADF-STEM image of a ring and a linescan across the edge of it (inset).

Thus, the top of the reactor (Figure A.10b) encountered a large concentration of reactants but relatively low concentrations of hydrocarbons and water, whereas the bottom layer (Figure A.10c) encountered a high concentration of water and products but relatively little H_2 and CO. After 200 h, the top layer showed little change with respect to the reduced state, whereas the bottom layer changed drastically, showing 1000 nm cobalt egg-shells with a thickness of about 50 nm rather than aggregates. An EDX line-scan (Figure A.10d) showed most cobalt was

located in the shell, with only a small amount found on the inside of the shell. Simple calculations show that if a 1000 nm aggregate were to transform into a 50 nm shell, this shell should have a diameter of about 1900 nm. However, this was not observed. Thus, this suggests the cobalt had not only moved from the core of the aggregate to the outer shell, but had moved to a different location entirely, such as the outside of the catalyst grain as evidenced by SEM (see Chapter 4, Figure 4.7).

Table A.1. N_2-physisorption on fresh, spent and calcined spent catalysts.

Catalyst	BET surface area (m^2/g_{cat})	Pore volume (mL/g_{cat})	Average pore diameter (nm)
Fresh	350	0.63	6.0
CoPtD100 Spent	250	0.49	5.4
CoPtD175 Spent	210	0.43	5.4
CoD100 Spent	180	0.35	5.0
CoD175 Spent	165	0.32	4.9
CoPtD100 Wax removed	350	0.66	6.2
CoD175 Wax removed	340	0.64	6.1

Porosity of Spent Catalysts. Four spent catalysts taken from the bottom half of the reactors were analyzed more extensively. N_2-physisorption illustrated a decrease in BET surface area and pore volume with increasing deactivation, suggesting increased deactivation was associated with a loss of silica integrity. However, a decrease in pore diameter was also observed, whereas an increase in pore diameter might be expected if the deactivation had been related to destruction of the silica. Since the catalysts were only stripped with H_2, it was assumed heavy waxes were still gathered in the pores. Because of this, two of the spent catalysts were additionally heat treated at 500 °C in air to burn off the waxes, and then re-measured. After this treatment, structural values almost identical to the original fresh catalyst were found, suggesting the destruction of the silica support was minimal.

Table A.2. TEM cobalt particle sizes of fresh catalysts, and after 240h on-stream.

Catalyst	Particle size fresh catalyst (nm)	Particle size spent catalyst (nm)
CoPtD100	9.0 (± 2.4)	9.6 (± 2.6)
CoPtD175	8.6 (± 2.6)	8.9 (± 2.3)
CoD100	8.7 (± 2.0)	9.7 (± 2.5)
CoD175	9.5 (± 2.3)	9.8 (± 2.9)

XRD Analysis on Spent Catalysts. XRD analysis of the four spent catalysts before the calcination treatment is shown in Figure A.11. All catalysts exhibited very small CoO crystallites, likely in the form of passivated layers around the original Co particles. In addition, an increasing amount of metallic Co (fcc) was found for increasing deactivation rate constants, which could indicate large aggregates on the outside of the catalyst grains. However, the intensity remained low and the peak broadening was not significantly different for the different catalysts. Thus, while a trend was observed, it was inconclusive.

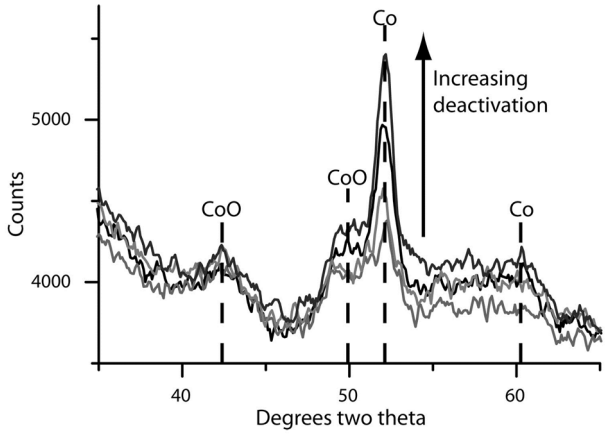

Figure A.11. XRD analysis on spent catalysts. An increase in metallic Co is observed for catalysts with increasingly larger deactivation constants.

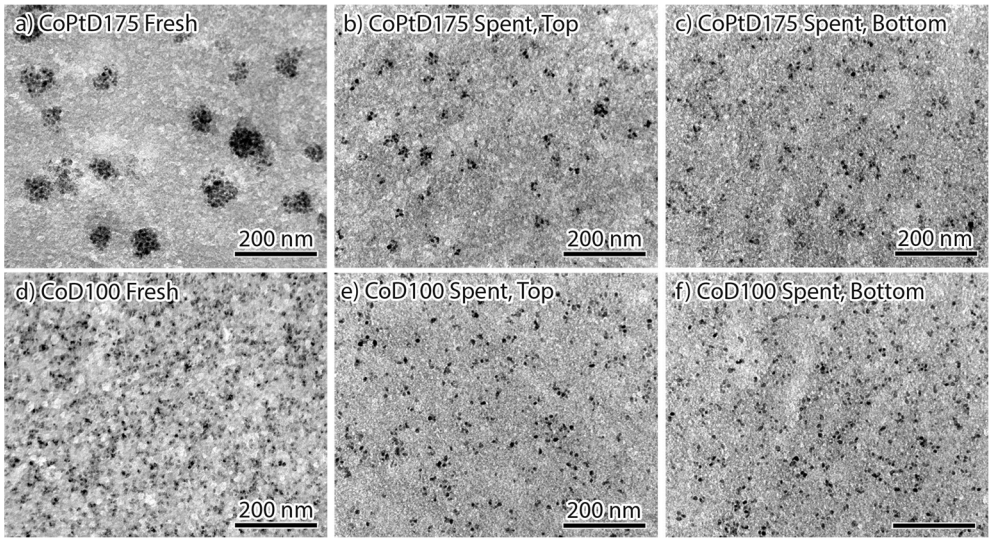

Figure A.12. TEM comparison of fresh and spent catalysts. (a) CoPtD175 after reduction, (b) CoPtD175 after reaction from the top of the reactor and (c) CoPtD175 after reaction from the bottom of the reactor. (d) CoD100 after reduction, (e) CoD100 after reaction from the top of the reactor and (f) CoD100 after reaction from the bottom of the reactor.

Additional Microscopy. The same four catalysts were analyzed using TEM to investigate a change in particle size before and after catalysis. Catalysts showed an initial particle size of 8.5 to 9.5 nm in good agreement with the H_2-chemisorption measurements (see Chapter 4, Table 4.2), which became 9 to 10 nm after catalysis (Figure 4.5 and Figure A.12). Due to the large standard deviations of 2 to 3 nm for each catalyst, this increase was found to be insignificant. In addition, the catalyst that showed the highest deactivation (CoD175) showed the smallest increase of 0.3 nm, showing there was no correlation between the deactivation and an increase in cobalt particle size (Table A.2 on page 155).

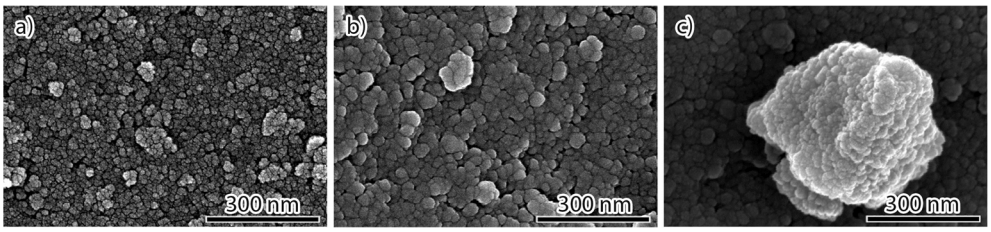

Figure A.13. High magnification SEM of CoPtD100 before (a) and after catalysis (b) taken from the bottom half of the reactor, and an example of an aggregate from CoD175 (c) after catalysis from the bottom half of the reactor, which appears to consist of many smaller particles suggesting it is porous. Comparison of the external surface of the catalyst before and after reaction (a and b) suggests silica might have been altered during reaction conditions. However, N_2-physisorption data shows that this is a local effect, and could also be due to residual carbon left on the support.

SEM analysis of the four catalysts is shown in Figure A.15. In each case, the fresh catalysts showed no cobalt on the external surface of the catalyst grains. Samples from the top half and bottom half of the reactor taken after catalysis exhibited large aggregates of cobalt on the external surface in each case, more so for the catalysts with large initial aggregate sizes (CoD175 and CoPtD175).

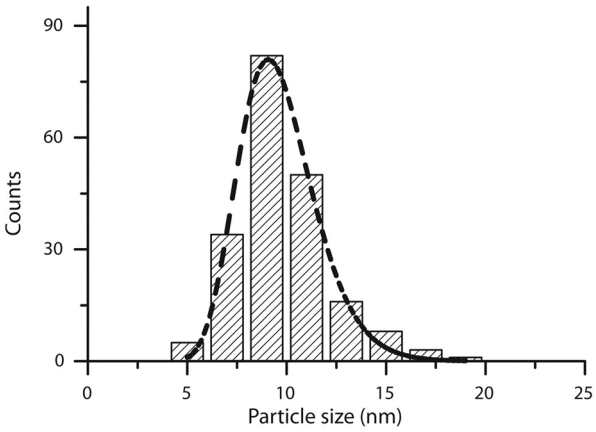

Figure A.14. Histogram analysis on the cobalt particle sizes found within aggregates located on the external surface of CoD175 (Figure 4.7 from Chapter 4). An average of 9.7 nm was obtain (± 2.2), which is equal to the size of the particles found on the inside of the catalyst grain before and after catalysis (Table A.2).

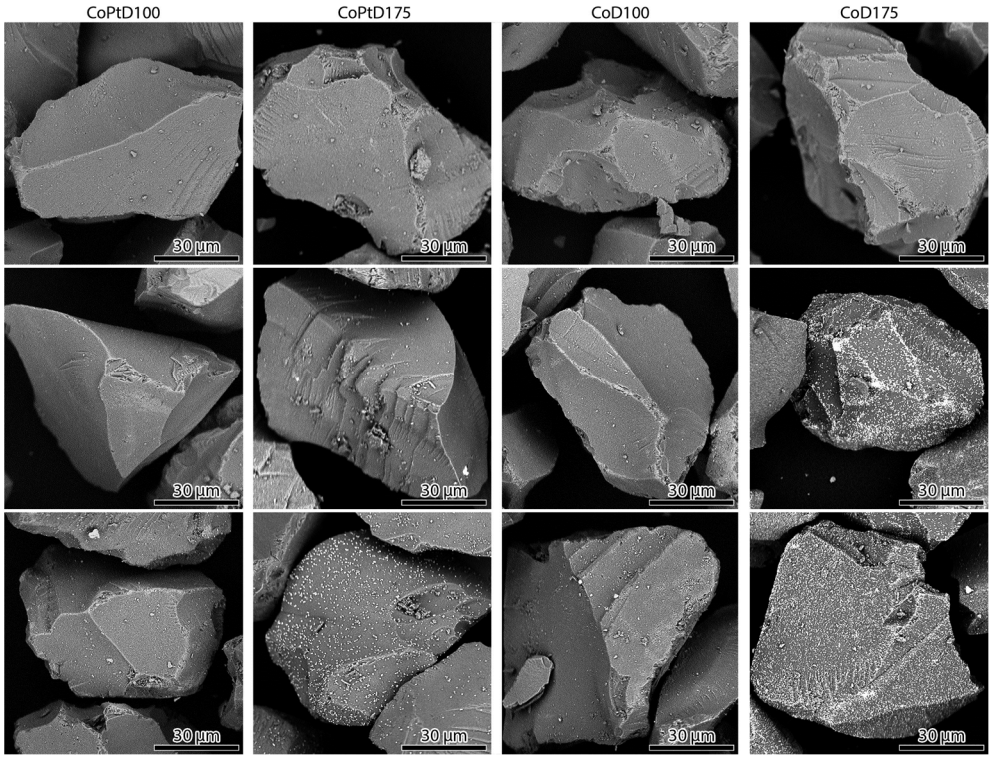

Figure A.15. SEM comparison of 4 catalysts. Left column) CoPtD100, middle left) CoPtD175, middle right) CoD100, right column) CoD175. Top row) After reduction, middle row) from the top half of the reactor, bottom row) from the bottom half of the reactor.

Tomography. Tomography was performed on CoD175 catalyst particles taken from the bottom of the reactor after catalysis. Particles were directly transferred to a TEM grid without further treatment, so that micrometer sized silica particles could be observed. From the edge of such a sample, an aggregate was identified and a tilt series was taken in HAADF-STEM mode from -60° to +60° at 2° interval at the highest tilt angles, and at 3° interval for the rest (between -50° and 50°). The corresponding movies can be downloaded from the Supporting Information of the published article. Alignment of the tilt series was performed in IMOD software using a feducialless alignment, and can be viewed in Video_S1_tiltseries. The tilt series was reconstructed using the back projection method, which can be viewed in Video_S2_reconstruction. In both the tilt series and reconstruction, cobalt is shown as white (high contrast).

ADDITIONAL REFERENCES

(1) Bartholomew, C. H. *Appl. Catal. A Gen.* **1993**, *107*, 1–57.
(2) Bukur, D. B.; Pan, Z.; Ma, W.; Jacobs, G.; Davis, B. H. *Catal. Letters* **2012**, 1382–1387.

Appendix B

Effects of Drying Conditions on the Synthesis of Co/SiO_2 and Co/Al_2O_3 Fischer-Tropsch Catalysts

ADDITIONAL TEM CHARACTERIZATION

Micrometer Sized Aggregates after Direct NO Calcination. A direct heat treatment in 1% NO/N_2 flow after impregnation without a drying step in an N_2 flow led to a wide distribution of aggregate sizes. While Figure 5.2b of the main chapter shows an image representative of the average aggregate size, the aggregates were as large as several micrometer, as shown in Figure B.1. High magnification of such an aggregate revealed it nonetheless consisted of individual 4 - 7 nm particles.

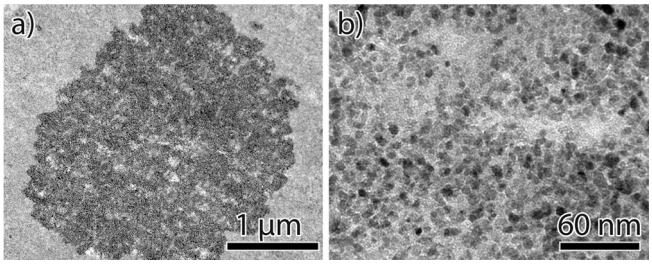

Figure B.1. Low (a) and high (b) magnification TEM of Co_3O_4/SG8 obtained by direct NO calcination after impregnation without a drying step, showing an aggregate of several micrometer in size supported on otherwise mostly empty silica.

γ-Alumina – NO Calcination. On γ-alumina (GA9), applying an NO calcination led to such small particles that their contrast against the γ-Al_2O_3 background was very small, even for ultramicrotomed slices of the catalyst particles. A examples are shown in Figure B.2, whereby the sample was impregnated, dried at 75 °C and calcined in NO, after which the procedure was repeated to increase the cobalt weight loading. No convincing distinction can be made between the γ-Al_2O_3 support needles, which can lie at random angles including pointing at the reader, and Co_3O_4 particles, which were about 3 - 4 nm according to XRD (not shown).

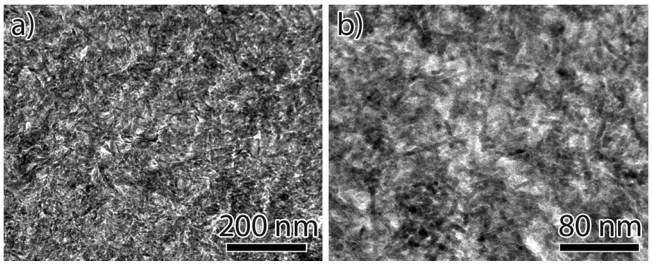

Figure B.2. Examples of bright field TEM images obtained for $Co_3O_4/\gamma\text{-}Al_2O_3$ (GA8) after a double impregnation, drying (75 °C in N_2) and calcination (350 °C in NO), illustrating the difficulty in distinguishing the support from the 3 - 4 nm cobalt oxide particle.

γ -Alumina – Alternative Drying. Drying on γ-alumina (GA8) was also performed at 60, 120 or 150 °C in stagnant air, or in a semi-enclosed contained to inhibit the removal of water. Drying at 60 and 120 °C resulted in medium sized aggregates of 30-60 nm in size (Figure B.3a and b), similar to drying at 90 °C in stagnant air described in chapter 5. Drying at 150 °C in stagnant air resulted in larger 100 - 150 nm aggregates (Figure B.3c), whereas drying while inhibiting the removal of water resulted in aggregates up to 1000 nm in size (Figure B.3d). This underlined the importance of efficiently removing water and decomposition products during the drying step.

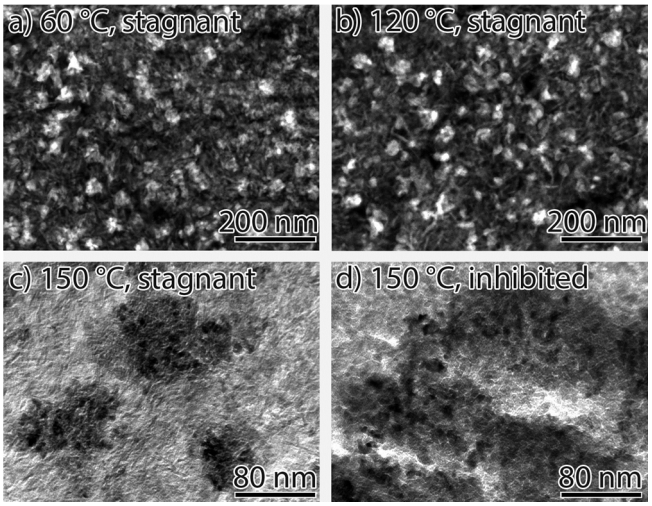

Figure B.3. HAADF-STEM (top, cobalt in white) and bright field TEM (bottom, cobalt in dark) of $Co_3O_4/\ \gamma\text{-}Al_2O_3$ (GA8) using different drying treatments, followed by calcination in N_2. (a) dried at 60 °C in stagnant air, (b) dried at 120 °C in stagnant air, (c) dried at 150 °C in stagnant air, (d) dried at 150 °C while inhibiting the removal of water. (note the different scale bars)

Pore Size Distributions. The BJH pore size distributions based on the desorption branch of the N_2-physisorption measurements of the various support materials are provided in Figure S4. For SG3, the adsorption branch was used instead of the desorption branch due to the forced closure of the desorption branch at $p/p_0 = 0.42$, wrongfully indicating a sharp peak at a pore size of 4.3 nm. All catalysts exhibited relatively narrow pore size distributions, with no pores larger than 50 nm.

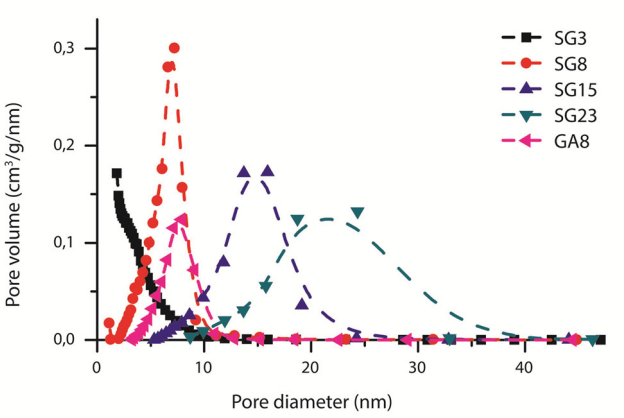

Figure B.4. BJH pore size distributions based on the desorption branch obtained from N_2-physisorption measurements of the used support materials. For SG3, the adsorption branch was used instead.

MACROSCALE REDISTRIBUTION

Large Pore Silica. A silica gel with even larger 23 nm pores was also investigated (BET 300 m^2/g, V_p 1.7 mL/g, final cobalt weight loading 27 wt.%). SG23 showed similar results on a nanoscale; drying at 100 °C followed by calcination in N_2 flow resulted in cobalt particles homogeneously distributed, whereas after drying at 150 °C 50 - 100 nm aggregates were found. However, for this large pore silica an additional effect was observed. Figure B.5 shows low magnification TEM and SEM micrographs of SG23 after different drying temperatures and subsequent N_2 calcination. Drying at 25 °C resulted in a homogeneous macroscopic distribution across the catalyst grain (Figure B.5a and d), as observed for all other supports with smaller pore sizes. However, drying at 100 °C (figure B.5b and e) resulted in an egg-shell distribution, exhibiting a macroscopic inverse cellular network, whereby the cells were filled with cobalt while the cell walls were mostly silica depleted of cobalt. At 150 °C (figure B.5c and f), an egg-shell distribution was also observed, but in this case a branching structure was evident.

To study this change in macroscopic distribution, the decomposition of cobalt nitrate in the pores of SG23 was compared to that in SG8, where no macroscopic effects were apparent. To this end, TGA-MS and DRIFTS measurements during a heat treatment from 25 to 300 °C were performed (Figure B.6). TGA-MS on SG8 showed initial dehydration, followed by a single decomposition step starting around 150 °C after most water had been removed (Figure B.6a). DRIFTS measurements showed a change in the –O-N-O_2 band from 1480 to 1600 cm^{-1} corresponding to dehydration and a change in ligand going from water to nitrate, before final decomposition occurred above 150 °C after all the water was removed. For SG23, a similar initial dehydration was observed. However, TGA-MS showed a two-step decomposition at 150 and 180 °C. DRIFTS showed that this two-step decomposition was accompanied by a large and broad band between 1480 and 1600 cm^{-1}, which is where nitrate bands are located. Thus, it was concluded that an intermediate species was formed in the pores of SG23.

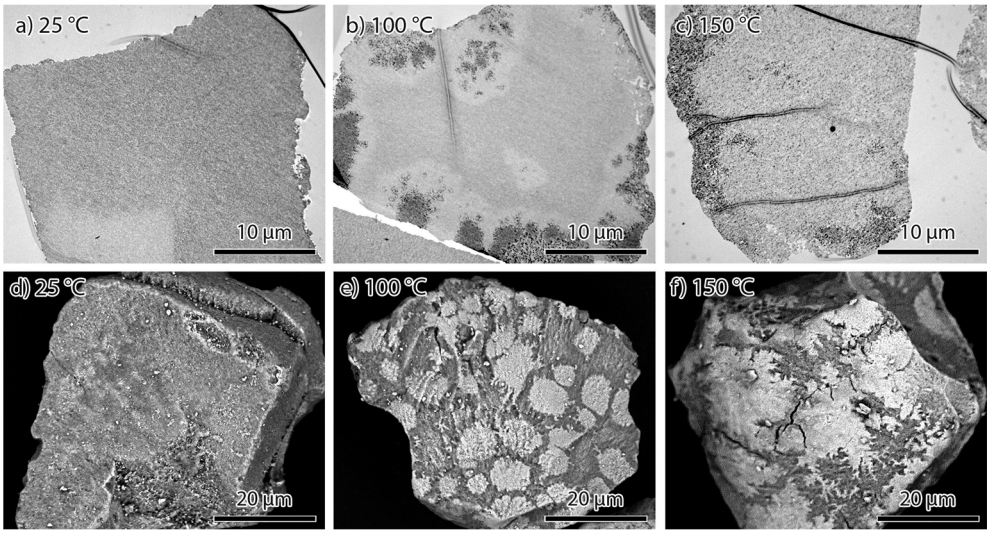

Figure B.5. TEM (top, cobalt as black, showing the inside of the grains) and SEM (bottom, cobalt as white, showing the external surface) of different macroscopic distributions obtained for *ex-nitrate* cobalt catalysts on a silica gel with 23 nm pores. (a,d) dried at 25 °C, resulting in a homogeneous distribution. (b,e) dried at 100 °C, showing a cellular network of cobalt islands. (c,f) dried at 150 °C, which led to a branching network.

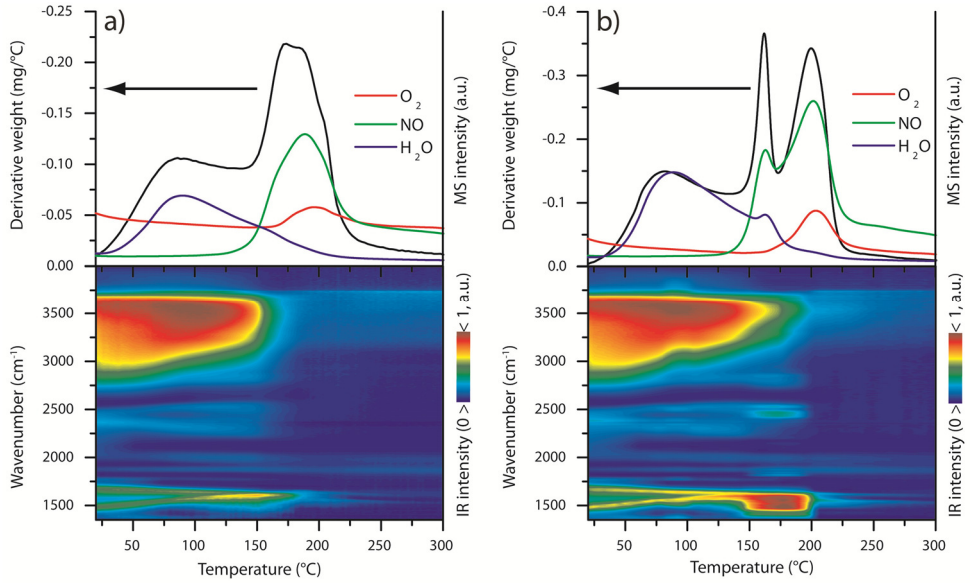

Figure B.6. TGA-MS (top) and DRIFTS (bottom) of two silica gels impregnated with a 4.2M cobalt nitrate solution. (a) SG8, (b) SG23. For TGA, the ramp rate was higher resulting in the shift in temperature. A similar behavior is observed at low temperature, while at 150 °C SG23 exhibits the formation of an additional intermediate, before decomposing completely.

While this intermediate was difficult to assign, its formation could have implications for the macroscopic distribution. Through modelling studies it was previously shown that the drying of low melting point transition metal nitrates goes through several stages.[1] Initially, convection causes redistribution of the precursor towards the outside of the catalyst grain. As the water content decreases, drying slows down and back-diffusion becomes more dominant. As long as the concentration of the initial solution was high enough, enough molten metal nitrate remains to keep the entire catalyst grain wetted, so that back-diffusion results in a homogeneous redistribution. We postulate that the formation of the intermediate species found in large pores interrupted the process of back-diffusion and equilibration. Instead, the intermediate species precipitated at a point when most of the precursor had just moved to the outside. It appears the rate of this process depended on the temperature, resulting in a cellular network when the process was relatively slow, while a branching pattern was developed at a higher temperature when the process was somewhat faster, similar to what was found for low and intermediate drying temperatures (see Figures 5.2a and 5.3a of the main chapter).

The water content of the precursor was previously shown to play a large role in the synthesis of supported catalysts when using freeze drying.[2] There, melt infiltration was used to load the precursor directly without the need for a solvent, reducing the water content. Thus, an attempt to minimize the macroscopic redistribution was made by using melt infiltration of the cobalt nitrate into the SG23 support, whereby the amount of cobalt nitrate used per gram of support was equal to that used in the impregnation method. Subsequently, the material was dried at 100 °C or 150 °C in a N_2 fluidized bed and further heated to 350 °C in N_2, in the same way as the impregnated samples. Results showed the cobalt oxide was mostly homogeneously distributed across the catalyst grains (Figure B.7). Thus, reducing the amount of water in the precursor greatly reduced the macroscopic redistribution. It was postulated that reducing the water content while keeping the amount of cobalt nitrate similar reduced the time needed between the start of drying and the precipitation of cobalt nitrate species or the formation of the observed intermediate. This reduced the time available for macroscopic redistribution towards the outside of the catalyst grain.

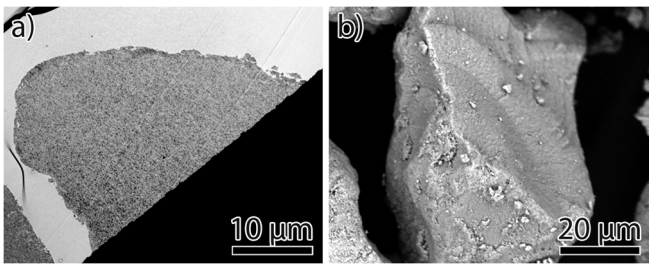

Figure B.7. (a) TEM (cobalt as black, showing the inside of the grains), and (b) SEM (cobalt as white, showing the external surface) of a sample melt infiltrated, dried at 150 °C and calcined at 350 °C in N_2. Neither the inside nor the outside of the grain showed inhomogeneities on the macroscale.

ADDITIONAL REFERENCES

(1) Liu, X.; Khinast, J. G.; Glasser, B. J. *Chem. Eng. Sci.* **2012**, *79*, 187.
(2) Eggenhuisen, T. M.; Munnik, P.; Talsma, H.; de Jongh, P. E.; de Jong, K. P. *J. Catal.* **2013**, *297*, 306.

Appendix C

Nanoparticle Growth in Supported Nickel Catalysts during Methanation Reaction – Larger is Better

ADDITIONAL CATALYST CHARACTERIZATION

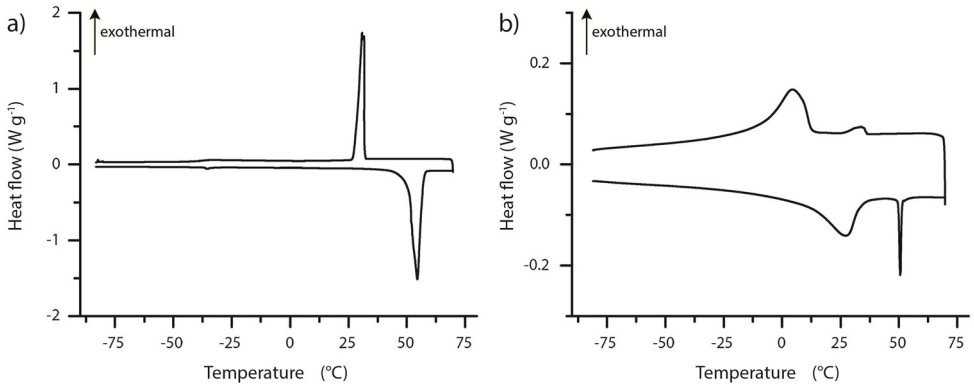

Figure C.1. DSC of (a) nickel nitrate hexahydrate and (b) silica melt infiltrated with nickel nitrate hexahydrate.

Precursor Phase Behavior. To ensure the freeze-drying conditions would be sufficient to solidify the precursor and keep it frozen during the freeze-drying process, DSC measurements were performed. Figure C.1 shows that nickel nitrate hexahydrate had a melting point of 54 °C in bulk, but exhibited a depressed melting point after melt infiltration into the silica pores. Intraporous nickel nitrate hexahydrate started melting below 0 °C, with the main peak around 25 °C. Because of this broad melting peak, samples were cooled to liquid nitrogen temperatures and the first freeze-drying step was performed at -45 °C to prevent any redistribution during drying. In addition, a small peak at 54 °C after melt infiltration was evidence that about 4% of the added nickel nitrate was still present in bulk, likely located in large pores or on the external surface of the macroscopic silica grains. This resulted in some large particles of several hundred

nanometers on the outer surface of the silica grains for each catalyst, as is often observed for samples impregnated or melt infiltrated.·

Interparticle Distance Calculations. All the particles in several high magnification images were identified to measure the distances between neighboring particles (Tables 6.1 and C.1. See Figure C.4 and Table C.2 for the full histograms, average sizes and number of particles measured). This method provided the surface to surface distance in a 2D projection of the 50 nm thick section. A 2D projected distance of 4 nm was found for Ni-D8, whereas the other catalysts showed a 2D projected distance of below 1 nm. Calculated values using the volume averaged particle size, nickel loading and support coverage, showed expected 2D projected distances of 6 nm for Ni-D8 and distances of below 1 nm for the other catalysts, in good agreement with the experimentally measured data (Table C.1). Subsequently, the Euclidian distance, reported in Table 6.1, was calculated by assuming the particles were maximally spaced throughout the covered support pore volume using hexagonal packing. While these were simplified estimates, they showed the Euclidean surface-to-surface distances for Ni-C9, Ni-C4 and Ni-C3 were similar at 7 nm. The particles in Ni-D8 were further apart, calculated at 16 nm. For Ni-C9, measurements could not be made due to the nature of the aggregates making it extremely difficult to get reliable values, thus only the Euclidean values were calculated.

Table C.1. Measured nickel particle sizes and EDX nickel weight loadings of fresh and spent catalysts and the measured and calculated nearest neighbor surface to surface distance of fresh catalysts in a 2D projection.

	Volume-weighted nickel particle size (TEM)			2D projected nearest neighbor distance (fresh catalyst)[a]		Nickel weight loading inside catalyst grains (EDX)		
Catalyst	Initial (nm)	15 h (nm)	150 h (nm)	Measured (nm)	Calculated (nm)	Fresh (wt. %)	15 h (wt. %)	150 h (wt. %)
Ni-D8	7.5	8.2	9.0	4.1 (±2.7)	6.3	20.8% (±1.5)	20.3% (±1.1)	16.9% (±1.5)
Ni-C9	9.0	9.9	11.1	n.d.	n.d.	n.d.	n.d.	n.d.
Ni-C4	4.3	13.9	19.8	0.6 (±1.2)	0.3	21.7% (±1.2)	18.3% (±4.5)	23.0% (±2.7)
Ni-C3	3.2	16.6	22.4	0.9 (±1.2)	0.6	18.7% (±2.4)	20.1% (±0.9)	15.6% (±3.0)

[a]The resulting Euclidean distances in 3D space are found in Table 6.1 from chapter 6.

Elemental Analysis. Elemental analysis was performed for the 'inside' of the catalyst grains by EDX from thin sections obtained by ultramicrotomy by placing the objective aperture such that the electron beam only illuminated the inside of the catalyst grain. By doing this, the nickel to silica ratio was measured and converted into the nickel weight loading for the

fresh catalysts, as well as for the spent catalysts after 15 and 150 h. Between 5 and 10 catalyst grains were measured, resulting in the average values shown in Table C.1. For the fresh catalysts, averages between 19 and 22 wt.% were found, in good agreement with the nominal loading of 21 wt.%. After catalysis, the grains showed more variation, with nickel weight loadings lying between 16 and 23 wt.%. Whenever the loading was much lower than the nominal value, large nickel particles of a few hundred nanometers were also found on the external surface of the catalyst grain. If the EDX spot was enlarged to encompass both the inside and the outside of the grain, Ni/Si ratios that corresponded closely to 21 wt. % were found again. Thus, this could indicate that some nickel had migrated from the inside to the outside of the grain, but did not leave the reactor. Moreover, due to the preparation of the catalysts some heterogeneity is expected in the metal loading which would result in a grain-to-grain variability. Statistical fluctuations are therefore expected in the EDX measurements. This could explain the reason for which Ni-C4 exhibited more nickel than expected after 150 h on stream (23 wt.% compared to the 21 wt.% nominal loading).

Because volatile $Ni(CO)_4$ species play an important role in the present paper, independent calculations were performed to find the maximum possible loss via vapor phase nickel carbonyl from the reactor. Assuming a nickel particle size of 8 nm in diameter, the $Ni(CO)_4$ partial pressure was found be around 0.1 Pa (see Equation C.8). Thus, the maximum nickel carbonyl that can be carried away by 6 mL(STP)/min, which was the flow through the reactor, was about $5\ 10^{-12}\ mol_{Ni(CO)4}\ s^{-1}$. However, 10 mg of catalyst with 20 wt.% of nickel contains $3.4\ 10^{-5}$ mole of nickel, so that during 150h on stream the catalyst can lose at most about 8 wt.% nickel. This value over-estimates the actual loss of nickel for the following two reasons. First, it assumes that the diffusion of the nickel carbonyl from the catalyst grains to the gas flow is infinitely rapid. Second, the assumed value of 8 nm corresponds to a supersaturation of 2.6, which is larger than the one prevailing during most of the time on stream (see Figure C.10). Therefore, the amount of nickel lost from the reactor via nickel carbonyl must have been less than 8 wt.%, and was considered insignificant compared to the observed deactivation of 50 to 90%.

Additional TEM, Particle Size and Pore Size Distributions. TEM of the spent catalysts after 15 h are provided in Figure C.2 (TEM of the fresh catalysts and spent catalysts after 150 h can be found in Figures 6.1 and 6.xxx of chapter 6, respectively). The pore size distribution of the silica gel support is shown in Figure C.3, calculated from both the BJH adsorption and desorption isotherms. Because the BJH method was developed for ideal cylindrical pores and is known to underestimate the actual pore size of highly heterogeneous materials such as silica gels, the pore size distribution was estimated between 5 and 15 nm.

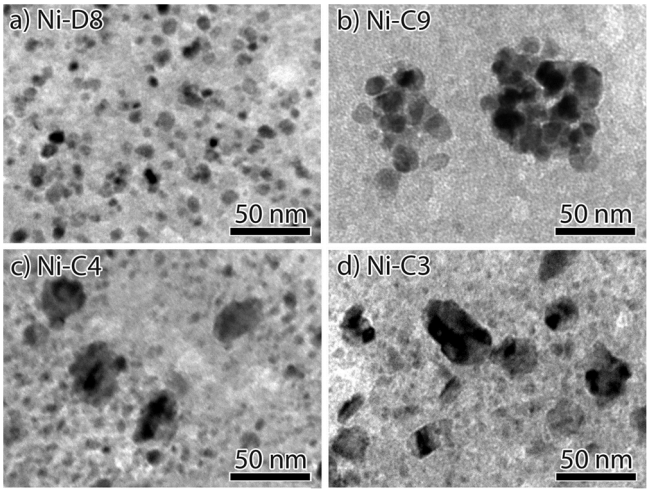

Figure C.2. TEM of microtomed 50 nm slices of catalyst particles after 15 hours on-stream. (a) Ni-D8, (b) Ni-C9, (c) Ni-C4 and (d) Ni-C3.

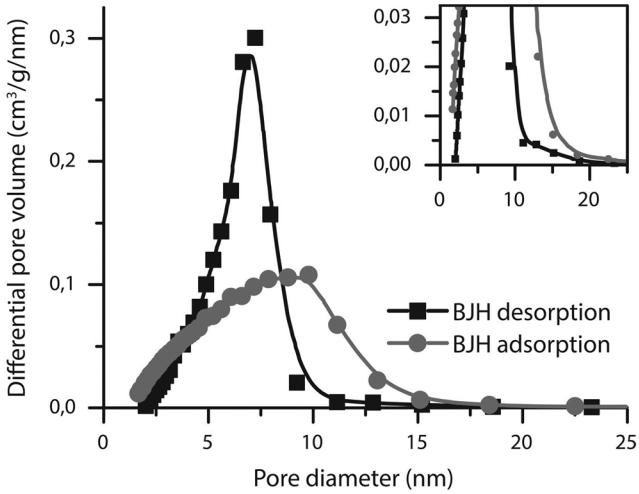

Figure C.3. BJH pore size distribution plotted from the N_2-physisorption desorption isotherm (black squares) and adsorption isotherm (grey circles). Close inspection shows pores up to 15 - 20 nm exist (inset).

This estimate is added as a guide to the eye in Figure C.4, which shows the area-weighted particle size distributions of each catalysts at the various stages. Note that the particle sizes from which the distributions in Figure C.4 were obtained were likely overestimated due to projection effects, whereby several overlapping particles are mistaken for one large particle. This measurement bias is particularly evident in the samples with medium particles Ni-C9 and Ni-D8, in which the tails of the size distributions in the fresh catalysts erroneously extend beyond the pore size. These few outlier particles, however, have no significant effect on the average particle sizes. The total number of particles measured, and the number-, area- and volume-weighted averaged particles sizes for each catalyst are reported in Table C.2. The large difference observed between the number-weighted and volume-weighted average for Ni-C3

and Ni-C4 is indicative of many small particles that still exist, while the majority of the nickel was located in large particles.

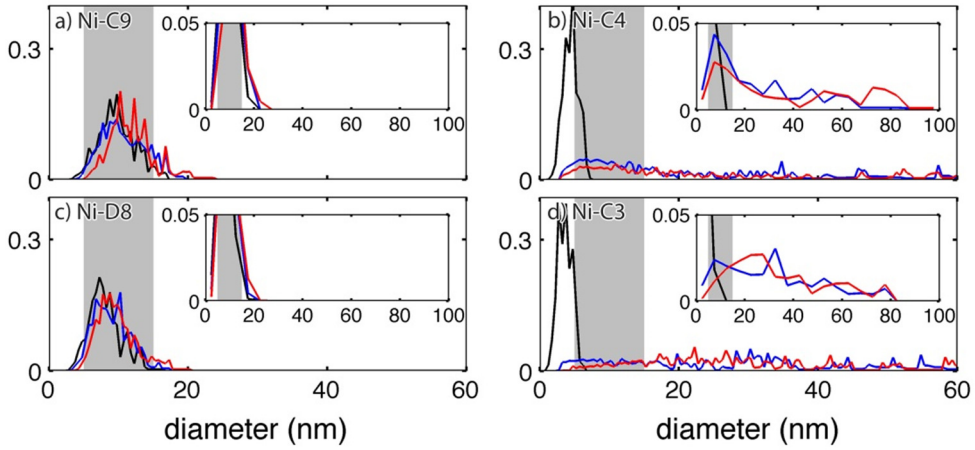

Figure C.4. Area-weighted particle size distributions of catalysts (a) Ni-C9, (b) Ni-C4, (c) Ni-D8 and (d) Ni-C3, obtained from TEM for the fresh catalyst (black), after 15h on stream (blue) and after 150h on stream (red). The distributions have been normalized to the total area of the particles. The insets plot the same distributions over a wider range of particle diameters. The grey area is a guide to the eye extending from 5nm to 15nm in diameter, suggestive of the probable pore size distribution of the support.

Table C.2. Total number of particles measured for each catalyst at various times on–steam, and the corresponding number-, area- and volume-weighted average particle sizes.

	Ni-C9			Ni-D8			Ni-C4			Ni-C3		
Time (h)	0	15	150	0	15	150	0	15	150	0	15	150
Measured	316	365	333	472	478	465	1895	1988	2043	2682	1329	904
Number	8.3	9.0	10.3	6.8	7.5	8.3	3.7	7.7	8.8	2.5	8.4	14.2
Area	8.7	9.4	10.7	7.2	7.9	8.6	4.0	10.1	12.8	2.9	12.0	18.0
Volume	9.0	9.9	11.1	7.5	8.2	9.0	4.3	13.9	19.8	3.2	16.6	22.4

Ordered Mesoporous Catalyst. SBA-15 with a pore size of 8.3 nm was synthesized following the procedure outlined elsewhere.[1] Melt infiltration with nickel nitrate was followed directly by a calcination in 1% v/v NO/N_2 resulting in a catalyst similar to Ni-C4 with no large particles on the in- or outside. The catalyst was reduced in-situ and tested for the methanation reaction for 15 h. Afterwards, a tilt series of 11 images from -55° to +55° was taken from which a low resolution 3D reconstruction was made, showing many large particles with a volume-weighted average particle size of 29.6 nm (number average 22.4 nm, area-weighted average 25.6 nm, 204 particles measured) inside the SBA-15 grain and a few on the external surface.

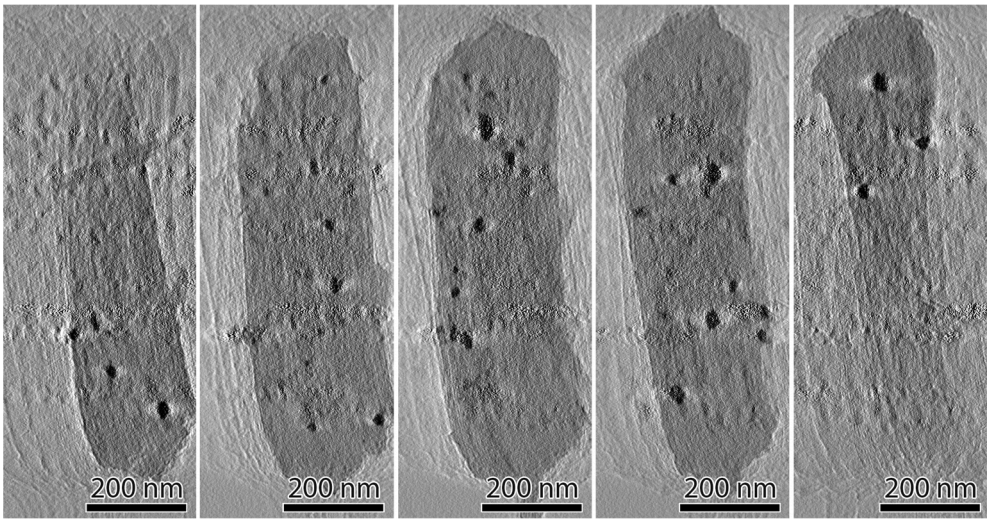

Figure C.5. Five slices from the reconstructed tomogram of Ni/SBA-15 after 15 hours on-stream. Many large nickel particles are observed inside of the ordered mesopores, the particles being much larger than the pore diameter of the support.

CATALYST DEACTIVATION

The experimental activity versus time curves were fitted with a General Power Law Expression (GPLE) of the form[2]:

$$da/dt = -k_D \cdot (a-a_s)^n \qquad \text{(Equation C.1)}$$

where $a(t)$ is the normalized activity as a function of the time-on-stream, a_s is the normalized activity at equilibrium when $t \rightarrow \infty$, k_D is the deactivation rate constant and the exponent n is either 1 or 2. Equation C.1 can be integrated and rewritten to yield a linear relationship between the normalized activity and time-on-stream:

$$(a-a_s)^{1-n} = (n-1) \cdot k_D \cdot t + 1 \qquad \text{(Equation C.2)}$$

such that the slope of $(a-a_{eq})^{1-n}$ gives the deactivation rate constant. Figure C.6 shows this relation plotted assuming a second-order deactivation for each catalyst (n = 2). The values of a_s were fitted as a parameter using Equation C.1, finding values of 0.25, 0.20, 0.03 and 0.06 for D8, C9, C4 and C3, respectively. The observed fits do not go through $a(0)$ = 1, which was attributed to fast initial deactivation in the first few hours, which has previously been tentatively attributed to carbon buildup occurring in the initial stages of catalysis.[3] Due to this anomaly, the fits were taken starting at t = 5 hours.

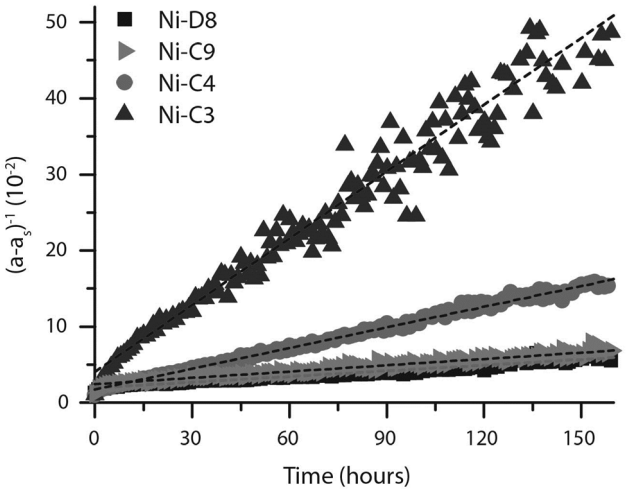

Figure C.6. Normalized activities a minus the activities at equilibrium a_s as a function of time-on-stream, fitted with a GPLE (equation C.2) with $n = 2$.

NICKEL CARBONYL PRESSURE AND DIFFUSION

The global reaction for the formation of $Ni(CO)_4$ is the following

$$Ni(CO)_4 \leftrightarrow Ni + 4CO \qquad \text{(Equation C.3)}$$

which, at a given temperature, results in the following equilibrium condition

$$P_{Ni(CO)4} = KP_{CO}^4 \qquad \text{(Equation C.4)}$$

where the equilibrium constant is expressed in the usual way in terms of the chemical potentials of the various species

$$K = exp\left(\frac{-1}{k_B T}\left[\ \mu^0_{Ni(CO)4} - \ \mu_{Ni} - 4\,\mu^0_{CO}\right]\right) \qquad \text{(Equation C.5)}$$

the superscript ^{0} refers to atmospheric pressure. In the case of nanometer-sized nickel particles, the chemical potential μ_{Ni} has to be corrected for the Laplace pressure. In other words

$$\mu_{Ni} = \mu^0_{Ni} + \Omega\frac{2\gamma}{R} \qquad \text{(Equation C.6)}$$

where Ω is the volume of a nickel atom, γ is the surface tension, and R is the radius of curvature of the metal surface. This results in the following size-dependent relation

$$P_{Ni(CO)4} = K^0 \mathrm{e}^{\lambda/R} P_{CO}^4 \qquad \text{(Equation C.7)}$$

where K^0 is the equilibrium constant corresponding to a macroscopic nickel particle, and $\lambda = 2 \gamma \Omega / (k_B T)$. Equation C.7 is sometimes referred to as Kelvin's equation, or as the Gibbs-Thomson equation.

The value of K^0 at 500 K was calculated using thermodynamic data from the literature and HSC Chemistry 7.1,[4] namely $\Delta H = -1.61\ 10^5$ J/mol and $\Delta S = -4.10\ 10^2$ J/mol/K (at a pressure P = 1 atm), which led to $K^0 = 2.784\ 10^{-5}$ atm^{-3}. As for λ, the following values were used. From the density and molar mass of nickel (ρ = 8.908 g cm^{-3} and M = 58.7 g mol^{-1}) the atomic volume was found to be Ω = 10.94 Å^3/atom. Combining that volume with the surface tension of nickel γ = 2.45 J m^{-2},[5] one finds λ = 7.8 nm at 500 K. However, the surface tension of metals is significantly reduced in presence of chemisorbing molecules; the order of magnitude of the reduction is a factor 2.[6] Applying that corrective factor to the surface tension of nickel led to λ = 3.9 nm. This is the value used in the main chapter.

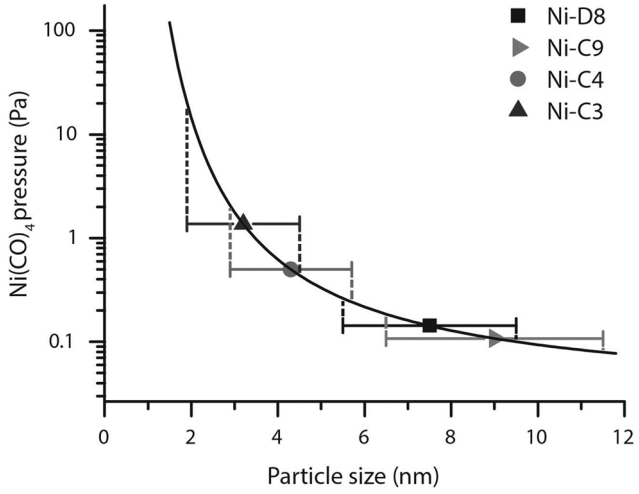

Figure C.7. The $Ni(CO)_4$ partial pressure as a function of particle size according to the Kelvin equation. Dotted lines indicate the $Ni(CO)_4$ partial pressure at the particle size ± the standard deviation as determined by TEM.

The black curve in Figure C.7 shows the dependency of the equilibrium pressure of $Ni(CO)_4$ at 500 K with P_{CO} = 33 kPa, as a function of the particle size. This shows that the pressure can become 50 times larger for particles of 3 nm due to their large curvature, such as found in Ni-C3. From this, the flux between two particles with a size plus and minus one standard deviation as found in TEM was calculated for each fresh catalyst using the average interparticle distances (Table 6.1). Even assuming a conservative gas diffusion coefficient of 0.01 cm^2/s the time it would take for a particle with a size $d_{average} - d_{stdv}$ to be completely volatized and transferred to a particle with size $d_{average} + d_{stdv}$ varies from 0.2 s for Ni-C9 to 0.1 ms for Ni-C3. These timescales are much shorter than the observed deactivation timescale.

CALCULATED ACTIVITIES AND SIZE DISTRIBUTIONS

Two different growth models, based on unhindered growth and hindered growth were used to calculate the expected time-dependent activity behavior and expected particle sizes. More information on these models can be obtained in the Supporting Information of the published article. The time-dependent activities of all catalysts predicted from the unhindered growth model are shown in Figure C.8. This model predicted a rapid deactivation for all catalysts in dependent of their initial particle size distributions. After about 3 h on-stream, the model predicted all the catalysts should have the same activity (see inset).

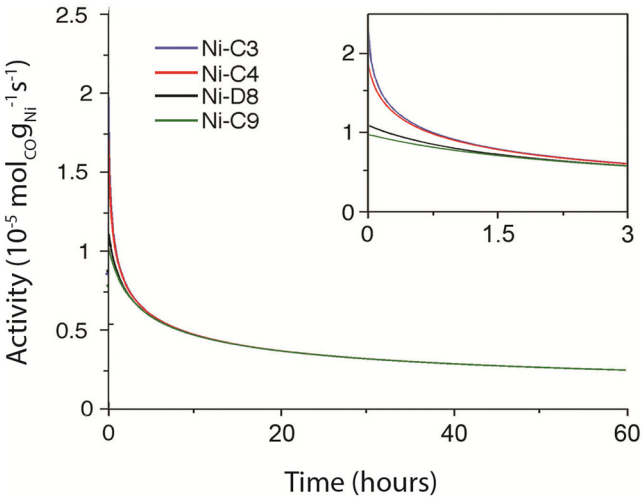

Figure C.8. Calculated deactivation curves of catalysts Ni-C3, Ni-C4, Ni-D8 and Ni-C9 assuming unhindered growth of the nanoparticles. The inset is a magnified view of the early time behavior showing that the effect of the initially different particle size distributions is short-lived: after about 3 h, the four curves are indistinguishable.

Figure C.9 shows the same distributions non-normalized. Note that the predicted size distributions were identical for each catalyst after 15h on-stream. The distributions predicted by the unhindered growth model were in fair agreement with the experimental distributions of Ni-C3 and Ni-C4. Expectedly, the model was unable to account for the stable particle size distributions of Ni-C9 and Ni-D8.

The right side of Figure C.9 shows the particle size distributions predicted by the confined growth model. As expected the latter distributions converged to a narrow function centered on the pore size (assumed to be exactly 10 nm for the calculation). The finite breadth of the distribution resulted from both the elastic deformation of the support and from the numerical dissipation of the finite-volume scheme used to integrate the equations numerically. The agreement of the confined model was fair for Ni-C9 and Ni-D8, but not for Ni-C3 and Ni-C4. The slight increase in particle size that was experimentally observed for Ni-C9 and Ni-D8, and which was not accounted for by the model, could result from a variety of phenomena. For example, nickel could be transported from the particles confined in smaller pores towards those confined in larger pores. Another possible explanation would be the viscoelasticity of silica, which may lead to a slow deformation of the support under constant pressure.

The unhindered growth model alone did not account for the presence of small particles in the experimental distributions of Ni-C4 (around 10 nm, see Figure C.4), which coexisted with the large particles that were predicted by the model. This hinted at the succession of unhindered and confined growth modes for the catalysts with small particles.

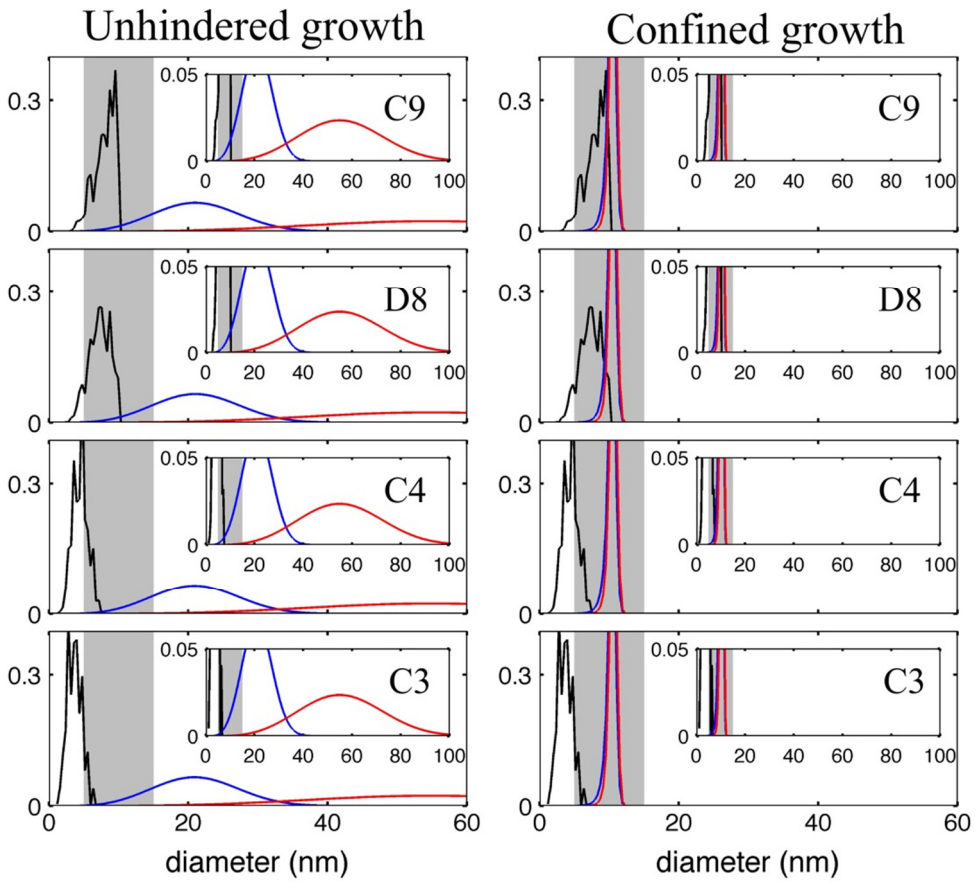

Figure C.9. From top to bottom: calculated area-weighted particle size distributions of catalysts Ni-C9, Ni-D9, Ni-C4 and Ni-C3. Black line: starting experimental distribution of the fresh catalyst, identical to Figure C.4 but cut to the assumed pore size of 10 nm. Blue line: Calculated distribution after 15 h on stream. Red line: Calculated distribution after 150 h on stream. The distributions have been normalized to the total area of the particles. The distributions on the left assume unhindered growth, while confined growth is assumed on the right. The insets plot the same distributions over a wider range of particle diameters. The grey area is the same guide to the eye as in Figure C.4.

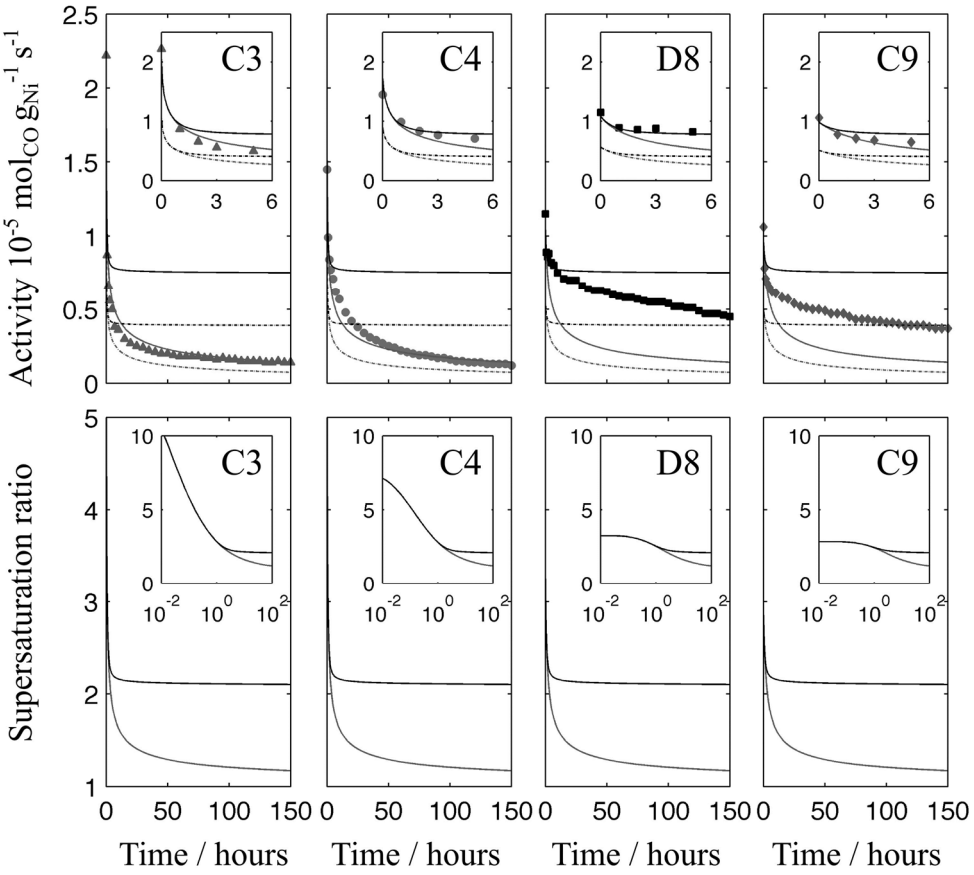

Figure C.10. Top row: comparison of the experimental activities of catalysts Ni-C3, Ni-C4, Ni-D8 and Ni-C9 (from left to right) with the predictions of the unhindered (grey line) and confined (black line) growth model. The solid lines are calculated from the TOF of the fresh catalysts and the dashed line from the TOF of the spent catalyst. The insets are close-up view on the first 6 hours. Bottom row: corresponding supersaturation ratio *S* calculated in the case of unhindered growth (grey (bottom) line) and of confined growth (black (top) line). The same data is plotted on semi-logarithmic scales in the insets to highlight the short-time variation of *S*(t).

The activities corresponding to the discussed particle size distributions are shown in Figure C.10 (top row), which is similar to Figure 6.5 of chapter 6, only extended to all catalysts. The corresponding time-dependent supersaturation ratios are plotted on the bottom row, for both the unhindered and the confined growth models. The supersaturation was found to depend on the initial particle size distribution mainly during the first hour on-stream. For longer times, the supersaturation only depended on the growth regime, unhindered or confined. Whether the nanoparticles were able to break the support or not depended on the supersaturation during that short initial period. Even though the average particle size of Ni-C3 and Ni-C4 may become similar to that of Ni-D8 and Ni-C9 at a later point in time, it was the presence of the

few particles that broke though the pores that was responsible for the further deactivation of Ni-C3 and Ni-C4. This notably explains the crossing of the activity curves shown in the insets of Figures 6.3 and 6.5.

ADDITIONAL REFERENCES

(1) Sayari, A.; Han, B.-H.; Yang, Y. *J. Am. Chem. Soc.* **2004**, *126*, 14348.
(2) Bartholomew, C. H. *Appl. Catal. A Gen.* **1993**, *107*, 1.
(3) Agnelli, M.; Kolb, M.; Mirodatos, C. *J. Catal.* **1994**, *148*, 9.
(4) Goldberger, W. M.; Othmer, D. F. *Ind. Eng. Chem. Proc. DD* **1963**, *2*, 202.
(5) Van Stiphout, P. C. M.; Stobbe, D. E.; V.D. Scheur, F. T.; Geus, J. W. *Appl. Catal.* **1988**, *40*, 219.
(6) Ouyang, R.; Liu, J.-X.; Li, W.-X. *J. Am. Chem. Soc.* **2013**, *135*, 1760.

List of Publications and Presentations

THIS THESIS IS BASED ON

P. Munnik, P. E. de Jongh, K. P. de Jong: *"Recent Developments in the Synthesis of Supported Catalysts"*
Chemical Reviews, Proposal accepted, article submitted

P. Munnik, P. E. de Jongh, K. P. de Jong: *"Control and Impact of the Nanoscale Distribution of Supported Cobalt Particles Used in Fischer-Tropsch Catalysis"*
Journal of the American Chemical Society **2014**, *136*, 7333-7340.

P. Munnik, N. A. Krans, P. E. de Jongh, K. P. de Jong*: "Effects of Drying Conditions on the Synthesis of Co/SiO_2 and Co/Al_2O_3 Fischer-Tropsch Catalysts"*
ACS Catalysis, **2014**, *4*, 3219-3226.

P. Munnik, M. E. Z. Velthoen, P. E. de Jongh, K. P. de Jong, C. J. Gommes: *"Nanoparticle Growth in Supported Nickel Catalysts during Methanation Reaction – Larger is Better"*
Angewandte Chemie – International Edition **2014**, *53*, 9493-9497.

P. Munnik, T. M. Eggenhuisen, H. Talsma, P.E. de Jongh, K.P. de Jong: *"Freeze-Drying for Controlled Nanoparticle Distribution in Co/SiO_2 Fischer–Tropsch Catalysts"*
Journal of Catalysis **2013**, *297*, 306-313.

OTHER PUBLICATIONS

P. Munnik, M. Wolters, A. Gabrielsson, S.D. Pollington, G. Headdock, J.H. Bitter, P.E. de Jongh, K.P. de Jong: *"Copper Nitrate Redispersion to Arrive at Highly Active Silica-Supported Copper Catalysts"*
Journal of Physical Chemistry C **2011**, *115*, 14698-14706.

M. Wolters, P. Munnik, J.H. Bitter, P.E. de Jongh, K.P. de Jong: *"How NO Affects Nickel and Cobalt Nitrates at Low Temperatures To Arrive at Highly Dispersed Silica-Supported Nickel and Cobalt Catalysts"*
Journal of Physical Chemistry C **2011**, *115*, 3332-3339.

M. Wolters, I.C.A. Contreras Andrade, P. Munnik, J.H. Bitter, P.E. de Jongh, K.P. de Jong: *"Impact of NO on the decomposition of supported metal nitrate catalyst precursors and the final metal oxide dispersion"*
Studies in Surface Science and Catalysis **2010**, *175*, 69-76.

E.S. Vasiliadou, T.M. Eggenhuisen, P. Munnik, P.E. de Jongh, K.P. de Jong, A.A. Lemonidou: *"Synthesis and Performance of Highly Dispersed Cu/SiO_2 Catalysts for the Hydrogenolysis of Glycerol"*
Applied Catalysis B **2014**, *145*, 108-119.

PATENT APPLICATIONS

M. Wolters, P. Munnik, J.H. Bitter, P.E. de Jongh, K.P. de Jong: *"Method for Producing a Supported Metal Nitrate"*
WO 2010109216 A1

ORAL PRESENTATIONS

P. Munnik, P. E. de Jongh, K. P. de Jong: *"Co/SiO_2 Fischer-Tropsch Catalysts: Origin and Impact of Nanoscale Cobalt Distribution and Aggregation"*
Debye Lecture, Utrecht, Netherlands, May 7 (2014)

P. Munnik, M. E. Z. Velthoen, C. J. Gommes, P. E. de Jongh, K. P. de Jong: *"Structure Stability Relationships of Supported Nickel Catalysts for Methanation"*
15th Nederlands Catalysis and Chemistry Conference (NCCC), Noordwijkerhout, Netherlands, March 10-12 (2014)

P. Munnik, P. E. de Jongh, K. P. de Jong: *"Co/SiO_2 Fischer-Tropsch Catalysts: Origin of Nanoscale Cobalt Distribution and Aggregation"*
13th Europacat, Lyon, France, September 1-7 (2013)

P. Munnik, P. E. de Jongh, K. P. de Jong: "*Co/SiO_2 Fischer-Tropsch Catalysts: Origin of Nanoscale Cobalt Distribution and Aggregation"*
23rd North American Meeting (NAM), Louisville, America, June 2-7 (2013)

P. Munnik, P. E. de Jongh, K. P. de Jong: "*Co/SiO_2 Fischer-Tropsch Catalysts: Origin of Nanoscale Cobalt Distribution and Aggregation"*
14th Nederlands Catalysis and Chemistry Conference (NCCC), Noordwijkerhout, Netherlands, March 11-13 (2013)

P. Munnik, T. M. Eggenhuisen, P. E. de Jongh, K. P. de Jong: *"Freeze-Drying for Uniform Nanoparticle Distribution in Co/SiO2 Fischer-Tropsch Catalysts"*
Syngas Convention, Cape Town, South Africa, April 1-4 (2012)

P. Munnik, T. M. Eggenhuisen, P. E. de Jongh, K. P. de Jong: *"Freeze-Drying for Uniform Nanoparticle Distribution in Co/SiO2 Fischer-Tropsch Catalysts"*
13th Nederlands Catalysis and Chemistry Conference (NCCC), Noordwijkerhout, Netherlands, March 5-7 (2012)

POSTER PRESENTATIONS

P. Munnik, P.E. de Jongh, K.P. de Jong: *"Control and Impact of the Nanoscale Distribution of Supported Cobalt Particles in Fischer-Tropsch Catalysis"*
BASF Research Forum 2014, Antwerp, Belgium, March 25-26 (2014)

P. Munnik, P.E. de Jongh, K.P. de Jong: *"Control and Impact of the Nanoscale Distribution of Supported Cobalt Particles in Fischer-Tropsch Catalysis"*
13th Europacat, Lyon, France, September 1-7 (2013)

P. Munnik, P.E. de Jongh, K.P. de Jong: *"Co/SiO_2 Fischer Tropsch Catalysts: Impact of Nanoscale Cobalt Distribution on Catalysis"*
10th Natural Gas Conversion Symposium (NGCS), Doha, Qatar, 2-7 March (2013)

P. Munnik, T.M. Eggenhuisen, P.E. de Jongh, K.P. de Jong: *"Freeze-Drying for a Uniform Cobalt Distribution in Co/SiO2 Fischer-Tropsch Catalysts"*
15th International Congress on Catalysis (ICC), Munich, Germany, July 1-6 (2012)

P. Munnik, P.E. de Jongh, K.P. de Jong: *"Low-Angle Dark Field TEM of Supported Cobalt Oxide Clusters"*
2011 NVvM Materials Science Meeting, Eindhoven, Netherlands, November 10 (2011)

Dankwoord

These past years have truly flown by, and now all that is left is to thank everyone who not only helped make this thesis possible, but also made my time in Utrecht extremely enjoyable and fun, both at and outside of work. I will always look back fondly at these past years.

Allereerst wil ik **Krijn** bedanken voor een bijzonder prettige samenwerking. Je hebt mij altijd aangemoedigd creatief te zijn en mij erg vrij gelaten wat ik heel prettig vond. Ik heb van jou geleerd hoe je goed onderzoek moet doen, maar ook inhoudelijk wist je gesprekken en discussies altijd weer naar een hoger niveau te brengen. Op een conferentie zei een collega PhD student van een buitenlandse universiteit ooit "*man, professor de Jong, he is an expert in* everything", en je weet al die kennis ook heel goed over te brengen.

Petra, jij ook heel erg bedankt voor al je hulp en kennis. Ook jij wist me altijd te inspireren. Dit proefschrift en de gepubliceerde artikelen zijn door je kritische blik en "out-of-the-catalysis-box thinking" veel beter en begrijpelijker geworden, ook dankzij jou oog voor detail betreft schrijfwijze en opmaak ("*wat staat er nou écht in die zin*"). Ik heb me zelfs al betrapt hetzelfde commentaar dat ik van jou vaak kreeg aan anderen uit te delen.

De CatPrep en SynGas teams zijn erg belangrijk geweest om ideeën, problemen en resultaten te delen. **Mariska**, van jou heb ik de basis van de katalysatorbereiding geleerd. **Tamara**, ik heb met veel plezier met jou samengewerkt en heb veel geleerd van onze samenwerking wat tot mijn eerste experimentele hoofdstuk heeft geleid (hoofdstuk 3). **Hirsa**, you helped me setup my first catalytic testing installation (FT2) and taught me a lot about the practical aspects of catalytic testing. **Gonzalo**, your knowledge on both catalyst preparation and syngas conversion has been extremely valuable. I also enjoyed tackling the concept that was ultramicrotomy together with you and **Jovana**, which proved to be an invaluable technique that is used extensively throughout this thesis. **Arjan**, het was erg fijn om altijd ideeën te kunnen delen en te kunnen sparren, en we hebben vele problemen met onze nieuwe katalytische testing unit succesvol opgelost samen met **Thomas**. Ook discussies met **Roy** brachten altijd weer interessante ideëen en aspecten naar boven. **Cedric**, even though it took us a while to get it right and convince the reviewers, without you chapter 6 would never have been what it is now, and I believe this was only the beginning of what your knowledge on physical modelling and out-of-the-box thinking can contribute to the group.

Dit onderzoek zou niet mogelijk zijn geweest zonder de vaste staf en technici van de groep. **Dymph** en **Monique**, jullie waren altijd heel erg behulpzaam en ook nog altijd vrolijk. **Ad M**, zonder jou zou het lab zeker instorten. **Ad E.**, jij zorgt dat alles veilig gebeurt en stond altijd open voor vragen. **Fouad**, bedankt voor alle hulp met de DRIFT. **Rien**, je kennis over hogedruk was onmisbaar bij alle nieuwe hogedruk apparatuur. **Mies**, je geduld bij het

vriesdrogen, alsook de karaoke sessies zijn legendarisch. Ook wil ik **Hans** bijzonder bedanken voor alle hulp bij de elektronenmicroscopen, je was altijd bereid vragen te beantwoorden, dacht altijd mee en ik kon altijd aankloppen voor een probleem of een gezellig praatje als afwisseling van het donkere microscopiehok. Ik hoop dat je niet overrompeld wordt met microtomy-verzoekjes nu ik het niet meer doe. Ook **Chris, Elly** en **Marjan** wil ik bedanken voor alle EM, microtoom en XRD gerelateerde hulp. **Harry**, bij jou kon je altijd aankloppen en je was de vaste schakel bij de koffie en lunchpauzes die ik het laatste jaar zeer gemist heb.

Ik heb met veel plezier vier studenten mogen begeleiden tijdens mijn promotie. **Carlos**, your literature study on FT was very helpful throughout my PhD. **Marjolein**, het heeft een hele tijd geduurd voordat we het begrepen, maar uiteindelijk hebben jou experimenten tot een mooie publicatie geleid (hoofdstuk 6). **Nynke**, ook jou werk heeft zijn weg gevonden in een succesvolle publicatie (hoofdstuk 5). **Ilse**, ook jij had erg interessante resultaten maar helaas heb ik geen tijd meer gehad om dit verder te onderzoeken. Ik heb jullie allemaal met veel plezier begeleid, en wens jullie allemaal veel succes met jullie eigen onderzoek.

Even though it was a long time ago in a building far far away, I would like to thank my office mates with whom it all began. **Upa**, **Hirsa**, **Inge**, and **Rene**, you made me feel welcome and at home right away. Also thanks to **Jesper**, **Hendrik**, **Sophie**, **Mustafa** and **Yuen** whom I enjoyed sharing the office space with, as well as everyone that came by for a chat at my lovely corner desk!

Na een lange dag in het lab is het heerlijk om te gaan sporten, en ik wil alle sporters dan ook heel erg bedanken! **Clare** en **Ilona**, maar vooral **Annelie**, jullie stond altijd aan de andere kant van dat touw om me weer op te vangen en ik ga die vele uren in de klimhal zeker missen. **Marleen**, ik vond het heerlijk om rondjes om de uithof te skeeleren. **Ilona**, krav-maga was een leuk avontuur en ik vond het altijd heerlijk om mee te gaan naar **Rufus**!

I also want to thank everyone already mentioned and all the other colleagues with whom I enjoyed many coffee breaks, borrels, barbeques, park visits, parties and general awesome times: **Rob**, **Joe**, **Tomas**, **Daniel**, **Zoran**, **Carlo**, **Arjen**, **Wenhao**, **Qingyun**, **Rafael**, **Korneel**, **Dimitrije**, **JX**, **Evelien**, **Joris**, **Frank**, **Peter N**, **Zafar**, **Rogier**, **Robin**, **Nazila**, **Gang**, **Peter B**, **Jeroen**, **Ramon**, **Sam**, **Jinbao**, **Elena**, **Gareth**, **Fiona**, **Chris**, **Jan-Philip**, **Matti**, **Fernando**, **Luis**, **Ines**, **Javi**, **Davide**, **Piter**, **Dilek**, **Anne**, **Bart**, and anyone that I may have unintentionally missed. Thank you all, these have truly been amazing years that would not have been possible without all of you.

Naast alle collegas wil ik ook **mijn ouders** bedanken, jullie hebben mij altijd vrij gelaten te doen wat ik wil en hebben mij altijd ondersteund in mijn keuzes, hier ben ik heel erg dankbaar voor.

Als laatste **Ilona**, ik weet nog goed dat we de eerste nacht van het NCCC 2010 (mijn eerste werkdag) tot diep in de nacht op de banken in de lobby zaten met bier uit de automaat. Bedankt voor alles.

Peter

Curriculum Vitae

Peter Munnik was born on October 4th, 1985 in De Bilt, the Netherlands. After graduating from pre-university education at the Keesboeke school in Bilthoven, he started his undergraduate studies at the international University College Utrecht in 2003. After completing a thesis at the National Institute for Nuclear and High Energy Physics (NIKHEF) in Amsterdam, entitled "*Antares Shower Reconstructions*", He obtained a bachelor of Science with extensive coursework in chemistry, physics and mathematics in 2006. In 2007, he started the master program Nanomaterials: Chemistry and Physics at Utrecht University. During this time, he successfully completed an internship at the University of Syndey, Australia, on "*Ionic Liquid Gels for Selective Membranes*", and graduated *cum-laude* in 2010 with the thesis "*Influence of Gas Atmosphere on the Decomposition of Transition Metal Nitrates*" under supervision of M. Wolters and K.P. de Jong. Thereafter, he started as a PhD student in the group of Inorganic Chemistry and Catalysis under the supervision of P.E. de Jongh and K.P. de Jong, the results of which are described in this thesis.